Newcastle University

Doctor of Philosophy

Electron Transfer Rates at a Metal, a Semiconductor and a Semimetal

Author:

Shaun K. Cook

Supervisor:

Dr. Benjamin R. Horrocks

March 2013

Abstract

Electrochemical kinetic measurements were made on viologens in acetonitrile and ferrocene moieties bound to n-type silicon. A collection of hitherto unreported rate constants were obtained, and novel approaches to analysing electrochemical data proposed and demonstrated.

A series of methyl viologen derivatives (C1-5) were found to exhibit simple and reversible redox behaviour in acetonitrile with tetrabutylammonium hexafluorophosphate ($TBAPF_6$) at slow scan rates. The standard rate constants for the first one-electron reductions of these derivatives, and of methyl viologen, at a platinum electrode were measured successfully using electrochemical impedance spectroscopy (EIS) and fast scan voltammetry (FSV). Reasonable agreement between EIS and FSV data was observed, however, it was suspected that an electrode fouling process may have affected the EIS data. The shorter time scale of the FSV experiment meant it was less susceptible to any fouling processes that might have occurred. For the electron transfer reactions studied, the observed standard rate constants (prior to Frumkin correction) found via FSV ranged from 1.1×10^{-1} to 2.8×10^{-1} cm s^{-1}. The same electron transfer reactions were also studied at a bismuth electrode using FSV and the observed standard rate constants (prior to Frumkin correction) found to range from 1.3×10^{-2} to 4.7×10^{-2} cm s^{-1}. These measurements were to serve as a means of comparing electron transfer at two surfaces, and across a series of derivatives.

So that these rate constants might be Frumkin corrected and compared in a valid manner, the capacitance of the platinum and bismuth electrodes were measured in acetonitrile with $TBAPF_6$ (0.1M) over a range of potentials using EIS. It was found that the behaviour of both electrodes could be modelled as constant phase elements (CPE), as the capacitance observed depended upon the frequency at which the EIS experiment was performed. A method was proposed for determining the appropriate capacitance of a CPE on the basis of the time scale of the experiment being performed. These capacitance values were used to model both surfaces using the Gouy-Chapman-Stern (GCS) model. Due to the metallic nature of the bismuth surface, the GCS model was found to be appropriate for use at bismuth despite the semimetallic nature of bulk bismuth. The model was then used to predict the charge drop across the electrode/electrolyte interface at the standard potential of each molecule.

Following Frumkin correction, the rate constants at platinum were found to range from 1.8×10^{-4} to 1.6×10^{-3} cm s^{-1}, and those at bismuth from 1.1×10^{-4} to 1.9×10^{-3} cm s^{-1}. It was shown that the unexpectedly high rate constants observed at the semimetallic bismuth electrode could be explained by assuming that the metallic nature of the bismuth surface controls the behaviour of this electrode during electrochemical experiments. Furthermore, it was shown that the relative rate constants observed at the two surfaces could be predicted on the basis of the relative Fermi-level density of states at the two surfaces. The relative rate constants for the individual derivatives were found to show a possible dependence upon the molecular volume of the molecule. This was tentatively explained as being an effect of an orientation requirement becoming more significant for the larger molecules.

The kinetic and thermodynamic properties of a series of ferrocene containing monolayers upon n-type silicon were studied using cyclic voltammetry (CV) and light step photoelectrochemical chronoamperometry (PC). CV experiments found that in an aqueous environment, a higher coverage was observed when alkyl chains were present alongside ferrocenyl chains in the monolayers. This was explained as being due to hydrophobic environment created by the alkyl chains protecting the ferrocenyl groups from hydrolysis. Non-ideal behaviour was observed for the monolayers when they were studied by CV. A means of examining non-ideal cyclic voltammogram surface waves via the reduced and oxidised redox species activity coefficient ratio was proposed. Evidence found by this method indicated that the non-ideal behaviour was unlikely to be primarily due to repulsive interactions between surface ferrocenium moieties, and more likely to be primarily due to heterogeneity of environments in the monolayer.

It was found that a pseudo first-order rate constant for the oxidation of ferrocene could be measured easily using PC, but that the observed rate constant was affected by a back reaction involving conduction band electrons near the surface when the potential was close to flat-band potential. For ferrocene bound to silicon via an ethyl linker, an average rate constant of 1.4×10^3 s^{-1} was determined. For an ethenyl linker, a rate constant of 1.5×10^3 s^{-1} was determined. The lack of any significant difference between the determined rate constants suggests that the conductivity of the connecting linker has no effect on the rate of the ferrocene oxidation. When hexyl, octyl, and decyl chains were also present in the ferrocenyl monolayers, the effect of the back reaction was more significant, which was probably a result of the higher surface concentration of ferrocene in these mono-

layers. In addition to providing kinetic data, it was also shown that the PC experiment provided a simple means of determining whether a monolayer may discharge without illumination.

Acknowledgements

Firstly, I would like to express my deepest gratitude toward my supervisor Dr. Benjamin R. Horrocks, without whom none of the work presented here would have been possible. Gratitude is also owed to the molecular photonics department here at Newcastle University, particularly Dr. Peiyi Li for synthesising the methyl viologen derivatives which were crucial to much of this research, and to Prof. Andrew Benniston for donating those materials to our group. The work of Dr. Andrew Pike and Mufida Abdualla during the study of ferrocene monolayers was also essential and both deserve thanks for allowing me to take part in the analysis of their materials.

The work documented here was performed while working as part of the research group at Newcastle University's Chemical Nanoscience Laboratory. The expertise of CNL has been crucial throughout the project and the group have been a pleasure to work with.

Thanks also to my friends and family, in particular my parents, for their support.

Thanks to EPSRC for providing the funding that made this project possible.

Contents

Chapter 1

Introduction

1.1 Importance of Electron Transfer Reactions

An electron transfer (ET) reaction is an elementary reaction involving the transfer of one or more electrons from one species to another.[1] An example of such a reaction is shown in Scheme 1.1 which depicts the transfer of a single electron from an Fe^{2+} ion to a Ce^{4+} ion. The outcome of the reaction is the increase in the oxidation state of Fe, and the decrease of that of Ce. Despite their apparent simplicity, ET reactions are key to understanding a wide range of important phenomena including photosynthesis, the functioning of many enzymes and the operation of photovoltaic cells.

$$Fe^{2+} + Ce^{4+} \rightarrow Fe^{3+} + Ce^{3+} \tag{1.1}$$

Plants use sunlight as an energy source.[2] Photosystems within the plant absorb photons, causing electrons within the photosystems to be excited into high energy states. In an isolated photosystem the excited state will simply decay and the energy can be lost in the form of a photon. To prevent this, photosystems are surrounded by species which will accept these photoelectrons and subsequently transfer them to another acceptor, creating a spatial charge separation.[3] A series of donor/acceptor molecules which operate in this manner comprise what is known as an electron transport chain. These high energy electrons can then be used to drive the splitting of water. The electrons provided by the water splitting reaction can be used in the reduction of nicotinamide adenine dinucleotide phosphate ($NADP^+$) to give NADPH, which acts as a chemical energy storage molecule. At the same time, protons are produced which are driven through ATP synthase enzymes to drive the production of adenosine triphosphate (ATP) which also acts as a store of chemical energy.[4] For the process to occur with a high level of efficiency, each electron transfer reaction must happen at a rate which outpaces that of radiative decay of the excited states. The donor/acceptor species in the electron transport chain are structured so as to minimise the reorganisation energy barrier associated with changes in their oxidation states which ensures transfers are rapid, but relative energy levels of donor and acceptor states must provide an energy gradient steep enough to allow fast transfer across the chain but not so steep that excessive energy is wasted in the spatial separation of the charges. The energy levels of the high energy electrons within each species are also tuned to ensure electron transfer happens across the chain in one direction only.[5] Considerable effort has been expended in designing systems which mimic this process to produce high en-

ergy chemicals from a sunlight driven reaction.[6–12] Macromolecular systems of fine-tuned donor/acceptor systems which form electron transfer chains remain a highly active area of research.[11]

Many enzyme catalysed reactions involve an electron transfer reaction occurring between a substrate molecule and the active site of the enzyme. The study of these active sites can be aided by the investigation of electron transfers occurring between the active sites and electrodes via redox mediators.[13] Redox mediators are generally small molecules which diffuse rapidly between the electrode and an enzyme. The mediator can easily reach the active site of the enzyme, either accepting an electron from or donating an electron to the active site, and the oxidation state of the mediator can then be restored by the electrode, allowing it to participate in further redox chemistry with the active site of the enzyme.

Other areas where understanding of electron transfer phenomena is valuable include biosensors,[13–15] molecular electronics,[16] scanning electrochemical microscopy,[17] electrochemical synthesis,[18] and electrochemical molecular characterisation.[19,20]

1.1.1 Heterogeneous Electron Transfer Reactions

The development of electrochemical techniques and apparatus has meant that electron transfers occurring between a molecule and a metal surface may be carefully controlled and examined in great detail. The high Fermi-level density of states (DOS) of metals and their ability to carry a substantial current mean that these materials can act as an inexhaustible supply of electrons when an electronic

circuit is set up to allow electroneutrality to be maintained.[21] Scheme 1.2 depicts the reduction of a methyl viologen dication (MV^{2+}) by a metal surface. Electron concentration within the metal is essentially unchanged, the metal atoms themselves need not be considered in the reaction, and the reaction becomes pseudo first-order with respect to MV^{2+}. A material which supplies electrons or accepts electrons to drive a redox reaction at its surface in this way is known as the working electrode.[19]

$$MV^{2+} + e^- \rightarrow MV^+ \tag{1.2}$$

The rate of ET reactions can be quantified using the standard rate constant, k^0. At some potential, $E^{0'}$, the concentrations of the reduced and oxidised form of a reversible redox couple will be equal at equilibrium. At this potential the rate constants of the forward and backward reactions are equal and their value is k^0 by definition. The current that arises from a redox reaction is then a function of the applied potential, E, and is given by the Butler-Volmer equation, Equation 1.3.[19]

$$\begin{aligned} i = nFAk^0 \Bigg[C_{O(x=0)} \exp\left(-\alpha \frac{F(E-E^{0'}}{RT}\right) - \\ C_{R(x=0)} \exp\left((1-\alpha)\frac{F(E-E^{0'})}{RT}\right)\Bigg] \end{aligned} \tag{1.3}$$

The quantities $C_{O(x=0)}$ and $C_{R(x=0)}$ refer to the concentrations of the

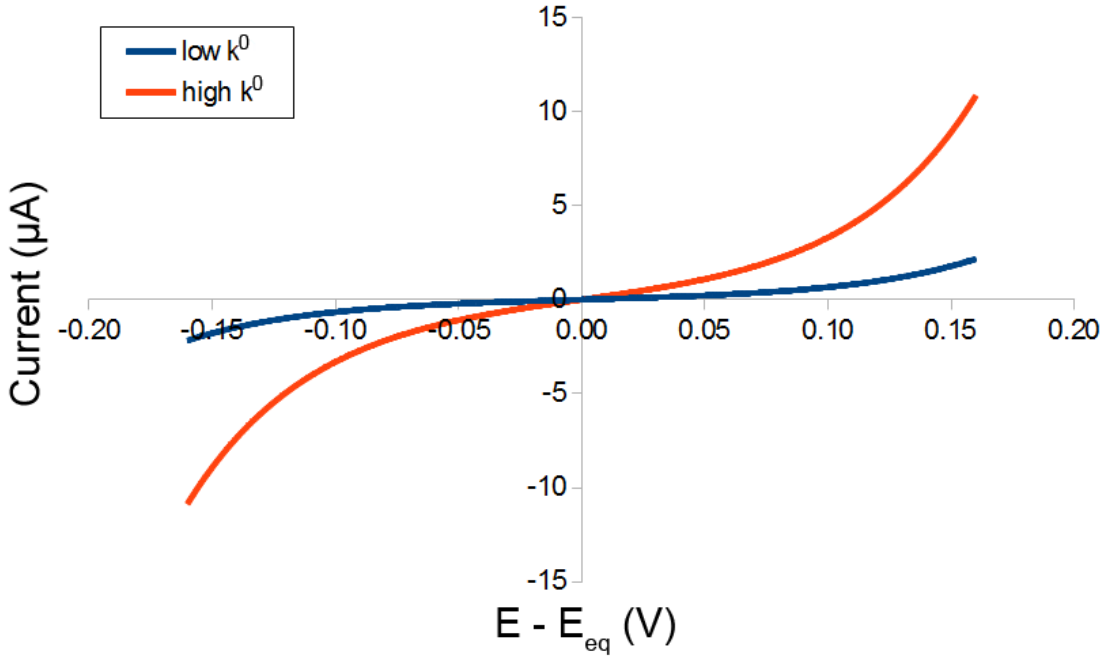

Figure 1.1: A plot showing how current varies with potential according to the Butler-Volmer model. Both plots are generated using $A = 1$ cm^2, $T = 298$K, $\alpha = 0.5$, and $C_O = C_R = 1$ mM. The blue line corresponds to $k^0 = 1$ cm s^{-1}. The red line corresponds to $k^0 = 5$ cm s^{-1}.

oxidised and reduced species at the surface of the working electrode. Practical use of the equation requires consideration of how these surface concentrations relate to the bulk concentrations of the species. The quantity α is known as the transfer coefficient, or the symmetry coefficient, and is a measure of how closely the transition state resembles the reduced form. The coefficient α takes a value between 0 and 1, and is usually between 0.3 and 0.7.[19]

The standard rate constant, k^0, is a characteristic property of the redox couple. Knowledge of k^0 values allows the comparison of rates of different electron transfer reactions. Figure 1.1 shows how current varies with potential according to the Butler-Volmer model for two different values of k^0. The parameters used to create the plots are given in the figure caption. The values that k^0 can take span

several orders of magnitude. For ferrocene, k^0 has been measured as being between 1 and 4 cm s^{-1} at Pt,[22] and values below 10^{-9} cm s^{-1} have been reported for other redox couples.[23] There exist a number of commonly used electrochemical techniques for measuring rapid electron transfer rates including electrochemical impedance spectroscopy (EIS),[24–28] fast scan voltammetry (FSV),[29–31] and scanning electrochemical microscopy (SECM).[32–36] Each technique has its own limitations and sources of systematic errors which can lead to very different values being determined for the same rate constant.[22,37] Some of these techniques will be discussed in more detail in Section 2.2.

There are several difficulties associated with the measurement of standard rate constants. The separation of electron transfer current from capacitive current presents a problem in many cases. The effect of resistance through the electrolyte solution may also cause a problem. A significant solution resistance will result in some of the measured potential difference being that which occurs through the electrolyte solution lowering the driving force behind, and thus the speed of, the electron transfer reaction. This effect is greatly reduced for ultramicroelectrodes, for which solution resistance is often negligible.[38–40] Ultramicroelectrodes are electrodes with a critical dimension of 25 μm or less. In the case of a disc electrode, this means a radius of 25 μm or less.

A number of factors effect the size of k^0 for a given electron transfer reaction. Of particular importance is the reorganisation energy associated with the reaction. The high k^0 associated with ferrocene oxidation can be largely attributed to the low reorganisation energy associated with that ET reaction. By contrast, the oxidation of aque-

ous Fe^{2+} to Fe^{3+} is associated with a relatively large reorganisation energy. An aqueous Fe ion will be surrounded by H_2O ligands, and upon a change in the oxidation state of the Fe, the Fe-O bond lengths change significantly. With a k^0 measured at 4.3×10^{-3} cm s^{-1} (at Pt in 0.1 H_2SO_4), the couple is significantly less facile than that of ferrocene.[41] The Fermi-level density of states (DOS) of the electrode surface is also an important factor. The DOS is the number of electronic states in a given energy range. The Fermi-level DOS of platinum is 1.2×10^{23} cm^{-3} eV^{-1},[42–45] which means that within a cubic centimetre of platinum, within an energy range of 1 eV around the Fermi-level, there are 1.2×10^{23} available electronic states. The DOS can be thought of as a measure of electrons available to carry charges or participate in ET reactions. It has been shown that even for a given material, variations in the local DOS where the ET reaction takes place affect the ET rate at that location.[46] A model which predicts the effect of changes in the Fermi-level DOS of an electrode on the rates of electron transfer reactions happening at that electrode has been proposed and found to predict rate constants to within approximately one order of magnitude of their measured values.[47] The presence of surface defects and their density upon the electrode is also of extreme importance in many cases, as well as affecting the Fermi-level DOS, a defect may catalyse an ET reaction leading to a faster ET rate occurring at the locality of the defect.[48]

Carbon nanotube (CNT) electrodes provide an important example of a situation where an understanding of how electrode surface characteristics may affect electron transfer rates is crucial. Several studies suggest that, when defects are absent, the sidewalls of single-walled CNTs are electrochemically inactive, and that almost all electrochemical activity observed at CNT electrodes is the result of activity

at the tube end.[49,50] However, recently it has been possible to observe ET processes at a single CNT without contributions from the end walls and not only have low-defect CNT surface walls been shown to be electrochemically active, but ET rates measured at surface walls were not appreciably lower than those measured at tube ends.[32,51] A more complete understanding of CNT electrochemistry which accounts for the apparently contradictory reports can be gained by consideration of CNT defects and how they affect the local surface characteristics of the CNT.

1.2 Double Layer Structure and Capacitance

As well as driving electron transfer reactions, application of a potential to an electrode will cause charges on the solution side of the electrode/electrolyte interface to move in response to the charge on the electrode surface. This response by the dissolved ions can be considered a means of preserving electroneutrality. For a given charge on an electrode surface, an equal charge of opposite sign must be located in the region of that surface. For an electrolyte solution, the solution-side charge can take the form of an imbalance of electrolyte species at the immediate surface of the electrode. Positive ions will collect at a negatively charged electrode's surface and vice versa. The plane at a distance from the electrode surface where the centre of species adsorbed on its surface are located is known as the inner Helmholtz plane. The centres of non-adsorbed species are located at what is known as the outer Helmholtz plane (OHP). Beyond the OHP in a solution of high ionic strength, the absolute potential of the solution will be close to that of the bulk solution. That is, most

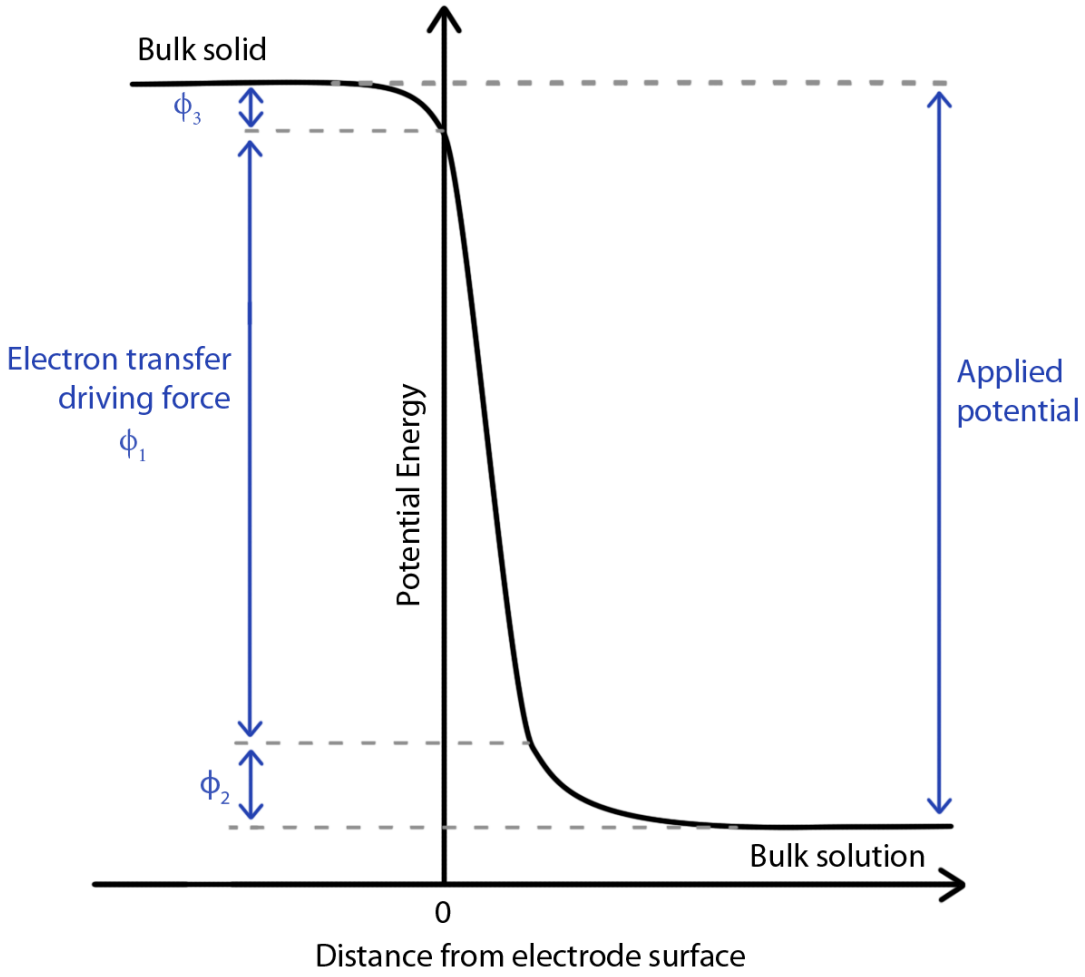

Figure 1.2: A qualitative picture of the potential profile near the surface of an electrode.

of the potential change that occurs between the bulk of the electrode and the bulk of the solution occurs across the Helmholtz plane. In the absence of a significant uncompensated resistance, the remaining potential change occurs through what is known as the diffuse layer. This is a region in which the distribution of charges is imbalanced, but those charges are not rigidly held in place and are free to diffuse within that region. The Helmholtz and diffuse layers are known collectively as the double layer.[19,52,53] Further balancing of the surface charge may take the form of a depletion or accumulation of electrons within the electrode near the surface.[54]

A qualitative picture of the potential profile across an electrode / electrolyte interface is shown in Figure 1.2. The potential difference between the surface of the electrode and the OHP is denoted by ϕ_1 and is the potential difference which drives electron transfer reactions at the surface. The potential difference between the OHP and the bulk solution is denoted ϕ_2 and its effect on electron transfer reactions will be discussed in Section 5.5. Herein, any potential change occurring within the solid is denoted ϕ_3. These three regions where a change in potential occurs will all behave as capacitors, giving rise to a potential dependent differential capacitance being observed at electrode surfaces.

Knowledge of the double layer capacitance at an electrode/electrolyte interface can used in the characterisation of the electrode surface. Capacitance measurements have been used in the past to provide estimates of Fermi-level density of states of electrode surfaces, and recent work has shown that the measurement of double layer capacitance at an electrode coated with an electroactive monolayer can provide an experimentally simple means of measuring Fermi-level den-

sity of states and electron transfer kinetics simultaneously.[54–56]

1.3 Metallic Platinum

Metals are very commonly employed in electrochemical studies due to metals possessing a number of properties that are highly desirable in electrodes. Metals are generally highly conductive meaning that their bulk will add very little resistance to an electrochemical system. Their conductive nature also means that charges applied to them will be located at their surfaces and screened from the bulk, making complex theoretical treatment of the potential energy within the solid unnecessary. The fabrication of electrodes which are well defined geometrically is also possible with many metals. However, no one metal is suitable for all applications.

Liquid mercury is particularly well suited to use as a working electrode.[19] As a liquid, the surface of mercury can be expected to be extremely smooth and homogeneous. The surface can also be easily renewed during experiment when it is used as a hanging drop electrode.[57] It is for mercury electrodes that many of the theoretical models used in electrochemistry, such as the Gouy-Chapman-Stern model, were tested.[52] Despite the often ideal behaviour of their surfaces, the use of mercury electrodes is often avoided due to their high toxicity and the difficulties associated with using mercury cleanly and safely. In cases where an ideal surface is highly desirable, a bismuth electrode will sometimes be used in place of mercury (see Section 1.5).

Platinum and gold are common choices of working electrode. Their inert nature means that they are highly robust and with an appropriate choice of electrolyte solution and working electrode potential, passive oxide layers do not form upon their surfaces.[18] Additionally they may both be fashioned into electrodes with diameters as small as just a few micrometres, though this can be difficult to accomplish with gold. The drawback to using these electrodes is that they possess rough, polycrystalline surfaces. The microscopic geometric features of the surface, and the distribution of exposed crystal faces will effect the double layer structure of the material to some extent, but it is impractical to take these factors into account when attempting to theoretically model the double layer.[58,59]

1.4 Semiconductor Silicon

Silicon is a semiconductor and the ET transfer behaviour observed at silicon electrodes is very different to that observed at metals.[19] The material possesses a valence band and a conduction band separated by a band gap. According to simplistic theoretical treatments of silicon's electronic structure, this band gap is a forbidden region in which no electronic states can exist, though in reality, states within the forbidden region can play an important role in silicon's electrochemical behaviour.[60] In pure silicon, the conduction band will be empty unless electrons are excited into it from the valence band. Upon excitation, an empty state known as a hole will be left in the valence band. Conduction band electrons and valence band holes may both act as charge carriers when present in silicon. If an imbalance of carriers exist, that with a higher concentration is known as

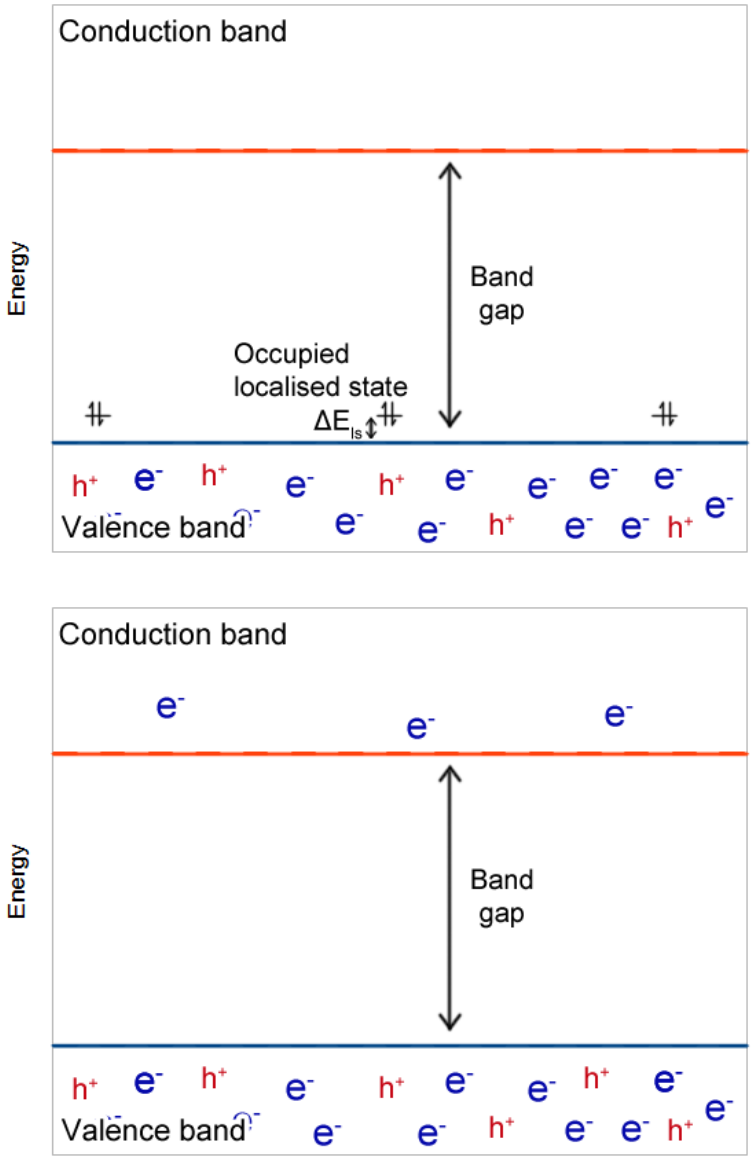

Figure 1.3: Top: qualitative picture of the distribution of charge carriers in p-type silicon without illumination. Localised states above the valence band are populated by valence band electrons and holes are left in the valence band. These holes act as charge carriers. Bottom: qualitative picture of the distribution of charge carriers in p-type silicon under illumination (localised states are not shown). Charge is mostly carried by holes in the valence band, but electrons in the conduction band also carry some of the charge.

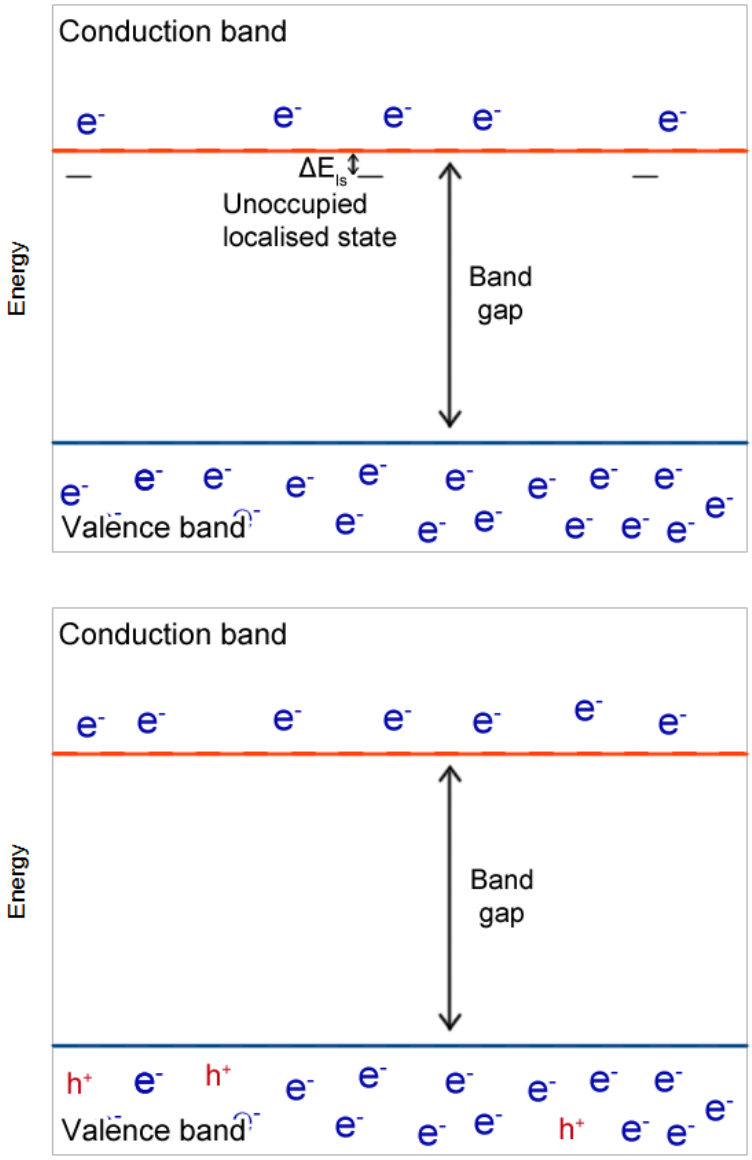

Figure 1.4: Top: qualitative picture of the distribution of charge carriers in n-type silicon without illumination. Localised states below the conduction band are depopulated and their electrons populate the conduction band. Charges are carried by these conduction band electrons. Bottom: qualitative picture of the distribution of charge carriers in n-type silicon under illumination (localised states are not shown). Charge is mostly carried by electrons in the conduction band, but holes in the valence band also carry some of the charge.

the majority carrier, and the other known as the minority carrier. In silicon such an imbalance can be produced by incorporating another element into the silicon; a process known as doping. Doping with phosphorus will introduce electrons into the conduction band and silicon doped in this way is known as n-type silicon. Doping with boron will produce holes in the valence band and silicon doped in this way is known as p-type silicon. The band structures of p-type and n-type silicon are illustrated in Figure 1.3 and Figure 1.4. The introduction of the dopant produces localised states within the band gap. These states are near the valence band in p-type silicon and when populated by valence band electrons, holes are left within the valence band. In n-type silicon these localised states are near the conduction band and act as donor states, providing electrons which may populate the conduction band. The energy gap between these states and the nearest band, labelled ΔE_{ls} in the figures, is much smaller than $\kappa T/e$, meaning that electrons will easily be thermally excited across ΔE_{ls}.[61]

Reduction reactions occurring at a silicon surface require an electron to be supplied by the silicon while oxidation reactions require the silicon to supply a hole. For a silicon electrode where electrons are the majority carrier, reduction reactions will generally occur at a much greater rate than oxidation reactions, and vice versa. An increase in minority carrier concentration can be effected by illumination of the silicon surface, thereby exciting valence electrons into the conduction band. Consequently, we can trigger reactions at silicon by the illumination of the surface.[62–65]

The energy profile of the valence and conduction bands near the silicon electrode/electrolyte interface for n-type silicon is qualitatively

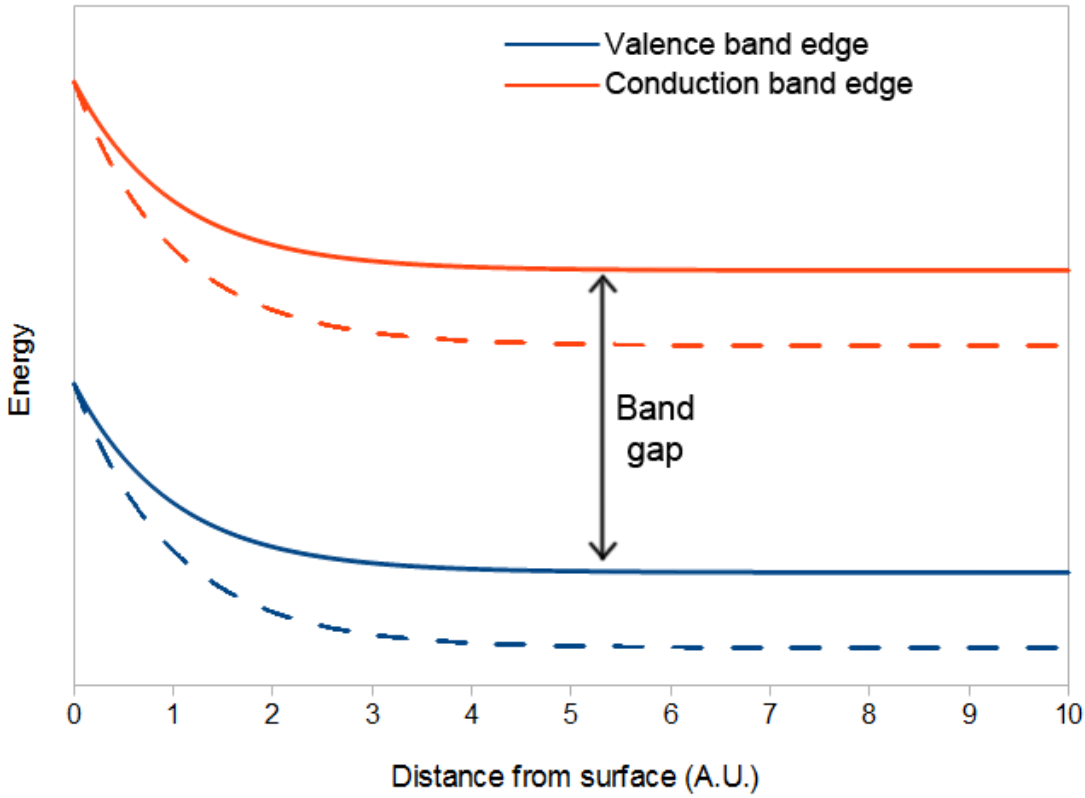

Figure 1.5: Qualitative picture of band bending in a biased n-type silicon electrode in near the electrode/electrolyte interface. The energy of the bands increases near the surface causing majority carriers (conduction band electrons) to move away from surface, and minority carriers (valence band holes) to move toward the surface. The dashed lines show the effect of changing the applied potential: the band energies change in the bulk, but are fixed at the interface.

illustrated by Figure 1.5. The energy of the band edges is linear in the bulk of silicon, and their energies can be modified by changing the applied potential. However, near the interface "bending" of the bands is observed, with the energy levels approaching a potential-independent level. The degree of bending is therefore controlled via the application of potential to the silicon electrode. The dashed lines in Figure 1.5 show an increase in the bending that results from the potential being made more positive. For n-type silicon, photoeffects can be observed when a silicon electrode is biased such that an up-

ward bend is produced, which drives valence band holes (the minority carriers) to the surface and conduction band electrons (the majority carriers) away from the surface. For p-type silicon, photoeffects can be observed when a downward bend is produced as this will drive conduction electrons (the minority carriers) to the surface and valence band holes (the minority carriers) away from the surface. The concentration of silicon minority carriers is often much lower than the concentration of electrolyte ions on the solution side of the interface, resulting in the capacitance of the space-charge region being lower than that of the Helmholtz plane and diffuse layer. When a potential difference is applied across capacitors in series, the potential difference across each capacitor will depend upon its capacitance, with lower capacitance resulting in a greater portion of the potential difference being located at that capacitor. This will often cause the band energies at the surface of silicon to be fixed in place because almost all the potential difference across the electrode/electrolyte interface occurs across the space-charge region.[62,66]

The possible fates of electrons and holes at a semiconductor surface in the presence of surface bound ferrocene (Fc) are illustrated in Figure 1.6. The presence of holes within the valence band allows oxidation of ferrocene to occur via pathway k_O. If electrons exist within the conduction band near the surface, the empty state that is generated in the Fc HOMO allows reduction to occur via pathway k_R. These processes are in competition with recombination of the two carriers via pathway k_1. This recombination typically occurs via a surface state within the band gap (e.g. an energy state on the ferrocene).

Electron transfer rates at silicon do not show the same exponential

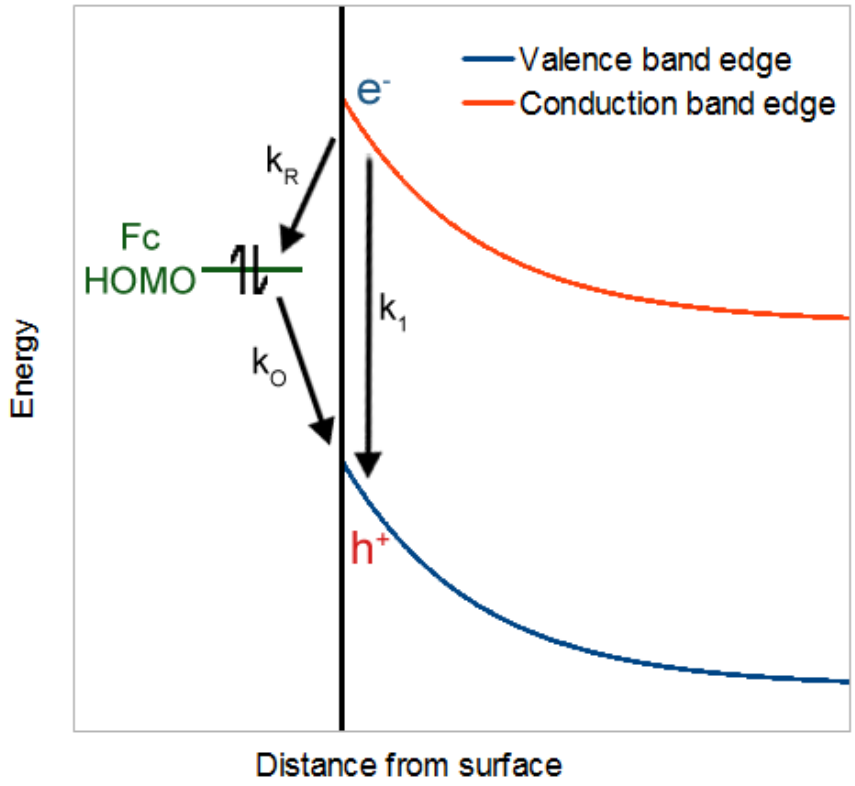

Figure 1.6: Possible fates of conduction band electrons and valence band holes at a semiconductor surface in the presence of surface bound ferrocene.

potential dependence as is seen with metal electrodes. By increasing the degree of band bending, the concentration of minority carriers at the surface can be increased resulting in an increase in the rate of reaction, however the rate of reactions between redox active molecules and minority carriers are often found to be independent of potential due to them exhibiting pseudo first-order behaviour when the concentration of minority carriers becomes much greater than that of the redox active species.[62,67]

The double layer capacitance observed at a silicon electrode will also behave differently from that of a metal. As a charge is placed at

the surface of a silicon electrode, a region of opposing charge will develop within the silicon to restore electroneutrality. This is known as a space-charge region and it gives rise to capacitance on the solid side of the interface. In the case of a metal, the surface charge is completely shielded from the solid causing the opposing charge to be entirely located on the solution side of the interface.[68]

As well as capacitive currents that result from changes in electrode potential, a capacitance resulting from the change in the flux of photons to the silicon surface can also be observed. This is known as photocapacitance. The process occurs because photons absorbed by the silicon can cause the generation of new carriers in the space-charge region of the silicon. In the case of n-type silicon, an electron will be excited into a state within the conduction band near the surface and the energy of that state will be higher than many of the unoccupied states in the conduction band further from the surface. The electron will therefore move down the potential gradient into the bulk of the solid into these lower energy states. The hole that is generated in the valence band will favour higher energy states and thus move in the opposite direction. The opposite signs on their charges means that the movement of majority and minority carriers in opposite directions corresponds to the movement of charge in the same direction. This movement of charge is observed as photocapacitance. This current will decay exponentially as a potential difference across the space-charge region of the semiconductor is generated. The decay constant associated with this process is determined by the rate of carrier recombination at the semiconductor surface. Recombination generally occurs via an unoccupied surface state in the band gap of the semiconductor and the decay constant associated with the photocapacitive current is equal to a pseudo first-order rate constant for the

recombination process. The rate of the recombination process generally exhibits a pseudo first-order dependence upon the concentration of surface states via which recombination may proceed.[69,70]

Silicon is the material of choice in the design of microelectronics. However, the design of components via the physical modification of a silicon surface is severely limited by the minimum scale upon which these modifications can be accomplished accurately. This limitation may ultimately be dispensed with by the development of devices built entirely through bottom-up molecular approaches. However, a more realistic approach at the present is to construct molecular components which are chemically bound to silicon. Obviously, a means of communication between the silicon wafer and the molecular components upon its surface is required for this approach to be of any use. An electron transfer which occurs between the silicon surface and the surface molecule is the obvious candidate. Modification of a silicon surface to allow the incorporation of redox active molecules can be achieved in numerous ways.[71–74] One approach is to first remove the oxide layer that forms upon silicon surfaces and replace it with a layer of silicon hydride, and subsequently alkylate the silicon hydride. This can be accomplished by first etching the silicon surface with NH_4F, and then refluxing a solution of toluene containing an alkene chain and the hydride terminated silicon. This technique allows the formation of alkyl chain monolayers upon the silicon surface.[71,72]

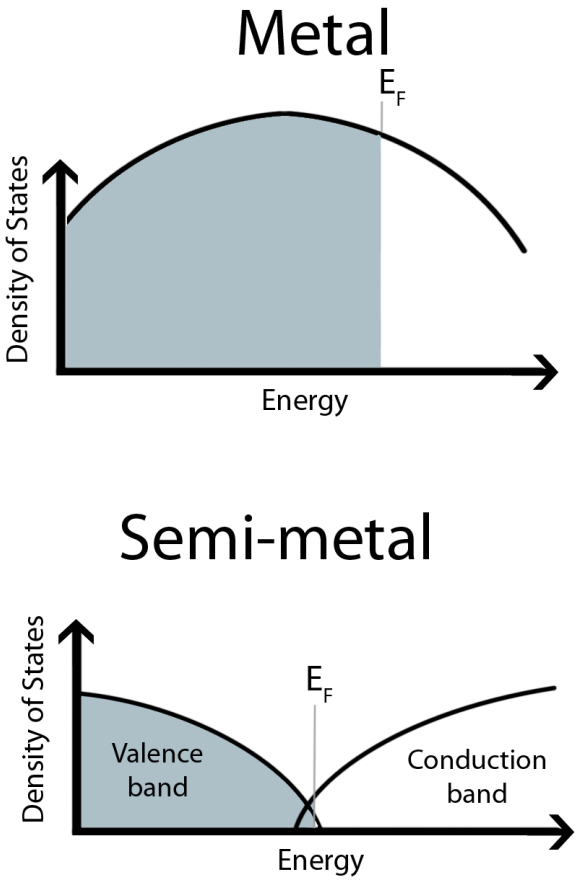

Figure 1.7: Qualitative pictures of how density of states varies with energy near the Fermi-level for metals and semimetals. Filled states are shaded blue. The energy corresponding to the Fermi-level is marked E_F.

1.5 Semimetallic Bismuth

Bismuth is a semimetal: a material which behaves as a metal in some regards, but like a semiconductor in others.[60] The band structure of a semimetal is similar to that of a semiconductor, but in this case the band gap is decreased to the extent that it is negative, i.e. the conduction band overlaps the valence band on the energy scale. The consequence of this is that the high energy electrons in the valence band require no energetic excitation to enter the conduction band

and the conduction band will contain electrons at absolute zero and without illumination, unlike an intrinsic (undoped) semiconductor. However, supplying energy in the form of heat will allow more valence band electrons to enter the conduction band, which can increase the conductivity of the material, unlike a metal where significant filling of the conduction band is difficult to effect.

A semimetal can also be thought of as being a metal with a low Fermi-level density of states (DOS). The Fermi-level DOS of platinum is 1.2×10^{23} cm^{-3} eV^{-1},[42–45] and bismuth, by contrast, has a Fermi-level DOS of approximately 3×10^{17} cm^{-3} eV^{-1}.[60] A qualitative comparison of how density of states varies with energy in platinum and bismuth is shown in Figure 1.7.

The above discussion of bismuth is valid for the bulk of the material only; the surface of bismuth cannot be considered semimetallic.[75–77] Though differences in the properties of materials in the bulk and at the surface are often observed as a result of dangling bonds, bismuth is an extreme case. The Fermi-level DOS of bismuth increases by several orders of magnitude near the surface and measurements of the DOS at (111),[78] (110),[79,80] and (100)[81] surfaces have all determined that the DOS is similar to that of a metal. For an explanation of the cause of this extreme increase in the Fermi-level DOS of bismuth, the reader is advised to consult Hofmann's review of the area and the references therein.[75] Given this extreme difference in the properties of the bulk and the surface of bismuth, careful consideration must be made regarding which set of physical properties is relevant to the particular experiment, though in some cases it may not be clear which set of properties that is.[77]

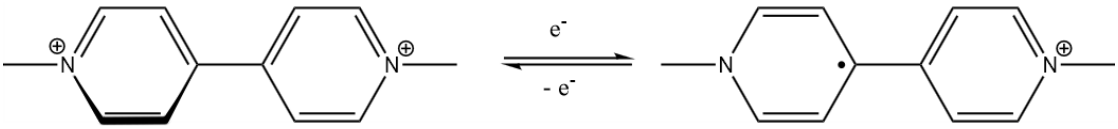

Figure 1.8: The redox couple which exists between the methyl viologen dication (MV^{2+}) and the methyl viologen monocation (MV^{+}).

The most common use of bismuth in the field of electrochemistry has been as a substitute for mercury. The surface of bismuth is also exceptional in that it can be made extremely smooth relatively simply by means of remelting and chemical etching.[57,82] Though mercury surfaces remain superior in terms of their smoothness, bismuth is a non-toxic solid making it a much more desirable material for some applications.

1.6 Methyl Viologen

Methyl viologen (MV^{2+}) belongs to a class of 1,1'-disubstituted-4,4'-bipyridilium salts known as the viologens. Many of these molecules are dications capable of undergoing a one-electron reduction to form stable radical cations.[83] These in turn may undergo a one-electron reduction to yield a neutral species. In the case of methyl viologen, both of these reactions are reversible in appropriate electrochemical systems. The structure of MV^{2+} and its reduction to its monocation radical form (MV^{+}) are shown in Figure 1.8. The reversibility of these reactions requires the absence of oxygen as the radical species is extremely air sensitive.[84] However, in some cases the radical product is stable enough to be isolated.[85]

Viologens have long been used as herbicides,[86,87] and more recently

have found use in electrochromatic systems,[88–91] artificial photosynthesis,[92] and chemical sensors.[93,94] The facile and reversible nature of the reduction of the dication has made methyl viologen an analyte of choice in many studies of electron transfer kinetics and redox behaviour.

Water has been a popular choice of solvent for electrochemical studies of MV^{2+}. The behaviour of the molecule in water is of particular relevance to the toxicity of the molecule and its capacity to act as a redox mediator. However, the redox behaviour of MV^{2+} has been found to be complicated by dimerisation and adsorption upon the surface of working electrodes.[95–101]

The two aromatic rings of methyl viologen can form a 12 electron π-system, meaning the two aromatic rings do not form a single aromatic system. Indeed, computational studies have found that MV^{2+} does not favour a planar conformation. Several studies have found that the lowest energy conformation for this molecule has an inter-ring torsion angle near 45°,[85,102] although the barrier to rotation is low enough to allow free rotation about the inter-ring bond. Upon reduction the molecule adopts a planar form which allows for full delocalisation of the radical and the remaining charge across both aromatic ring systems.[83,103] The rotation about the inter-ring bond will be of particular interest in the work presented here as a relationship between the torsion angle and the rate of the reduction of the molecule to a radical species will be tested.

A series of methyl viologen derivatives have been synthesised in which the inter-ring torsion angle is constrained by means of a linking tether between the two aromatic rings. Initial studies suggest that these

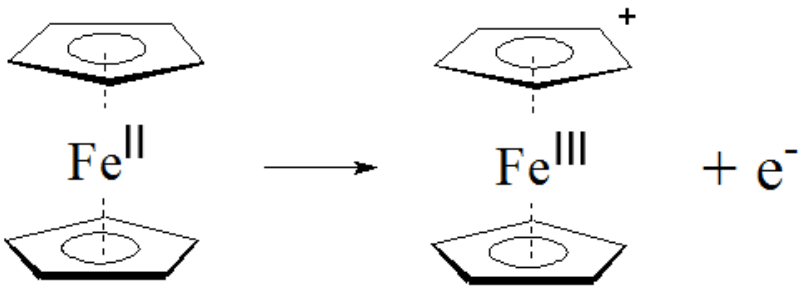

Figure 1.9: The redox couple which exists between ferrocene (Fc) and ferrocenium (Fc^+).

molecules are ideal for kinetic study.[103] These molecules will be studied in depth in Chapter 3.

1.7 Ferrocene

Ferrocene consists of a central iron atom bound to two cyclopentadienyl groups. The iron atom will generally possess an oxidation state of +2 due the higher stability of this state, but can be oxidised to +3 electrochemically, yielding ferrocenium. Ferrocene has a solubility of 0.15M in acetonitirile at 298K,[104] and neither ferrocene nor ferrocenium exhibit any oxygen sensitivity. The ferrocene/ferrocenium redox couple is also highly reversible at low scan rates and highly facile at a metal surface.[22] These facts make ferrocene a common choice of redox active species in electrochemical studies and applications. The structure of ferrocene and its oxidation to ferrocenium are depicted in Figure 1.9.

The ferrocene/ferrocenium redox couple is highly facile at platinum and the measurement of the standard rate constant for the ET reaction has been a source of some confusion in the field of ET kinetics.

The rate constants published for this couple span several orders of magnitude as a result of the large variation in the systematic errors associated with the different techniques available for measurement.[22,37] The development of ultramicroelectrodes has allowed a significant reduction in the uncertainty of these measurements,[38,39] and k^0 for the oxidation is generally agreed to be between 1 and 4 cm s^{-1},[22] though systematic errors still prevent a more precise determination of k^0 for the redox couple.

The capacity of the cyclopentadienyl rings to undergo functionalisation is often exploited in order to incorporate ferrocene into functional systems such as electrochemical sensors.[105–108] In the case of glucose sensing, for example, it was shown that redox mediators in the form of functionalised ferrocene can be used in conjunction with surface-bound glucose oxidase to form an effective sensor.[109] In this example, functionalisation serves to make the ferrocene derivative water soluble. Another set of important examples of ferrocene-based electrochemical systems are those designed in order to examine the effect of the distance between ferrocene and the electrode surface upon the rate of the electron transfer reaction thereby testing the validity of Marcus theory for high transfer rates.[110–113] For short distances, the high speed of the electron transfer necessitated the use of the indirect laser-induced-temperature-jump (ILIT) method as a means of measuring the ET rates.[114–116] The ET rates observed using ILIT for surface bound ferrocene are currently the fastest ET rates that have been measured.

The binding of ferrocene to silicon surfaces is of particular interest as it could form a role in integrating molecular electronics with silicon based microelectronics and in particular has shown potential for use

in dynamic random access memory (DRAM) applications.[105,117] The electron transfer between ferrocene and silicon could act as a means of communication between a molecular component and the silicon device. The kinetics of the electron transfer between ferrocene monolayers and silicon surfaces have been studied for a range of monolayers upon p-type silicon.[117–119] The switching of the ferrocene oxidation state may also provide a form of binary information storage in future applications with the ferrocene and ferrocenium corresponding to different binary states. Ferrocene based DRAM devices could potentially require less power than current SiO_2 based DRAM devices because they require lower potential differences (< 1V) to drive oxidation and charge the monolayer, and once charged, discharge occurs more slowly than for SiO_2 based devices.[105]

Bibliography

[1] R. Marcus and N. Sutin, *Biochimica et Biophysica Acta (BBA) - Reviews on Bioenergetics*, 1985, **811**, 265–322.

[2] R. E. Blankenship, *Molecular Mechanisms of Photosynthesis*, Wiley-Blackwell, 2001.

[3] N. Nelson and C. F. Yocum, *Annual Review of Plant Biology*, 2006, **57**, 521–565.

[4] J. M. Berg, J. L. Tymoczko and L. Stryer, *Biochemistry: International Edition*, W. H. Freeman, 6th edn., 2006.

[5] J. H. A. Nugent, *European Journal of Biochemistry*, 1996, **237**, 519–531.

[6] D. Gust, T. A. Moore and A. L. Moore, *Accounts of Chemical Research*, 2001, **34**, 40–48.

[7] T. J. Meyer, *Accounts of Chemical Research*, 1989, **22**, 163–170.

[8] J. H. Alstrum-Acevedo, M. K. Brennaman and T. J. Meyer, *Inorganic Chemistry*, 2005, **44**, 6802–6827.

[9] M. R. Wasielewski, *Chemical Reviews*, 1992, **92**, 435–461.

[10] A. J. Bard and M. A. Fox, *Accounts of Chemical Research*, 1995, **28**, 141–145.

[11] Y. Tachibana, L. Vayssieres and J. R. Durrant, *Nature Photonics*, 2012, **6**, 511–518.

[12] M. Grätzel, *Nature*, 2001, **414**, 338–344.

[13] K. Habermuller, M. Mosbach and S. Wolfgang, *Fresenius' Journal of Analytical Chemistry*, 2000, **366**, 560–568.

[14] A. Chaubey and B. Malhotra, *Biosensors and Bioelectronics*, 2002, **17**, 441–456.

[15] M. Gerard, A. Chaubey and B. Malhotra, *Biosensors and Bioelectronics*, 2002, **17**, 345–359.

[16] R. L. McCreery, *Chemistry of Materials*, 2004, **16**, 4477–4496.

[17] P. Sun, F. O. Laforge and M. V. Mirkin, *Physical Chemistry Chemical Physics*, 2007, **9**, 802.

[18] *Organic Electrochemistry, Fifth Edition*, ed. O. Hammerich and B. Speiser, CRC Press, 5th edn., 2012.

[19] A. J. Bard and L. Faulkner, *Electrochemical Methods: Fundamentals and Applications*, John Wiley & Sons, 2nd edn., 2001.

[20] M. E. Orazem and B. Tribollet, *Electrochemical Impedance Spectroscopy*, Wiley-Blackwell, 2008.

[21] N. Hush, *Journal of Electroanalytical Chemistry*, 1999, **470**, 170–195.

[22] W. R. Fawcett and M. Opallo, *Angewandte Chemie International Edition in English*, 1994, **33**, 2131–2143.

[23] N. Tanaka and R. Tamamushi, *Electrochimica Acta*, 1964, **9**, 963–989.

[24] H. Yu, Y. Wang, D. Asakura, E. Hosono, T. Zhang and H. Zhou, *RSC Advances*, 2012, **2**, 8797–8807.

[25] V. Yurkiv, A. Utz, A. Weber, E. Ivers-Tiffée, H.-R. Volpp and W. G. Bessler, *Electrochimica Acta*, 2012, **59**, 573–580.

[26] K.-C. Jiang, S. Xin, J.-S. Lee, J. Kim, X.-L. Xiao and Y.-G. Guo, *Physical Chemistry Chemical Physics*, 2012, **14**, 2934–2939.

[27] N. G. Tsierkezos and U. Ritter, *Analytical Letters*, 2011, **44**, 1416–1430.

[28] J. Y. Xiang, J. P. Tu, Y. Q. Qiao, X. L. Wang, J. Zhong, D. Zhang and C. Gu, *The Journal of Physical Chemistry C*, 2011, **115**, 2505–2513.

[29] A. Murthy and A. Manthiram, *Electrochimica Acta*, 2011, **56**, 6078–6083.

[30] Y. Xu and B. J. Venton, *Physical Chemistry Chemical Physics*, 2010, **12**, 10027–10032.

[31] A. B. Meneses, S. Antonello, M. C. Arévalo, C. C. González, J. Sharma, A. N. Wallette, M. S. Workentin and F. Maran, *Chemistry – A European Journal*, 2007, **13**, 7983–7995.

[32] A. G. Güell, N. Ebejer, M. E. Snowden, K. McKelvey, J. V. Macpherson and P. R. Unwin, *Proceedings of the National Academy of Sciences*, 2012, **109**, 11487–11492.

[33] V. S. Joshi, S. K. Haram, A. Dasgupta and G. V. P. Kumar, *The Journal of Physical Chemistry C*, 2012, **116**, 9703–9708.

[34] M. Shen and A. J. Bard, *Journal of the American Chemical Society*, 2011, **133**, 15737–15742.

[35] L. Johnson, A. Niaz, A. Boatwright, K. Voisey and D. A. Walsh, *Journal of Electroanalytical Chemistry*, 2011, **657**, 46–53.

[36] S. E. Salamifar, M. A. Mehrgardi, S. H. Kazemi and M. F. Mousavi, *Electrochimica Acta*, 2010, **56**, 896–904.

[37] A. D. Clegg, N. V. Rees, O. V. Klymenko, B. A. Coles and R. G. Compton, *Journal of Electroanalytical Chemistry*, 2005, **580**, 78–86.

[38] K. Aoki, *Electroanalysis*, 1993, **5**, 627–639.

[39] C. G. Zoski, *Electroanalysis*, 2002, **14**, 1041–1051.

[40] C. P. Andrieux, P. Hapiot and J. M. Saveant, *Chemical Reviews*, 1990, **90**, 723–738.

[41] Z. Galus and R. N. Adams, *The Journal of Physical Chemistry*, 1963, **67**, 866–871.

[42] F. Y. Fradin, D. D. Koelling, A. J. Freeman and T. J. Watson-Yang, *Physical Review B*, 1975, **12**, 5570–5574.

[43] J. van der Klink and H. Brom, *Progress in Nuclear Magnetic Resonance Spectroscopy*, 2000, **36**, 89–201.

[44] M. Weinert and A. J. Freeman, *Physical Review B*, 1983, **28**, 6262–6269.

[45] A. H. MacDonald, J. M. Daams, S. H. Vosko and D. D. Koelling, *Physical Review B*, 1981, **23**, 6377–6398.

[46] H. V. Patten, K. E. Meadows, L. A. Hutton, J. G. Iacobini, D. Battistel, K. McKelvey, A. W. Colburn, M. E. Newton, J. V.

Macpherson and P. R. Unwin, *Angewandte Chemie International Edition*, 2012, **51**, 7002–7006.

[47] W. J. Royea, T. W. Hamann, B. S. Brunschwig and N. S. Lewis, *The Journal of Physical Chemistry B*, 2006, **110**, 19433–19442.

[48] B. R. Horrocks, M. V. Mirkin and A. J. Bard, *The Journal of Physical Chemistry*, 1994, **98**, 9106–9114.

[49] A. F. Holloway, K. Toghill, G. G. Wildgoose, R. G. Compton, M. A. H. Ward, G. Tobias, S. A. Llewellyn, B. Ballesteros, M. L. H. Green and A. Crossley, *The Journal of Physical Chemistry C*, 2008, **112**, 10389–10397.

[50] A. Chou, T. Böcking, N. K. Singh and J. J. Gooding, *Chemical Communications*, 2005, 842–844.

[51] I. Dumitrescu, P. V. Dudin, J. P. Edgeworth, J. V. Macpherson and P. R. Unwin, *The Journal of Physical Chemistry C*, 2010, **114**, 2633–2639.

[52] D. C. Grahame, *Chemical Reviews*, 1947, **41**, 441–501.

[53] D. C. Grahame, *Annual Review of Physical Chemistry*, 1955, **6**, 337–358.

[54] H. Gerischer, *The Journal of Physical Chemistry*, 1985, **89**, 4249–4251.

[55] P. R. Bueno, G. Mizzon and J. J. Davis, *The Journal of Physical Chemistry B*, 2012, **116**, 8822–8829.

[56] H. Gerischer, R. McIntyre, D. Scherson and W. Storck, *The Journal of Physical Chemistry*, 1987, **91**, 1930–1935.

[57] E. Lust, A. Jänes, V. Sammelselg, P. Miidla and K. Lust, *Electrochimica Acta*, 1998, **44**, 373–383.

[58] R. Parsons, *Chemical Reviews*, 1990, **90**, 813–826.

[59] A. Hamelin, T. Vitanov, E. Sevastyanov and A. Popov, *Journal of Electroanalytical Chemistry and Interfacial Electrochemistry*, 1983, **145**, 225–264.

[60] N. W. Ashcroft and N. D. Mermin, *Solid State Physics*, Brooks/Cole, 1976.

[61] W. Gomes and F. Cardon, *Progress in Surface Science*, 1982, **12**, 155–215.

[62] L. M. Peter, *Chemical Reviews*, 1990, **90**, 753–769.

[63] E. Ponomarev and L. Peter, *Journal of Electroanalytical Chemistry*, 1995, **397**, 45–52.

[64] E. Ponomarev and L. Peter, *Journal of Electroanalytical Chemistry*, 1995, **396**, 219–226.

[65] L. Peter, E. Ponomarev and D. Fermín, *Journal of Electroanalytical Chemistry*, 1997, **427**, 79–96.

[66] H. Gerischer, *Electrochimica Acta*, 1990, **35**, 1677–1699.

[67] L. Abrantes and L. Peter, *Journal of Electroanalytical Chemistry and Interfacial Electrochemistry*, 1983, **150**, 593–601.

[68] M. Sparnaay, *Advances in Colloid and Interface Science*, 1967, **1**, 278–333.

[69] L. Peter, J. Li and R. Peat, *Journal of Electroanalytical Chemistry and Interfacial Electrochemistry*, 1984, **165**, 29–40.

[70] J. Li and L. Peter, *Journal of Electroanalytical Chemistry and Interfacial Electrochemistry*, 1985, **193**, 27–47.

[71] J. M. Buriak, *Chemical Communications*, 1999, 1051–1060.

[72] A. B. Sieval, R. Linke, H. Zuilhof and E. J. R. Sudhölter, *Advanced Materials*, 2000, **12**, 1457–1460.

[73] S. Onclin, B. J. Ravoo and D. N. Reinhoudt, *Angewandte Chemie International Edition*, 2005, **44**, 6282–6304.

[74] D. Aswal, S. Lenfant, D. Guerin, J. Yakhmi and D. Vuillaume, *Analytica Chimica Acta*, 2006, **568**, 84–108.

[75] P. Hofmann, *Progress in Surface Science*, 2006, **81**, 191–245.

[76] Y. Liu and R. E. Allen, *Physical Review B*, 1995, **52**, 1566–1577.

[77] M. Muntwiler and X.-Y. Zhu, *New Journal of Physics*, 2008, **10**, 113018.

[78] A. Ofitserov and V. Edelman, *Physica B: Condensed Matter*, 2003, **329-333, Part 2**, 1094–1095.

[79] S. Agergaard, C. Søndergaard, H. Li, M. B. Nielsen, S. V. Hoffmann, Z. Li and P. Hofmann, *New Journal of Physics*, 2001, **3**, 15–15.

[80] J. I. Pascual, G. Bihlmayer, Y. M. Koroteev, H.-P. Rust, G. Ceballos, M. Hansmann, K. Horn, E. V. Chulkov, S. Bluegel, P. M. Echenique and P. Hofmann, *Physical Review Letters*, 2004, **93**, 196802.

[81] P. Hofmann, J. E. Gayone, G. Bihlmayer, Y. M. Koroteev and E. V. Chulkov, *Physical Review B*, 2005, **71**, 195413.

[82] E. Lust, A. Jänes, K. Lust, V. Sammelselg and P. Miidla, *Electrochimica Acta*, 1997, **42**, 2861–2879.

[83] Y. Huang and J. B. Hopkins, *The Journal of Physical Chemistry*, 1996, **100**, 9585–9591.

[84] K. B. Yoon and J. K. Kochi, *Journal of the American Chemical Society*, 1988, **110**, 6586–6588.

[85] T. M. Bockman and J. K. Kochi, *The Journal of Organic Chemistry*, 1990, **55**, 4127–4135.

[86] J. H. Ross and R. I. Krieger, *Journal of Agricultural and Food Chemistry*, 1980, **28**, 1026–1031.

[87] L. Michaelis and E. S. Hill, *The Journal of General Physiology*, 1933, **16**, 859–873.

[88] H. J. Kim, J. K. Seo, Y. J. Kim, H. K. Jeong, G. I. Lim, Y. S. Choi and W. I. Lee, *Solar Energy Materials and Solar Cells*, 2009, **93**, 2108–2112.

[89] K. Hoshino, Y. Oikawa, I. Sakabe and T. Komatsu, *Electrochimica Acta*, 2009, **55**, 165–170.

[90] J.-H. Ryu, J.-H. Lee, S.-J. Han and K.-D. Suh, *Colloids and Surfaces A: Physicochemical and Engineering Aspects*, 2008, **315**, 31–37.

[91] R. J. Mortimer, *Electrochimica Acta*, 1999, **44**, 2971–2981.

[92] S. Saha and J. F. Stoddart, *Chemical Society Reviews*, 2007, **36**, 77–92.

[93] S. W. Thomas, G. D. Joly and T. M. Swager, *Chemical Reviews*, 2007, **107**, 1339–1386.

[94] M. E. Ghica and C. M. Brett, *Analytica Chimica Acta*, 2005, **532**, 145–151.

[95] K. Y. Tam, R. L. Wang, C. W. Lee and R. G. Compton, *Electroanalysis*, 1997, **9**, 219–224.

[96] J. A. Alden, J. A. Cooper, F. Hutchinson, F. Prieto and R. G. Compton, *Journal of Electroanalytical Chemistry*, 1997, **432**, 63–70.

[97] M. Rueda, R. Compton, J. Alden and F. Prieto, *Journal of Electroanalytical Chemistry*, 1998, **443**, 227–235.

[98] L. Xiao, G. G. Wildgoose and R. G. Compton, *New Journal of Chemistry*, 2008, **32**, 1628.

[99] L. Pospísil, J. Kuta and J. Volke, *Journal of Electroanalytical Chemistry*, 1975, **58**, 217–227.

[100] E. Engelman and D. H. Evans, *Journal of Electroanalytical Chemistry*, 1993, **349**, 141–158.

[101] P. M. S. Monk and N. M. Hodgkinson, *Electrochimica Acta*, 1998, **43**, 245–255.

[102] L. Ould-Moussa, O. Poizat, M. Castella-Ventura, G. Buntinx and E. Kassab, *The Journal of Physical Chemistry*, 1996, **100**, 2072–2082.

[103] A. C. Benniston, A. Harriman, P. Li, J. P. Rostron, R. W. Harrington and W. Clegg, *Chemistry - A European Journal*, 2007, **13**, 7838–7851.

[104] K. M. De Fina, C. Ezell and W. E. Acree, *Physics and Chemistry of Liquids*, 2001, **39**, 699–710.

[105] B. Fabre, *Accounts of Chemical Research*, 2010, **43**, 1509–1518.

[106] C. M. Casado, I. Cuadrado, M. Morán, B. Alonso, B. Garcıa, B. González and J. Losada, *Coordination Chemistry Reviews*, 1999, **185–186**, 53–80.

[107] P. D. Beer and J. Cadman, *Coordination Chemistry Reviews*, 2000, **205**, 131–155.

[108] S. R. Bayly, P. D. Beer and G. Z. Chen, in *Ferrocenes*, ed. P. Š. F. o. Science, John Wiley & Sons, Ltd, 2008, p. 281–318.

[109] A. E. G. Cass, G. Davis, G. D. Francis, H. A. O. Hill, W. J. Aston, I. J. Higgins, E. V. Plotkin, L. D. L. Scott and A. P. F. Turner, *Analytical Chemistry*, 1984, **56**, 667–671.

[110] C. E. D. Chidsey, C. R. Bertozzi, T. M. Putvinski and A. M. Mujsce, *Journal of the American Chemical Society*, 1990, **112**, 4301–4306.

[111] J. F. Smalley, S. W. Feldberg, C. E. D. Chidsey, M. R. Linford, M. D. Newton and Y.-P. Liu, *The Journal of Physical Chemistry*, 1995, **99**, 13141–13149.

[112] S. B. Sachs, S. P. Dudek, R. P. Hsung, L. R. Sita, J. F. Smalley, M. D. Newton, S. W. Feldberg and C. E. D. Chidsey, *Journal of the American Chemical Society*, 1997, **119**, 10563–10564.

[113] C. E. D. Chidsey, *Science*, 1991, **251**, 919–922.

[114] J. F. Smalley, C. Krishnan, M. Goldman, S. W. Feldberg and I. Ruzic, *Journal of Electroanalytical Chemistry*, 1988, **248**, 255–282.

[115] J. F. Smalley, M. D. Newton and S. W. Feldberg, *Electrochemistry Communications*, 2000, **2**, 832–838.

[116] S. W. Feldberg, M. D. Newton and J. F. Smalley, *Electroanalytical Chemistry*, 2004, **22**, 101.

[117] K. M. Roth, A. A. Yasseri, Z. Liu, R. B. Dabke, V. Malinovskii, K.-H. Schweikart, L. Yu, H. Tiznado, F. Zaera, J. S. Lindsey,

W. G. Kuhr and D. F. Bocian, *Journal of the American Chemical Society*, 2003, **125**, 505–517.

[118] A. A. Yasseri, D. Syomin, R. S. Loewe, J. S. Lindsey, F. Zaera and D. F. Bocian, *Journal of the American Chemical Society*, 2004, **126**, 15603–15612.

[119] K. Huang, F. Duclairoir, T. Pro, J. Buckley, G. Marchand, E. Martinez, J.-C. Marchon, B. De Salvo, G. Delapierre and F. Vinet, *ChemPhysChem*, 2009, **10**, 963–971.

Chapter 2

Experimental

2.1 Materials

Water of nominal resistivity 18 MΩ·cm was obtained using a Barnstead Nanopure™ purification train. Tertbutylammonium hexafluorophosphate ($TBAPF_6$) ($\geq$ 99.0% purity) and potassium chloride (KCl) ($\geq$99.5% purity) were purchased from Sigma-Aldrich and used as received. ReagentPlus® acetonitrile (MeCN) was purchased from Sigma-Aldrich and dried over calcium hydride before distillation prior to use.

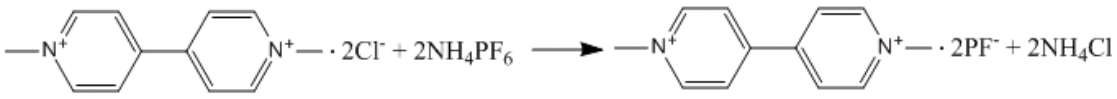

Figure 2.1: Production of the PF_6 salt of methyl viologen.

Methyl viologen dichloride hydrate (98% purity) and NH_4PF_6 (99.99% purity) were purchased from Sigma-Aldrich and dissolved in water.

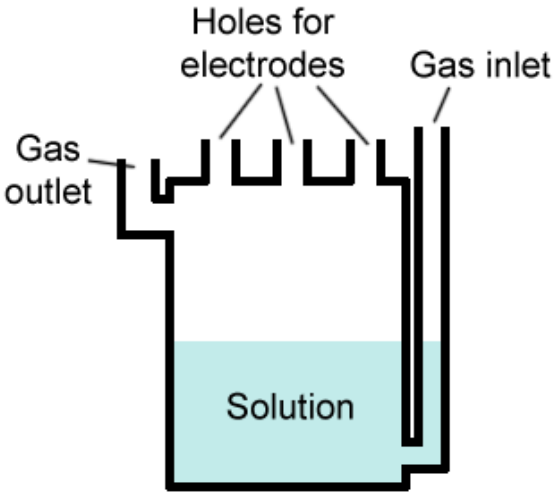

Figure 2.2: The glass cell used used to house analyte solutions during electrochemical experiments requiring deaeration.

The salt metathesis reaction shown in Figure 2.1 results, and the PF_6 salt of methyl viologen was collected as a white precipitate which was washed with water and dried. This product was then used to produce acetonitrile solutions of methyl viologen, without further purification. The methyl viologen derivatives used in this study were prepared by Dr. Peiyi Li as has been described previously.[1] Prior to all electrochemical experiments involving methyl viologen and its derivatives, the electrochemical cell used was deoxygenated by bubbling nitrogen through the solution for 15 minutes. The cell used for solution based electrochemistry is shown in Figure 2.2.

Unless stated otherwise, all potentials in MeCN were measured against a Ag/Ag^+ reference electrode. This reference consisted of a silver wire in MeCN with $AgNO_3$ (10 mM) and $TBAPF_6$ (0.1M). The reference solution was separated from the analyte solution by a glass frit. Unless stated otherwise tungsten wire was used as the counter electrode. All potentials in water were measured against a solid state

Ag/AgCl wire reference electrode in the presence of 0.1M Cl^-.

A platinum working electrode of radius 1 mm, and platinum microelectrodes of 25 μm and 5 μm radius were regularly employed. Microelectrodes of 25 μm radius were prepared by sealing a platinum wire into a glass tube, cutting through the glass to reveal a platinum disc, and then polishing this disc to give a flat surface. The 5 μm electrodes were SECM tips purchased from IJ Cambria. Platinum wire was purchased from Goodfellow. Bismuth powder (99.999%) was purchased from Sigma-Aldrich and bismuth electrodes were created by placing this powder into a glass tube of 1 mm bore, melting the powder by heating the tube with a blowtorch, inserting a copper wire into the molten bismuth, and polishing flat the exposed bismuth disc after solidification, with care taken not to expose the copper wire at the disc's surface. Prior to use, all electrodes were polished using alumina.

Preparation of silicon monolayers was performed by Mufida Abdualla (Chemical Nanoscience Laboratory, Newcastle University). Silicon surfaces were prepared by boiling in 1,1,2-trichlorethane (semiconductor grade) for 20 minutes, sonicating in methanol (semiconductor grade), 2-propanol (semiconductor grade) and subsequently water at room temperature for 5 minutes, oxidising in piranha solution (1:4 H_2O_2:H_2SO_4) for 20 minutes, rising with water, and finally drying under nitrogen. Ethylferrocene monolayers were formed by then refluxing in toluene with ethenylferrocene.[2] In the case of mixed monolayers, the reflux was performed in the presence of 1-hexene, 1-octene, or 1-decene, with the alkene and the ethylferrocene at some known concentration ratio. Ethenylferrocene monolayers were prepared by dissolving ethynylferrocene (10 mg) in a minimum

amount of dichloromethane and leaving this solution on the chip surface under illumination at room temperature overnight. Ethynylferrocene monolayers were prepared by mixing ethynylferrocene (55 mg, 0.26 mmol) in HF with n-butyllithium (0.15 mL, 1.6M) and stirring rapidly under N_2 for 15 minutes before the silicon was placed in the stirred solution and left overnight at room temperature. Ethynylferrocene monolayer surfaces were subsequently cleaned by sonication for 5 minutes in solution of 1% TFA in diethyl ether, diethyl ether, 4% TFA in dichloromethane and dichloromethane.[3] Silicon electrodes were created by sealing silicon chips in a PTFE holder with a circular section of 1.93 mm radius exposed to light, within a 2.85 mm radius section exposed to solution. A screw cap allowed replacement of the silicon chip, and a Vitron® O-ring was used to create a seal between the screw cap and the silicon surface. The PTFE cell was housed within a glass cell and the exposed electrode surface aimed at a quartz window in the side of the glass cell. The light source was placed against this window and used to illuminate the silicon electrode during photoelectrochemical experiments. Figure 2.3 is a schematic illustrating the construction of the silicon electrode cell. A cross section view showing the cell sealed within the PTFE holder is shown in Figure 2.4

Silicon surfaces were cleaned with reagent grade acetone prior to use in silicon electrodes.

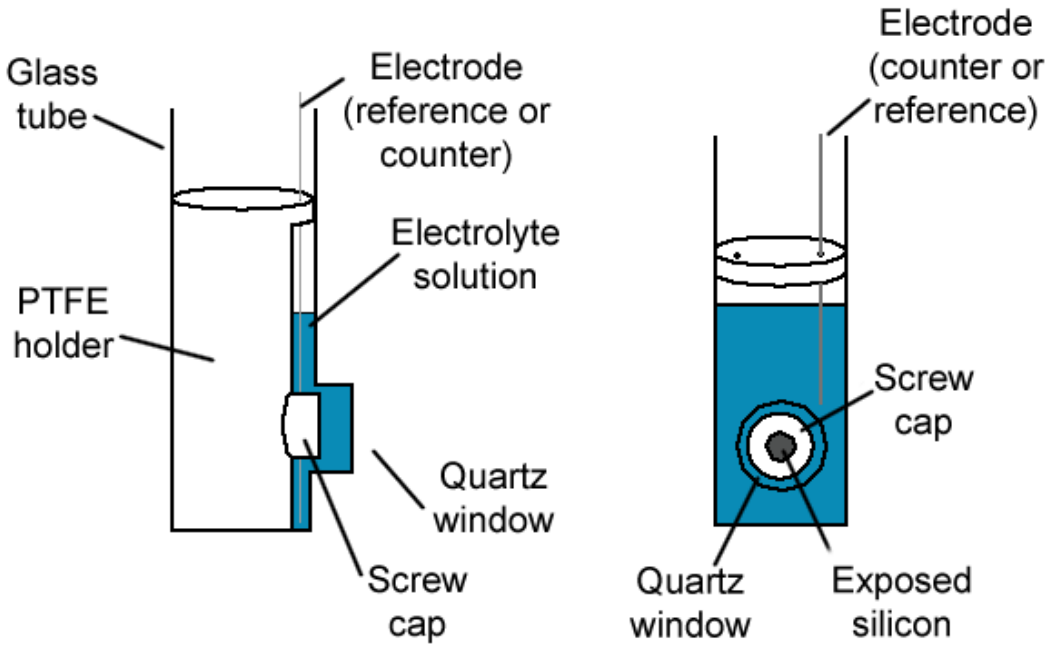

Figure 2.3: Schematic of the silicon cell used during experiments using silicon electrodes. The glass cell holds a solution which is in contact with a circular section of the silicon chip housed in the PTFE holder. The light source is then positioned against the quartz window and can illuminate the silicon surface.

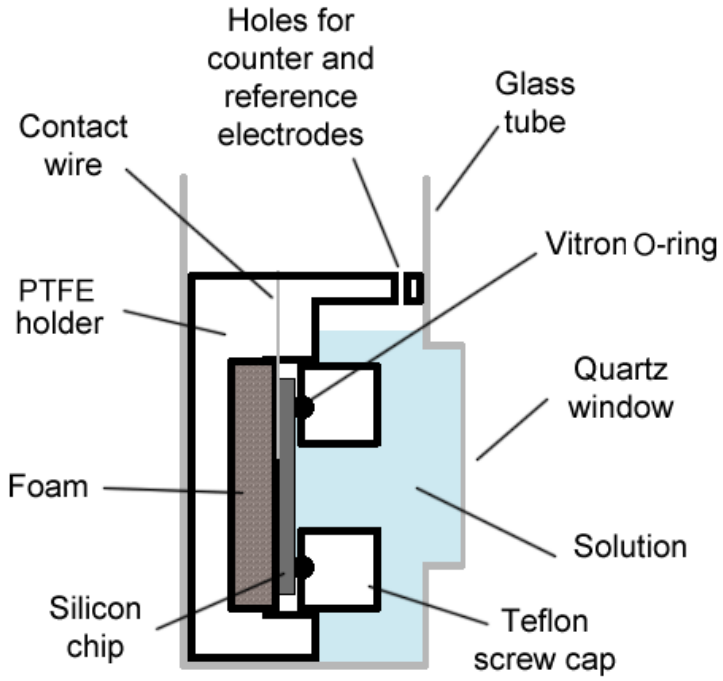

Figure 2.4: Cross section of the silicon electrode cell showing the silicon chip sealed within the PTFE holder. The Vitron® O-ring contact ensures that solution is in contact with a circular surface area of the chip.

2.2 Techniques

2.2.1 Computational Chemistry

Molecular modelling was carried out using the Spartan 04 (Wavefunction Inc., CA, USA) software package. This software was used to find ground state geometries via density functional theory (DFT) at the B3LYP level of theory with a 6-31G* basis set.

2.2.2 Electrochemistry

Electrochemical experiments under potentiostatic control are performed by creating a potential difference between two surfaces within an electrolyte solution and monitoring the current flow that results through one of those surfaces. A typical set up consists of a solution containing a 1:1 salt as supporting electrolyte at some concentration (e.g. 0.1M) and an analyte molecule at some lower concentration (e.g. 1 mM). Three electrodes are placed into this solution to act as a working, counter and reference electrode. A potential difference can then be created and maintained between the working and reference electrode, and the current flow between the working and counter electrode monitored. A suitable choice of materials will result in a system that allows electron transfer reactions between the working electrode and analyte molecule to be monitored by means of current flow.

Working electrodes are generally sufficiently inert materials with a known surface area. Flat discs of platinum are a common choice.

A suitable counter electrode is one which can pass sufficient current that current flow is only limited by processes at the working electrode, and is inert within the electrolyte solution. Tungsten is often used for this purpose, as it a relatively cheap, inert metal. A suitable reference electrode is one which maintains a fixed potential difference between its surface and the electrolyte solution. Given such an electrode, any changes in potential between the working and reference electrode, will result in a potential change which manifests almost entirely across the working electrode surface. A high concentration of supporting electrolyte then serves to compact this potential change at the working electrode surface, and shields analyte molecules from potential gradients within the solution. In the context of electrochemical experiments, the terms "applied potential" and "measured potential" will refer to the difference in potential between the cable connection at the working electrode and the cable connection at the reference electrode. Given that no significant resistance exists at these connection points, this potential difference is equal to the difference between the bulk of the reference electrode material, and the bulk of the working electrode (though not necessarily the difference in potentials near the electrode surfaces).[4]

The effect of changes in potential across the working electrode surface on electron transfer reactions occurring at that surface, and the nature of the potential change across that surface are topics that will be investigated in great detail throughout this thesis.

2.2.3 Cyclic Voltammetry

Herein, cyclic voltammetry (CV) refers to experiments in which a time-dependent current response is observed and scan rates do not approach 1 kV s^{-1}. For descriptions of the time-independent and fast scan versions of the technique, see sections 2.2.4 and 2.2.5 respectively.

CV experiments are performed by scanning the applied potential (E) in time (t) from one value to another at a constant scan rate (v), and then scanning the potential back at the same rate. A scan rate, measured in units of V s^{-1}, is defined by Equation 2.1, which is equal for the forward and backward scan. The CV experiment can be fully described by v, a minimum potential (E_{min}), a maximum potential (E_{max}), the initial scan direction, and the number of cycles performed.

Simulated CV data, for a solution in which only the oxidised form of the analyte is present in the bulk, is shown below for an experiment with the following parameters: $v = 0.1$ V s^{-1}, $E_{max} = 0$; $E_{min} = -1$V; initial scan direction = negative; cycles = 1. The potential profile with time is shown in Figure 2.5. A simulated current response is shown in Figure 2.6.[4] The current response shown corresponds to a working electrode disc of radius (r) 1 mm, in a solution with analyte concentration (C) of 1 mM at a temperature (T) of 20°C. Uncompensated resistance (R_u) through the solution is 100 Ω, and electrode capacitance (C_{dl}) is 1×10^{-4} F cm^{-2}. The analyte molecule has a diffusion coefficient (D) of 1×10^{-5} cm^2 s^{-1} and undergoes a one-electron transfer reaction with a formal potential ($E^{0'}$) of -0.5V. The voltammogram produced by the simulation, with its two peaks

of opposite current, is characteristic of a reversible redox reaction. The voltammogram possesses several features which correspond to the parameters of the system.

$$v = \left| \frac{\partial E}{\partial t} \right| \tag{2.1}$$

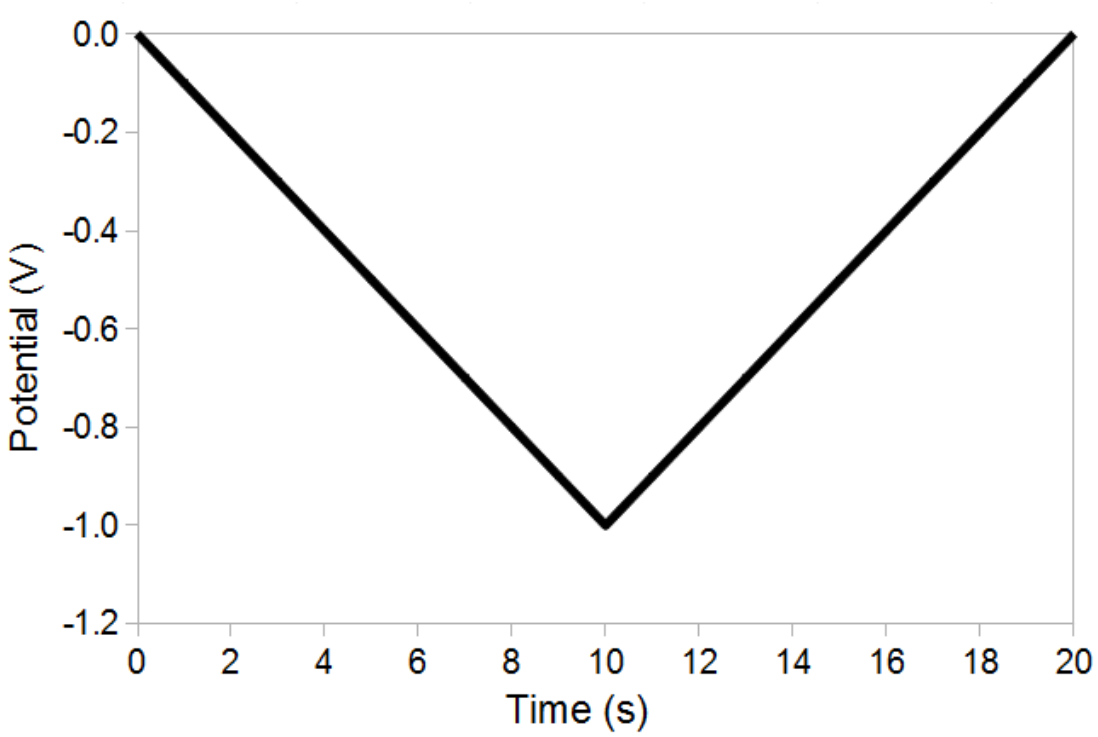

Figure 2.5: Variation of potential with time during a simulated CV experiment with the following parameters: $v = 0.1$ V s^{-1}; $E_{max} = 0$; $E_{min} = -1$V; initial scan direction = negative; cycles = 1.

Peak Positions

The average of the cathodic peak potential, E_p^c, and the anodic peak potential, E_p^a, for a redox couple in solution travelling by diffusion is given by Equation 2.2. For redox couples involving surface bound

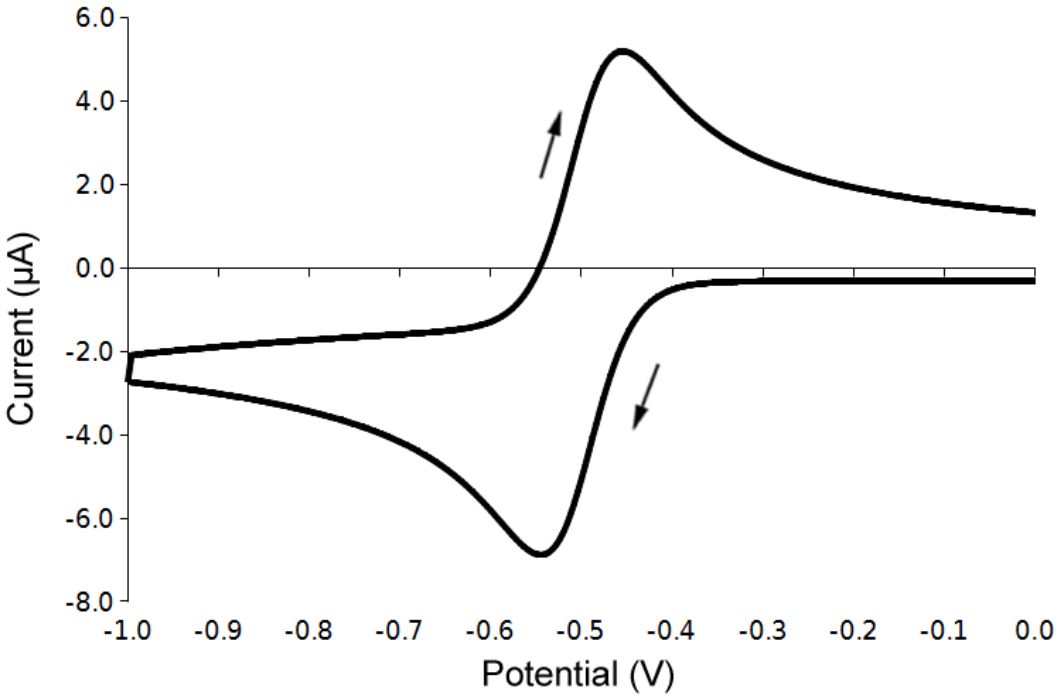

Figure 2.6: A simulated current response for a CV experiment. The voltammogram shows the reduction of a molecule present in bulk solution in the oxidised form only. The parameters used to generate the simulation are listed above.

species, it is expected that $E_p^c = E_p^a = E^{0'}$, though for solutions of high R_u some separation may be observed.

$$\frac{E_p^c + E_p^a}{2} = E_{\frac{1}{2}} = E^{0'} + \frac{RT}{nF} \ln \left(\frac{D_R}{D_O} \right)^{\frac{1}{2}} \tag{2.2}$$

Peak Heights

The relative peak heights depend on the chemical reversibility of the reaction. For a fully reversible reaction, an equal peak height will be observed in both scan directions. In the case where the species gen-

erated by the forward scan is highly unstable, the species generated may not be visible in the reverse scan, or the size of the reverse peak may be reduced. For example, the generation of a radical species in the presence of oxygen will often be an irreversible process. The height of the peaks, i_p, in the fully reversible case at 298K for a redox couple in solution is given in amperes by Equation 2.3, where A is given in units of cm^2, D in $\mathrm{cm}^2\ \mathrm{s}^{-1}$, C^* in $\mathrm{mol\ cm}^{-3}$, and v in $\mathrm{V\ s}^{-1}$. For species strongly adsorbed upon, or bound to an electrode surface, the peak current is given by Equation 2.4. When it is unclear whether the redox active species is in solution or adsorbed upon the electrode, the relationship between peak height and scan rate can help distinguish these two cases.

$$i_p = 2.69 \times 10^5 n^{\frac{3}{2}} A D^{\frac{1}{2}} C^* v^{\frac{1}{2}} \tag{2.3}$$

$$i_p = \frac{n^2 F^2}{4RT} v A \Gamma \tag{2.4}$$

Peak Area

The peak area divided by the scan rate has units of coulombs and is a measure of the total charge passed, Q, by means of the electron transfer. The Faraday constant, F, can be used to determine how many moles of electrons this charge corresponds to, and thus the net number of molecules that have been reduced or oxidised. This is of particular use in the analysis of electroactive surfaces where every surface bound molecule can be made to undergo an electron transfer reaction. Using Equation 2.5, the surface concentration, Γ,

of the redox active molecule can be determined when Q and n are known.

$$\int_{E_{initial}}^{E_{final}} i(t)dt = Q = \Gamma nFA \tag{2.5}$$

Background Current

The capacitive current that passes during the experiment is given by Equation 2.6, where c_{dl} is the differential capacitance of the electrode, assuming c_{dl} is independent of E. Since this is a constant, it is easily measured in the region where no faradaic current passes.

$$i_{capacitive} = c_{dl}v \tag{2.6}$$

2.2.4 Steady State Voltammetry

In steady state voltammetry (SSV), a time-varied potential identical in description to that of CV is applied, but the technique is characterised by a current response which is independent of scan rate and scan direction. For a voltammogram recorded around the standard potential of a redox couple, in the absence of any changes to the bulk of the analyte solution, or the working electrode surface, retraceability would occur when the voltammogram is recorded by making successive infinitesimal changes to the potential applied to the system. While such an experiment is impossible in practice, by incrementing the potential at increasingly slower rates, the current

response may approach the limiting case of retraceability. In practice, this generally requires the use of an electrode with a radius of 25 μm or less for disc shaped electrodes. The absence of any impact of scan rate upon the observed current during a SSV experiment is in stark contrast to the current response of a CV experiment. Clearly, the analysis of SSV data must differ from that of CV data. Therefore we may consider SSV as being distinct from CV.

For a facile, reversible redox couple, a SSV has two main features. The maximum current is reached when the ET reaction rate becomes diffusion limited and this current is given by Equation 2.7. For a uniformly accessible electrode, the potential at which the current is equal to $i_p/2$ is given by Equation 2.8. At this point $\left|\frac{\partial i}{\partial E}\right|$ will pass through a maximum. Near $E^{0'}$ the current will increase as the potential driving force for the reaction increases. Far from $E^{0'}$ the current will be independent of potential in the absence of other processes due to the process being either diffusion limited or the potential not being great enough to drive the reaction at an appreciable rate.

$$i_p = 4nFADC^* \tag{2.7}$$

$$E_{\frac{1}{2}} = E^{0'} + \frac{RT}{nF} \ln\left(\frac{D_R}{D_O}\right) \tag{2.8}$$

2.2.5 Fast Scan Voltammetry

Fast scan voltammetry (FSV) is identical to CV in terms of applied potential, however, it is performed at much higher scan rates

(typically ≥ 1 kV/s) than in typical CV experiments. FSV may be thought of as being distinct from regular CV due to the differences in the nature of the information that can be obtained via the two techniques. FSV can be used to probe the kinetics of a facile redox couple,[5] while regular CV will generally give information relating to the thermodynamics of such a couple.

2.2.6 Chronoamperometry

Chronoamperometry (CA) is the application of a sudden (ideally, instantaneous) change in applied potential, and the observation of the resultant current transient response. Equations 2.9 and 2.10 describe the applied potential. At some time, $t = 0$, the potential is stepped from its initial value, $E_{initial}$, to some different value, $E_{stepped}$. A large transient current will result at $t = 0$ and will rapidly decay. If the onset of some process occurs at a potential between $E_{initial}$ and $E_{stepped}$, the transient may contain information about the process.

$$E(t) = E_{initial} \quad (t < 0) \tag{2.9}$$

$$E(t) = E_{stepped} \quad (t \geq 0) \tag{2.10}$$

Generally, when examining a redox couple involving a molecule in solution, $E_{initial}$ is chosen such that the current, $i = 0$. The value of $E_{stepped}$ is then chosen such that i will rapidly become limited by the flux of material to the surface. For a molecule fluxing to the surface

of a flat disc shaped electrode via semi-infinite planar diffusion only, i at time t will then be given by Equation 2.11, known as the Cottrell equation. A CA experiment in which current response obeys this equation is usually identifiable from a linear relationship between $i(t)$ and $t^{-0.5}$.

$$i(t) = \frac{nFAC^*\sqrt{D}}{\sqrt{\pi t}} \tag{2.11}$$

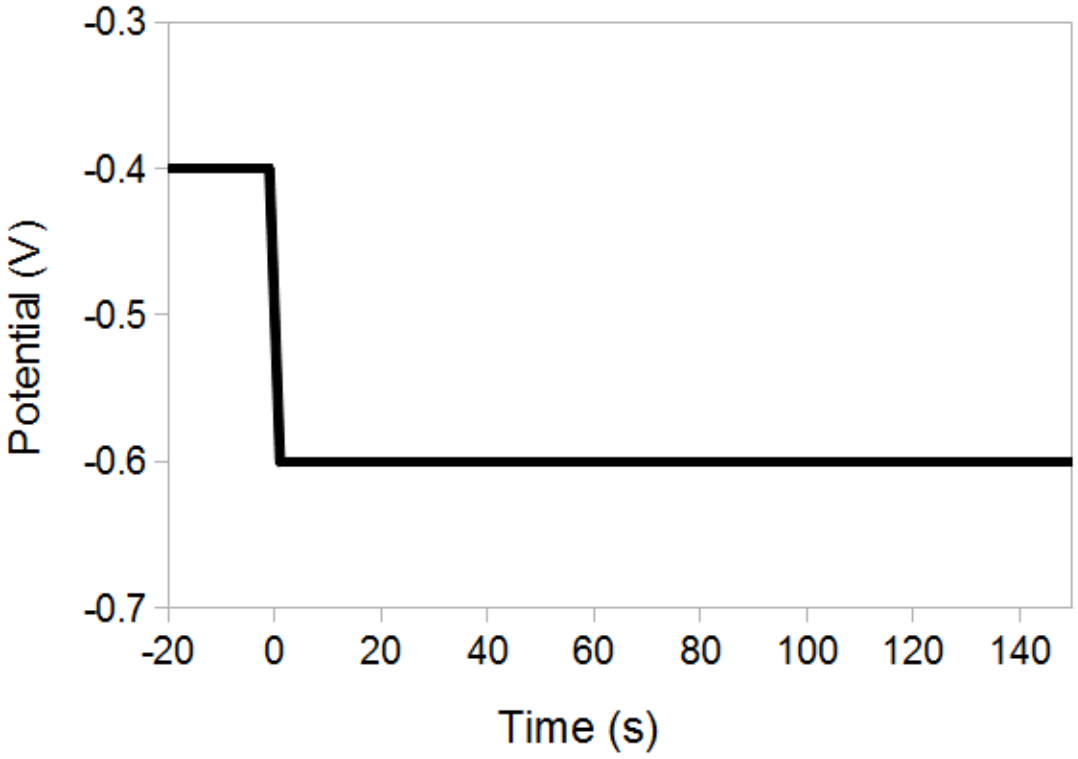

Figure 2.7: The applied potential for a chronoamperometry experiment with $E_{initial} = -0.4$V and $E_{stepped} = -0.6$V.

For a CA experiment with $E_{initial} = -0.4$V and $E_{stepped} = -0.6$V, the potential will vary with time as shown in Figure 2.7. If the system to which this potential step was applied contained a redox active molecule, and the standard potential for the redox couple was -0.5V,

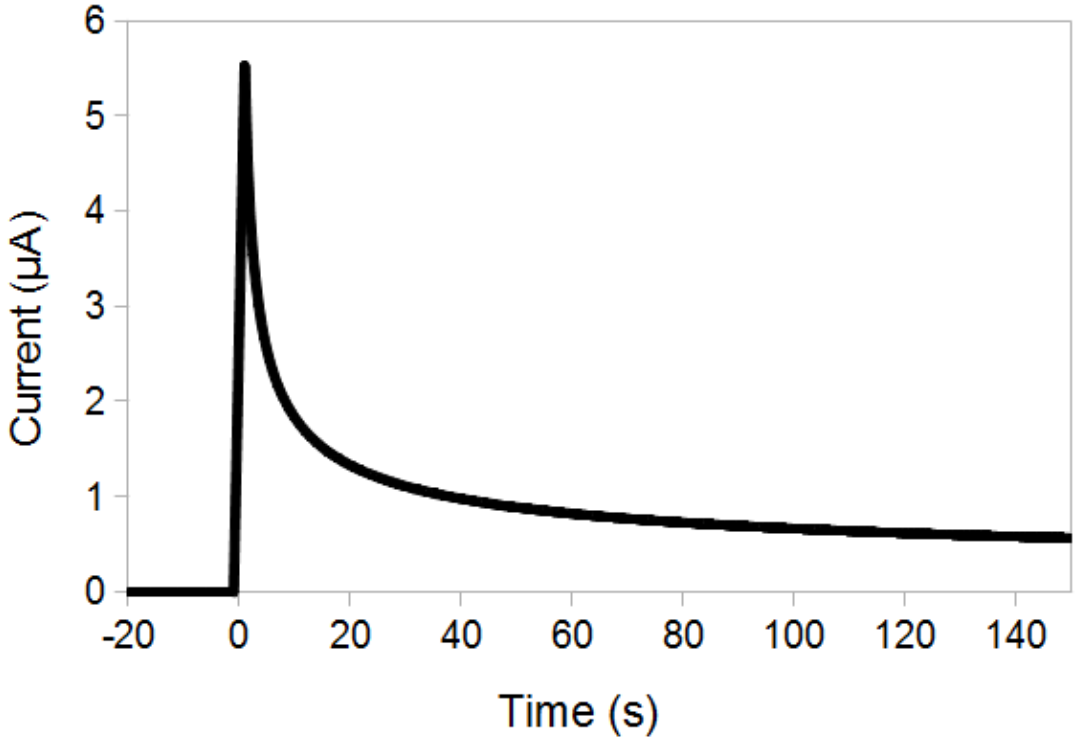

Figure 2.8: A simulated current response for a CA experiment. The parameters used to generate the simulation are listed above. The plot represents only an approximate picture of the current response.

then the current response may be similar to that shown in Figure 2.8.[6] This current is simulated using an analyte concentration 1 mM, an electrode radius of 1 mm, and an analyte diffusion coefficient of 10^{-5} cm^2 s^{-1}.

2.2.7 Square Wave Voltammetry

In square wave voltammetry (SWV), the applied potential waveform consists of a square wave superimposed upon a potential ramp. The square wave can be defined by its frequency, f and its amplitude, E_{amp}. A square wave with $E_{amp} = 25$ mV and $f = 15$ Hz is shown

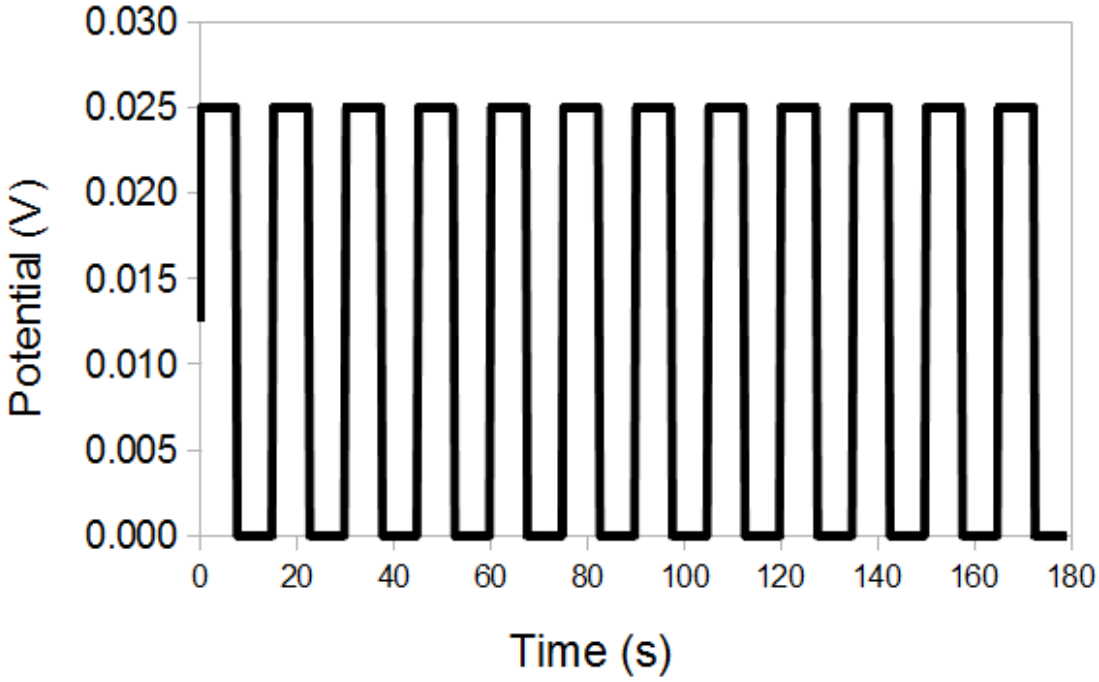

Figure 2.9: A square wave.

in Figure 2.9. This square wave is superimposed upon a potential staircase. The staircase can be defined by its step size, E_{step}, and the step frequency, f, equal to the frequency of the square wave. Figure 2.10 illustrates a staircase waveform with $E_{step} = 4$ mV and $f = 15$ Hz. The result of the superimposition of these waveforms is illustrated by Figure 2.11.

The current response of the system is not considered at every point of the potential waveform. Instead current is sampled immediately before a step in potential occurs, and the current observed after a negative step is subtracted from that observed after a positive step to give a current difference, Δi. The significance of Δi is in the fact that when the potential is near $E^{0'}$ of the redox couple, capacitive current and background current contribute little to Δi compared

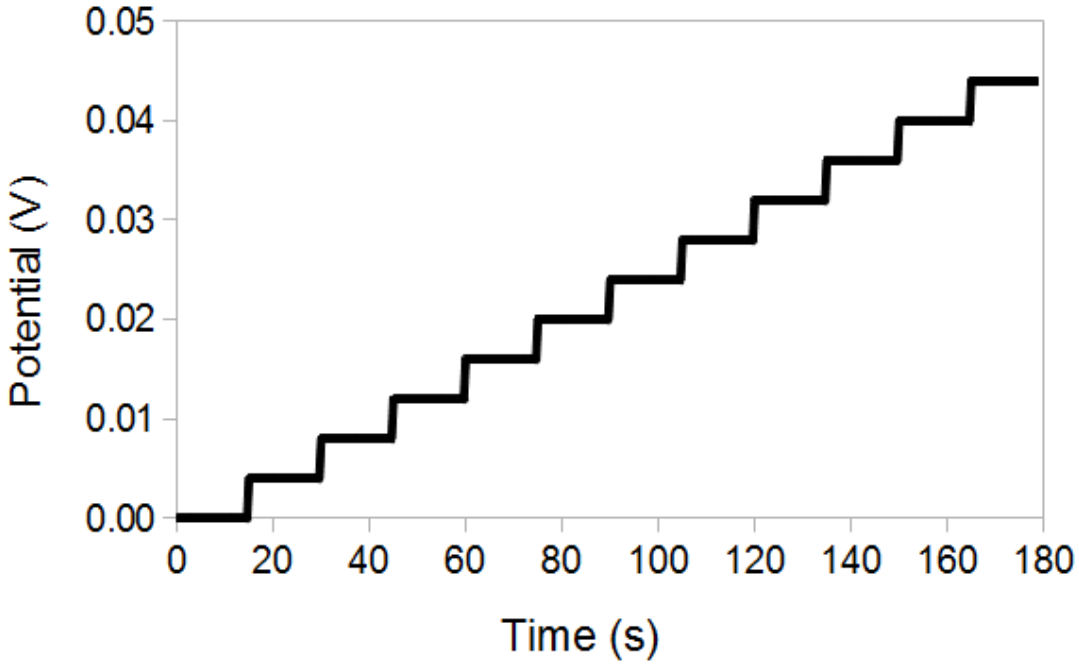

Figure 2.10: A staircase waveform.

the potential dependent redox process. At potentials far from $E^{0'}$ the current corresponding to the redox couple will be insensitive to potential due to either an insufficient potential driving force existing to drive the reaction, or due to the process being diffusion limited. If the diffusion coefficients of the reduced and oxidised form of the redox active molecule are equal, the current will peak when the potential is equal to $E^{0'}$.

2.2.8 Electrochemical Impedance Spectroscopy

Electrochemical impedance spectroscopy (EIS) is an alternating current (AC) technique performed by applying a sinusoidal potential waveform to the system, which can be described by Equation 2.12,

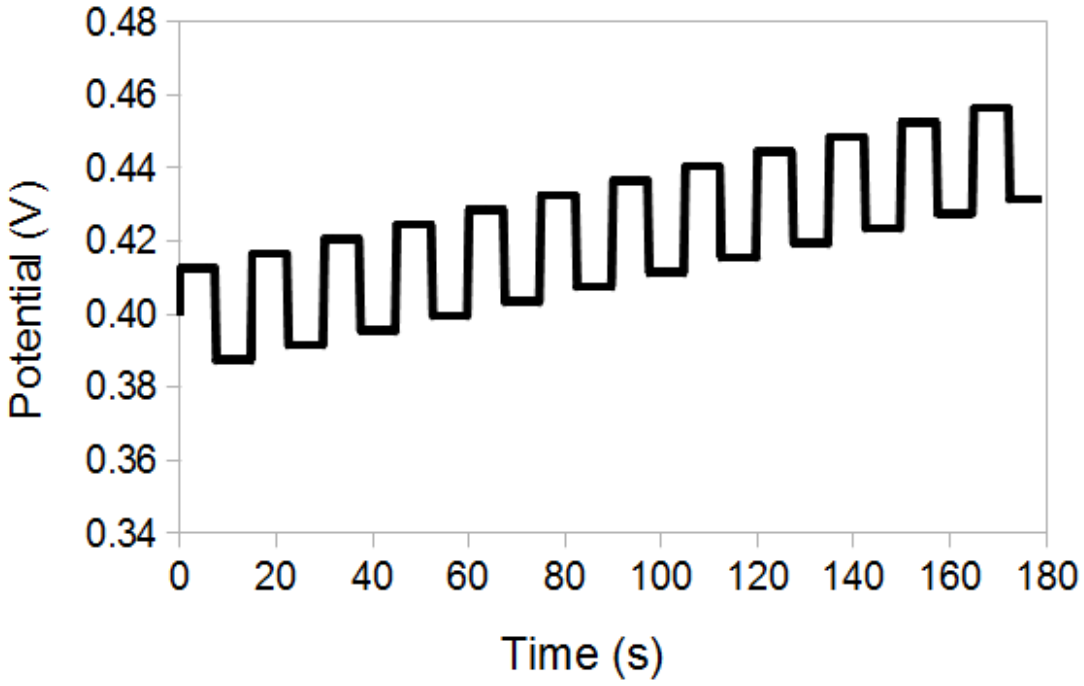

Figure 2.11: The superimposition of a square wave upon a staircase waveform. This is the potential waveform applied to the system during square wave voltammetry.

where E_{dc} is the DC value of the applied potential, and ω and E_{amp} are the angular frequency and amplitude of the waveform respectively.

$$E(t) = E_{dc} + E_{amp}\sin(\omega t) \tag{2.12}$$

For sufficiently low values of E_{amp}, a linear relationship exists between current and potential, i.e. a sinusoidal current waveform, $i(t)$, with frequency ω will be observed in response to $E(t)$. The complex quantity, $i(\omega)$, describes the amplitude of this current waveform, and its phase relative to the applied potential. The current response, $i(\omega)$, is generally used to calculate the impedance, Z, of the system.

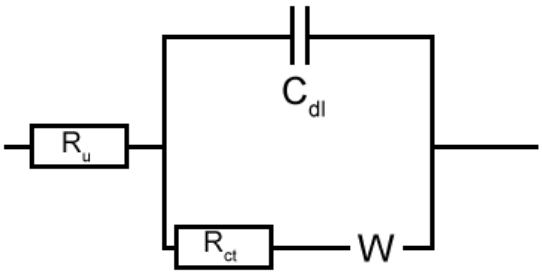

Figure 2.12: Randles' circuit

Measurement of Z over a range of ω values yields the impedance spectrum of the system. Since the current response associated with two different processes may have different phase angles, this technique can often be used to separate two components of a system's current response.[7]

Circuit Analysis

In the analysis of EIS data, it is common to design an equivalent circuit with behaviour similar to that of the electrochemical cell. In a meaningful circuit analysis, the elements of the circuit will represent elements of the electrochemical system, and the parameters describing the elements in the circuit will correspond to parameters describing the electrochemical system. For example, the double layer capacitance of the working electrode may be modelled using a capacitor. The capacitance that must be given to the capacitor in the model circuit should then be equal to the capacitance of the working electrode. During the analysis it is important to understand the limitations of the model. In this example the capacitor in the model cannot replicate the frequency dependence of the capacitance at a working electrode surface which is not perfectly smooth. Nor

can it replicate changes in the working electrode capacitance with changes in potential.

In the field of electron transfer kinetics, Randles' circuit is often used as a model for an ET occurring on an electrode when ω is high. The circuit is depicted in Figure 2.12 and contains 4 circuit elements, all of which correspond to physical phenomena in the system. All current must pass through the electrolyte solution, and the resistance associated with this passage can be modelled by a resistor, R_u. The circuit then branches to represent the two means by which current can travel through the system. Current travelling through the top branch in Figure 2.12 must flow across a capacitor, c_{dl}, which models the capacitive behaviour of the electric double layer. The bottom branch contains two elements. The resistor R_{ct} models the resistance associated with the ET reaction. Although ET rates have an exponential dependence on potential, for small perturbations a linear dependence can be approximated and the current/potential relationship considered ohmic. The second element, W, represents Warburg impedance. Warburg impedance is a measure of the impedance to ET current caused by the need for reactant molecules to diffuse through solution. As ω increases, W becomes less significant and eventually negligible.

Mott-Schottky Analysis

Mott-Schottky analysis is a form of analysis performed to locate the flatband potential of a semiconductor electrode. EIS spectra are collected over a range of potentials, and the capacitance of the electrode surface is determined using circuit analysis. Far from flatband poten-

tial (E_{fb}), the capacitance of the semiconductor can be described by Equation 2.13 where ϵ_{SC} is the dielectric constant of the semiconductor, e is the elementary charge, N_D is the carrier density and κ is the Boltzmann constant. For each frequency, a plot of c^{-2} as a function of potential is created. Over some potential range it is expected that the data for each frequency will form a straight line which can be extrapolated to identical x-intercepts. The potential at this intercept corresponds to $E_{fb} + {}^{\kappa T}/_{e} \approx E_{fb}$ of the semiconductor.[8]

$$C_{dl}^{-2} = \left(\frac{2}{\epsilon_{SC} e N_D A^2}\right)\left((E - E_{fb}) - \frac{\kappa T}{e}\right) \tag{2.13}$$

2.2.9 Photoelectrochemical Chronoamperometry

Photoelectrochemical chronoamperometry (PC) is the application of a sudden (ideally, instantaneous) change in light intensity at the electrode surface, and the observation of the resultant current transient. At time, $t = 0$, the intensity of the light is stepped from its initial value, $L_{initial}$, to some other value, $L_{stepped}$. The variation in light intensity with time is described by Equation 2.14 and Equation 2.15. Herein, $L_{initial} = 0$ is used in all PC experiments unless stated otherwise. The technique is analogous to CA, but potential is held constant throughout the measurement. However, subsequent PC experiments may be performed over a range of potentials. The shape of the transient may give some insight into the kinetic behaviour of processes occurring at the surface of the working electrode.[9]

$$L(t) = L_{initial} \quad (t < 0) \tag{2.14}$$

$$L(t) = L_{stepped} \quad (t \geq 0) \tag{2.15}$$

In the case of a silicon bound redox active species reacting with minority carriers, a potential can be chosen such that there is sufficient overpotential for an electron transfer current to be observed, and the reaction can be triggered by the light step. In the dark minority carrier concentration will be too low for a reaction to occur at a measurable rate. However, upon illumination of the surface, the surface molecules will react at a rate determined by minority carrier concentration. Under the assumption that the molecule has an equal chance of reacting at any given instant, the surface bound molecules have a measurable half-life and the concentration of unreacted molecules will decay exponentially.[10] Minority carriers will also be consumed via recombination with majority carriers resulting in a photocapacitive current which also decays exponentially. The current response will therefore be a transient which can be modelled as a sum of two exponential decays described by Equation 2.16 where k_1 and k_2 are first-order rate constants corresponding to the two forms of minority carrier decay, I_0 is the height of the transient, I_∞ is the current at $t = \infty$, and β is the fraction of the current which flows via the process with rate k_1. A simulation using the parameters $I_0 = 10^{-5}$ A; $k_1 = 800$ s^{-1}; $k_2 = 500$ s^{-1}; $\beta = 0.7$; $I_\infty = 0$ is shown in Figure 2.13. Fitting of the Equation 2.16 to the solid black curve can yield the parameters in the equation. Fitting can be accomplished via non-linear least squares regression using software such as Gnuplot.

$$i(t) = I_0 \left[\beta \exp(-k_1 t) + (\beta - 1) \exp(-k_2 t)\right] + I_\infty \tag{2.16}$$

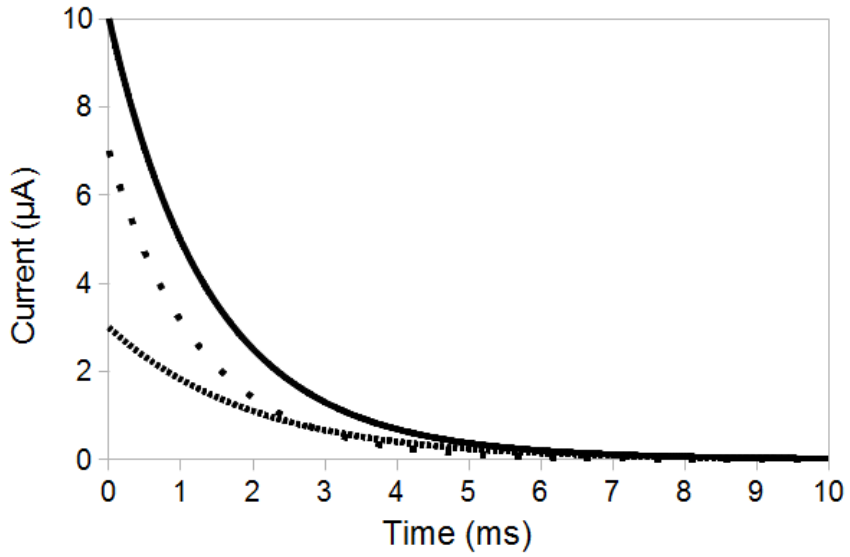

Figure 2.13: Simulated PC current response using parameters $I_0 = 10^{-5}$ A; $k_1 = 800$ s^{-1}; $k_2 = 500$ s^{-1}; $\beta = 0.7$; $I_\infty = 0$. The solid black curve is the current response as would be measured. The dotted line shows the current with decay constant k_1 and the dashed line the current with decay constant k_2.

In the absence of the photocapacitive current contribution, the observed current during the PC experiment can be related to the redox behaviour of the monolayer, with oxidation and reduction contributing to the current with opposing signs. For a monolayer containing ferrocene (Fc) in some equilibrium with ferrocenium (Fc^+), this relationship between the current and the procession of redox reactions can be described by Equation 2.17.

$$\frac{\partial \Gamma_{Fc}}{\partial t} = k_R[e^-_{CB}]\Gamma_{Fc^+} - k_O[h^+_{VB}]\Gamma_{Fc} \tag{2.17}$$

Oxidation of the ferrocene is a second-order process with rate constant k_O and has a first-order dependence on both the surface ferrocene concentration, Γ_{Fc}, and the concentration of holes within the silicon valence band, $[h^+_{VB}]$. Reduction of ferrocenium can be de-

scribed in a similar manner with second-order rate constant k_R and first-order dependence on both the conduction band electron concentration, $[e^-_{CB}]$, and the surface concentration of ferrocenium, Γ_{Fc^+}. However, during the PC experiment a single rate constant corresponding to faradaic processes, k_2, is observed. This rate constant depends on the rate of both oxidative and reductive processes, as described by Equation 2.18.

$$k_2 = k_R[e^-_{CB}] + k_O[h^+_{VB}] \tag{2.18}$$

When the applied potential is made sufficiently positive, an n-type silicon surface enters depletion, that is $[e^-_{CB}] \approx 0$. In this situation it is possible to measure the rate of oxidation because $k_2 \approx k_O[h^+_{VB}]$. The parameter k_2 thus becomes a pseudo first-order rate constant, and the true rate constant, k_O, can be determined with knowledge of $[h^+_{VB}]$.

2.3 Electrochemical Instrumentation

A CH Instruments 760b potentiostat was used for solution based cyclic voltammetry (CV), square wave voltammetry (SWV), chronoamperometry (CA), fast scan voltammetry (FSV), and electrochemical impedance spectroscopic (EIS) study of solution based molecules.

Electrochemical impedance spectroscopy studies of platinum and bismuth electrodes were performed using an Ivium CompactStat.

Photoelectrochemical studies were performed using an Ivium CompactStat connected to an Ivium Modulight. The ModuLight is a light source which can produce white (or single wavelength) light of variable intensity, up to a maximum of 57 lm. The intensity of this light may be varied in time to produce sinusoidal waveforms or intensity steps. The use of time-varied light intensity is described in Section 2.2.9 A Tektronix DPO 3032 digital phosphor oscilloscope was also connected to the CompactStat via a peripheral port expander, for use in high speed experiments. Simultaneous connection of the peripheral port expander and the Modulight to the CompactStat was accomplished via a custom made splitter, allowing two connections to the CompactStat's single expansion port. Unless stated otherwise, the intensity of the light source was set to its maximum level. In all cases, white light was used to illuminate the silicon. The flux of the photons reaching the silicon electrode used in these experiments was estimated at 10^{15} photons s^{-1} using the steady-state photocurrent at p-Si of methyl viologen (aq).

Bibliography

[1] A. C. Benniston, A. Harriman, P. Li, J. P. Rostron, R. W. Harrington and W. Clegg, *Chemistry - A European Journal*, 2007, **13**, 7838–7851.

[2] J. E. Bateman, R. D. Eagling, D. R. Worrall, B. R. Horrocks and A. Houlton, *Angewandte Chemie International Edition*, 1998, **37**, 2683–2685.

[3] A. G. Marrani, F. Cattaruzza, F. Decker, P. Galloni and R. Zanoni, *Electrochimica Acta*, 2010, **55**, 5733–5740.

[4] A. J. Bard and L. Faulkner, *Electrochemical Methods: Fundamentals and Applications*, John Wiley & Sons, 2nd edn., 2001.

[5] J. Savéant and D. Tessier, *Journal of Electroanalytical Chemistry and Interfacial Electrochemistry*, 1975, **65**, 57–66.

[6] G. Denuault, M. V. Mirkin and A. J. Bard, *Journal of Electroanalytical Chemistry*, 1991, **308**, 27–38.

[7] M. E. Orazem and B. Tribollet, *Electrochemical Impedance Spectroscopy*, Wiley-Blackwell, 2008.

[8] R. D. Gryse, W. P. Gomes, F. Cardon and J. Vennik, *Journal of The Electrochemical Society*, 1975, **122**, 711–712.

[9] L. M. Peter, *Chemical Reviews*, 1990, **90**, 753–769.

[10] L. Peter, J. Li and R. Peat, *Journal of Electroanalytical Chemistry and Interfacial Electrochemistry*, 1984, **165**, 29–40.

Chapter 3

Electrochemical Behaviour of Methyl Viologen and Some Derivatives in Acetonitrile

3.1 Aims

A series of molecules were chosen for use in the study of the effects of molecular structure and electrode material upon the kinetics of electron transfer reactions. This chapter introduces those molecules and details studies of their electrochemical behaviour. The aim of these studies was to gain some understanding of the thermodynamics of the redox behaviour of the molecules, and to identify an appropriate electrolyte system. In Chapter 5 this information is utilised in the kinetic study of these molecules.

3.2 Molecular Structure

Methyl viologen (MV^{2+}) and a set of derivatives (C1-5) were chosen for kinetic study. The bonding structure of these molecules is shown in figure 3.1 and 3D ball and stick models are shown in Figure 3.2. These 3D models correspond to the ground state geometries determined using Spartan 04 (Wavefunction Inc., Irvine, CA, USA)[1] via density functional theory at the B3LYP/6-31G* level. The derivatives were originally synthesised by Dr. Peiyi Li with the aim of investigating the effect of the inter-ring torsional angle on the thermodynamics of their redox couples. Benniston et. at. have shown that by adding a linking tether connecting the aromatic rings of methyl viologen, the inter-ring torsional angle can be constrained and that by adjusting the length of the tether, this angle can be modified.[2] These derivatives were kindly donated by Professor A. Benniston for the purpose of this study.

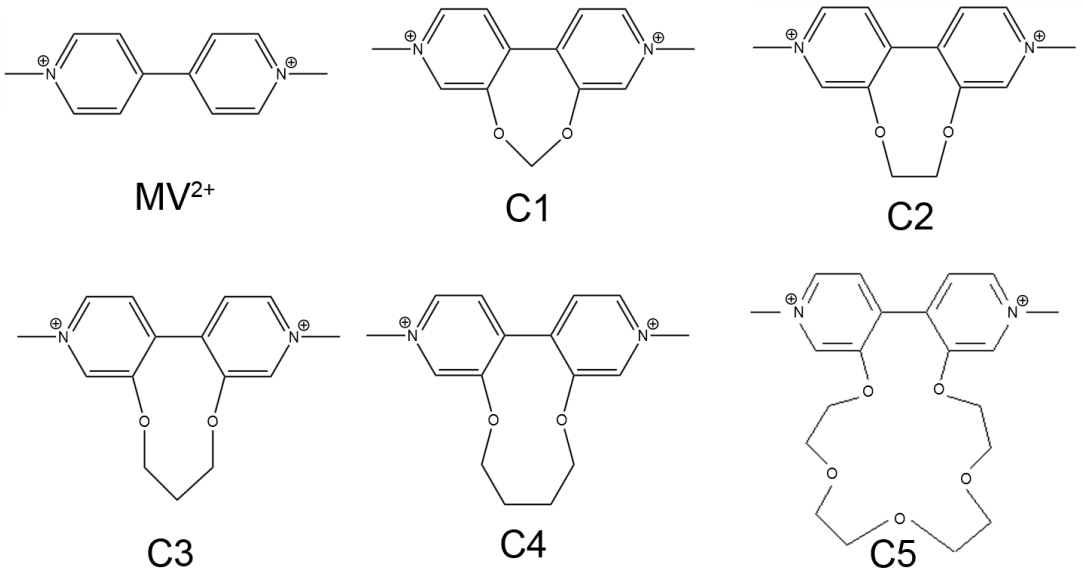

Figure 3.1: Methyl viologen (MV^{2+}) and a series of derivatives (C1-5).

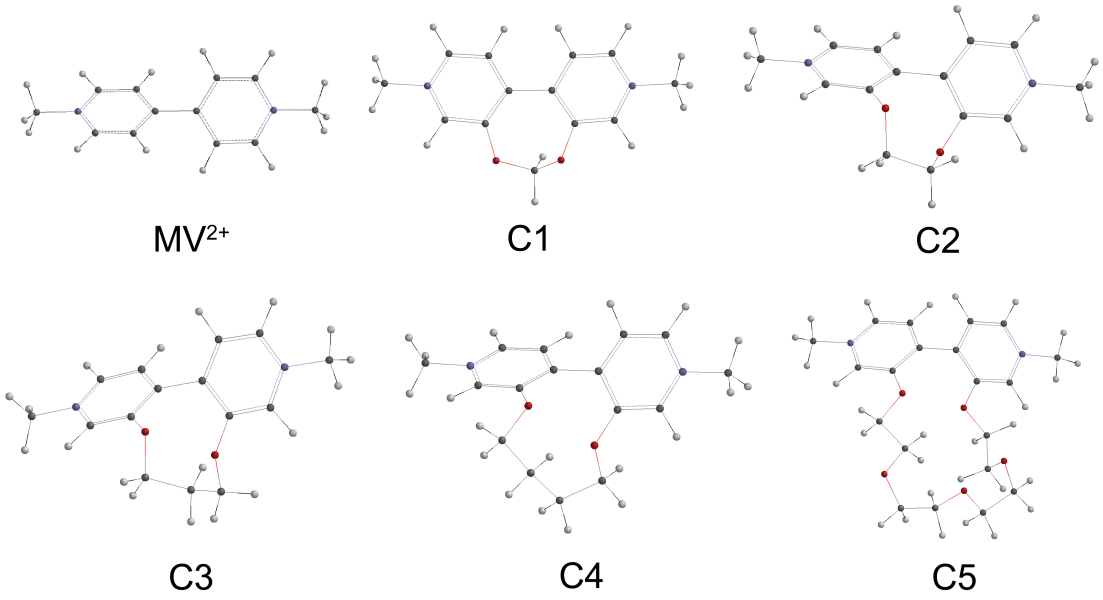

Figure 3.2: Methyl viologen (MV^{2+}) and a series of derivatives (C1-5). Ball and stick models corresponding to the ground state geometries determined using Spartan via density functional theory at the B3LYP/6-31G* level

The similarities in the structures of these molecules mean that it may be possible to attribute differences in rates at which they are reduced to differences in their molecular structure. This chapter will focus on the electrochemical behaviour of these molecules, particularly the redox couple involving the first one-electron reduction of each. The purpose of examining these reduction reactions will be to demonstrate the suitability of those reductions as a subject of kinetic study, and the comparability of the molecules.

Computational studies of these molecules were performed to determine the ground state molecular volumes and LUMO energies for each species. The effects of solvent and counter ions were neglected during these studies. The parameters obtained are given in Table 3.1. In addition, computational studies have been previously performed on these molecules by others, and the torsion angles of the dications

Molecule	Volume (Å)	LUMO Energy (eV)
MV^{2+}	215.02	−10.2
C1	237.66	−10.2
C2	256.20	−9.8
C3	274.03	−9.5
C4	291.89	−9.4
C5	393.09	−8.9

Table 3.1: Parameters determined computational at the B3LYP/6-31G* level of theory. The effects of solvent and counter ions are neglected in these calculations.

Molecule	Dication Torsion Angle (°)	Monocation Torsion Angle (°)
MV^{2+}	43	1
C1	35.7	10.1
C2	62.3	22.8
C3	51.3	25.3
C4	56.1	21.3
C5	54.1	21.1

Table 3.2: Parameters determined computational at the B3LYP/6-31G(d,p) level of theory for the molecules in MeCN with solvent effects being modelled using a polarised continuum model. [2]

and monocations measured to give the values in Table 3.2. Those studies were performed using the Gaussian03 software package[3] at the B3LYP/6-31G(d,p) level with solvent (MeCN) effects being modelled using a polarised continuum model.[2] The trends in the torsion angle observed in this computational study are consistent with x-ray crystal structures determined for the same molecules.[2]

The trends in the angle data indicate that these molecules will rearrange to minimise the size of the inter-ring torsion angle upon reduction. The effect of the torsion angle upon the rate of the reduction is examined in Section 5.7.

3.3 Qualitative Electrochemical Studies

In order that these molecules may be studied electrochemically, a solvent and electrolyte system must be chosen. The analyte molecule must be fully soluble before and after reduction in the chosen solution at the concentrations used and must not react with the electrolyte. Furthermore, the standard potential of redox couples under study must fall well within the operational range of the solvent. That is, the solvent must not be reduced or oxidised to any significant extent at the applied potentials used in the experiments. MeCN is a popular choice of solvent in organic electrochemistry due largely to its wide potential window. The solubilities of the PF_6 salt of methyl viologen and C1-5 were found to be sufficiently high in MeCN. Therefore, this solvent has been employed in the electrochemical study of these molecules.

In electrochemical kinetic studies, the ability to apply precise potentials is crucial for accurate determination of kinetic parameters. The potential of a reference electrode may change gradually and unpredictably, meaning that the same potential applied on two occasions against the same reference electrode, might result in a significantly different potential change across the working electrode/electrolyte interface. When a Ag/Ag^+ reference electrode was used with this system, it was found that no measurable potential drift occurred over time scales spanning several hours. Silver quasi-references and aqueous AgCl references were found to be extremely unstable, and any potentials measured using these references to be of little worth. Over short time scales ($<$ 1 hour), platinum wire quasi-reference electrodes exhibited surprising stability in this system. Unless stated

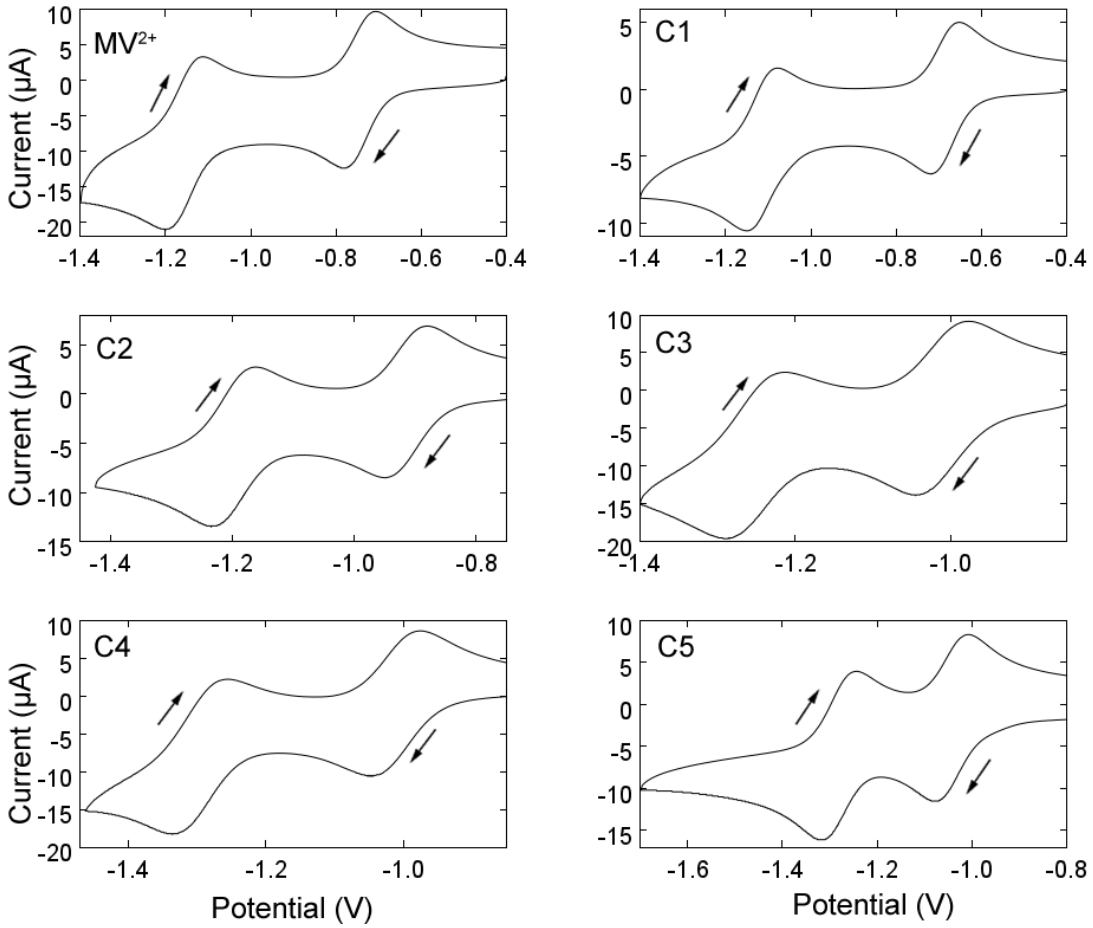

Figure 3.3: Cyclic voltammograms of MV^{2+} and derivatives C1-5 recorded at a 1 mm radius platinum disc working electrode. Analyte concentrations were 1 mM with 0.1M $TBAPF_6$ as supporting electrolyte in MeCN.

otherwise, potentials are recorded against a Ag/Ag^+ reference containing $AgNO_3$ at a concentration of 10 mM and $TBAPF_6$ at 0.1M in MeCN.

Cyclic voltammograms of MV^{2+} and C1-5 are shown in figure 3.3. It is clear from these voltammograms that each species exhibits similar redox behaviour to MV^{2+} in that each molecule can undergo two successive one-electron reductions, and each reduction exhibits some degree of reversibility. Furthermore, no other electron transfer

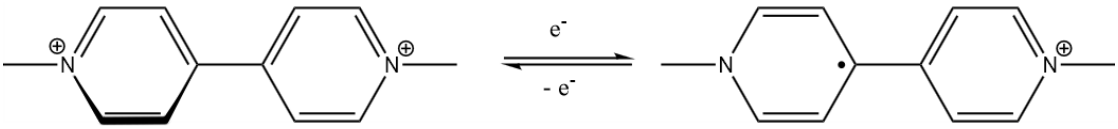

Figure 3.4: The redox couple corresponding to the first one-electron reduction of MV^{2+}. The aromatic rings of the radical form (right) are coplanar, while the aromatic rings of the dication form (left) are not.

processes are observed near the standard potentials of these redox couples. The electron transfer reactions which give rise to the peaks in the MV^{2+} CV are well understood. The reaction scheme for the first one-electron reduction of the molecule is shown in figure 3.4. Reduction generates a monocation radical capable of undergoing oxidation to reproduce the dication.[4–7] Presumably, analogous reactions exist for derivatives C1-5. These initial qualitative findings indicate that the solvent and electrolyte chosen are appropriate for the redox couples under study. The nature of the redox couple corresponding to the first one-electron reduction of these molecules is studied in greater detail below.

3.4 Determination of Formal Potentials

Half potentials for the first and second one-electron reduction of MV^{2+} and C1-5 were measured using square wave voltammetry. Square wave voltammograms for the first and second reduction are shown in Figure 3.5 and Figure 3.6 respectively. For the second one-electron reduction of MV^{2+}, some distortion of the square wave voltammogram is observed which may indicate that absorption is occurring upon reduction to the neutral form. The values obtained are tabulated in Table 3.3. The relationship between these half po-

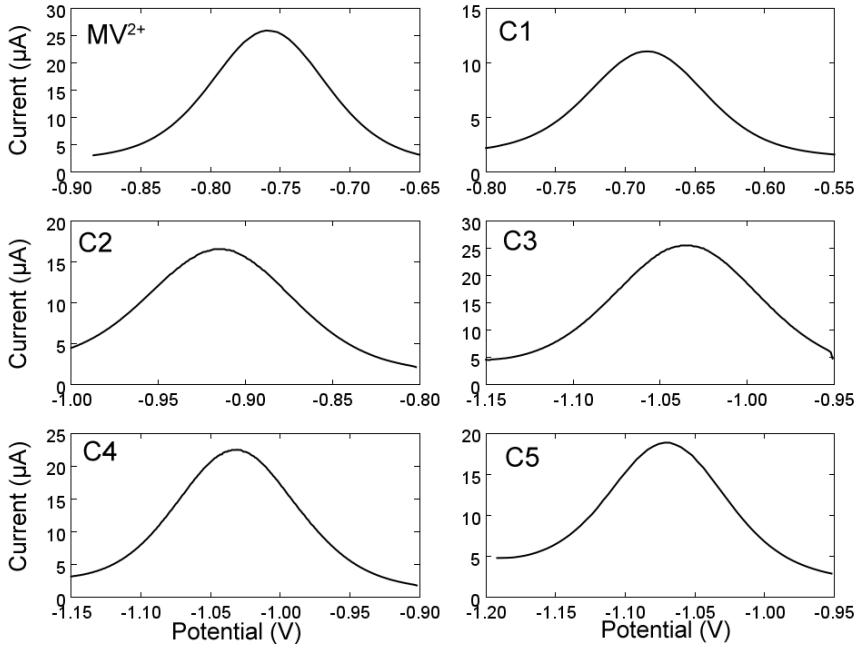

Figure 3.5: Square wave voltammograms recorded for methyl viologen and derivatives C1-5 (1 mM) with $TBAPF_6$ (0.1M) in MeCN. The peaks correspond to the first one-electron reduction for each molecule.

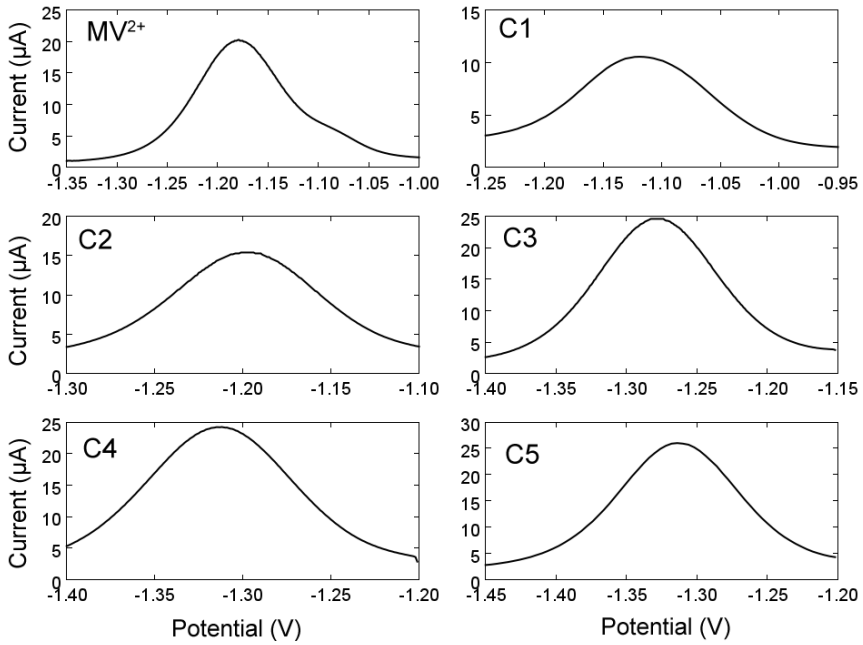

Figure 3.6: Square wave voltammograms recorded for methyl viologen and derivatives C1-5 (1 mM) with $TBAPF_6$ (0.1M) in MeCN. The peaks correspond to the second one-electron reduction for each molecule.

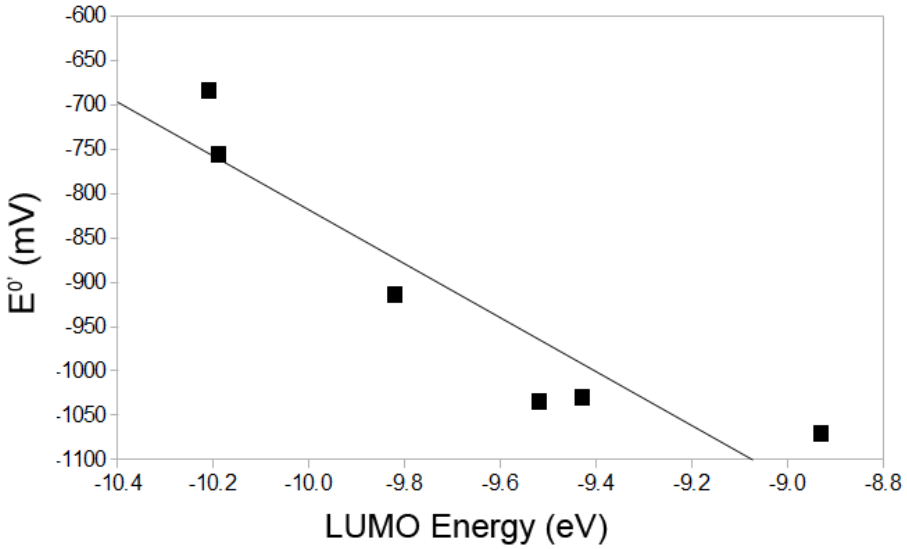

Figure 3.7: Relationship between the measured formal potentials for the first one-electron reduction and the LUMO energy determined computationally using B3LYP/6-31G* level of theory, for each molecule

tentials and the formal potentials of the redox couples is given by Equation 3.1, where D_O and D_R refer to the diffusion coefficients of the oxidised and reduced forms respectively. If equality of the diffusion coefficients before and after reduction can be assumed, then the measured half potential can be assumed to be equal to the formal potential of the redox couple. The validity of this assumption is checked below (Section 3.6). A plot of these measured half potentials against the calculated LUMO energies is shown in Figure 3.7. As expected, a correlation is observed between the two variables.

$$E_{\frac{1}{2}} = E^{0'} + \frac{RT}{nF} \ln \left(\frac{D_R}{D_O} \right)^{\frac{1}{2}} \tag{3.1}$$

	$E^{\frac{1}{2}}{}_a$ (mV)	$E^{\frac{1}{2}}{}_b$ (mV)
MV^{2+}	−759	−1179
C 1	−684	−1119
C 2	−914	−1197
C 3	−1034	−1278
C 4	−1030	−1312
C 5	−1070	−1314

Table 3.3: Redox potentials for the first $\left(E^{\frac{1}{2}}{}_a\right)$ and second one-electron $\left(E^{\frac{1}{2}}{}_b\right)$ reduction of MV^{2+} and derivatives C1-5 measured against a Ag/Ag^+ (10 mM) reference in MeCN with 0.1M $TBAPF_6$.

3.5 Reversibility

The study of the thermodynamics of the first one-electron reduction of these molecules would be greatly simplified if these electron transfer reactions were fully reversible. If an electron transfer reaction is fully reversible, the CV is expected to meet the following criteria:[8]

1. The forward and reverse peaks are $\frac{59}{n}$ mV apart
2. The height of the forward and reverse peaks are equal
3. Both peak heights are directly proportional to the square root of scan rate
4. The peak positions are independent of scan rate

To test the reversibility of these systems, a cyclic voltammogram across a potential range around the standard potential of the first one-electron reduction for each redox couple was simulated.[8] This simulation was then fitted to a CV measured across the same potential range. Potential ranges were chosen such that the second

Parameter	Value
Scan rate (v)	0.1 V s^{-1}
Electrode area (A)	3.14×10^{-2} cm^2
Electrons transferred (n)	1
Temperature (T)	293 K
Uncompensated resistance (R_u)	100 Ω

Table 3.4: Fixed parameters used in all CV simulations.

one-electron reduction of each molecule did not appear in the voltammogram. A number of fixed parameters, valid for each system, were used, and these are given in Table 3.4. The formal potential of the couple ($E^{0'}$) and the precise analyte concentration (C^*) is then used for each system and the diffusion coefficient floated to match the voltammogram. These voltammograms and the fitted simulations are shown in Figure 3.8.

If the simulation fits well to both the forward and reverse peak, this is a strong test of reversibility criteria 1 and 2. In many cases, significant deviation from the simulation is observed at potentials negative of the standard potential of the redox couple, a likely cause being faradaic current that results from the second one-electron reduction occurring to a small extent at those potentials. In terms of peak height and separation, these voltammograms show a good match between the experimental and simulated data, with C2 being an exception. In the case of C2, the experimentally observed reverse wave is smaller than that predicted by simulation, suggesting some degree of irreversibility. However, the effect is small and should not cause problems during high speed kinetic measurements.

For an electron transfer reaction occurring at an electrode surface involving a single molecule in solution, a linear relationship between the square root of the CV scan rate, and the height of the forward

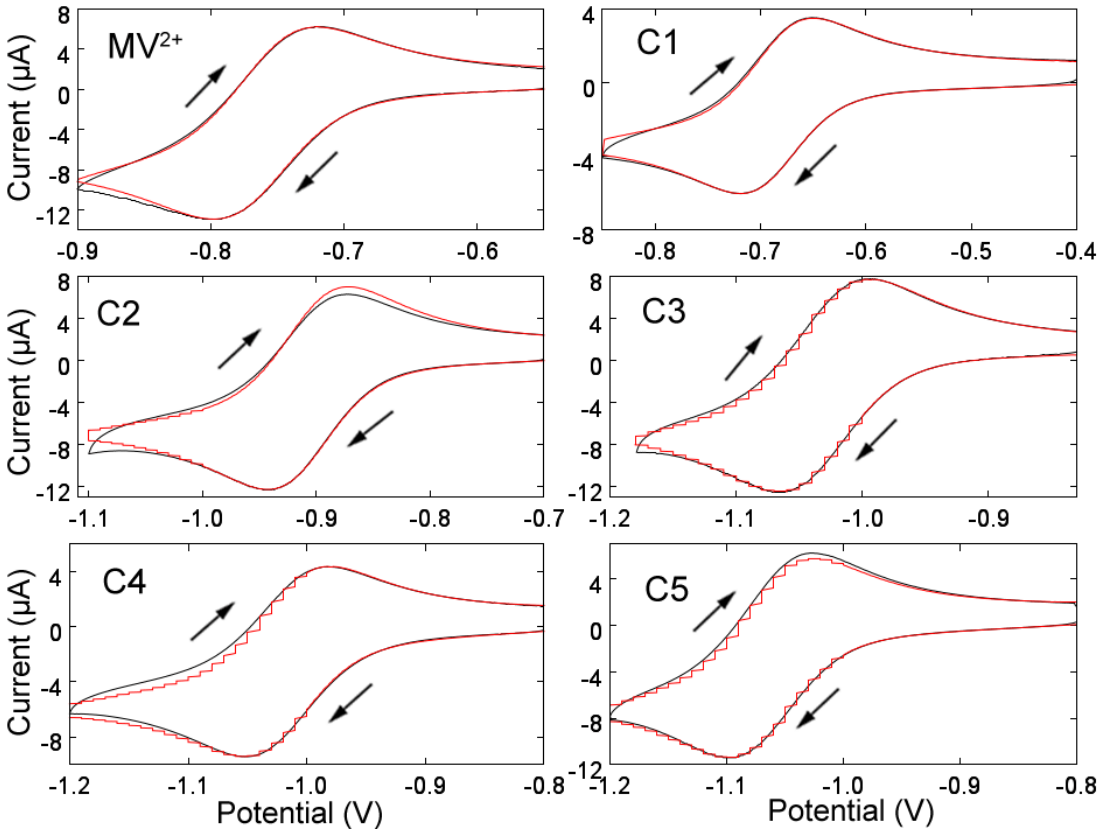

Figure 3.8: Voltammograms recorded for MV^{2+} and C1-5 (1 mM) in MeCN with $TBAPF_6$ (0.1M) are shown as black lines. Simulations fitted to these voltammograms are plotted as red lines.

and reverse peaks in the CVs is expected. For a species adsorbed upon the electrode surface, a linear relationship between the scan rate and the peak current is expected. In a case where the molecule is absorbed upon the surface to some extent, an intermediate case is expected. Therefore, a plot of the peak CV current as a function of the square root of the scan rate can be used to determine the extent of adsorption. Any curve in the trend in experimental data that results in current being higher than that predicted by a linear trend is diagnostic of adsorption, and the extent of the curvature can give a quantitative measure of the extent of adsorption. Such plots for the molecules are displayed in Figure 3.9. (The peak heights used for the plot are taken before the subtraction of background current, therefore the relative heights of the two peaks cannot be compared using this data.) In each case, deviation from linearity is very small, over scan rates spanning several orders of magnitude. Significant deviation of the current from linearity is observed for the forward wave of C1, however this may be due to current from the second redox couple or adsorption of the neutral species at highly negative potentials. The extent of the deviation is less for the reverse wave, and remains small. This indicates that adsorption of each species did not occur to any great extent in MeCN and the redox couple meets criteria 3 for reversibility. This is in contrast to observations at platinum, gold, mercury and glassy carbon electrodes in aqueous solutions, where adsorption occurs to a significant extent.[9–12]

A variation in the position of the forward and reverse wave peaks as scan rate is varied is observed, however for high scan rates, a significant potential drop may occur across the electrolyte solution due to the high currents involved. This potential drop is equal to the solution resistance multiplied by the current. Since current is linear

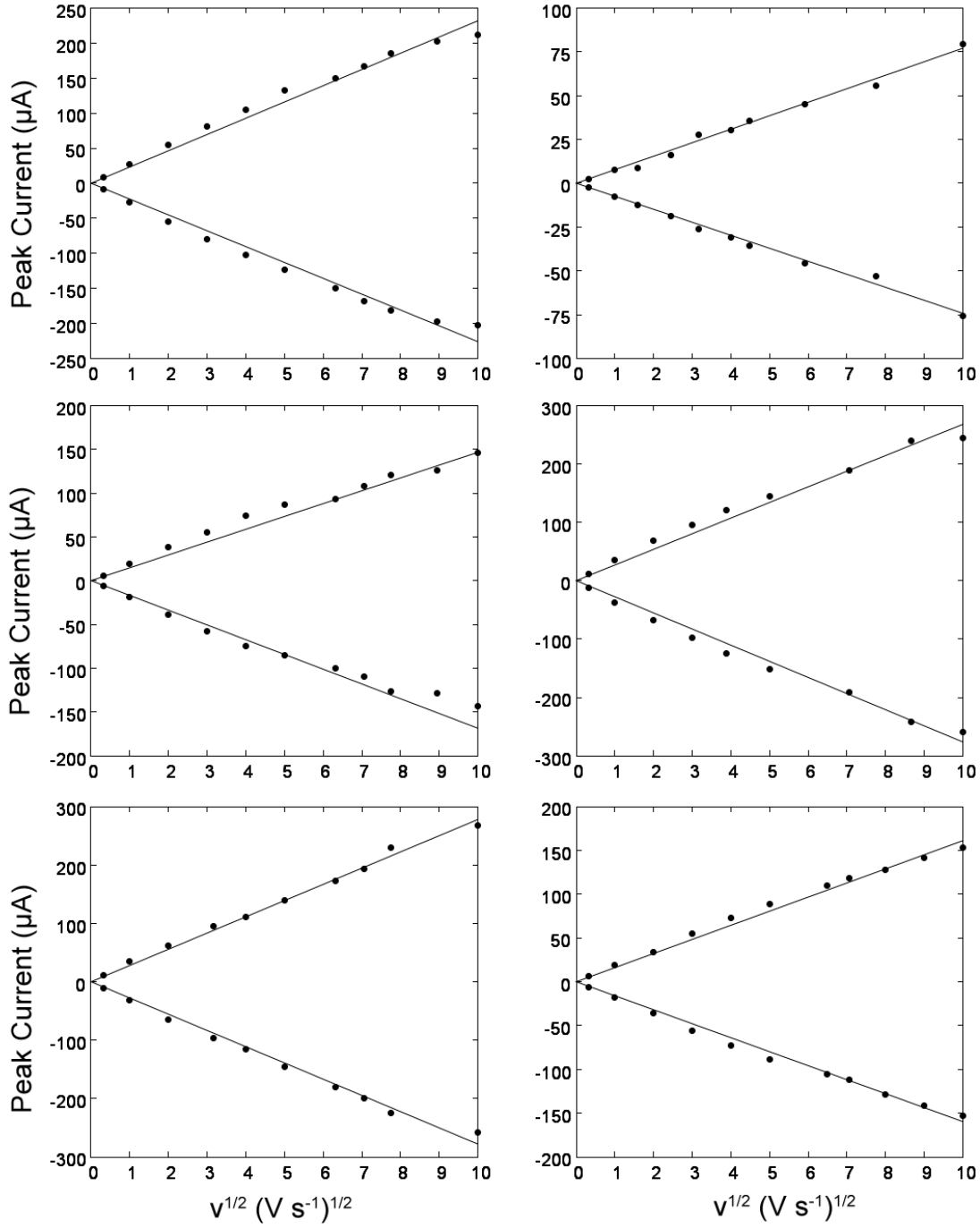

Figure 3.9: Peak heights for the forward and reverse wave for the first one-electron reduction of MV^{2+} and C1-5 (1 mM) with $TBAPF_6$ (0.1M) in MeCN were found to have a linear dependence on the square root of scan rate. Data collected at a 1 mm radius platinum disc working electrode. Current values are taken prior to subtraction of background current thus a comparison of the relative peak heights cannot be made using this data.

with the square root of current, resistance effects will cause the peak positions to be linear with the square root of current also. Peak position data as a function of the square root of scan rate is plotted in Figure 3.10. The grey data points represent the peak positions found before the correction for resistance effects. In all cases the position is linear with the square root of current. The size of the peak current at each scan rate is multiplied by a constant solution resistance to correct for resistance effects. The solution resistance was floated in each case to minimise the sum of the squared slopes of the corrected peak positions, shown as coloured points on the plot. This correction is then tested by taking the average of the two peak positions, $E_{1/2}$, which is found to also be independent of scan rate following correction. Thus peak positions are found to be independent of scan rate following correction for resistance effects and criteria 4 is satisfied.

The reasonable satisfaction of all four criteria in all cases means that these molecules may all be considered to be simple reversible redox couples.

3.6 Measurement of Diffusion Coefficients

Chronoamperometry at a 25 μm platinum radius disc was used to determine the diffusion coefficient for each molecule. In these experiments, the applied potential was stepped from a point at which the reduction of the molecule was not occurring to any significant extent, to a value at which the rate of reduction was diffusion limited. In these conditions the faradaic current is given by Equation 3.2, known

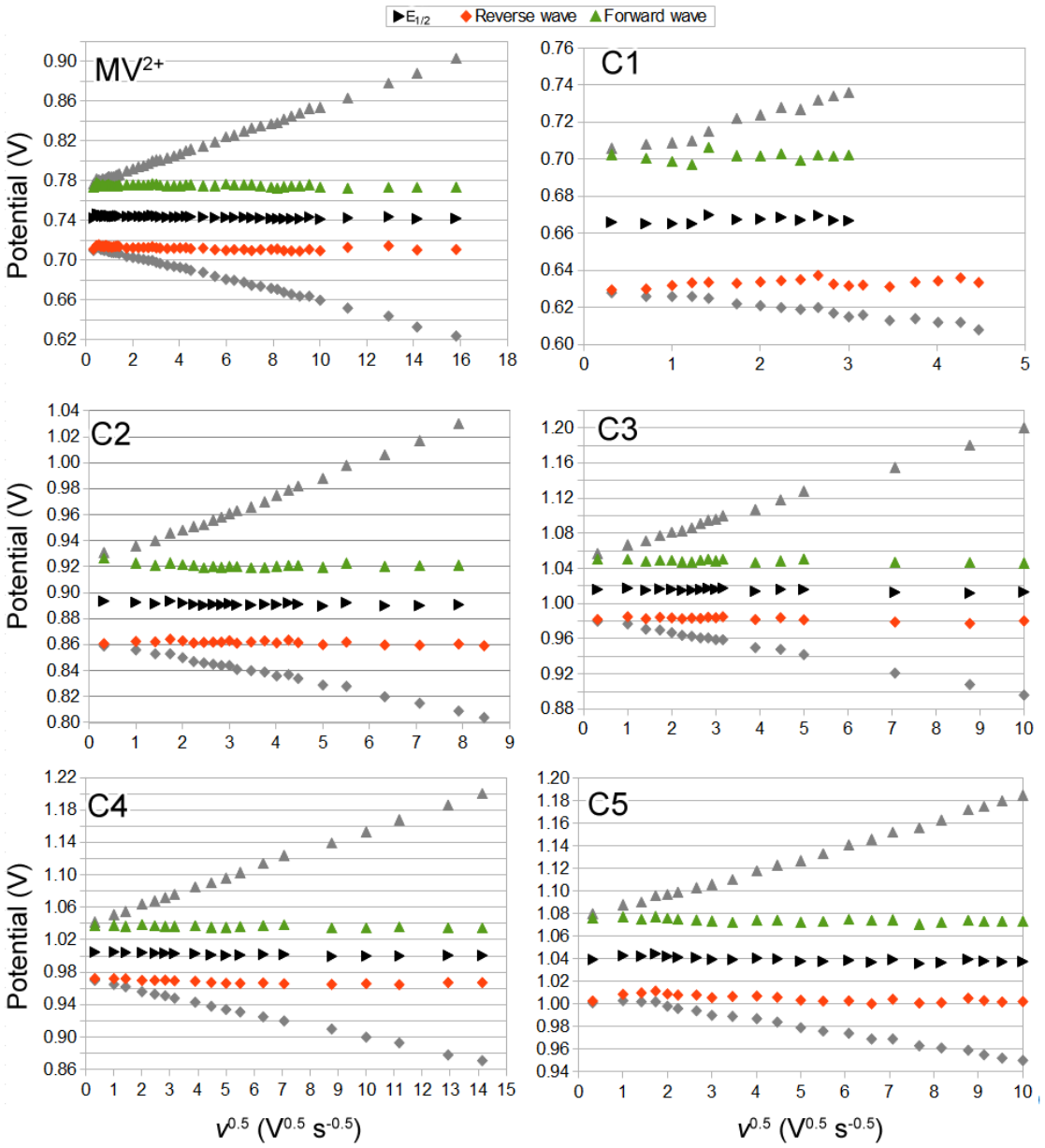

Figure 3.10: The positions of the forward and reverse CV waves plotted against the square root of scan rate. Grey data points represent the peak positions before correcting for solution resistance. CVs were recorded at a 1 mm radius platinum disc electrode in MeCN with 1 mM analyte and 0.1M $TBAPF_6$.

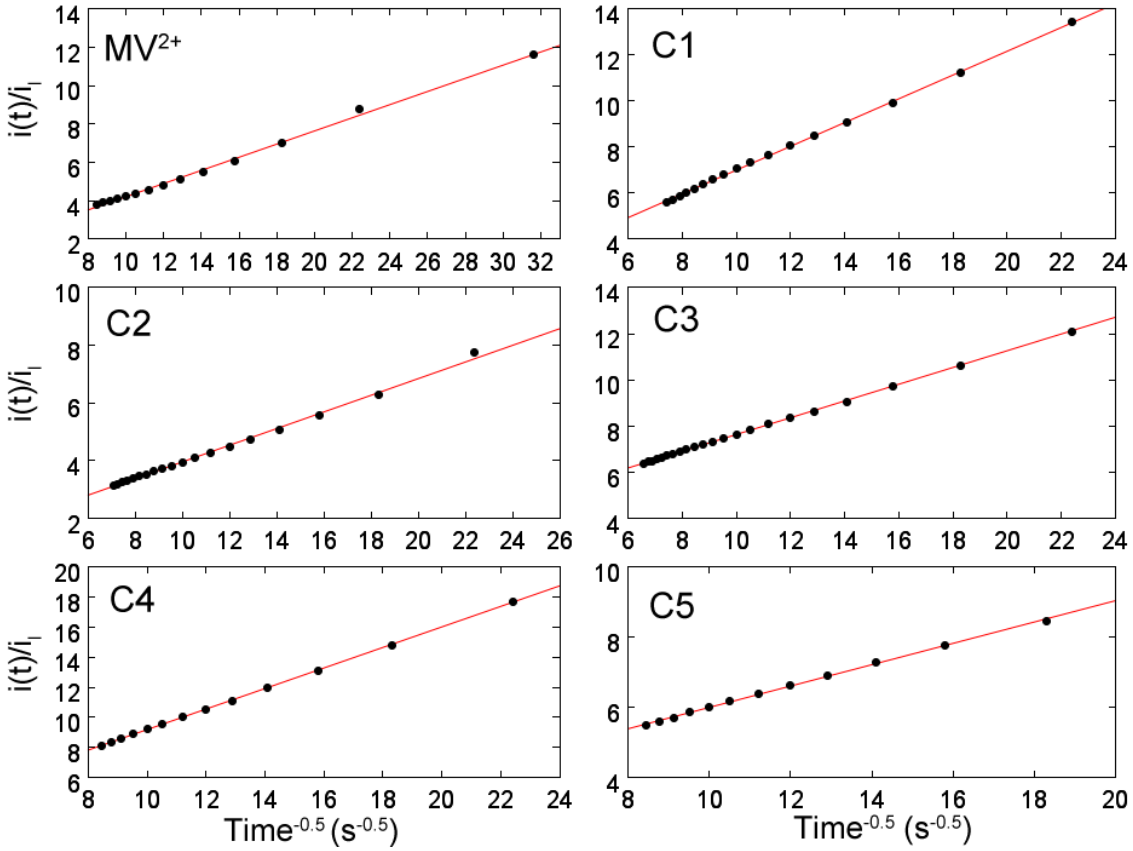

Figure 3.11: The ratio of the current, $i(t)$, to the limiting current, i_l, measured in chronoamperometry experiments as a function of $t^{-0.5}$. Data collected at a 25 μm radius platinum disc in MeCN with an analyte molecule (1 mM) and $TBAPF_6$ (0.1M).

as the Cottrell equation.

$$i(t) = \frac{nFAC^*\sqrt{D}}{\sqrt{\pi t}} \tag{3.2}$$

After several seconds, the current at an ultramicroelectrode will approach a limiting value, given by Equation 3.3.

$$i_l = 4rnFDC^* \tag{3.3}$$

Molecule	D_O (cm^2 s^{-1})
$\mathbf{MV^{2+}}$	$1.05 \pm 0.03 \times 10^{-5}$
C 1	$4.61 \pm 0.15 \times 10^{-6}$
C 2	$1.47 \pm 0.03 \times 10^{-5}$
C 3	$9.35 \pm 0.12 \times 10^{-6}$
C 4	$2.65 \pm 0.15 \times 10^{-6}$
C 5	$1.33 \pm 0.03 \times 10^{-5}$

Table 3.5: Values of D_O found for MV^{2+} and compounds C1-5 found using chronoamperometry at a 25 μm radius platinum disc electrode in MeCN with 0.1M $TBAPF_6$ and 1 mM analyte.

Division of Equation 3.2 by Equation 3.3 yields Equation 3.4.

$$\frac{i(t)}{i_l} = \frac{A}{4r\sqrt{D\pi t}} \tag{3.4}$$

The gradient of a plot of $\frac{i}{i_l}$ against $t^{-0.5}$ will then be as given by Equation 3.5.

$$\frac{1}{i_l}\frac{\partial i(t)}{\partial(t^{-0.5})} = \frac{A}{4r\sqrt{D\pi}} \tag{3.5}$$

Thus, with knowledge of the electrode radius, the diffusion coefficient for the reaction can be determined from this gradient.[13,14] The obtained coefficients are given in Table 3.5, with errors determined from the slope. Note that if the electrode is not perfectly circular, or its radius is not known accurately, then this will provide a source of error which is not contained in the error in the slope of the plot. Plots of $i(t)/i_l$ as a function of $t^{-0.5}$ are shown in Figure 3.11.

The diffusion coefficients of MV^{2+} and derivatives C1-5 are expected to be correlated with molecular volume to some extent. However, no such correlation is observed in Table 3.5, and the highest diffusion

Molecule	$\Delta E_{\frac{1}{2}}$ (mV)
$\mathbf{MV}^{2+}$	1
C 1	3
C 2	3
C 3	4
C 4	3
C 5	2

Table 3.6: Differences in half potentials measured in time-dependent and steady-state voltammograms for the one-electron reduction of MV^{2+} and compounds C1-5 measured against an Ag/Ag^{+} reference in MeCN with 0.1M $TBAPF_6$.

coefficient measured is for the largest molecule, C5. This surprising result is cause to doubt the validity of the coefficients in Table 3.5. Given that the analysis of the chronoamperometric data makes use of only the data at short time scales, it seems likely that the diffusion coefficient measurements have been affected by processes occuring at the platinum surface. The reduction of trace water, protons or platinum oxide on the platinum surface are processes that may have occured during the chronoamperometric experiments. An analysis which makes use of Equation 3.3 to deterine the diffusion coefficient based upon the limiting current at a UME would likely have allowed more accurate measurements of the diffusion coefficients.

The value of $E_{\frac{1}{2}}$ for steady-state voltammograms is given by Equation 3.6.[8]

$$E_{\frac{1}{2}} = E^{0'} + \frac{RT}{nF} \ln\left(\frac{D_R}{D_O}\right) \tag{3.6}$$

By combining Equation 3.1 and Equation 3.6, it can be shown that the ratio of the diffusion coefficients is related to difference in the values of $E_{\frac{1}{2}}$ measured in the time-dependent and steady-state regimes,

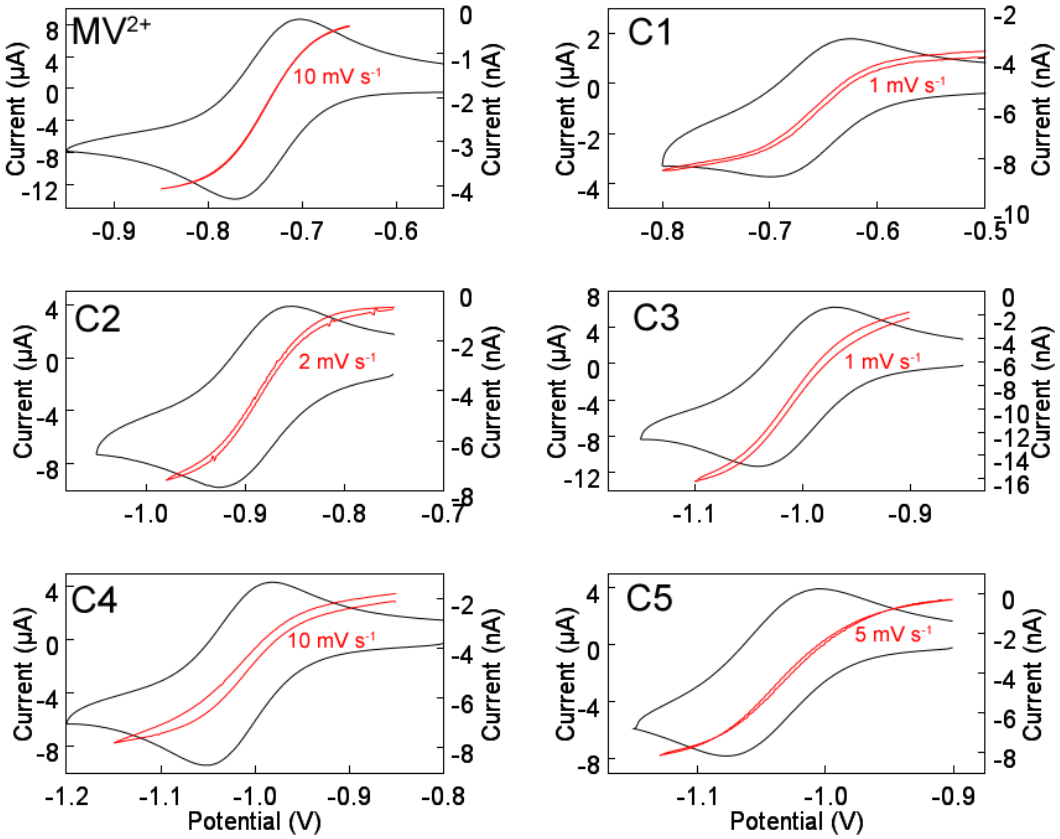

Figure 3.12: Time dependent CVs recorded at 1 mm radius platinum disc electrodes with a scan rate of 0.1 V/s (black, left y-axis). Overlayed are steady state voltammograms recorded at 5 μm radius platinum discs (red, right y-axis). The scan rates at which the SSVs were recorded are given in each plot. Solutions contained 1 mM of analyte with 0.1M $TBAPF_6$

ΔE, according to Equation 3.7.

$$\frac{D_O}{D_R} = \exp\left(\frac{2nF\Delta E}{RT}\right) \tag{3.7}$$

These differences were determined for each molecule and are tabulated in Table 3.6. To minimise the effect of small drifts in the potential of the reference electrode, these differences were determined from time-dependent and steady-state voltammograms recorded in quick

succession. Given that the differences in $E_{\frac{1}{2}}$ are small, they are more likely the result of reference electrode drift, or differences in solution resistance than the result of differences in diffusion coefficients.

Some of the recorded steady-state voltammograms, shown in Figure 3.12, that of C4 in particular, do not retrace themselves very closely. In these cases the first derivative of the forward wave was used to determine the half potential of the voltammogram. A maximum in the voltammogram's first derivative will occur at $E_{\frac{1}{2}}$. In some cases, slower scan rates resulted in poorer retraceability suggesting that the lack of retraceability was likely the result of electrode fouling. Electrode fouling is a common source of systematic error in electrochemical measurements as it lowers the effective area of the working electrode. Steady-state voltammograms take several minutes to record, meaning that if fouling is occurring, it may be a slow process that will not significantly effect high speed measurements.

3.7 Ion Pairing

Ion pairing is a phenomenon in which species of opposite charge travel through solution together, behaving, in some respects, as a single molecule. Such pairing will reduce the effective charge of the paired molecules and thus the ionic strength of the solution. The diffusion coefficient of an analyte molecule may be altered significantly by the effect of ion pairing, and the effect of potential gradients in solution upon the analyte will be similarly effected. In order to understand the behaviour of the molecules studied here at the electrode/electrolyte interface, some degree of understanding of ion

(a) $MV^{2+}-2\,PF_6^- + e^- \longrightarrow MV^+\text{-}PF_6^- + PF_6^-$
(b) $MV^{2+}-PF_6^- + e^- \longrightarrow MV^+-PF_6^-$
(c) $MV^{2+}-PF_6^- + e^- \longrightarrow MV^+ + PF_6^-$
(d) $MV^{2+} + e^- \longrightarrow MV^+$

Figure 3.13: Four plausible reduction mechanisms for MV^{2+}. Mechanisms (a) to (c) include some ion pairing between MV^{2+} and the PF_6^- ion present in solution. Mechanism (d) is for a case in which no ion pairing occurs.

pairing behaviour is crucial. Figure 3.13 displays four possible mechanisms for the reduction of methyl viologen, with and without ion pairing effects.

To determine the extent of ion pairing, the limiting current at an ultramicroelectrode was used to determine an effective diffusion coefficient as a function of the analyte and electrolyte concentration ratio. As the ionic strength of the solution is lowered, the charge on the working electrode will have a greater effect on analyte in solution and cause transport of charged analyte to the surface to be partially driven by electrostatic attraction, increasing the apparent rate of diffusion. Figure 3.14 shows how the limiting current of a steady-state voltammogram measured for a MV^{2+} (1 mM) solution changed with changes in electrolyte concentration. The observed increase in the limiting current is 15%. The rate of passive diffusion to the electrode surface should not be strongly affected by the electrolyte concentration. This increase in the observed rate of mass transport is therefore likely to be the effect of an increased magnitude of ϕ_2 upon a charged species. This evidence is incompatible with mechanism (a) as it involves a reactant with no effective charge. Mechanism (c) is incompatible with the linear relationship observed between the reverse peak current in CV and the square root of scan rate. This leaves mechanisms (b) and (d) as the only likely options.

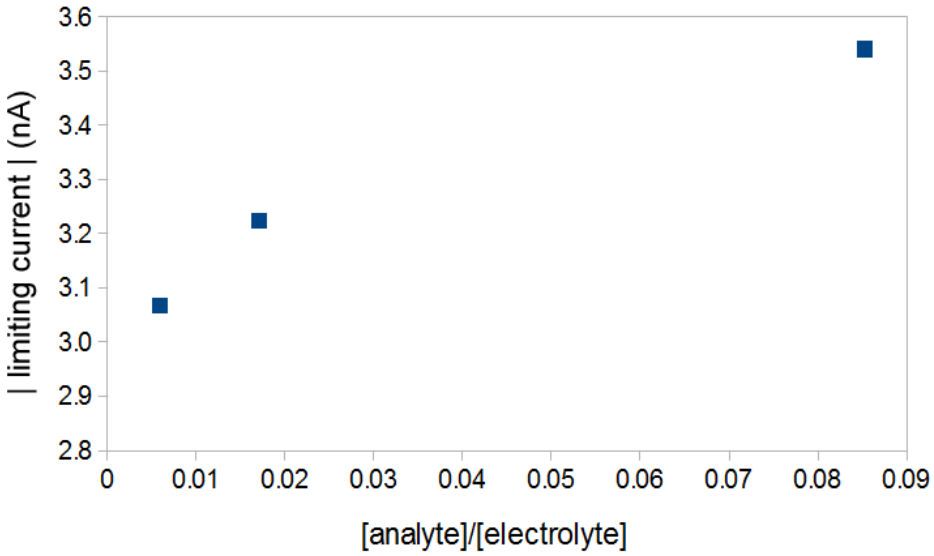

Figure 3.14: Limiting current of steady state voltammograms at a 5 mm radius platinum disc electrode plotted again analyte to electrolyte concentration ratios. Solutions contained 1 mM MV^{2+} and varying concentrations of $TBAPF_6$ in MeCN. The measured diffusion coefficient is seen to increase as the ratio of analyte concentration to supporting electrolyte concentration is decreased.

It has been shown that for MV^{2+} in dimethyl ether, the increase in limiting current that is observed when ionic strength is lowered can be explained using a model which does not involve any ion pairing effects.[15] Furthermore, the percentage increase in limiting current over the analyte to electrolyte concentration ratio range used here is roughly 15% in dimethyl ether. Given that a very similar increase in limiting current is observed here, it is likely that the same model is applicable to the system under study here, meaning that ion pairing is unlikely to be occurring to any significant extent. Other work has shown that for MV^{2+} (0.5 mM) in acetonitrile with tertbutylammonium perchlorate, an effective charge of +2 on MV^{2+} is required to explain the increases in current observed when electrolyte concentration is reduced.[16] The similarity of this system with that used here suggests that ion pairing effects will also be absent here. It

will be assumed that ion pairing effects are also absent in all solutions containing derivatives C1-5, given the similarities to MV^{2+} in their molecular and electronic structures. Knowledge of the effective charge of the molecules will be needed in Section 5.5 to allow Frumkin correction of their standard rate constants and in doing so, the findings of this section will be further tested.

Bibliography

[1] J. Kong, C. A. White, A. I. Krylov, D. Sherrill, R. D. Adamson, T. R. Furlani, M. S. Lee, A. M. Lee, S. R. Gwaltney, T. R. Adams, C. Ochsenfeld, A. T. B. Gilbert, G. S. Kedziora, V. A. Rassolov, D. R. Maurice, N. Nair, Y. Shao, N. A. Besley, P. E. Maslen, J. P. Dombroski, H. Daschel, W. Zhang, P. P. Korambath, J. Baker, E. F. C. Byrd, T. Van Voorhis, M. Oumi, S. Hirata, C.-P. Hsu, N. Ishikawa, J. Florian, A. Warshel, B. G. Johnson, P. M. W. Gill, M. Head–Gordon and J. A. Pople, *Journal of Computational Chemistry*, 2000, **21**, 1532–1548.

[2] A. C. Benniston, A. Harriman, P. Li, J. P. Rostron, R. W. Harrington and W. Clegg, *Chemistry - A European Journal*, 2007, **13**, 7838–7851.

[3] M. J. Frisch, G. W. Trucks, H. B. Schlegel, G. E. Scuseria, M. A. Robb, J. R. Cheeseman, J. A. Montgomery, Jr., T. Vreven, K. N. Kudin, J. C. Burant, J. M. Millam, S. S. Iyengar, J. Tomasi, V. Barone, B. Mennucci, M. Cossi, G. Scalmani, N. Rega, G. A. Petersson, H. Nakatsuji, M. Hada, M. Ehara, K. Toyota, R. Fukuda, J. Hasegawa, M. Ishida, T. Nakajima, Y. Honda, O. Kitao, H. Nakai, M. Klene, X. Li, J. E. Knox, H. P. Hratchian, J. B. Cross, V. Bakken, C. Adamo, J. Jaramillo, R. Gom-

perts, R. E. Stratmann, O. Yazyev, A. J. Austin, R. Cammi, C. Pomelli, J. W. Ochterski, P. Y. Ayala, K. Morokuma, G. A. Voth, P. Salvador, J. J. Dannenberg, V. G. Zakrzewski, S. Dapprich, A. D. Daniels, M. C. Strain, O. Farkas, D. K. Malick, A. D. Rabuck, K. Raghavachari, J. B. Foresman, J. V. Ortiz, Q. Cui, A. G. Baboul, S. Clifford, J. Cioslowski, B. B. Stefanov, G. Liu, A. Liashenko, P. Piskorz, I. Komaromi, R. L. Martin, D. J. Fox, T. Keith, M. A. Al-Laham, C. Y. Peng, A. Nanayakkara, M. Challacombe, P. M. W. Gill, B. Johnson, W. Chen, M. W. Wong, C. Gonzalez and J. A. Pople, *Gaussian 03, Revision C.02*.

[4] Y. Huang and J. B. Hopkins, *The Journal of Physical Chemistry*, 1996, **100**, 9585–9591.

[5] T. M. Bockman and J. K. Kochi, *The Journal of Organic Chemistry*, 1990, **55**, 4127–4135.

[6] L. Michaelis and E. S. Hill, *The Journal of General Physiology*, 1933, **16**, 859–873.

[7] J. H. Ross and R. I. Krieger, *Journal of Agricultural and Food Chemistry*, 1980, **28**, 1026–1031.

[8] A. J. Bard and L. Faulkner, *Electrochemical Methods: Fundamentals and Applications*, John Wiley & Sons, 2nd edn., 2001.

[9] P. M. S. Monk and N. M. Hodgkinson, *Electrochimica Acta*, 1998, **43**, 245–255.

[10] L. Xiao, G. G. Wildgoose and R. G. Compton, *New Journal of Chemistry*, 2008, **32**, 1628.

[11] E. Engelman and D. H. Evans, *Journal of Electroanalytical Chemistry*, 1993, **349**, 141–158.

[12] M. Rueda, R. Compton, J. Alden and F. Prieto, *Journal of Electroanalytical Chemistry*, 1998, **443**, 227–235.

[13] C. Winlove, K. Parker and R. Oxenham, *Journal of Electroanalytical Chemistry and Interfacial Electrochemistry*, 1984, **170**, 293–304.

[14] G. Denuault, M. V. Mirkin and A. J. Bard, *Journal of Electroanalytical Chemistry*, 1991, **308**, 27–38.

[15] C. Amatore, M. F. Bento and M. I. Montenegro, *Analytical Chemistry*, 1995, **67**, 2800–2811.

[16] J. D. Norton and H. S. White, *Journal of Electroanalytical Chemistry*, 1992, **325**, 341–350.

Chapter 4

Platinum and Bismuth Electrode Surfaces

4.1 Aim

In order to understand the differences in rate constants at platinum and bismuth, the properties of the two surfaces must be characterised. Primarily, the Fermi-level density of states (DOS) must be known and the nature of the potential change across the two electrode/electrolyte interfaces understood. In this chapter, differential capacitance measurements will be fitted to the Gouy-Chapman-Stern model in order to determine the size of the potential drop across the electrode surfaces. Additionally, the differential capacitance at a bismuth surface will be used to estimate the Fermi-level density of states of the material. The density of states value is important as it is a factor which determines the density of charge carriers at each

surface. This information will be utilised in the interpretation of the kinetic data in Chapter 5.

4.2 The Gouy-Chapman-Stern Model

The Gouy-Chapman-Stern (GCS) model allows prediction of the differential capacitance, c_{dl}, observed at the surface of a smooth, homogeneous electrode as a function of potential.[1] The model treats the electrode/electrolyte interface as two capacitors in series, the first, c_D, models the capacitance in the diffuse layer, and the second, c_H, models the capacitance across the Helmholtz plane and the electrode's immediate surface. The total capacitance is then given by Equation 4.1.

$$\frac{1}{c_{dl}} = \frac{1}{c_H} + \frac{1}{c_D} \tag{4.1}$$

In the model, the capacitance c_H is constant with potential and is described by Equation 4.2 where x_{OHP} is the distance between the outer Helmholtz plane (OHP) and the electrode surface, and ϵ_H is the dielectric constant corresponding to the molecules at a distance of x_{OHP} and below from the electrode surface. The parameter ϵ_H is often taken as 3. This low permittivity is a result of the molecules at the electrode surface being held in place by the charge of the electrode acting on their dipoles or charges and preventing them from moving to respond to other or additional charges. The physical constant ϵ_0 is the permittivity of free space.

$$c_H = \frac{\epsilon_H \epsilon_0}{x_{OHP}} \tag{4.2}$$

The capacitance c_D is dependent on potential and is given by Equation 4.3 for an electrolyte consisting of two ions of equal charge z. The parameters e, I and κ are the elementary charge, the ionic strength of the bulk solution, and the Boltzmann constant respectively. The parameter ϵ_S here refers to the dielectric constant of the bulk solvent. The potential dependence comes from the parameter ϕ_2, which must be measured or estimated.

$$c_D = \sqrt{\frac{2\epsilon_S \epsilon_0 z^2 e^2 I}{\kappa T}} \cosh\left(\frac{ze\phi_2}{2\kappa T}\right) \tag{4.3}$$

The potential difference between the bulk of the electrode and the bulk of the solution consists of the change occurring at the Helmholtz plane, ϕ_1, and the change occurring through the diffuse layer, ϕ_2. The total potential drop is then given by Equation 4.4.

$$\phi = \phi_1 + \phi_2 \tag{4.4}$$

Given that the function $\cosh(x)$ is at its minimum when $x = 0$, it is clear from Equation 4.3 that c_D reaches a minimum when $\phi_2 = 0$, and increases indefinitely as ϕ_2 increases. The potential at which $\phi = \phi_1 = \phi_2 = 0$, is known as the potential of zero charge (PZC), denoted E_{PZC}, and is the potential at which no excess charge is held by the electrode surface. As $|E - E_{PZC}|$ increases, the value of ϕ_2 and thus c_D is expected to increase without limit. When $c_D >> c_H$,

Equation 4.1 simplifies to Equation 4.5 and c_{dl} is constant.

$$c_{dl} = c_H \tag{4.5}$$

The GCS model therefore predicts that differential capacitance will be independent of potential when the applied potential is far from E_{PZC}, but a minimum in capacitance will be approached as the potential approaches E_{PZC}, and that this decline in capacitance will be greater when the electrolyte is of lower ionic strength.

The GCS model will be used as a basis for predicting ϕ_2 at the surface of a platinum electrode. The model works well for liquid electrodes and electrodes consisting of a single, carefully prepared crystal face at potential near the PZC but unfortunately, the model is not fully appropriate for the solid, polycrystalline electrodes employed here. Therefore, perfect fitting of the GCS model to the data cannot be expected.[2] Additionally, the presence of electroactive species in the electrolyte solution further complicates the measurement of double layer properties. Analyte molecules will therefore be absent during these studies of platinum capacitance and the double layer behaviour observed may not be fully identical to behaviour in the presence of analyte. These shortcomings must be borne in mind when considering the accuracy of the determined ϕ_2 values and any further conclusions that make use of them. Despite these shortcomings, the approach used here is the standard approach for measurement of ϕ_2.[1,3,4]

4.3 Capacitance Measurements at a Platinum Surface

A series of platinum electrode differential capacitance measurements were made over a range of potentials and frequencies using EIS. A 1 mm radius platinum disc electrode was used for this purpose and measurements were performed with the electrode immersed in an acetonitrile solution of $TBAPF_6$ at a concentration of 0.1M. It was assumed that no electron transfer reactions took place and that capacitance was therefore related to the measured impedance via Equation 4.6, where ω denotes angular frequency. Potentials were measured against a platinum wire reference electrode as this reference was found to be stable over short time scales and allowed collection of spectra at higher frequencies than the Ag/Ag^+ reference. A Keithley 6430 high impedance voltmeter was used to measure the potential difference between the platinum and Ag/Ag^+ references before and after the experiment was ran. The measured potential difference, $E_{\mathrm{Pt}} - E_{\mathrm{Ag/Ag+}}$, was found to be 0.0220V before the experiment and 0.0102V after. The average difference of 0.0161V was added to the recorded potential values. All potentials reported here refer to the potential after the conversion.

$$c_{dl} = \frac{-1}{\omega Z_{IM}} \tag{4.6}$$

Figure 4.1 shows the result of the capacitance measurements with each frequency plotted as a separate line. The minimum at -0.427V was identified as the PZC of the platinum electrode. It is clear from the data that the platinum electrode capacitance is somewhat dependent on frequency.

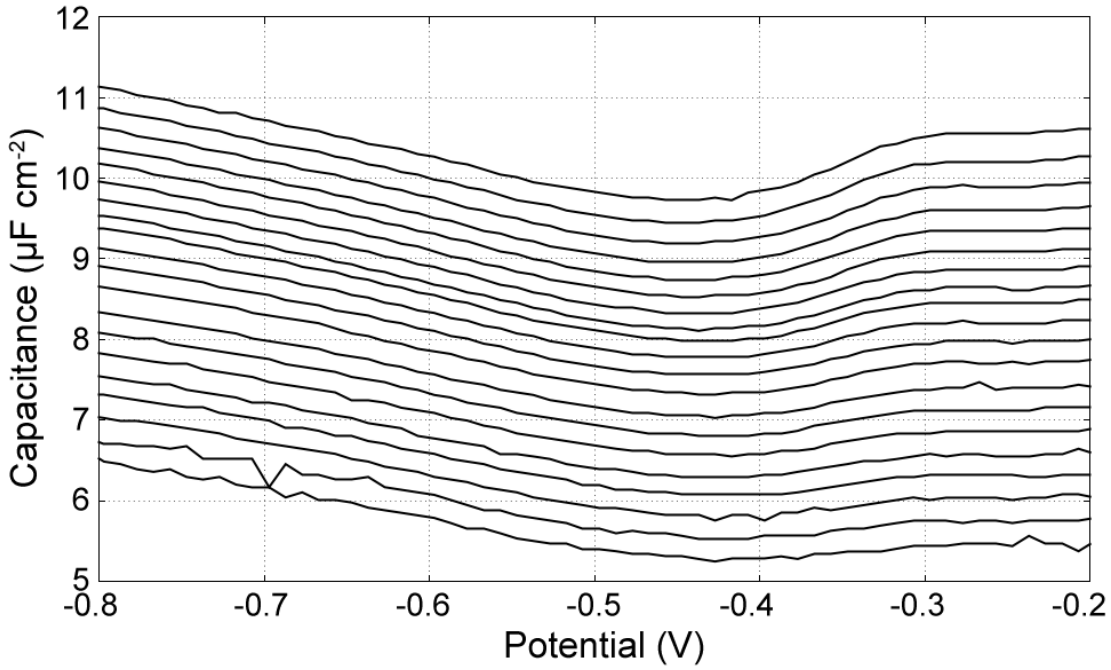

Figure 4.1: Differential capacitance measured at a 1 mm radius platinum disc electrode in MeCN with $TBAPF_6$ (0.1M) via electrochemical impedance spectroscopy. Capacitance is related to impedance via Equation 4.6. Measurements were made at frequencies of 50 kHz to 1 kHz.

The frequency dependence of the platinum differential capacitance presents a problem. Instead of behaving like a simple capacitor, the electrode must be modelled as a constant phase element (CPE). Equation 4.7 describes the impedance of a CPE as a function of angular frequency.[5]

$$Z(\omega) = \frac{1}{(j\omega)^{\gamma}Q} \tag{4.7}$$

The coefficient γ is a measure of the phase angle of the CPE's current with respect to voltage. An ideal capacitor has a phase angle of $\pi/2$ and corresponds to the case where $\gamma = 1$. In such a case Q is equal to the capacitance of the capacitor. In all other cases Q does not have units of capacitance.[2,6] The effective capacitance of a CPE is given by Equation 4.8.

$$c = Q\omega^{\gamma-1}\sin\left(\gamma\frac{\pi}{2}\right) \tag{4.8}$$

In Chapter 5 the information given here will be used in the correction of rate constants measured via fast scan voltammetry (FSV) with a scan rate of 20 kV s^{-1}. It is for this experiment that the appropriate electrode capacitance will be determined. A "true" value of the differential capacitance would correspond to the value defined by the thermodynamic relation, Equation 4.9, where σ is the charge held per unit area.

$$c = \frac{\partial\sigma}{\partial E} \tag{4.9}$$

However, during the FSV experiment the charge held by the electrode at a given potential is never allowed to reach the level that would be attained if the electrode was held at that potential indefinitely. This concept of "true" capacitance is therefore irrelevant. Instead, the frequency which corresponds to the scan rate of the FSV experiment is estimated using Equation 4.10, which gives the time scale available for charge build up to occur, τ.

$$\tau \approx \frac{|E^{0'} - E_{PZC}|}{v} \tag{4.10}$$

The appropriate frequency, corresponding to a CV experiment, can be approximated using the reciprocal of this time scale and the appropriate capacitance can thus be estimated from Equation 4.11.

$$c \approx Q \left(\frac{1}{\tau}\right)^{\gamma-1} \sin\left(\gamma\frac{\pi}{2}\right) \tag{4.11}$$

A $1/\tau$ of 2.1×10^5 rad s^{-1} was obtained using this method. As this roughly corresponds to the upper limit of the usable EIS data shown in Section 5.2 (2×10^5 rad s^{-1}), these values will also be considered appropriate for use in correcting rate constants obtained by EIS.

4.4 Determination of ϕ_2 at Platinum using the GCS Model

A theoretical capacitance curve based on the GCS model was fitted to the differential capacitance data obtained for platinum. The data

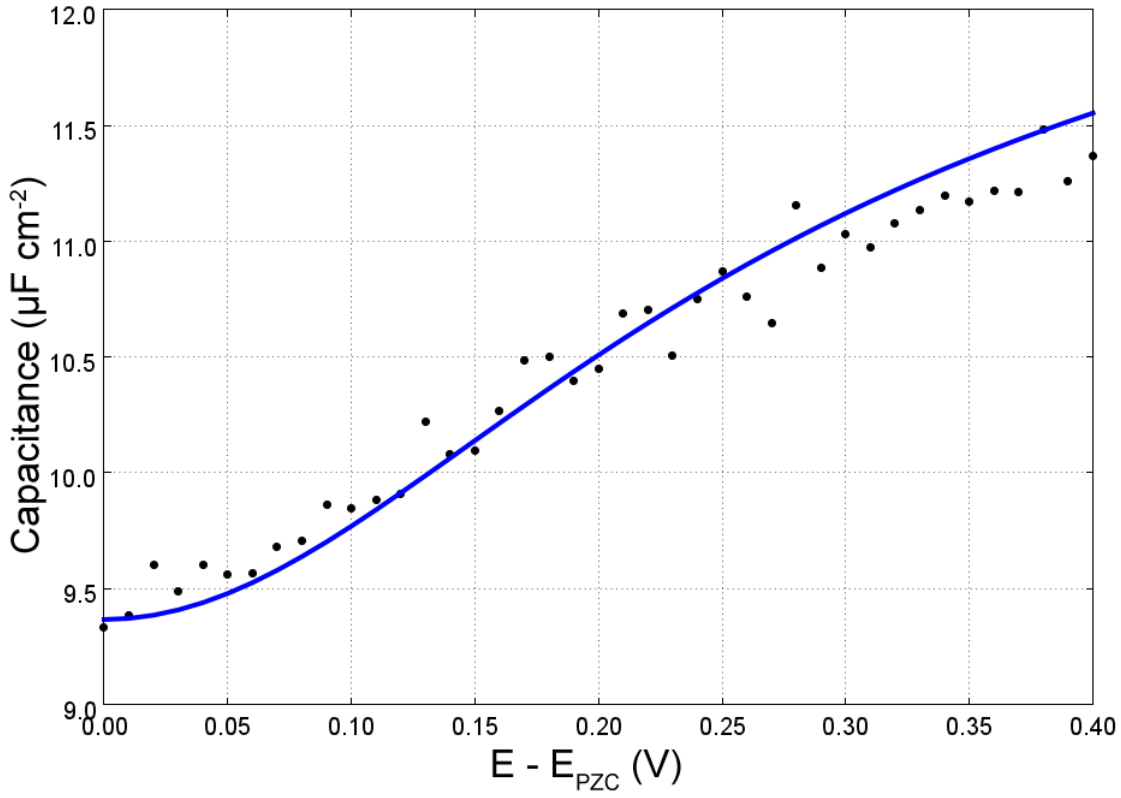

Figure 4.2: A theory curve based on the GCS model (equations 4.1 to 4.3) fitted to experimental measurements of capacitance at platinum in MeCN with $TBAPF_6$ (0.1M). The parameters $I = 0.4$, $\epsilon_H = 2.9$Å, and $x_{OHP} = 19.4$Åwere used.

and the fitted curve are shown in Figure 4.2. The corresponding ϕ_2 values are plotted against potential in Figure 4.3. The method used to calculate values of the theory curve, and how a value ϕ_2 for a given potential can then be determined using the parameters of the fit, are explained below.

$$\phi = E - E_{PZC} \tag{4.12}$$

Calculation of c_H can be accomplished easily using the constants supplied to create the fit, but c_D for a given potential requires knowledge

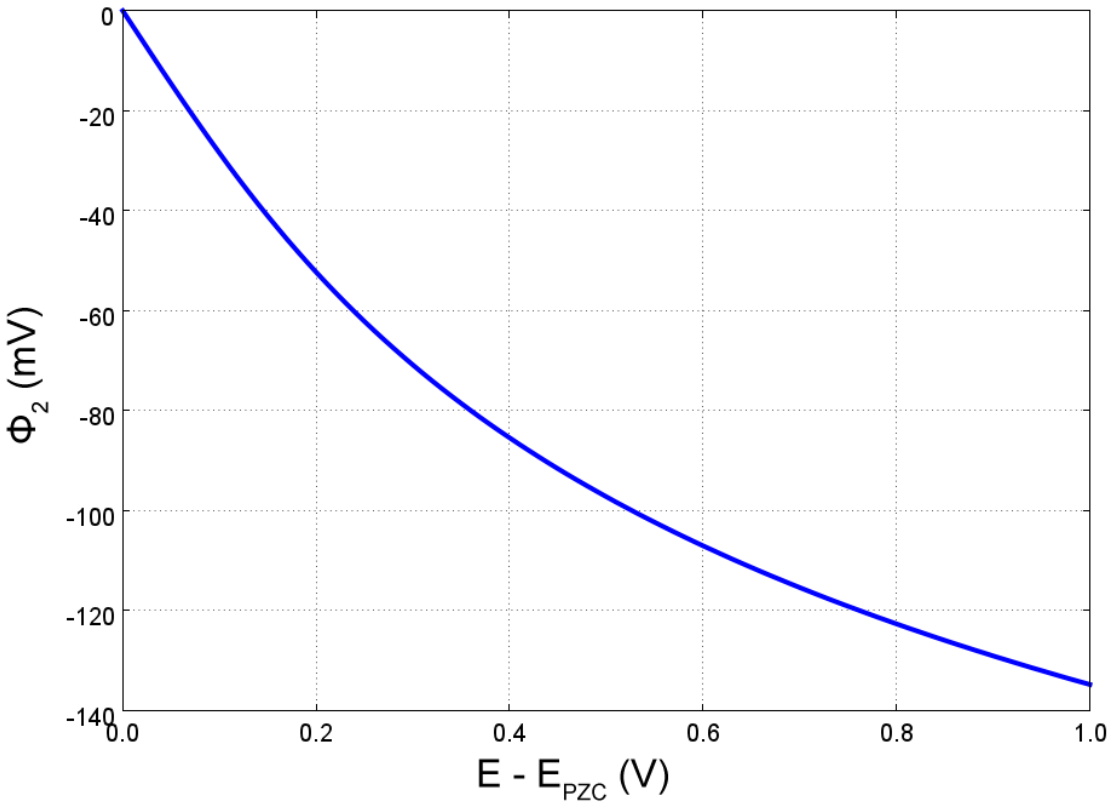

Figure 4.3: The potential change of ϕ_2 at platinum in MeCN with $TBAPF_6$ (0.1M) predicted using a GCS model fitted to the recorded capacitance data.

of ϕ_2 for that potential. To determine these values, numerical integration must be employed. If ϕ is given by Equation 4.12, ϕ_1 and ϕ_2 are 0 at $E = E_{PZC}$. At this potential, the value of c_D can be calculated because a value of ϕ_2 is known. According to the laws which govern potential differences across capacitors in series, upon changing ϕ, it can be estimated that ϕ_2 will change by an amount given by Equation 4.13. The quality of the estimation increases as $\Delta\phi$ approaches 0. Here, $\Delta\phi$ is equal to 10 mV between adjacent data points. Equation 4.13 allows determination of ϕ_2 and thus c_D at the next potential. In this manner values of c_{dl} and ϕ_2 for each potential can be successively determined.

$$\Delta\phi_2 \approx \Delta\phi \frac{\Delta\phi c_H}{c_H + c_D} \tag{4.13}$$

To perform the fit, the values of ϵ_H and x_{OHP} were floated, giving values of 2.9 and 19.4Å respectively. The ionic strength, I, was also floated to allow for ion pairing between TBA^+ and PF_6^-. A value of 0.4 was obtained for I indicating that a high amount of ion pairing occurred between TBA^+ and PF_6^-. Note that while no evidence for methyl viologen ion pairing was observed in Section 3.7, the screening of the methyl viologen charge by solvation is expected to be much greater due to the delocalisation of that charge, and its accessibility to solvent molecules. By contrast, the TBA^+ charge is localised to a single atom.

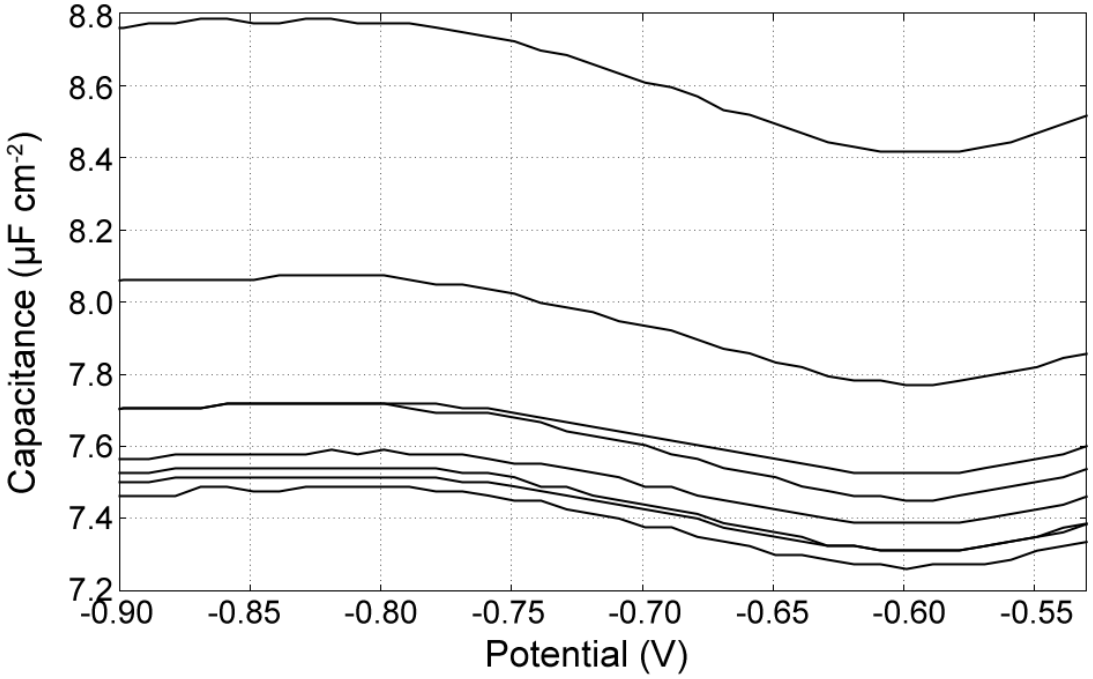

Figure 4.4: Differential capacitance measured at a 0.5 mm radius bismuth disc electrode in MeCN with $TBAPF_6$ (0.1M) via electrochemical impedance spectroscopy. Capacitance is related to impedance via Equation 4.6. Measurements were made at frequencies of 21 kHz to 5 kHz.

4.5 Capacitance Measurements at a Bismuth Surface

A series of bismuth electrode differential capacitance measurements were made over a range of potentials and frequencies using EIS. A 0.5 mm radius bismuth electrode was used for this purpose and measurements were performed with the electrode immersed in an acetonitrile solution of $TBAPF_6$ at a concentration of 0.1M. It was assumed that no electron transfer reactions took place and that capacitance was therefore related to the measured impedance via Equation 4.6. Potentials were measured against a platinum wire reference electrode as this reference was found to be stable over short time scales and allowed collection of spectra at higher frequencies than the Ag/Ag^+ reference. A Keithley 6430 high impedance voltmeter was used to measure the potential difference between the platinum and Ag/Ag^+ references before and after the experiment was ran. The measured potential difference, $E_{Ag/Ag+} - E_{Pt}$, was found to be 0.0018V before the experiment and 0.0112V after. The average difference of 0.0065V was subtracted from the recorded potential values. All potentials reported here refer to the potential after the conversion.

Figure 4.4 shows the result of the capacitance measurements with each frequency plotted as a separate line. The minimum at -0.600V was identified as the PZC of the bismuth electrode. Compared to the platinum, the differential capacitance of the bismuth electrode is much less affected by the frequency of the measurement as indicated by the high values of γ found for the fitted CPE shown in Figure 4.5. If the CPE behaviour of the electrode surfaces can be completely attributed to the roughness of these surfaces, then this suggests that the surface of the bismuth electrode was extremely smooth.[7] It has

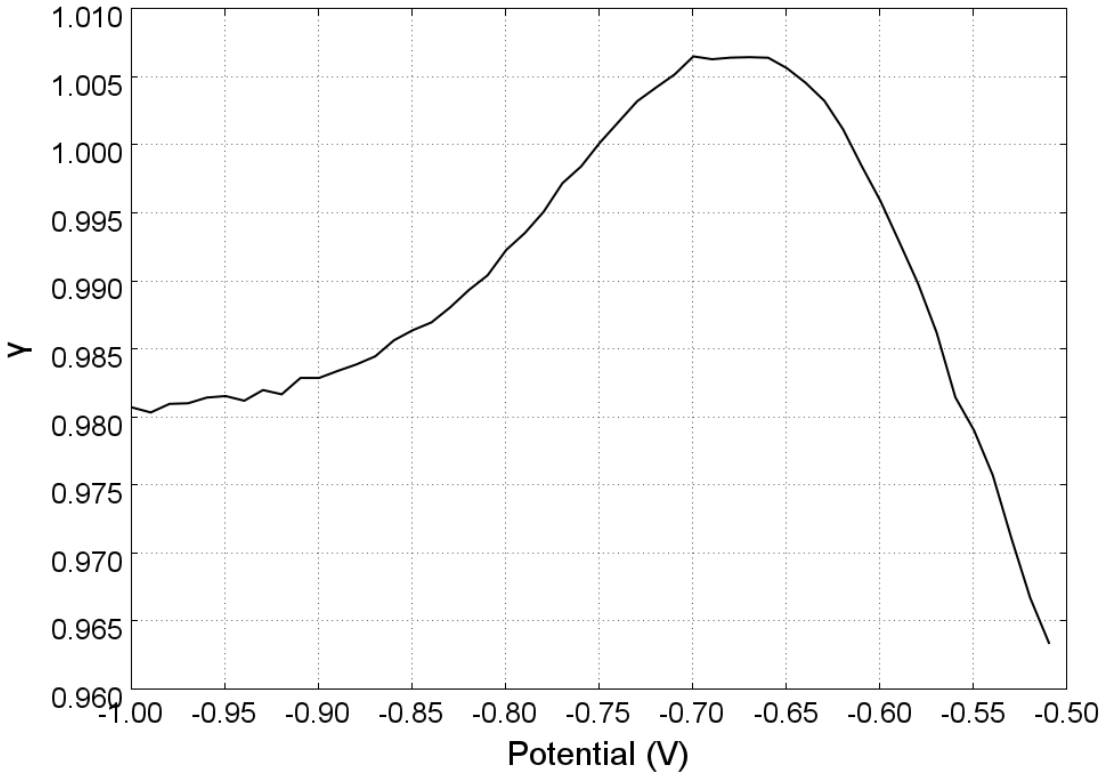

Figure 4.5: Values of γ for a CPE fitted to bismuth capacitance data measured at a 0.5 mm radius bismuth disc electrode in MeCN with $TBAPF_6$ (0.1M).

been shown previously by others that extremely smooth bismuth surfaces are not difficult to obtain, and can be used as substitutes for mercury in some applications (see Section 1.5).[8,9]

4.6 Applicability of the GCS Model at a Semimetal Surface

To apply the GCS model to a semimetal surface, the model must be extended to take into account possible depletion layer effects within the solid. An appropriate model will be developed here, and both the standard and extended GCS models will be tested against the bismuth capacitance data in the next section.

For an electrode made of a material with a low dielectric constant, a charge held by the electrode surface may result in a space charge region if the charge is not fully screened from the rest of the electrode. In such a region, a region of electron depletion can then form to maintain electroneutrality. As a result, such a space charge region will behave similar to a capacitor, and its capacitance must be included in the GCS model.[10] Equation 4.14 gives the predicted capacitance of an electrode surface when a space charge region develops within the electrode.

$$\frac{1}{c_{dl}} = \frac{1}{c_H} + \frac{1}{c_D} + \frac{1}{c_{SM}} \tag{4.14}$$

In addition to ϕ_1 and ϕ_2, a potential change across the space charge region, ϕ_3, will also occur so that ϕ is now given by Equation 4.15.

$$\phi = \phi_1 + \phi_2 + \phi_3 \tag{4.15}$$

The changes in ϕ_2 and ϕ_3 with ϕ are described by Equation 4.16 and Equation 4.17 respectively.

$$\Delta\phi_2 \approx \Delta\phi \frac{\Delta\phi c_H c_{SM}}{c_H + c_D + c_{SM}} \tag{4.16}$$

$$\Delta\phi_3 \approx \Delta\phi \frac{\Delta\phi c_H c_D}{c_H + c_D + c_{SM}} \tag{4.17}$$

The capacitance that results from formation of the space charge re-

gion is given by Equation 4.18.[10,11] The parameters ϵ_{SM} and $\rho(E_F)$ are the dielectric constant of the electrode material and the Fermi-level DOS respectively. The parameter ζ describes how the DOS changes with energy, E, and is given by Equation 4.19. The parameter θ_0 is the dimensionless potential change through the space charge region, as given by Equation 4.20.

$$c = \frac{e}{2}\sqrt{\epsilon_{SM}}\frac{\zeta\kappa T\theta_0^2 + 2\rho(E_F)\theta_0}{\left[\frac{1}{3}\zeta\kappa T\theta_0^3 + \rho(E_F)\theta_0^2\right]^{1/2}} \tag{4.18}$$

$$\zeta = \frac{\partial\rho}{\partial E} \tag{4.19}$$

$$\theta_0 = \frac{F\phi_3}{RT} \tag{4.20}$$

4.7 Determination of ϕ_2 at Bismuth using the Extended GCS Model

The fitting of the extended GCS model to bismuth capacitance data was performed in the same manner as for platinum. To perform the fit, the values of ϵ_H and x_{OHP} were floated to 2.9 and 23.9 Å respectively. This time I was held at the 0.4 value observed at platinum. For $\rho(E_F)$, the commonly cited Fermi-level density of states of bismuth, 3×10^{17} cm^{-3} eV^{-1},[12] was used. For ζ, an estimated value of 2×10^{22} cm^{-3} eV^{-2} was used based on a calculated density of states profile.[13] A published measurement of ϵ_{SM} for Bi, determined via extrapolation of IR reflectivity data to zero frequency, finds this value to be 99.6.[14] The resulting fit is shown in Figure 4.6 as a red line.

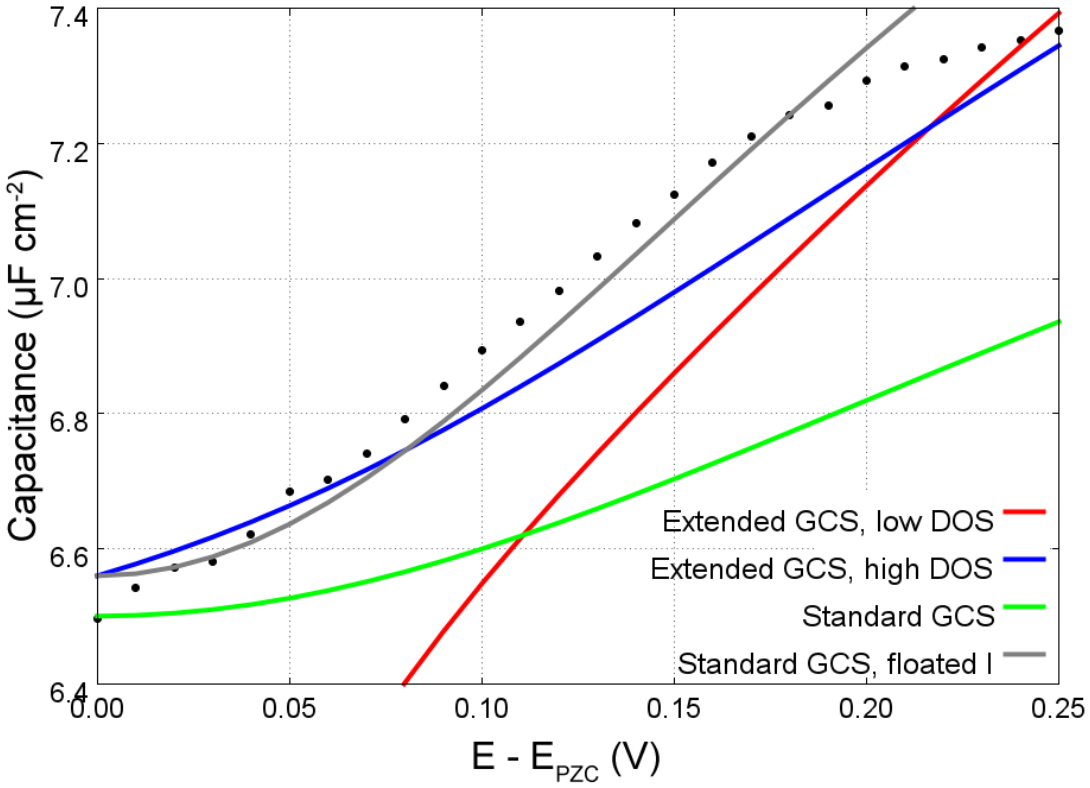

Figure 4.6: Attempts to fit the GCS model, and the extended GCS model to experimental measurements of capacitance at bismuth, using the ionic strength of 0.04 determined from platinum capacitance. The red line uses the extended GCS model with the bismuth DOS fixed at 3×10^{17} cm^{-3} eV^{-1}. The blue line uses the extended GCS model with a DOS floated to 9×10^{-20} cm^{-3} eV^{-1}. The green line uses the standard GCS model. The grey line uses the standard GCS model with the ionic strength floated to 0.02.

Clearly, the model fails to generate similar capacitance values over even small potential ranges when given sensible parameters based on what is known about the bulk of bismuth. A second attempt at fitting was made with $\rho(E_F)$ allowed to float. The result is shown as the blue line on Figure 4.6. A $\rho(E_F)$ value of 9×10^{20} cm^{-3} eV^{-1} was found to produce the highest quality fit. The values of ϕ_2 determined from this fit are plotted against potential in Figure 4.7. A fit with the value of ϵ_{SM} floated was also attempted, but this did not improve the quality of the fit.

The results of these attempts to fit the extended GCS model to the bismuth capacitance data strongly suggest that the properties of the bismuth surface, and not the bulk, must be considered in order to model the double layer present in this system (see Section 1.5). Scanning tunnelling spectroscopy (STS) has been used by others to measure the surface DOS of bismuth and those measurements indicate that the Fermi-level DOS is between 2.8×10^{21} and 2.8×10^{22} cm^{-3} eV^{-1}.[15] Measurements made using STS are of particular relevance as this technique allows a material's surface to be studied, with single atomic layer resolution, without measuring effects of the bulk material.[16]

While high values of $\rho(E_F)$ predict similar levels of capacitance at bismuth, the values of ϕ_3 do not appear to be realistic. Given the metallic nature of the surface, the dielectric constant obtained from the fit is unrealistic. Accurate measurement of ϵ_{SM} is experimentally challenging,[17] and no reasonable estimates were found in published literature. However, the metallic nature of the electrode means that use of the extended GCS model may be unnecessary. The standard GCS model was fitted to the capacitance data and produced the

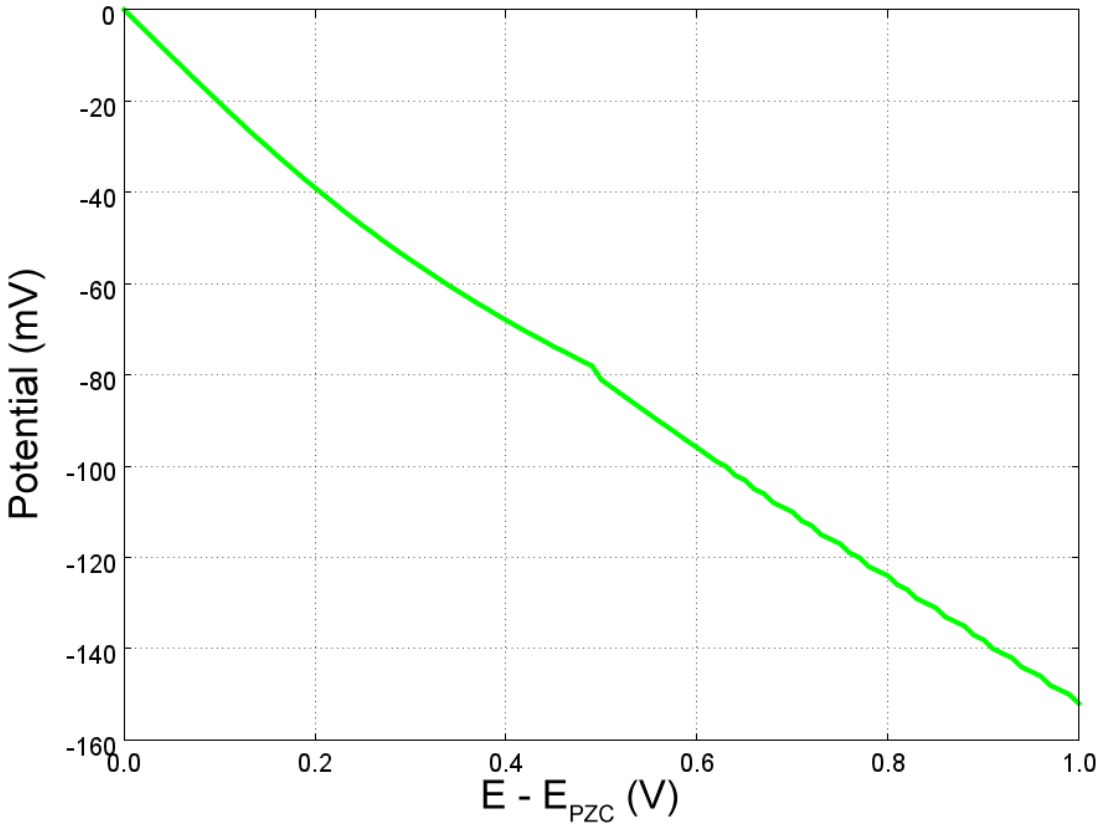

Figure 4.7: The potential of ϕ_2 at bismuth predicted by the fit of the extended GCS model with a floated DOS.

green curve shown in Figure 4.6. The values of ϵ_H and x_{OHP} were floated as before, with I held constant. The fit is of poorer quality than that obtained using the extended GCS model, although the parameters are probably a lot more realistic. It was found that a good fit could be obtained by setting the value of I to 0.02, shown as the grey line on Figure 4.6, but this contradicts the observations made at platinum and casts considerable doubt on physical meanings of the other parameters obtained from the fit.

It is not clear which fit should be used to produce the values of ϕ_2 needed in the following chapter. Fortunately, for the fit made

using the extended GCS model with a high value of $\rho(E_F)$ and for both fits of the standard GCS model, ϕ_2 did not vary significantly making the choice irrelevant. The values of ϕ_2 were taken from the extended GCS with floated $\rho(E_F)$ fit (shown in blue on the plot) for no reason other than this was the first reasonable fit produced. The presence of a potential drop inside the electrode could necessitate a further correction to the data, however, given the metallic nature of the bismuth surface, the likelihood of any significant space charge region appears unlikely. If a space charge region, and a significant ϕ_3 does exist, then it is far from clear what manner of correction must be applied to account for this. For these reasons ϕ_3 will not be considered in later sections.

4.8 Conclusion

Measurements of platinum electrode capacitance via EIS allowed identification of the platinum PZC in MeCN with 0.1M $TBAPF_6$. By modelling the metal upon a CPE, an appropriate capacitance value for a given frequency can be determined. Measurements of bismuth electrode capacitance via EIS allowed identification of the bismuth PZC in MeCN with 0.1M $TBAPF_6$. The dependence of the capacitance of the electrode upon frequency was found to be surprisingly weak. The capacitance values at platinum matched those predicted by a fitted GCS model well, allowing measurement of ϕ_2 at platinum over a range of potentials. Those at bismuth were not well predicted by the GCS model with or without consideration for capacitance within the semimetal. Values of ϕ_2 were nevertheless estimated over a range of potentials. The capacitance at bismuth

was found to be controlled by the surface properties of the material and not those of the bulk.

A means of determining the frequency which corresponds to a FSV experiment was devised which considered the time scale of the experiment and employed in determining the appropriate capacitance of the platinum and bismuth surfaces.

Bibliography

[1] A. J. Bard and L. Faulkner, *Electrochemical Methods: Fundamentals and Applications*, John Wiley & Sons, 2nd edn., 2001.

[2] P. Zoltowski, *Journal of Electroanalytical Chemistry*, 1998, **443**, 149–154.

[3] R. Parsons, *Chemical Reviews*, 1990, **90**, 813–826.

[4] A. Hamelin, *Modern Aspects of Electrochemistry 16*, 1985, vol. 16.

[5] G. Brug, A. van den Eeden, M. Sluyters-Rehbach and J. Sluyters, *Journal of Electroanalytical Chemistry and Interfacial Electrochemistry*, 1984, **176**, 275–295.

[6] C. H. Hsu and F. Mansfeld, *Corrosion*, 2001, **57**, 747–748.

[7] U. Rammelt and G. Reinhard, *Electrochimica Acta*, 1990, **35**, 1045–1049.

[8] E. Lust, A. Jänes, V. Sammelselg, P. Miidla and K. Lust, *Electrochimica Acta*, 1998, **44**, 373–383.

[9] E. Lust, A. Jänes, K. Lust, V. Sammelselg and P. Miidla, *Electrochimica Acta*, 1997, **42**, 2861–2879.

[10] H. Gerischer, R. McIntyre, D. Scherson and W. Storck, *The Journal of Physical Chemistry*, 1987, **91**, 1930–1935.

[11] H. Gerischer, *The Journal of Physical Chemistry*, 1985, **89**, 4249–4251.

[12] N. W. Ashcroft and N. D. Mermin, *Solid State Physics*, Brooks/Cole, 1976.

[13] S. B. Cronin, *Ph.D. thesis*, Massachusetts Institute of Technology, 2002.

[14] W. S. Boyle and A. D. Brailsford, *Physical Review*, 1960, **120**, 1943–1949.

[15] A. Ofitserov and V. Edelman, *Physica B: Condensed Matter*, 2003, **329-333, Part 2**, 1094–1095.

[16] S. Schintke and W.-D. Schneider, *Journal of Physics: Condensed Matter*, 2004, **16**, R49–R81.

[17] M. Muntwiler and X.-Y. Zhu, *New Journal of Physics*, 2008, **10**, 113018.

Chapter 5

Kinetic Studies of Methyl Viologen and Some Derivatives in Acetonitrile

5.1 Aims

The standard rate constants, k^0, of the first one-electron reductions of methyl viologen and a series of derivatives have been measured at platinum and bismuth surfaces. The initial aim of this chapter will be to explain how these rate constants were determined. Following that, an attempt will be made to understand the differences in the observed rate constants using what is known about their molecular structures (see Chapter 3), what is known about the platinum and bismuth electrode surfaces (see Chapter 4), and published theory.[1,2]

5.2 Electrochemical Impedance Spectroscopy

Initial attempts at measuring the standard rate constants for the MV^{2+} and C1-5 redox couples were made using electrochemical impedance spectroscopy (EIS). A platinum disc working electrode of radius 5 μm was employed for this purpose. The impedance of a reversible electron transfer reaction at a microhemisphere is given by Equation 5.1. The parameter Ω is given by Equation 5.2 where a is the electrode radius, D is the diffusion coefficient of the molecule and $\left({}^{\partial i}/_{\partial E}\right)_{rev,SS}$ is the slope of the current voltage curve for a steady-state process under reversible conditions.

$$Z^{-1} = (1 + \sqrt{i\Omega}) \left(\frac{\delta i}{\delta E} \right)_{rev,SS} \tag{5.1}$$

$$\Omega = \frac{a^2 \omega}{D} \tag{5.2}$$

The analytical approach employed modelled the system upon a Randles' circuit (see Section 2.2.8), but this form of analysis will only be valid when frequencies are high enough that the system can be expected to exhibit Randles' circuit behaviour. It is therefore necessary to estimate the minimum frequency at which this form of analysis can be used without an unacceptable level of error occurring due to deviation from Randles' circuit behaviour. Since the Randles' circuit for a planar electrode has no finite DC impedance, Equation 5.1 only holds when $(1 + \sqrt{i\Omega}) \approx \sqrt{i\Omega}$. To keep the errors which result from this approximation to within 5%, frequencies should be high enough that Equation 5.3 and thus Equation 5.4 hold true.

$$\frac{|\sqrt{i\Omega}|}{|1+\sqrt{i\Omega}|} > 0.95 \tag{5.3}$$

$$\Omega > \frac{0.95^2}{1-0.95^2}\sqrt{2} = 13.1 \tag{5.4}$$

Given the electrode radius of 5 μm and an estimated diffusion coefficient of 5×10^{-6} cm^{-2} s^{-1}, a minimum acceptable frequency of 83 Hz can be estimated, as shown in Equation 5.5. The impedance was measured at frequencies of up to 100 kHz and frequencies below 1 kHz were not employed in determining k^0 values. Therefore, equation 5.5 held true at all times.

$$f = \frac{\omega}{2\pi} > 83 \text{ Hz} \tag{5.5}$$

Nyquist plots recorded for MV^{2+} and derivatives C1-5 are shown in Figure 5.1. In each case, the real impedance of the system tends toward 0 at high frequencies indicating that the effect of uncompensated resistance, R_u, was negligible. Observations of such small values of R_u are common for ultramicroelectrodes.[3,4] The value of R_{ct} is often taken from the point at which the semi-circle formed by the data points in the Nyquist plot meets the real axis at low frequencies, minus R_u. However, such an analysis gives higher weight to the low frequency data than the high frequency data. The electron transfer reactions under study appeared too fast for this approach to be ideal, and instead the behaviour of a Randles' circuit at high frequency formed the model used in the analysis, thereby giving more weight to the high frequency measurements.

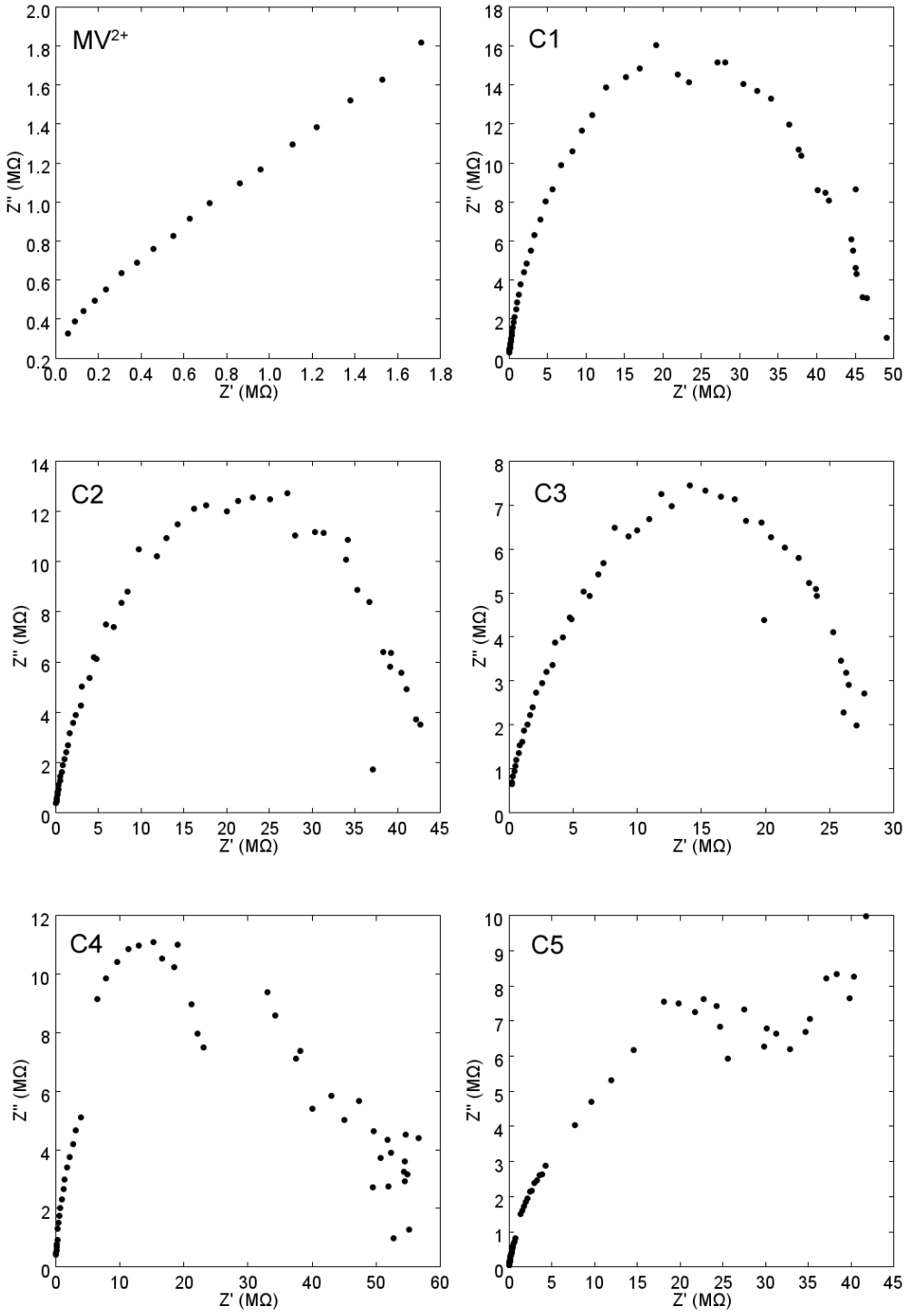

Figure 5.1: Nyquist plots recorded using EIS for MV^{2+} and derivatives C1-5 (1 mM) in MeCN with $TBAPF_6$ (0.1M) at a 5 μm radius platinum disc working electrode.

The values of the real impedance, Z_{RE}, and the imaginary impedance, Z_{IM}, can be determined for a given frequency on the basis of the model circuit, and are given by equations 5.6 and 5.7 respectively where W and σ are given by equations 5.8 and 5.9 respectively. [5]

$$Z_{RE} = R_u + \frac{R_{ct} + \sigma\omega^{-0.5}}{W^2 + \omega^2 c_{dl}^2 (R_{ct} + \sigma\omega^{-0.5})^2} \tag{5.6}$$

$$Z_{IM} = \frac{\omega c_{dl} (R_{ct} + \sigma\omega^{-0.5})^2 + \sigma\omega^{-0.5} W}{W^2 + \omega^2 c_{dl}^2 (R_{ct} + \sigma\omega^{-0.5})^2} \tag{5.7}$$

$$W = c_{dl}\sigma\omega^{0.5} + 1 \tag{5.8}$$

$$\sigma = \frac{RT}{n^2 F^2 A\sqrt{2}} \left(\frac{1}{D_O^{0.5} C_O^*} + \frac{1}{D_R^{0.5} C_R^*} \right) \tag{5.9}$$

For high values of ω, $\omega^{-0.5} \to 0$ and the equations for the real and imaginary component of the impedance will simplify to equations 5.10 and 5.11 respectively.

$$Z_{RE} = R_u + \frac{R_{ct}}{1 + \omega^2 c_{dl}^2 R_{ct}^2} \tag{5.10}$$

$$Z_{IM} = \frac{\omega c_{dl} R_{ct}^2}{1 + \omega^2 c_{dl}^2 R_{ct}^2} \tag{5.11}$$

When Equation 5.10 holds true, a plot of Z_{RE} as a function of ω^2

will have a gradient of $c_{dl}^2 R_{ct}^2$. When Equation 5.11 holds true, a plot of $^{-\omega}/_{Z_{IM}}$ as a function of ω^2 will have a gradient of c_{dl}. Thus by taking the slopes of both plots in the high frequency range of the spectrum, the values of c_{dl} and R_{ct} can both be determined. The validity of equations 5.10 and 5.11 can be checked using the linearity of the plots. The value of k^0 can then be determined from R_{ct} as explained below.

The faradaic current through an electrochemical system can by analysed using the Butler-Volmer equation, Equation 5.12.

$$i = i_0 \left[\exp\left(-\alpha \frac{F(E - E_{eq}}{RT} \right) - \exp\left((1-\alpha) \frac{F(E - E_{eq}}{RT} \right) \right] \tag{5.12}$$

This equation can be simplified by making use of the approximation given by Equation 5.13 which is valid for small values of x. In the case where potential is oscillated around $E^{0'}$ with a small amplitude, the approximation may be employed to yield Equation 5.14.

$$\exp(x) \approx 1 + x \tag{5.13}$$

$$i = -i_0 \frac{F(E - E_{eq})}{RT} \tag{5.14}$$

Given these approximations, a linear relationship between poten-

Molecule	k^0 **(cm s^{-1})**
MV^{2+}	$1.(2) \times 10^{-1}$
C1	$9.(5) \times 10^{-2}$
C2	$1.(4) \times 10^{-1}$
C3	$1.(6) \times 10^{-1}$
C4	$2.(4) \times 10^{-2}$
C5	$4.(5) \times 10^{-1}$

Table 5.1: Values of the standard rate constant, k^0, determined at a 5 μm radius platinum disc using EIS. These values were determined in MeCN with $TBAPF_6$ (0.1M) and MV^{2+} or a derivative (10 mM).

tial and current is now observed, i.e. the system exhibits ohmic behaviour. This means that by rearrangement of Equation 5.14 a pseudoresistance can be defined for the system, and related to the exchange current, i_0, of the system, as in Equation 5.15.

$$R_{ct} = -\frac{E - E_{eq}}{i} = \frac{RT}{i_0 F} \tag{5.15}$$

The exchange current is then related to k^0 through Equation 5.16.[5]

$$i_0 = C_O^* nFAk^0 \tag{5.16}$$

Measurements of impedance spectra for these molecules sometimes proved unreliable, and in many cases the observations were not consistent with the theoretical model. In order to determine a k^0 value for each molecule, the data sets analysed were those that exhibited behaviour which gave the closest match to the theoretical model, as determined by attempts to fit Equation 5.6 and Equation 5.7 to experimental data.

Figures 5.2 to 5.7 show impedance data collected for each of the

molecules. The value of $c_{dl}^2 R_{ct}^2$ can be determined from the slope of the first (uppermost) plot in each figure. The value of c_{dl} is then determined from the slope of the second plot. The value of σ is then floated to fit theory curves to the experimental measurements of $Z_{RE}(\omega)$ and $Z_{IM}(\omega)$, as shown in the third and fourth plot in each figure. The quality of the fit in these lower two plots gives an idea of how well the system's behaviour matches the theoretical model employed in the determination of R_{ct}. The k^0 values that correspond to the determined R_{ct} values are tabulated in Table 5.1.

Measurement of the transfer coefficient, α, associated with each reaction was attempted by performing the analysis over a range of potentials near $E^{0'}$. Figure 5.8 displays the observed relationship between R_{ct} and the applied potential for each compound. A minimum in R_{ct} is observed at $E = E^{0'}$ for most compounds as predicted by theory. However, attempts to determine α from the slope of these plots were abandoned due to the poor reliability of the technique and low quality of the data obtained.

]

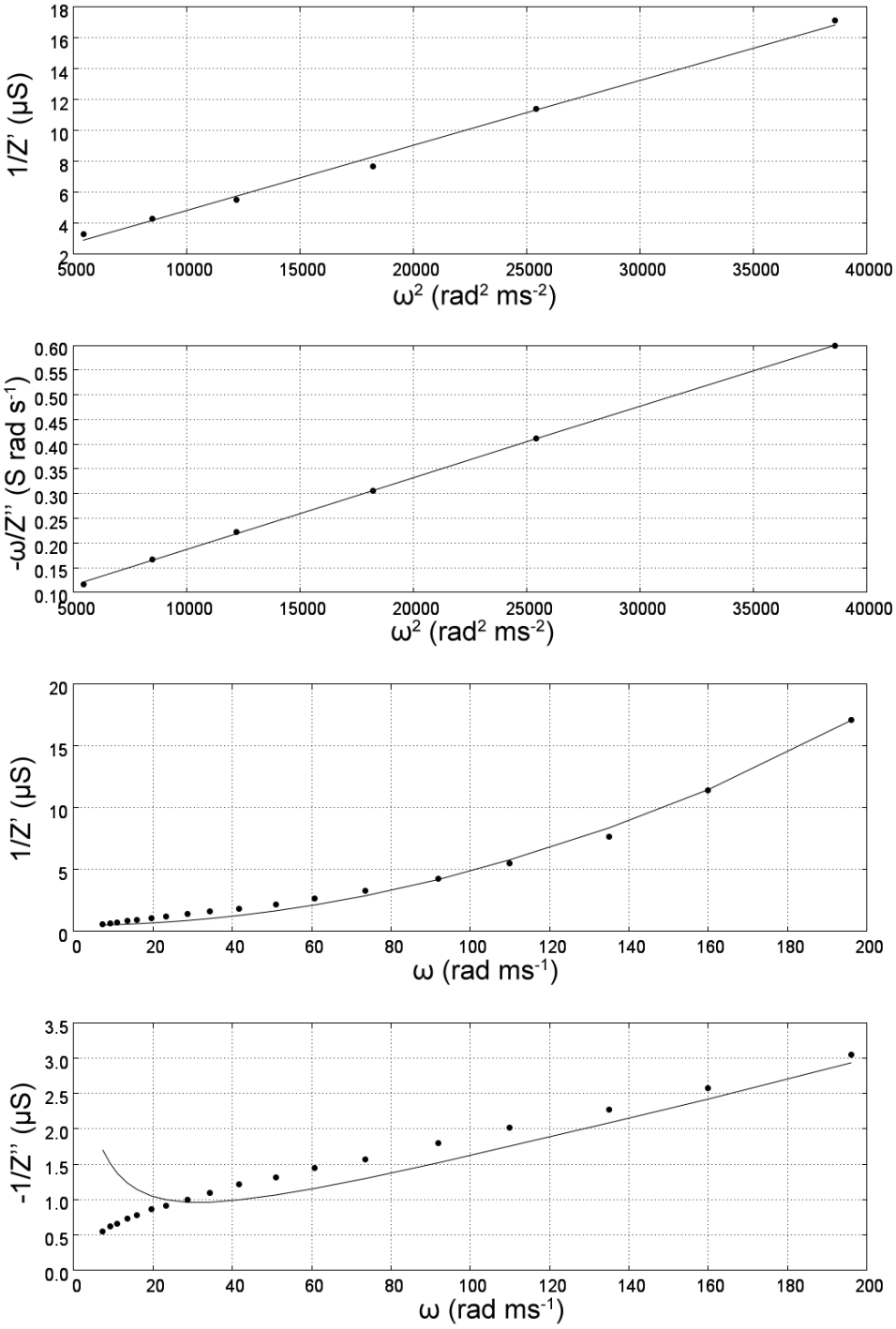

Figure 5.2: EIS data recorded at a 5 μm radius platinum disc working electrode in a solution of MV^{2+} (1 mM) and $TBAPF_6$ (0.1M). The slope of plots of 1/Z' and -ω/Z" as a function of ω^2 are used to determine $C_{dl}^2 R_{ct}$ and c_{dl} respectively. These variables are then used to produce the theory curves shown as solid lines in the plots of 1/Z' and $-1/Z''$ as a function of ω.

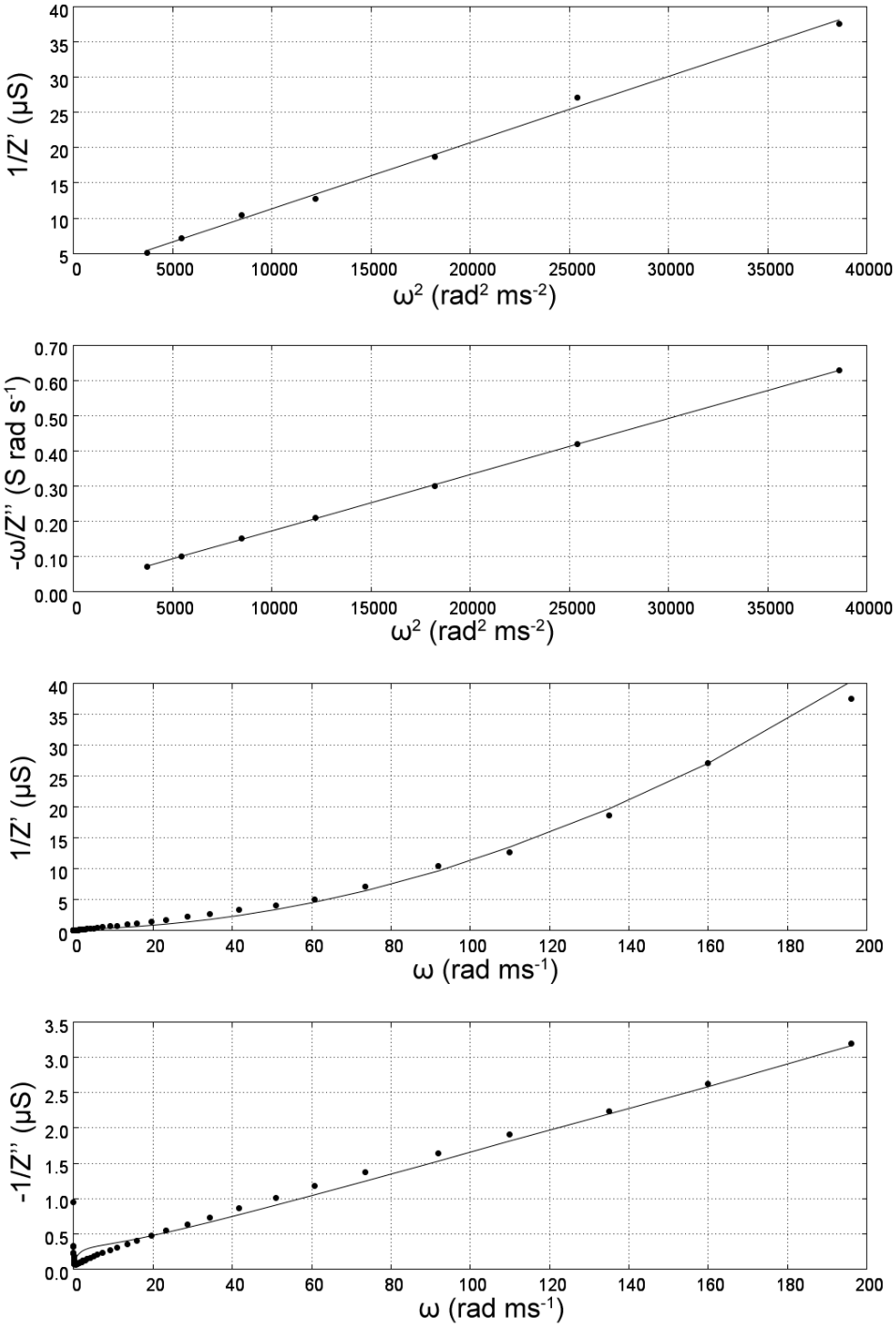

Figure 5.3: EIS data recorded at a 5 μm radius platinum disc working electrode in a solution of C1 (1 mM) and TBAPF$_6$ (0.1M). The slope of plots of 1/Z' and -ω/Z" as a function of ω^2 are used to determine $C_{dl}^2 R_{ct}$ and c_{dl} respectively. These variables are then used to produce the theory curves shown as solid lines in the plots of 1/Z' and $-1/Z''$ as a function of ω.

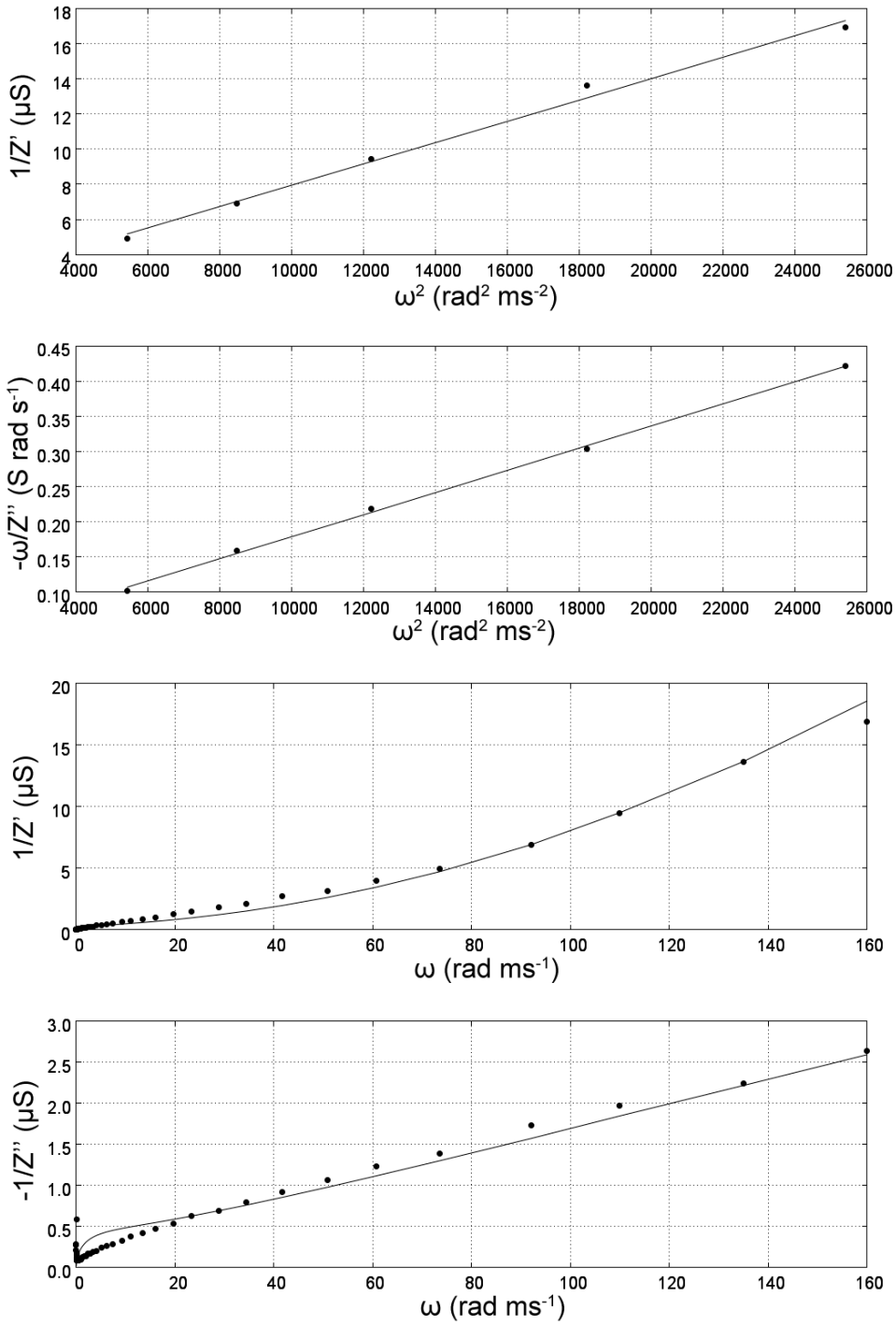

Figure 5.4: EIS data recorded at a 5 μm radius platinum disc working electrode in a solution of C2 (1 mM) and $TBAPF_6$ (0.1M). The slope of plots of 1/Z' and -ω/Z" as a function of ω^2 are used to determine $C_{dl}^2 R_{ct}$ and c_{dl} respectively. These variables are then used to produce the theory curves shown as solid lines in the plots of 1/Z' and $-1/Z''$ as a function of ω.

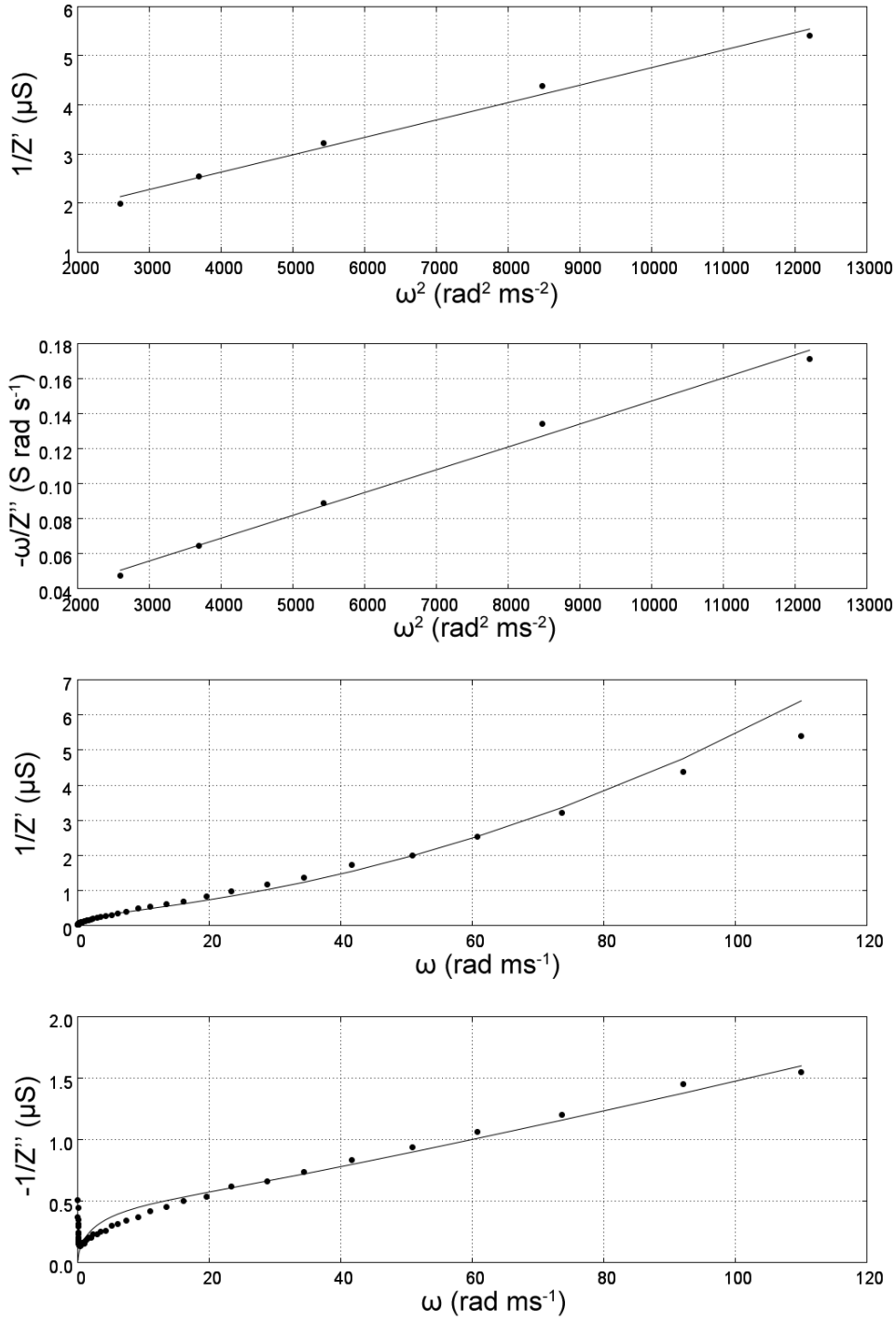

Figure 5.5: EIS data recorded at a 5 μm radius platinum disc working electrode in a solution of C3 (1 mM) and $TBAPF_6$ (0.1M). The slope of plots of 1/Z' and -ω/Z" as a function of ω^2 are used to determine $C_{dl}^2 R_{ct}$ and c_{dl} respectively. These variables are then used to produce the theory curves shown as solid lines in the plots of 1/Z' and $-1/Z''$ as a function of ω.

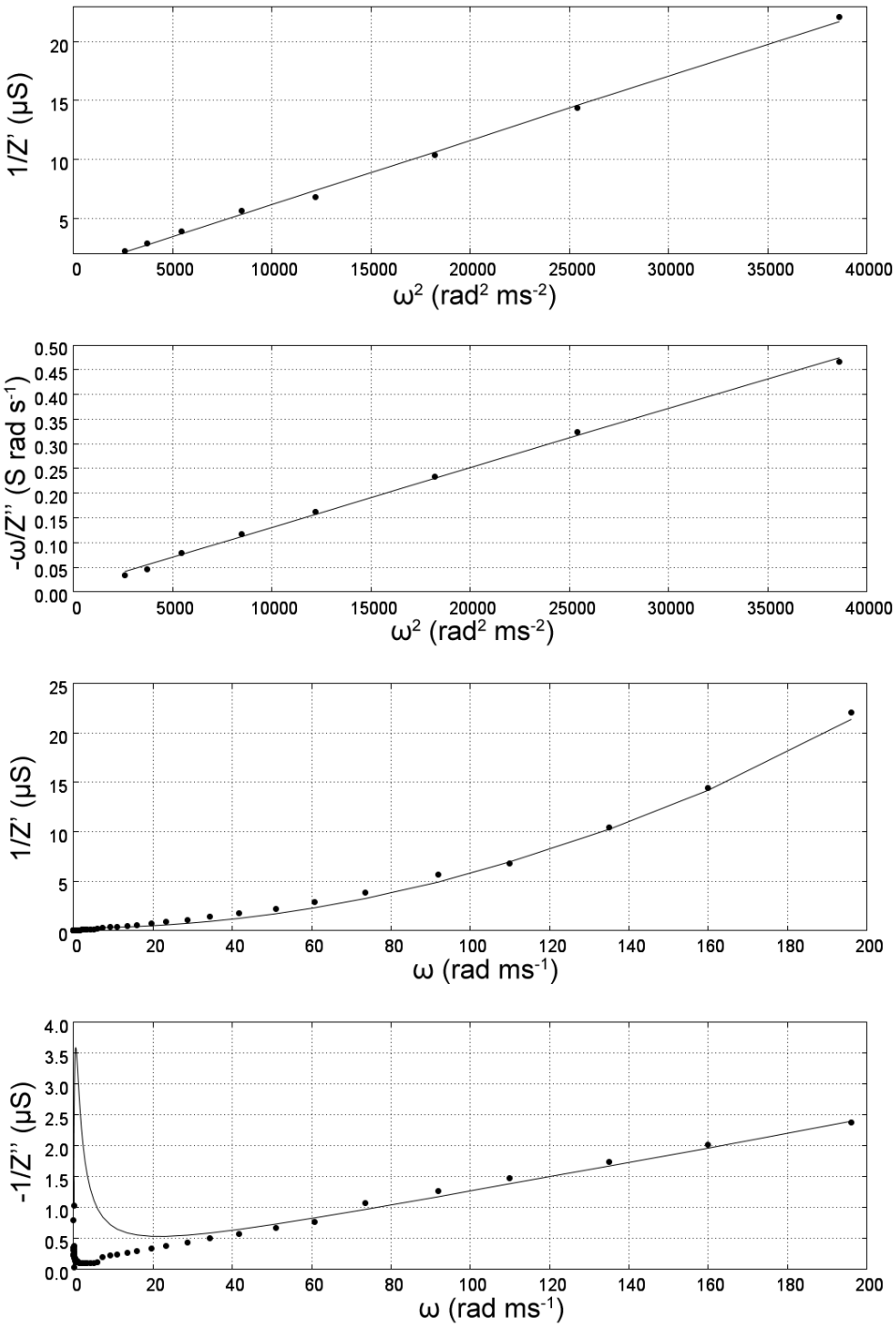

Figure 5.6: EIS data recorded at a 5 μm radius platinum disc working electrode in a solution of C4 (1 mM) and $TBAPF_6$ (0.1M). The slope of plots of 1/Z' and -ω/Z" as a function of ω^2 are used to determine $C_{dl}^2 R_{ct}$ and c_{dl} respectively. These variables are then used to produce the theory curves shown as solid lines in the plots of 1/Z' and $-1/Z''$ as a function of ω.

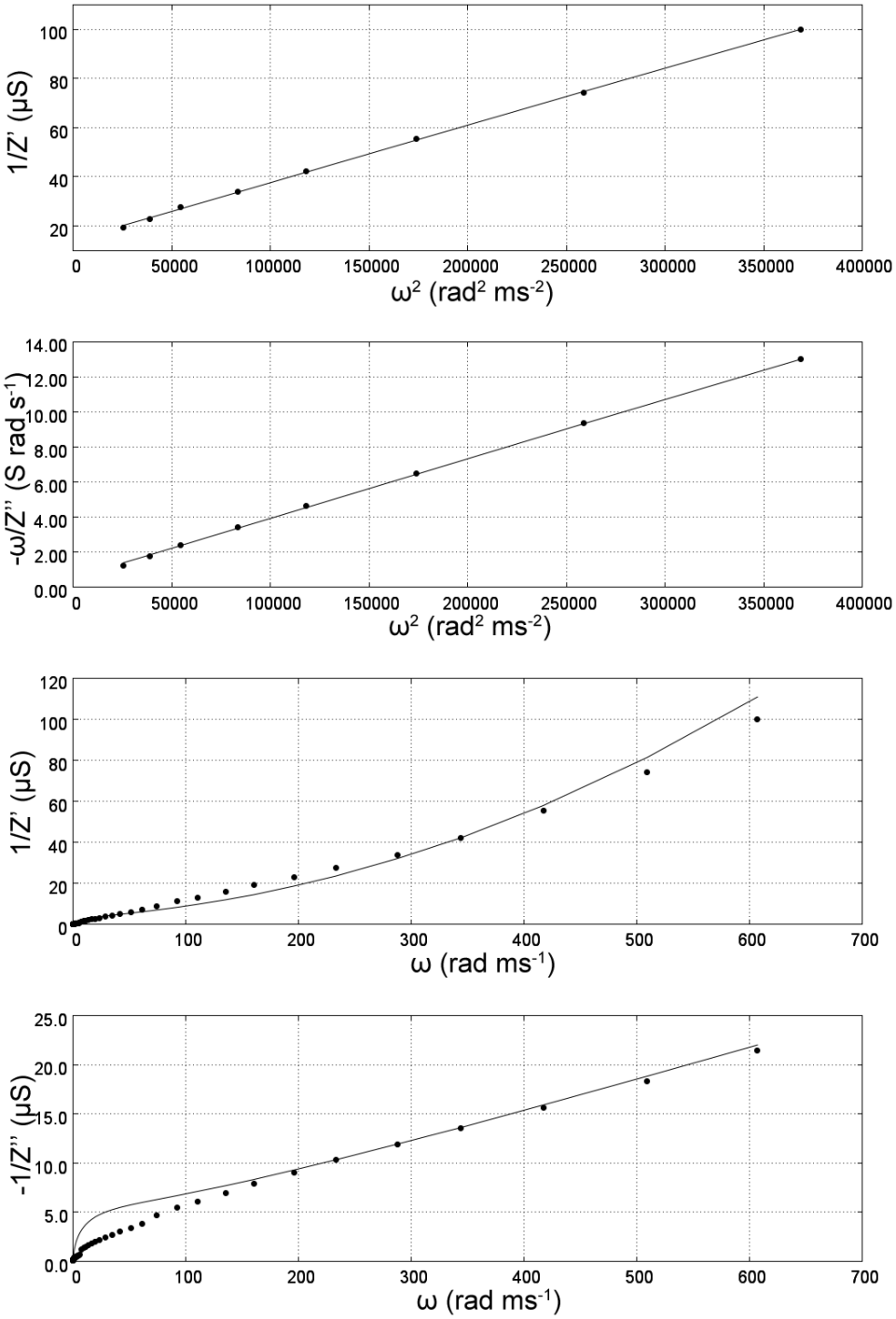

Figure 5.7: EIS data recorded at a 5 μm radius platinum disc working electrode in a solution of C5 (1 mM) and $TBAPF_6$ (0.1M). The slope of plots of 1/Z' and -ω/Z" as a function of ω^2 are used to determine $C_{dl}^2 R_{ct}$ and c_{dl} respectively. These variables are then used to produce the theory curves shown as solid lines in the plots of 1/Z' and $-1/Z''$ as a function of ω.

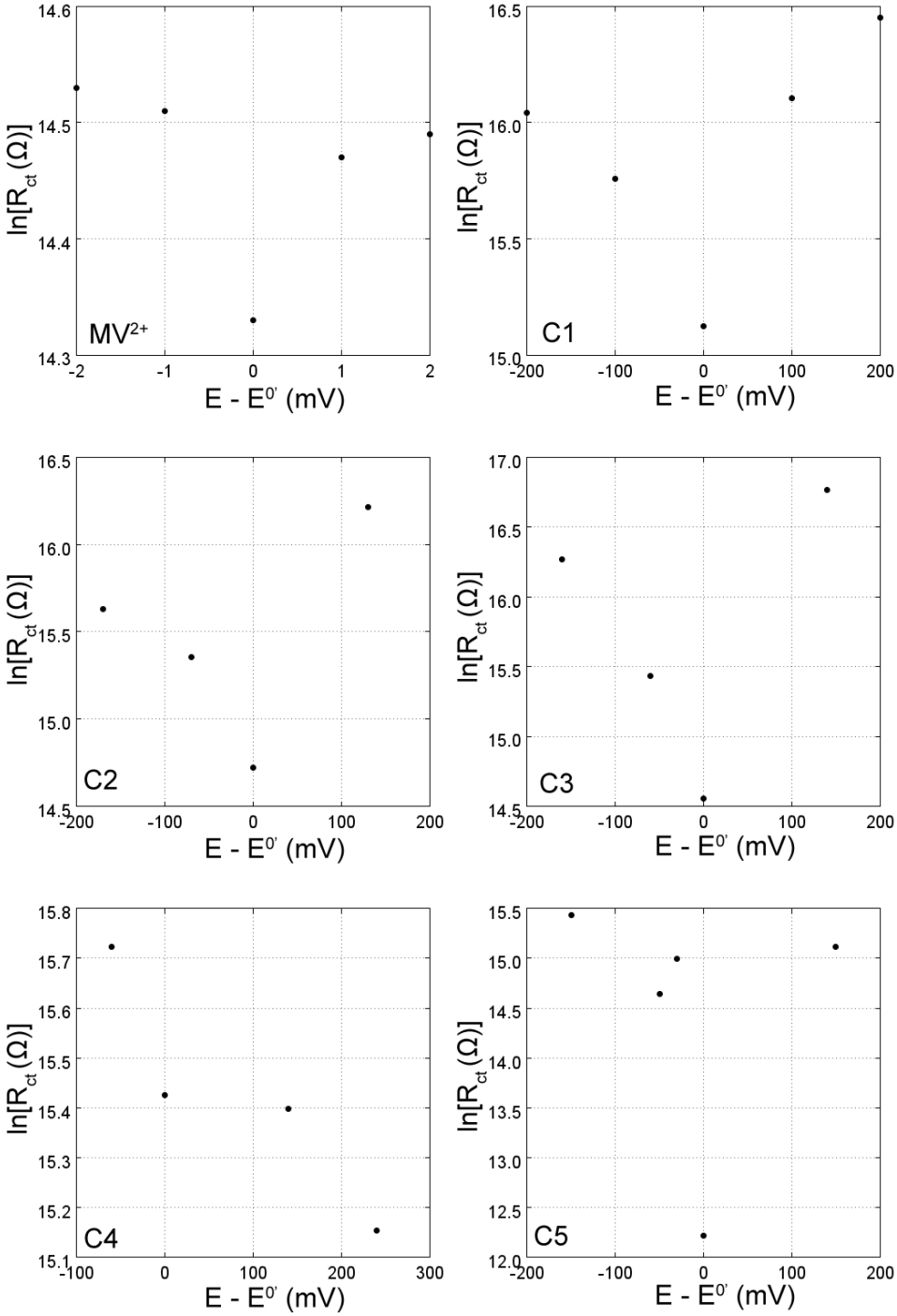

Figure 5.8: EIS data recorded at a 5 μm radius platinum disc working electrode in a solution of MV^{2+} or a derivative (1 mM) and $TBAPF_6$ (0.1M).

Though a k^0 value for each compound was measured successfully, the measured values of R_{ct} as a function of potential were in poor agreement with the theoretical model employed preventing determination of α for each reaction. One possible explanation is electrode fouling. In an EIS experiment, the signal to noise ratio is improved by running the experiment for longer times and the experiment can be slow compared to other techniques. It is estimated that the EIS data collected here, took approximately 2 seconds to record for each experiment. For these reasons, independent measurements of k^0, and measurements of α, via a faster technique were attempted.

5.3 Fast Scan Voltammetry

Fast scan voltammetry (FSV) with convolution analysis was employed in the determination of the standard rate constants of the molecules at platinum and bismuth. The technique holds several advantages over EIS. Measurements of the forward rate constant, k_f, over a range of potentials is generally easier with FSV methods and the experiment run time is typically shorter than that of an EIS experiment resulting in less time for electrode fouling.

Using the potential dependent forward and backward rate constants given by equations 5.17 and 5.18 respectively, the Butler-Volmer model allows us to describe the net faradaic current associated with an electron transfer reaction using 5.19.

$$k_f(E) = k^0 \exp\left[-\alpha \frac{F(E - E^{0'})}{RT}\right] \tag{5.17}$$

$$k_b(E) = k^0 \exp\left[(1 - \alpha) \frac{F(E - E^{0'})}{RT}\right] \tag{5.18}$$

$$\frac{i}{nFA} = C_{O(x=0)} k_f - C_{R(x=0)} k_b \tag{5.19}$$

If we then apply a large overpotential to the system to drive reduction, the rate of the oxidation reaction becomes negligible, i.e. $k_f >> k_b$, and Equation 5.19 simplifies to give Equation 5.20.

$$i = C_{O(x=0)} nFA k_f(E) \tag{5.20}$$

The gradient of a plot of $\ln(k_f)$ as a function of potential is then given by Equation 5.21, from which α can be determined.[5]

$$\frac{\delta \ln(k_f)}{\delta E} = -\frac{\alpha F}{RT} \tag{5.21}$$

In addition to current flowing via the electron transfer reaction under study, a non-faradaic current is commonly observed over the entire potential range of a voltammogram. This must be subtracted before the faradaic current can be properly analysed. To perform this subtraction, Equation 5.22 was fitted to the current in the region where no electron transfer reaction occurs. The value E_0 refers to the potential at which the voltammogram starts. The parameters

m_1, m_2, and i_{dl} are floated to fit without consideration for their physical meanings. Subtracting the current given by Equation 5.22 from the experimentally measured current then gives the faradaic current used in the convolution analysis.

$$i_{background} = m_1(E - E_0) + m_2 \exp\left(\frac{E - E_0}{Rc_{dl}}\right) - i_{dl} \tag{5.22}$$

Convolution analysis makes use of the semi-integral of the FSV current to allow determination of k^0 at sufficiently fast scan rates. The forward rate constant is given by Equation 5.23.[6] The parameters i, I and I_l are the current of the voltammogram at potential E, the current of the semi-integral at potential E, and the limiting current of the semi-integral respectively. The parameter θ is the dimensionless potential given by Equation 5.24.

$$\begin{aligned} &\ln\left[k_f(E)\ (\text{cm s}^{-1})\right] = \\ &\ln\left[\sqrt{D\ (\text{cm}^2\ \text{s}^{-1})}\right] - \ln\left[\frac{I_l - I(1 + I_l \exp[\theta])}{i}\right] \end{aligned} \tag{5.23}$$

$$\theta = \frac{F(E - E^{0'})}{RT} \tag{5.24}$$

The current produced during the the fast scan voltammetry experiment varies with time in two ways. Firstly, as the experiment proceeds, the applied potential changes, driving the electron transfer at a faster rate. Secondly, as the experiment proceeds, the thickness of the diffusion layer increases, causing mass transport to the electrode

to decrease and this effect will eventually lower the current observed. These two time based responses can be said to be convoluted with one another. To extract kinetic data from the voltammogram it is necessary to remove the contribution of changes in diffusion layer width to the observed current. Semi-integration is a mathematical technique that can be used to subtract the effect of diffusion layer width changes, giving the plot of semi-integral current against potential a form more like that of a steady-state voltammogram.

5.3.1 Fast Scan Voltammetry at Platinum

Figures 5.9 to 5.14 show FSV data collected at a 5 μm platinum disc working electrode for MV^{2+} and C1-5 (10 mM) in MeCN with $TBAPF_6$ (0.2M). Voltammograms recorded with scan rate 20 kV s^{-1} were ran 50 times and co-averaged to produce the voltammograms shown in the top plots in blue. The fitted background current is shown in grey and the background subtracted current is plotted on the same plot in red. Semi-integration of the background subtracted current is then used to generate the semi-integral plots shown as the centre plots. The bottom plots show the determined values of $\ln[k_f$ (cm s^{-1})] as a function of potential with a fit line through the points. The determined values of k^0 are tabulated in Table 5.2.

Due to the high scan rates employed, the voltammograms contain an oscillation in the current at the start of each run. These oscillations are a repeatable feature of the voltammogram and thus did not diminish upon co-averaging. While this artefact did not interfere with the measured current across the rest of the potential range, it did cause difficulty during the fitting of the background current. Conse-

quently, the fitting of the background current is expected to be the major source of error in the determination of α and k^0. The size of the effect of background subtraction is demonstrated by comparison between the values in Table 5.2 with those in 5.3. The latter contains rate constants determined using the voltammograms without background subtraction.

The semi-integral plots do not reach plateau points due to the onset of the second one-electron reduction reaction. The limiting current of the semi-integral is found by taking the discrete derivative of the semi-integral, which passes through a maximum at 50% of the semi-integral's maximum height.

Molecule	k^0 **(cm s^{-1})**	α
MV^{2+}	1.4×10^{-1}	0.34
C1	1.1×10^{-1}	0.34
C2	1.1×10^{-1}	0.63
C3	1.7×10^{-1}	0.45
C4	1.6×10^{-1}	0.40
C5	2.8×10^{-1}	0.50

Table 5.2: Values of the standard rate constant, k^0, and transfer coefficient, α, determined at a 5 μm radius platinum disc in MeCN with $TBAPF_6$ (0.2M) and MV^{2+} or a derivative (10 mM) using convolution analysis of FSV data. A scan rate of 20 kV s^{-1} was employed.

Molecule	k^0 **(cm s^{-1})** **no background subtraction**	α **no background subtraction**
MV^{2+}	2.7×10^{-1}	0.25
C1	3.6×10^{-1}	0.19
C2	6.4×10^{-1}	0.30
C3	6.2×10^{-1}	0.29
C4	2.9×10^{-1}	0.25
C5	7.9×10^{-1}	0.30

Table 5.3: Values of the standard rate constant, k^0, and transfer coefficient, α, determined at a 5 μm radius platinum disc in MeCN with $TBAPF_6$ (0.2M) and MV^{2+} or a derivative (10 mM) using convolution analysis of FSV data and no subtraction of background current from the voltammograms. A scan rate of 20 kV s^{-1} was employed.

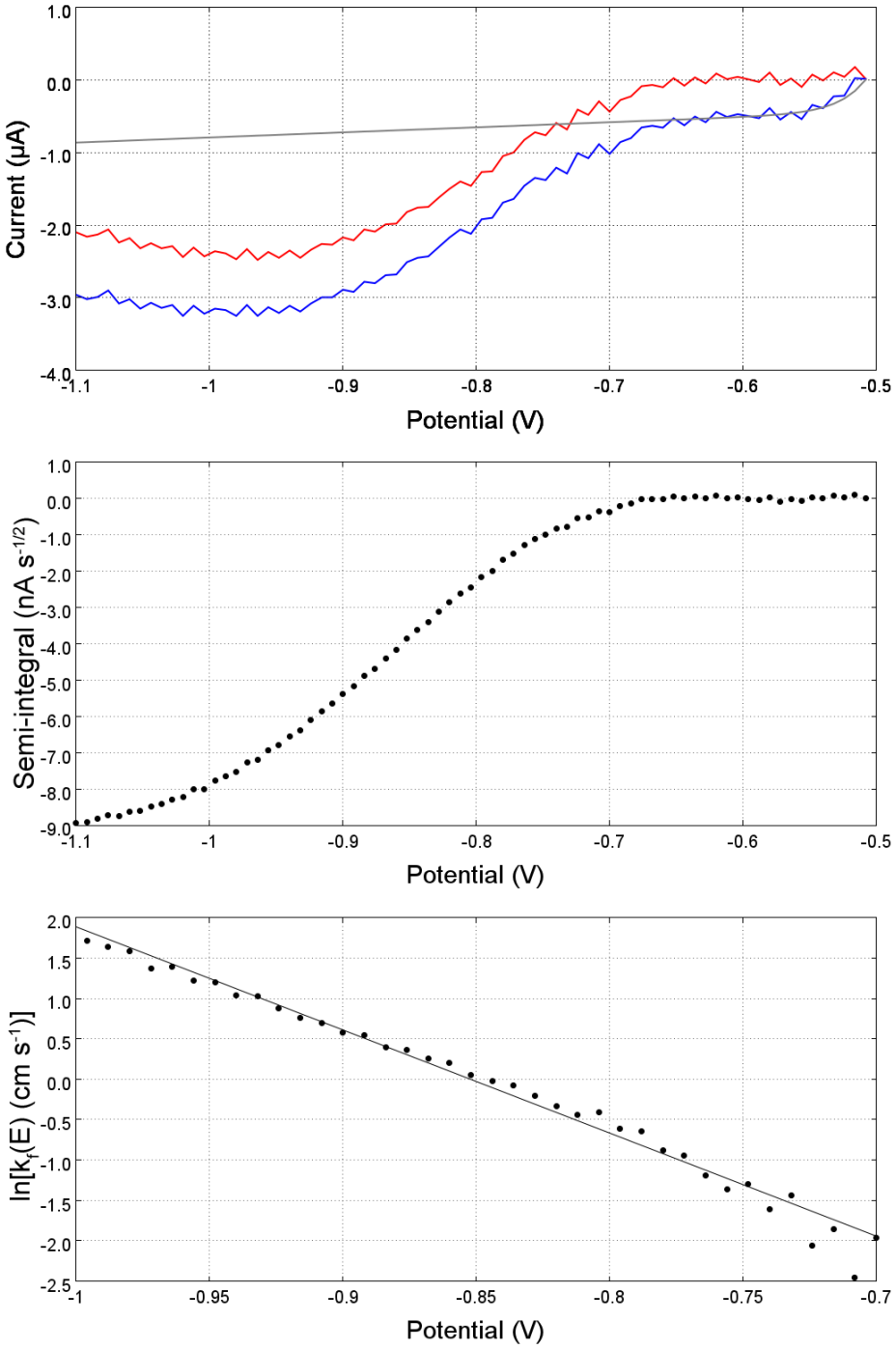

Figure 5.9: Top: A FSV recorded at scan rate 20 kV s^{-1} for MV^{2+} (10 mM) in MeCN with $TBAPF_6$ (0.2M) at a 5 μm radius platinum disc shown in blue. A fitted background is shown in grey and the background subtracted data shown in red. Middle: A semi-integral plot of the background subtracted FSV. Bottom: A plot of $\ln[k_f$ (cm s^{-1})] as a function of potential with the potential range constrained to the linear region which occurs after $E^{0'}$.

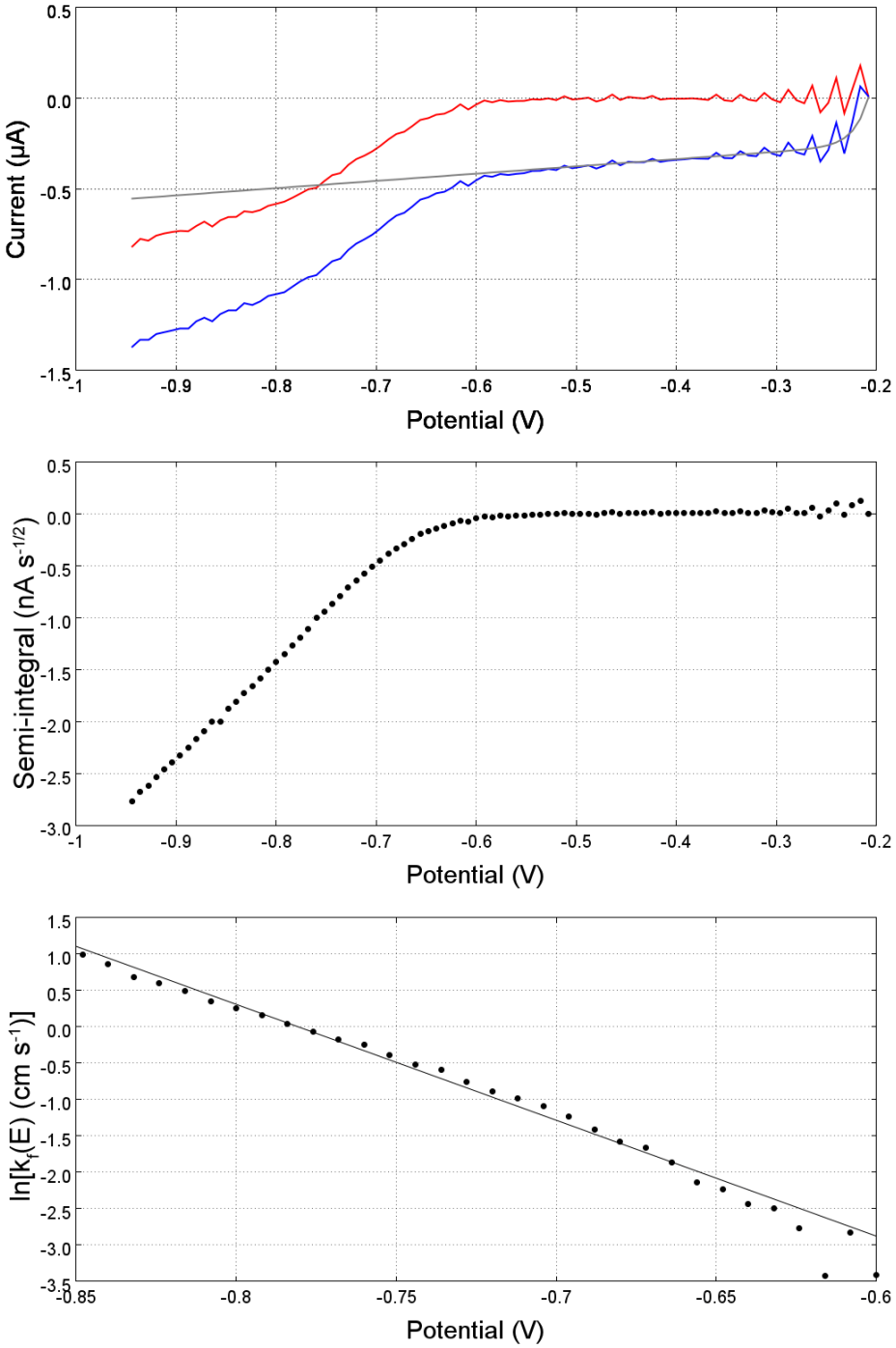

Figure 5.10: Top:A FSV recorded at scan rate 20 kV s^{-1} for C1 (10 mM) in MeCN with $TBAPF_6$ (0.2M) is shown in blue. A fitted background curve is shown in grey and a subtracting this background from the recorded CV gives the data shown in red. Middle: A semi-integral plot of the background subtracted FSV. Bottom: A plot of $\ln[k_f$ (cm s^{-1})] as a function of potential with the potential range constrained to the linear region which occurs after $E^{0'}$.

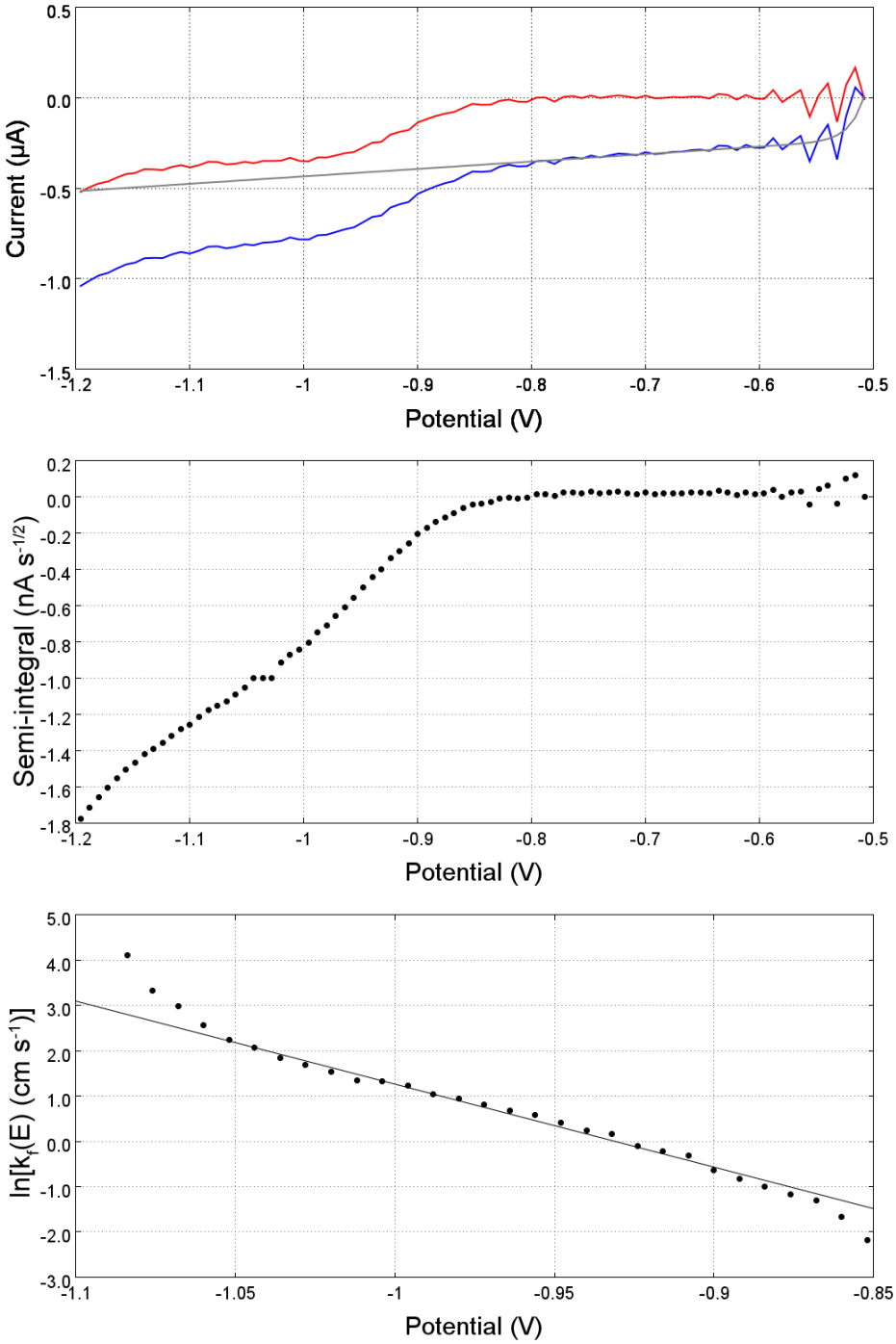

Figure 5.11: Top:A FSV recorded at scan rate 20 kV s^{-1} for C2 (10 mM) in MeCN with $TBAPF_6$ (0.2M) is shown in blue. A fitted background curve is shown in grey and a subtracting this background from the recorded CV gives the data shown in red. Middle: A semi-integral plot of the background subtracted FSV. Bottom: A plot of $\ln[k_f$ (cm s^{-1})] as a function of potential with the potential range constrained to the linear region which occurs after $E^{0'}$.

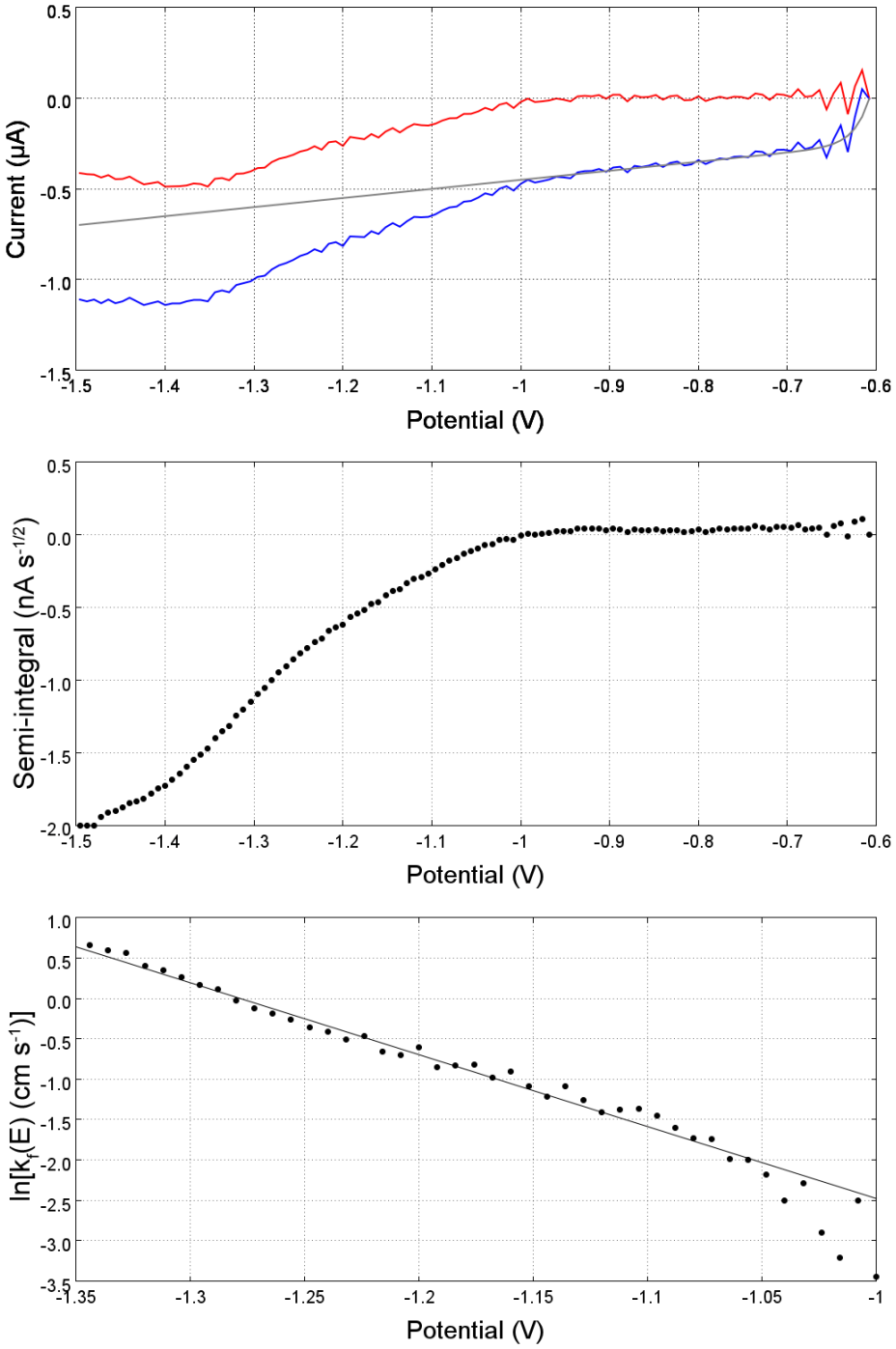

Figure 5.12: Top: A FSV recorded at scan rate 20 kV s^{-1} for C3 (10 mM) in MeCN with $TBAPF_6$ (0.2M) is shown in blue. A fitted background curve is shown in grey and a subtracting this background from the recorded CV gives the data shown in red. Middle: A semi-integral plot of the background subtracted FSV. Bottom: A plot of $\ln[k_f$ (cm s^{-1})] as a function of potential with the potential range constrained to the linear region which occurs after $E^{0'}$.

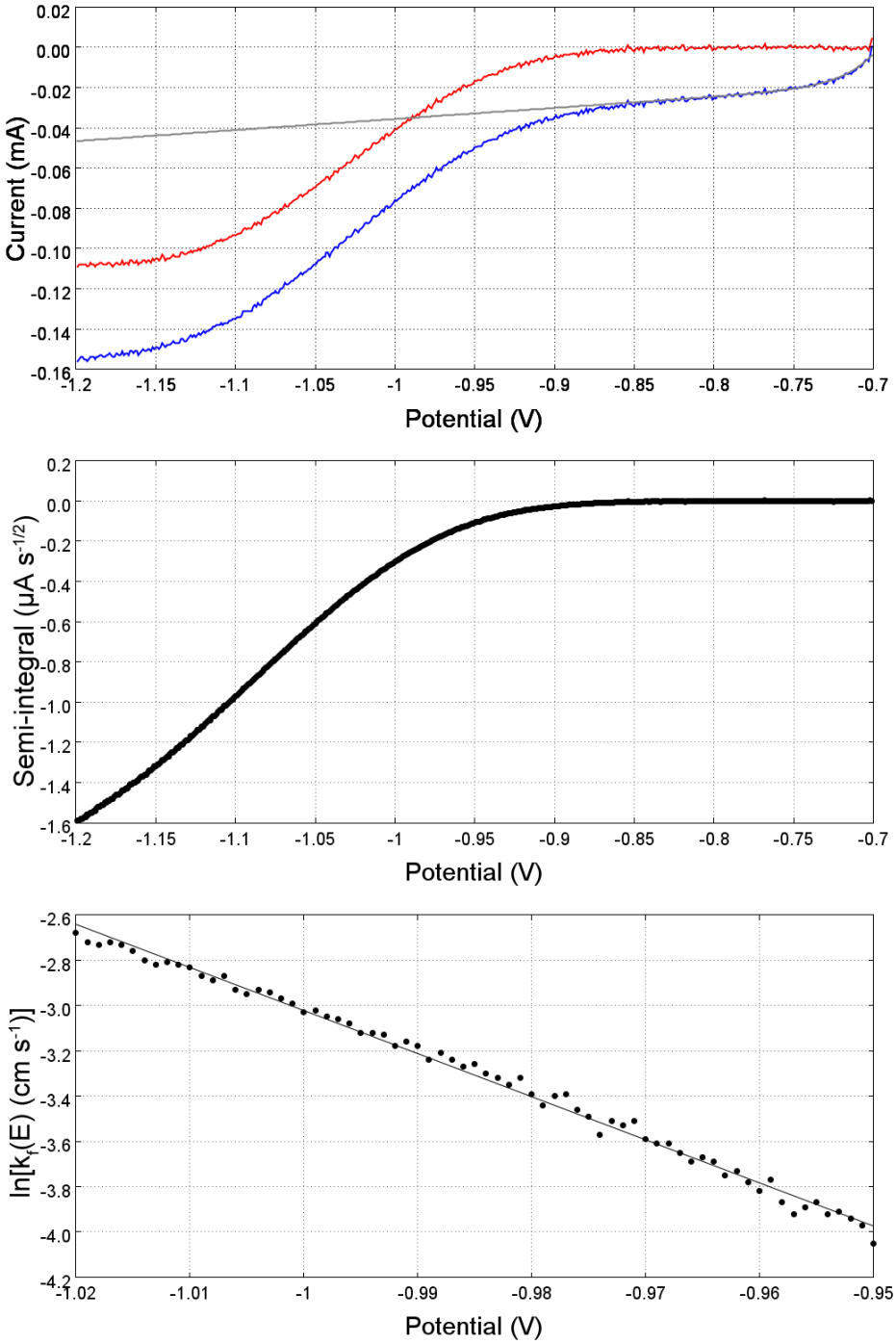

Figure 5.13: Top: A FSV recorded at scan rate 20 kV s^{-1} for C4 (10 mM) in MeCN with $TBAPF_6$ (0.2M) is shown in blue. A fitted background curve is shown in grey and a subtracting this background from the recorded CV gives the data shown in red. Middle: A semi-integral plot of the background subtracted FSV. Bottom: A plot of $\ln[k_f$ (cm s^{-1})] as a function of potential with the potential range constrained to the linear region which occurs after $E^{0'}$.

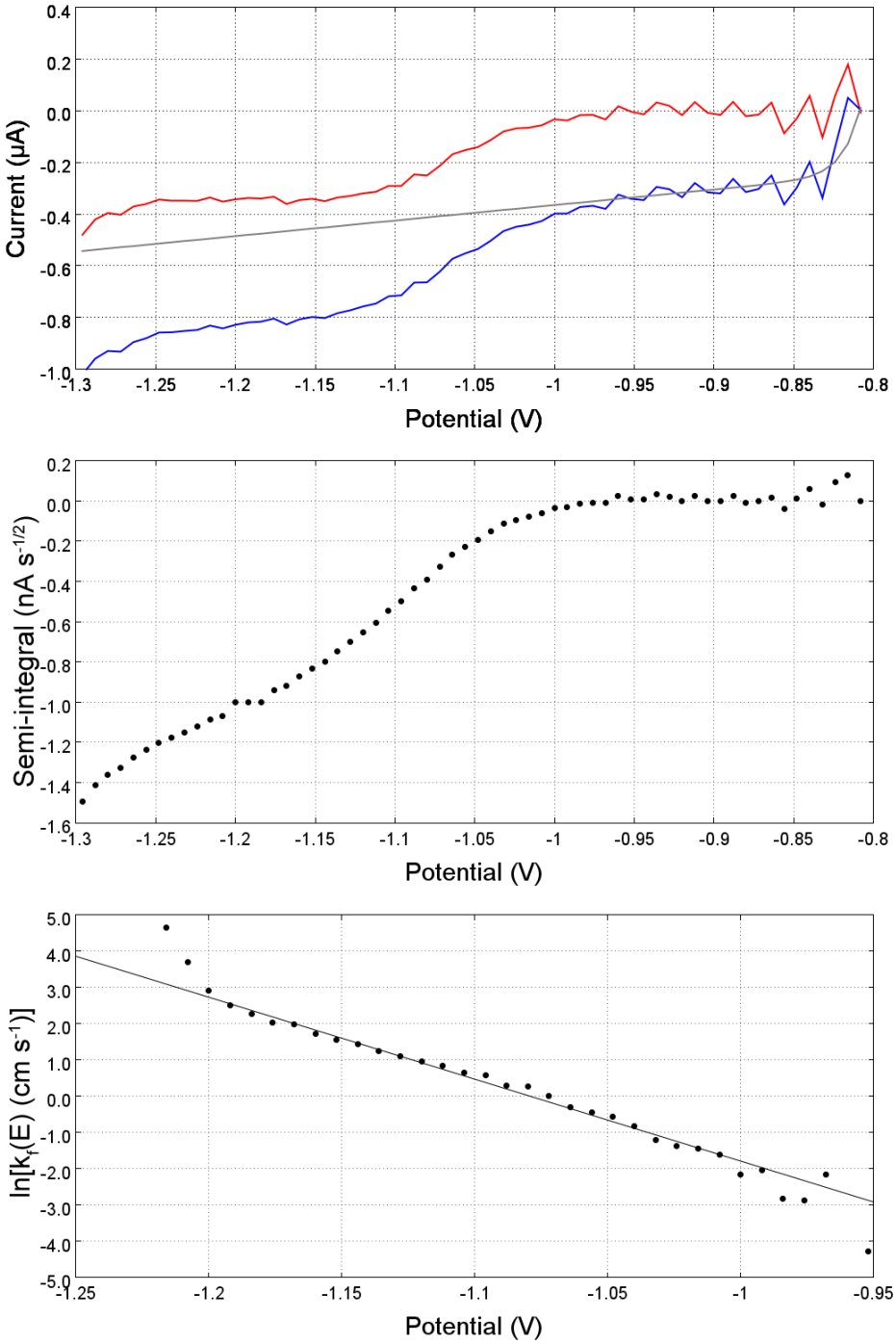

Figure 5.14: Top: A FSV recorded at scan rate 20 kV s^{-1} for C5 (10 mM) in MeCN with $TBAPF_6$ (0.2M) is shown in blue. A fitted background curve is shown in grey and a subtracting this background from the recorded CV gives the data shown in red. Middle: A semi-integral plot of the background subtracted FSV. Bottom: A plot of $\ln[k_f$ (cm s^{-1})] as a function of potential with the potential range constrained to the linear region which occurs after $E^{0'}$.

Molecule	k^0 **(cm s^{-1})**	α
MV^{2+}	1.8×10^{-2}	0.44
C1	1.3×10^{-2}	0.52
C2	2.4×10^{-2}	0.73
C3	4.7×10^{-2}	0.48
C4	2.8×10^{-2}	0.48
C5	1.5×10^{-2}	0.47

Table 5.4: Values of the standard rate constant, k^0, and transfer coefficient, α, determined at a 0.5 mm radius bismuth disc using convolution analysis of FSV data. These values were determined in MeCN with $TBAPF_6$ (0.2M) and MV^{2+} or a derivative (10 mM). A scan rate of 1 kV s^{-1} was employed.

5.3.2 Fast Scan Voltammetry at Bismuth

Figures 5.15 to 5.20 show fast scan voltammetry data collected at a 0.5 mm bismuth disc working electrode for MV^{2+} and C1-5 (10 mM) in MeCN with $TBAPF_6$ (0.2M). Voltammograms recorded with scan rate 1 kV s^{-1} are shown in the top plots in blue. The fitted background current is shown in grey and the background subtracted current is plotted on the same plot in red. Semi-integration of the background subtracted current is then used to generate the semi-integral plots shown in the centre plots. The bottom plots show the determined value of $\ln[k_f$ (cm s^{-1})] as a function of potential with a fit line through the points. The determined values of k^0 are tabulated in Table 5.4.

The lower scan rates used at bismuth meant that the fitting of the background could be performed much more precisely, making this source of error much less significant here. The size of the effect of background subtraction is demonstrated by comparison between the values in Table 5.4 with those in Table 5.5. The latter contains rate constants determined using the voltammograms without background subtraction.

Molecule	k^0 (cm s^{-1}) (no background subtraction)	α (no background subtraction)
MV^{2+}	2.5×10^{-2}	0.15
C1	3.2×10^{-3}	0.27
C2	6.5×10^{-2}	0.26
C3	8.6×10^{-2}	0.49
C4	8.5×10^{-2}	0.24
C5	8.9×10^{-2}	0.13

Table 5.5: Values of the standard rate constant, k^0, and transfer coefficient, α, determined at a 0.5 mm radius bismuth disc using convolution analysis of FSV data prior to background subtraction. These values were determined in MeCN with $TBAPF_6$ (0.2M) and MV^{2+} or a derivative (10 mM). A scan rate of 1 kV s^{-1} was employed.

The onset of a plateau in the semi-integral is obscured due to the onset of the second one-electron reduction reaction for each molecule. Though it may appear that the potentials were not scanned sufficiently negative, scanning more negative would yield no more useful information and reduction of the bismuth electrode could begin to occur. The limiting currents of the semi-integrals were determined by taking the discrete derivative of the semi-integral current and noting the potential at which the derivative peaks. This potential corresponds to the point at which the semi-integral current is at 50% of its limiting value meaning that the limiting current can be obtained by doubling the current at this potential.

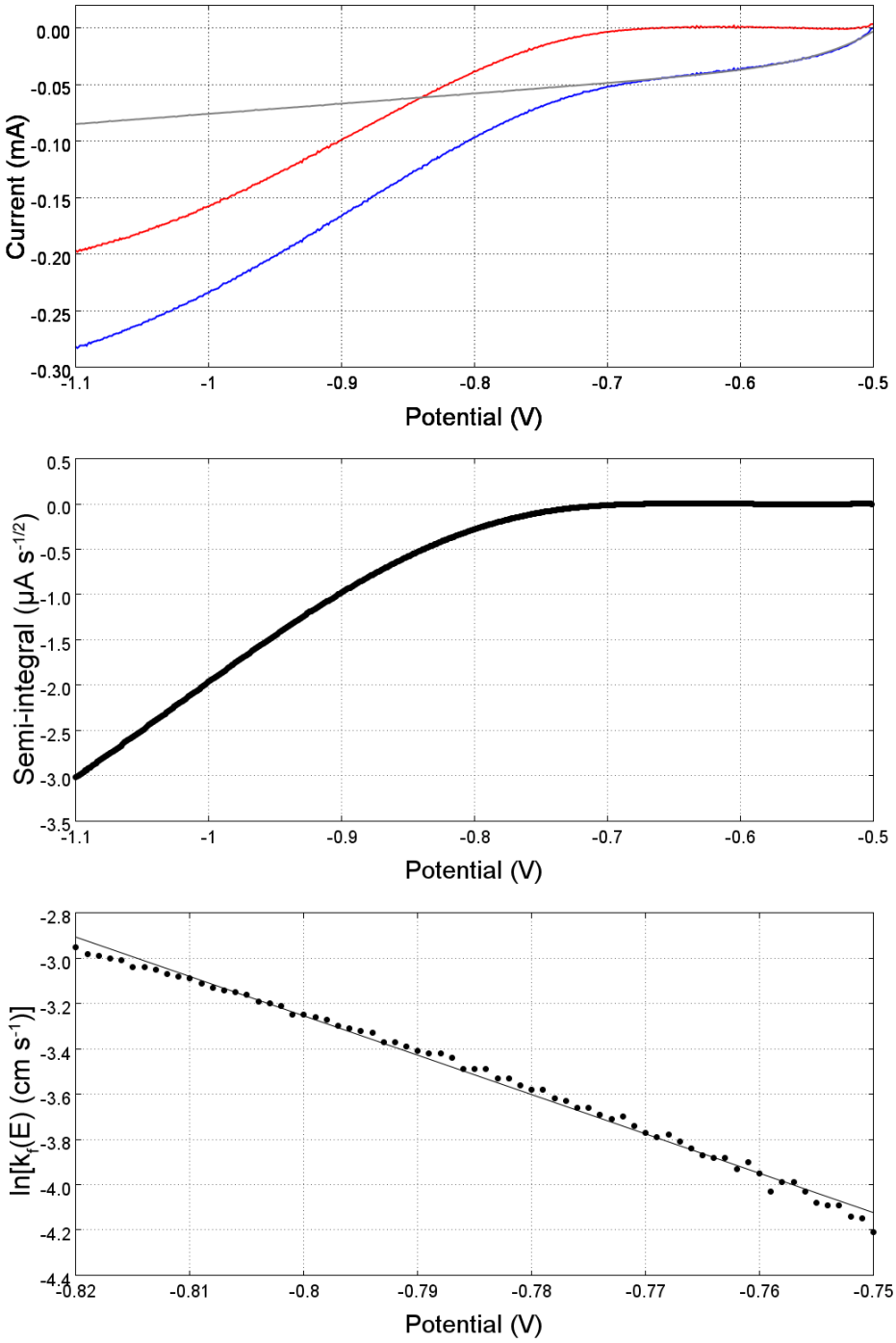

Figure 5.15: Top: A FSV recorded at scan rate 1 kV s^{-1} for MV^{2+} (10 mM) in MeCN with $TBAPF_6$ (0.2M) at a 0.5 mm radius bismuth disc shown in blue. A fitted background is shown in grey and the background subtracted data shown in red. Middle: A semi-integral plot of the background subtracted FSV. Bottom: A plot of $\ln[k_f$ (cm s^{-1})] as a function of potential with the potentials constrained to the linear region occurring after $E^{0'}$.

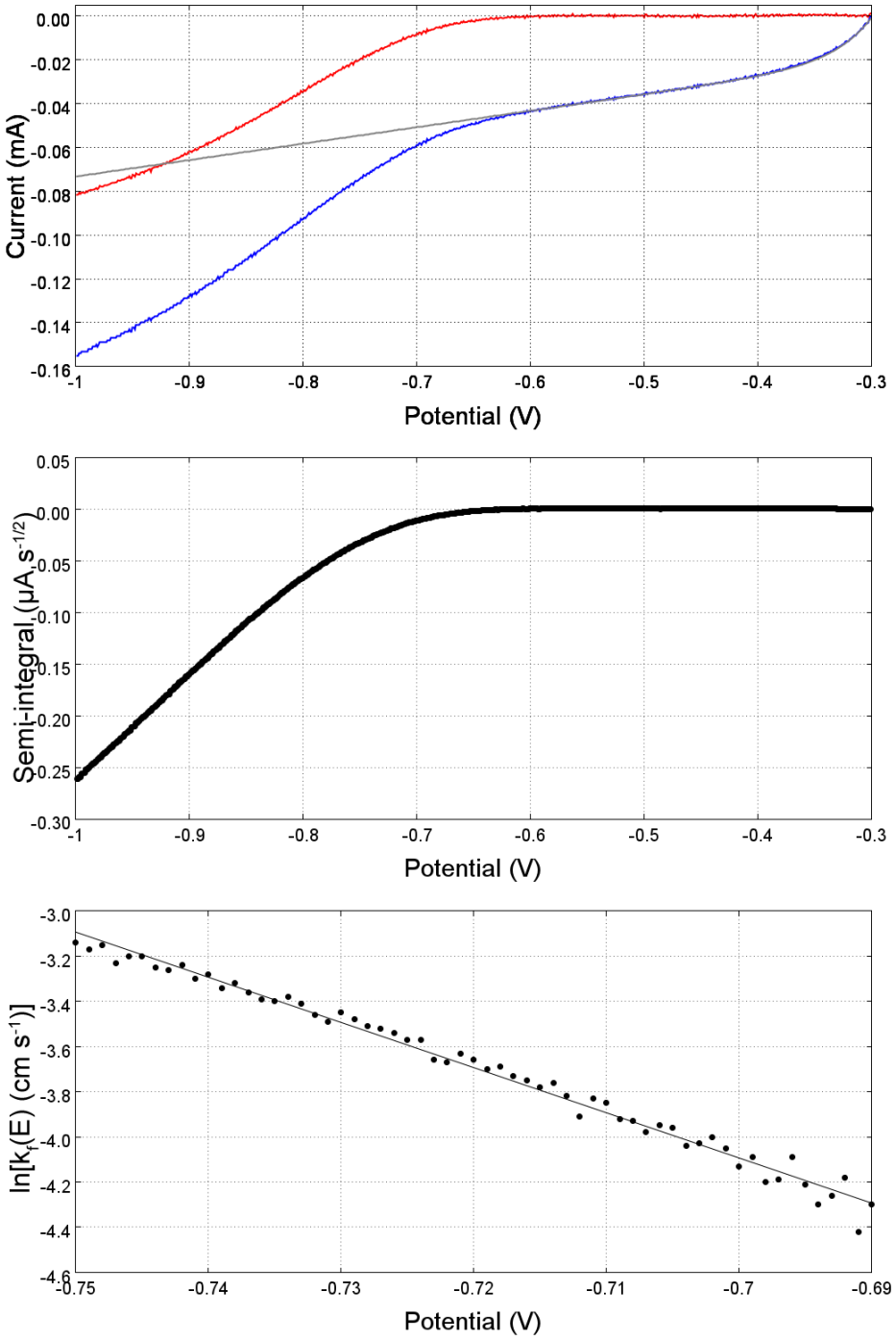

Figure 5.16: Top: A FSV recorded at scan rate 1 kV s^{-1} for C1 (10 mM) in MeCN with $TBAPF_6$ (0.2M) at a 0.5 mm radius bismuth disc shown in blue. A fitted background is shown in grey and the background subtracted data shown in red. Middle: A semi-integral plot of the background subtracted FSV. Bottom: A plot of $\ln[k_f$ (cm s^{-1})] as a function of potential with the potentials constrained to the linear region occurring after $E^{0'}$.

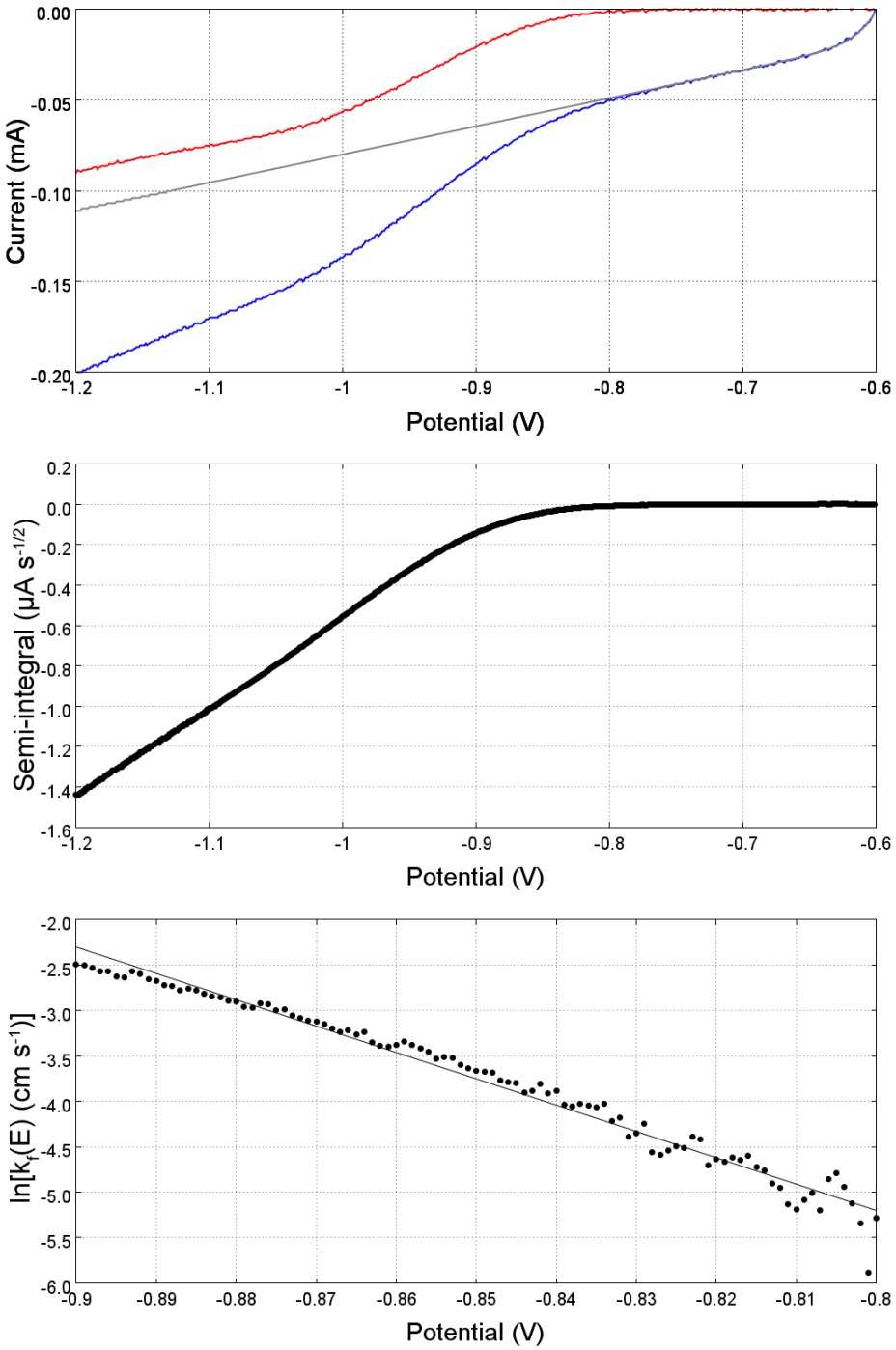

Figure 5.17: Top: A FSV recorded at scan rate 1 kV s^{-1} for C2 (10 mM) in MeCN with $TBAPF_6$ (0.2M) at a 0.5 mm radius bismuth disc shown in blue. A fitted background is shown in grey and the background subtracted data shown in red. Middle: A semi-integral plot of the background subtracted FSV. Bottom: A plot of $\ln[k_f$ (cm s^{-1})] as a function of potential with the potentials constrained to the linear region occurring after $E^{0'}$.

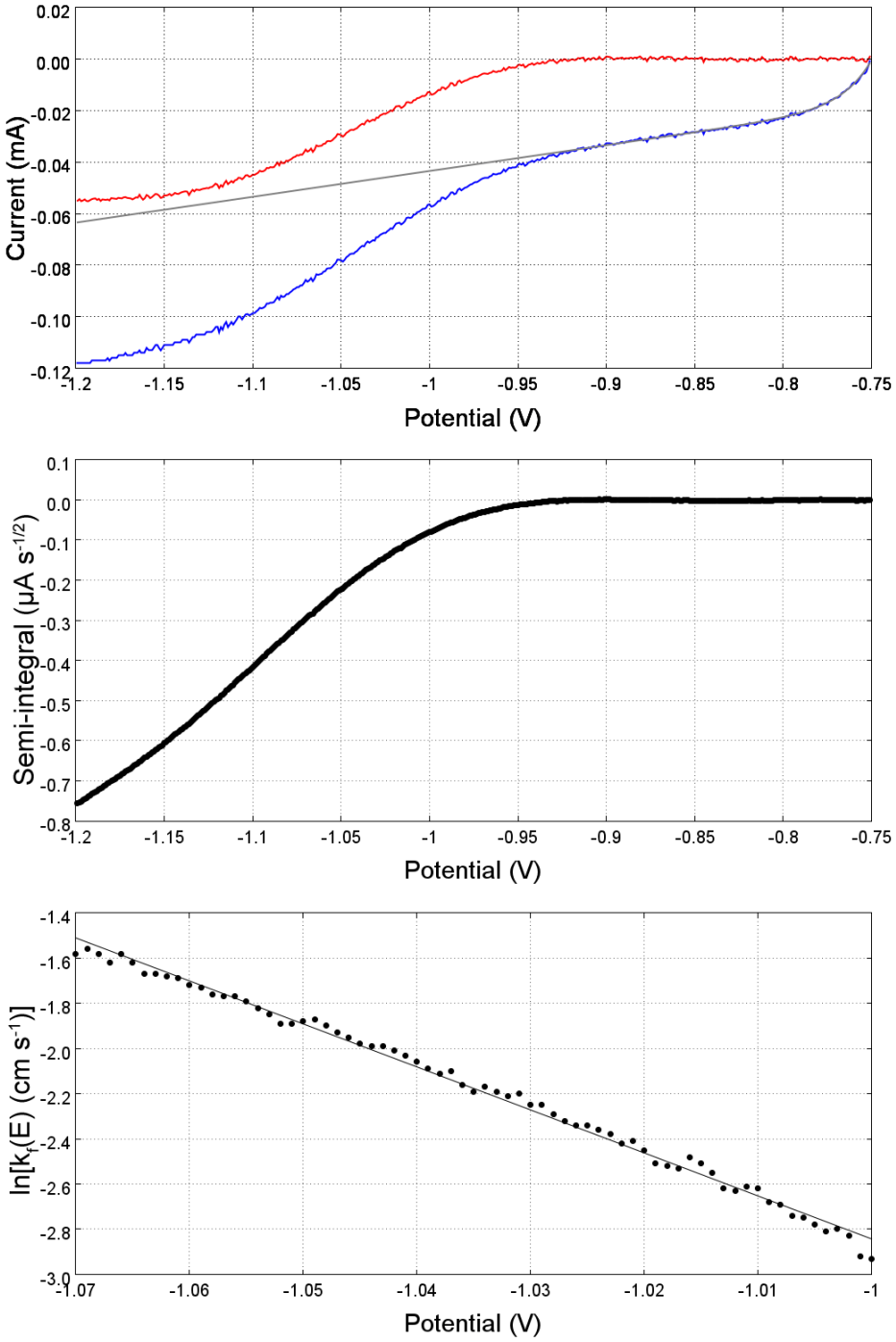

Figure 5.18: Top: A FSV recorded at scan rate 1 kV s^{-1} for C3 (10 mM) in MeCN with $TBAPF_6$ (0.2M) at a 0.5 mm radius bismuth disc shown in blue. A fitted background is shown in grey and the background subtracted data shown in red. Middle: A semi-integral plot of the background subtracted FSV. Bottom: A plot of $\ln[k_f$ (cm s^{-1})] as a function of potential with the potentials constrained to the linear region occurring after $E^{0'}$.

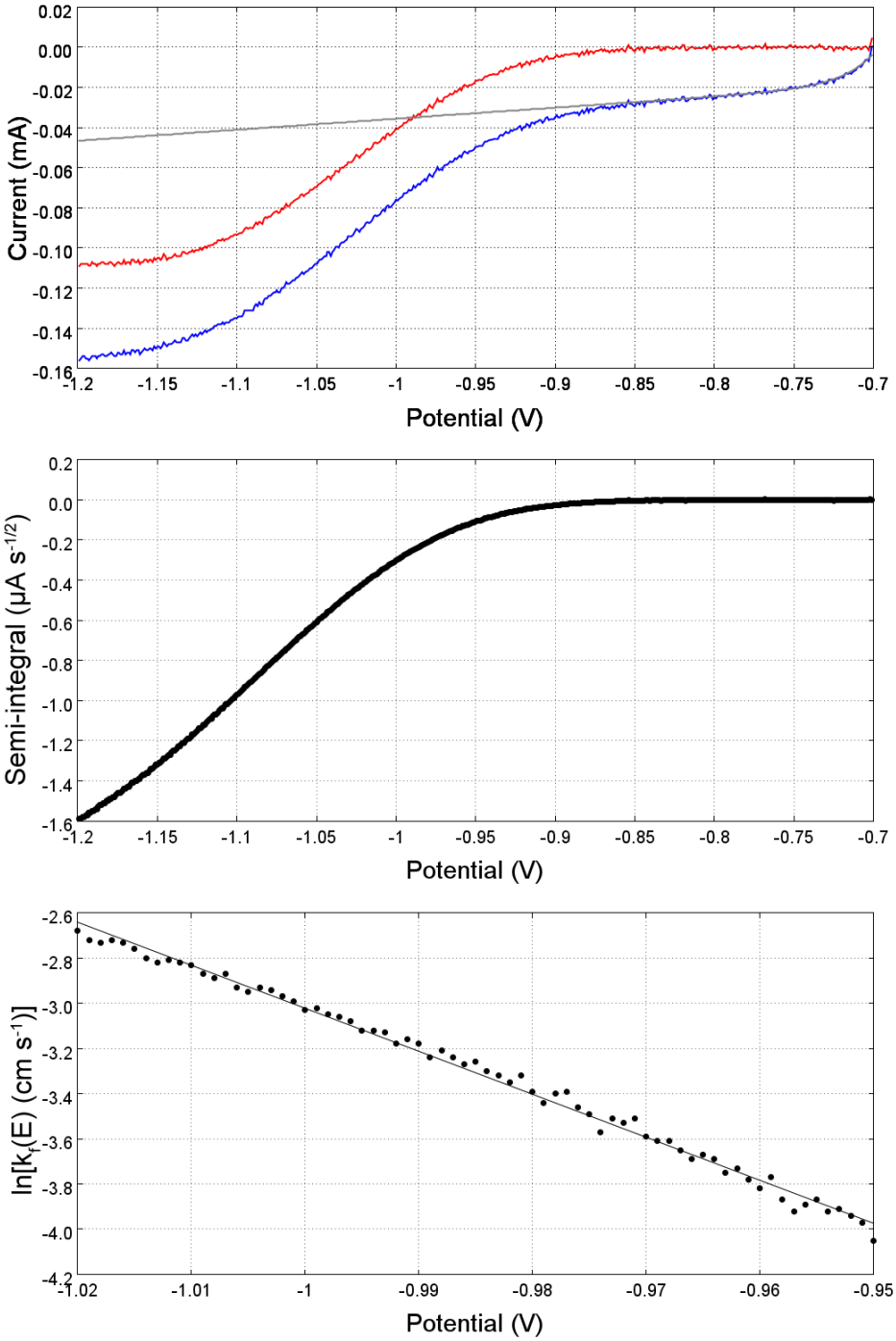

Figure 5.19: Top: A FSV recorded at scan rate 1 kV s^{-1} for C4 (10 mM) in MeCN with $TBAPF_6$ (0.2M) at a 0.5 mm radius bismuth disc shown in blue. A fitted background is shown in grey and the background subtracted data shown in red. Middle: A semi-integral plot of the background subtracted FSV. Bottom: A plot of $\ln[k_f$ (cm s^{-1})] as a function of potential with the potentials constrained to the linear region occurring after $E^{0'}$.

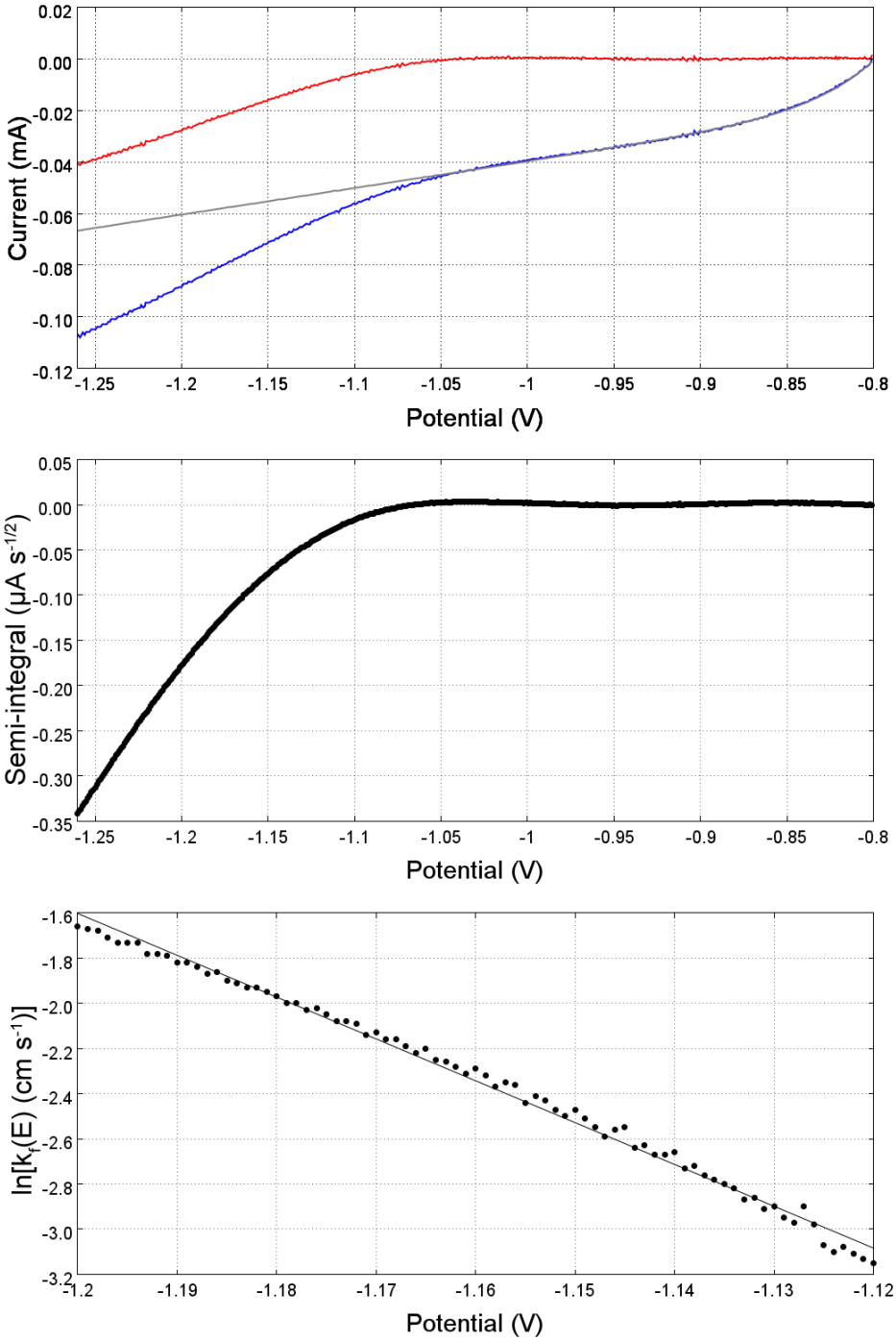

Figure 5.20: Top: A FSV recorded at scan rate 1 kV s^{-1} for C5 (10 mM) in MeCN with $TBAPF_6$ (0.2M) at a 0.5 mm radius bismuth disc shown in blue. A fitted background is shown in grey and the background subtracted data shown in red. Middle: A semi-integral plot of the background subtracted FSV. Bottom: A plot of $\ln[k_f$ (cm s^{-1})] as a function of potential with the potentials constrained to the linear region occurring after $E^{0'}$.

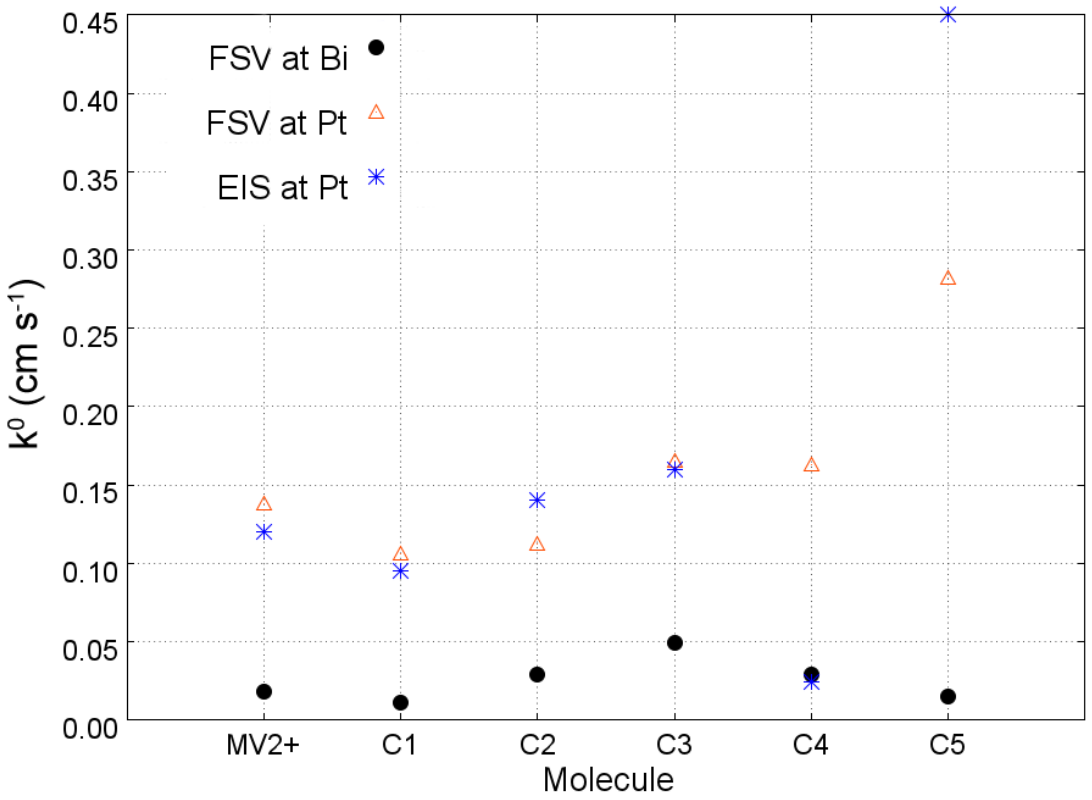

Figure 5.21: Values of the standard rate constant, k^0, for the first one-electron reduction of MV^{2+} and derivatives C1-5 recorded using EIS at platinum and FSV at platinum and bismuth. These k^0 values have not been Frumkin corrected.

5.4 Observed Values of k^0 and α at Platinum and Bismuth

The k^0 values determined using EIS at platinum and FSV at platinum and bismuth are plotted in Figure 5.21. Good agreement is observed between the platinum rate constants measured using EIS and FSV for molecules MV^{2+} and C1 to C3. This suggests that both techniques have provided accurate values for k^0. The theoretical models used to interpret the data in each case are based on very different assumptions due to EIS being a small perturbation technique and FSV data being analysed in the Tafel region. Additionally, the fast scan voltammograms each took approximately 50 μs to record,

meaning that the time taken to run the two experimental techniques differs substantially, and the degree of electrode fouling occurring is expected to be very different in each case. If there were large systematic errors in the determined k^0 value arising from the assumptions inherent in the experimental and analytical approaches, it is unlikely that these errors would be of the same size for both techniques. Poor agreement is seen for the k^0 values measured at Pt using EIS and FSV for C4 and C5. Given the higher quality of the FSV data, the data points obtained via this technique are likely to be more accurate. It is clear from the plot that the k^0 values obtained via FSV at bismuth are significantly lower, on average 5.9 times lower than those obtained via the same technique at platinum. Similar trends are observed between the platinum and bismuth rates.

A comparison of the α values measured at the two surfaces is shown in Figure 5.22. The two sets of values follow similar trends.

The standard potentials of these redox couples span a range of 0.386V. Within this potential range significant variation in the size of ϕ_2 across the electrode/electrolyte interface is observed (see Chapter 4). If the analyte molecules carry a charge, as indicated by experiment (see Section 3.7), then this variation may have a significant impact on the observed rates. The size of ϕ_2 at the two electrode surfaces at a given potential also differs. Therefore, the ϕ_2 effect must be corrected for before a meaningful comparison between individual rate constants can be made. The application of this correction will be discussed in the following section.

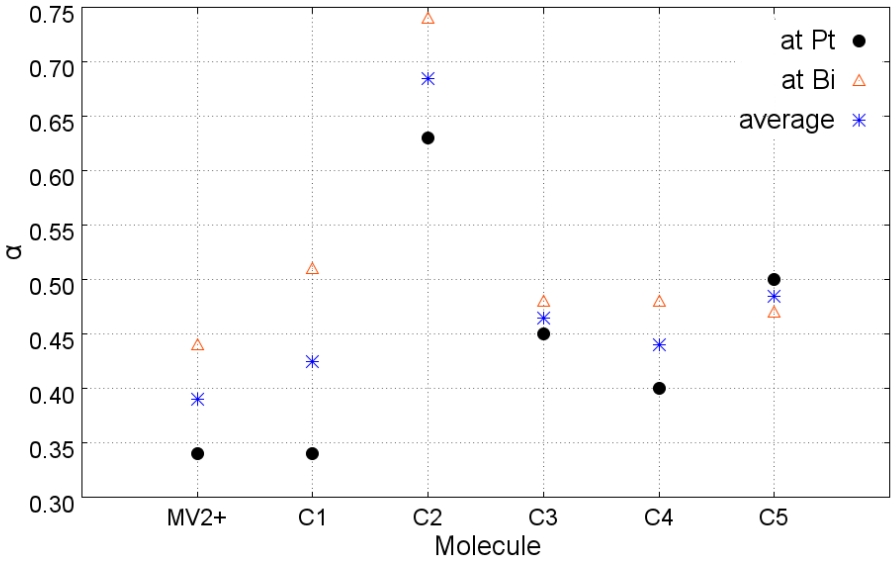

Figure 5.22: Values of the electron transfer coefficient, α, for the first one-electron reduction of MV^{2+} and derivatives C1-5 determined using FSV at platinum and bismuth. Data was recorded in solutions of $TBAPF_6$ (0.2M) and MV^{2+} or a derivative (10 mM) in MeCN. Platinum FSV data was recorded with a scan rate of 20 kV s^{-1} and bismuth data with a scan rate of 1 kV s^{-1}.

5.5 Frumkin Correction

Between the bulk of the solid electrode and the bulk of the electrolyte solution a potential difference, ϕ, exists. It is often approximated that the potential change occurs entirely across the electrode/electrolyte interface and that beyond the outer Helmholtz plane, the potential of the solution is at its bulk value. This approximation is often very poor in the determination of k^0 for a charged species and can lead to rate constants being raised or lowered by several orders of magnitude.[5] However, with knowledge of the molecular charge of the reactant (z), the transfer coefficient of the electron transfer reaction (α), and the size of the potential change occurring within the diffuse layer (ϕ_2), rates measured using this approximation can be corrected using Equation 5.25. This correction, known as the Frumkin correction, produces a corrected standard rate constant, k^0_{FC}, which

corresponds to the standard rate constant that would be observed if ϕ_2 were 0 and, assuming ϕ_3 is 0, ϕ_1 were equal to ϕ (see Chapter 4).[5]

$$k^0_{FC} = k^0 \exp\left(\frac{-(\alpha - z)F\phi_2}{RT}\right) \tag{5.25}$$

To perform this correction, ϕ_2 at the standard potential for each redox couple was obtained from the analysis performed in Chapter 4. Knowledge of the charge on each molecule, prior to the electron transfer reaction, is also required. However, determination of the molecular charge is non-trivial due to the possibility of ion-pairing. Here we attempt to perform the Frumkin correction using the three plausible values of molecular charge, $z = +2$, $+1$, 0. In absence of ϕ_2 effects, a plot of k^0 at platinum against k^0 at bismuth can be expected to produce a linear plot of zero intercept,[2] meaning that a comparison of such plots generated with different z values can be used to determine which z value best describes the system. To correct the rate constants measured by EIS at platinum, the α values determined via FSV at platinum were used. For $z = +2$, the corrected standard rate constants found using the platinum EIS data, the platinum FSV data, and the bismuth FSV data are given in Table 5.6. The resulting rate constants for the correction with charge +1 are given in Table 5.7. The resulting rate constants for the correction with charge 0 are given in Table 5.8.

Figure 5.23 shows a plot using the data from the correction performed with $z = +2$. The fit line has a slope of 0.75 ± 0.14, a y-intercept of $5.0 \times 10^{-5} \pm 1.4 \times 10^{-4}$, and R^2 of 0.88. The high value of R^2 and the y-intercept of 0 suggest that the data obtained via this correction is

valid.

Figure 5.24 shows a plot using the data from the correction performed with $z = +1$. Two fit lines are included for the FSV data. The red line considers all the data and has slope -2.1 ± 2.1, a y-intercept of 0.02 ± 0.02 cm s^{-1} and R^2 of 2.4×10^{-3}. The low R^2 and the negative slope mean that the data is certainly invalid. The black line omits the outlying data point corresponding to C5 because a Bi/Pt rate ratio of 0.086 is observed for this molecule compared to an average of 0.39 for all the molecules. This fit line has a slope of 1.2 ± 0.6, a y-intercept of $9.1 \times 10^{-3} \pm 5.0 \times 10^{-3}$ cm s^{-1} and R^2 of 0.60. The observed y-intercept remains significant, suggesting that this Frumkin correction is invalid.

Figure 5.25 shows a plot using the data from the correction performed with $z = 0$. Two fit lines are included for the FSV data. The red line considers all the data and has slope 2.3 ± 4.7, a y-intercept of 0.8 ± 0.6 cm s^{-1} and R^2 of 0.054. The low R^2 and the non-zero intercept suggest that the data is invalid. The black line omits the outlying data point corresponding to C5 because a Bi/Pt rate ratio of 0.027 is observed for this molecule compared to an average of 0.12 for all the molecules. This fit line has a slope of 4.7 ± 0.6, a y-intercept of 0.20 ± 0.08 cm s^{-1} and R^2 of 0.96. The observed y-intercept remains significant, suggesting that full ion pairing does not occur and that this Frumkin correction is invalid.

By comparison of the three sets of Frumkin corrected data, it is clear that the corrected values obtained for $z = +2$ are the most likely to be accurate as they form the only data set to produce a negligible y-intercept. This conclusion is further supported by the findings

in Section 3.7 where evidence was presented for the absence of ion pairing effects.

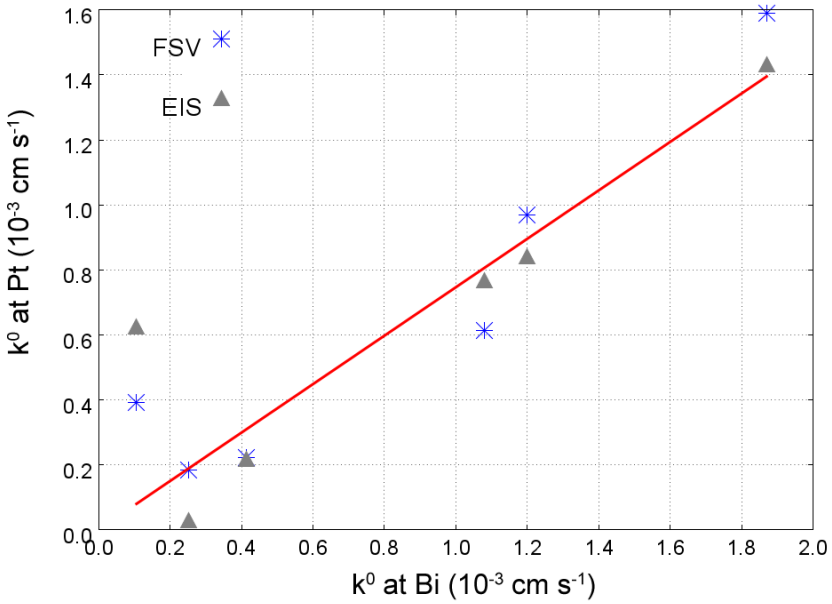

Figure 5.23: Frumkin corrected standard rate constants determined with $z = +2$ for MV^{2+} and C1-5 measured at platinum using FSV and EIS plotted against those measured at bismuth using FSV. A linear fit line to the FSV data is included in the plot.

Molecule	k^0_{FC} **at Pt (cm s^{-1})** measured by FSV	k^0_{FC} **at Pt (cm s^{-1})** measured by EIS	k^0_{FC} **at Bi (cm s^{-1})** measured by FSV
MV^{2+}	9.7×10^{-4}	8.4×10^{-4}	1.2×10^{-3}
C1	1.6×10^{-3}	1.4×10^{-3}	1.9×10^{-3}
C2	6.1×10^{-4}	7.7×10^{-4}	1.1×10^{-3}
C3	2.2×10^{-4}	2.2×10^{-4}	4.1×10^{-4}
C4	1.8×10^{-4}	2.7×10^{-5}	2.5×10^{-4}
C5	3.9×10^{-4}	6.2×10^{-4}	1.1×10^{-4}

Table 5.6: Frumkin corrected standard rate constants, k^0_{FC}, determined using $z = +2$.

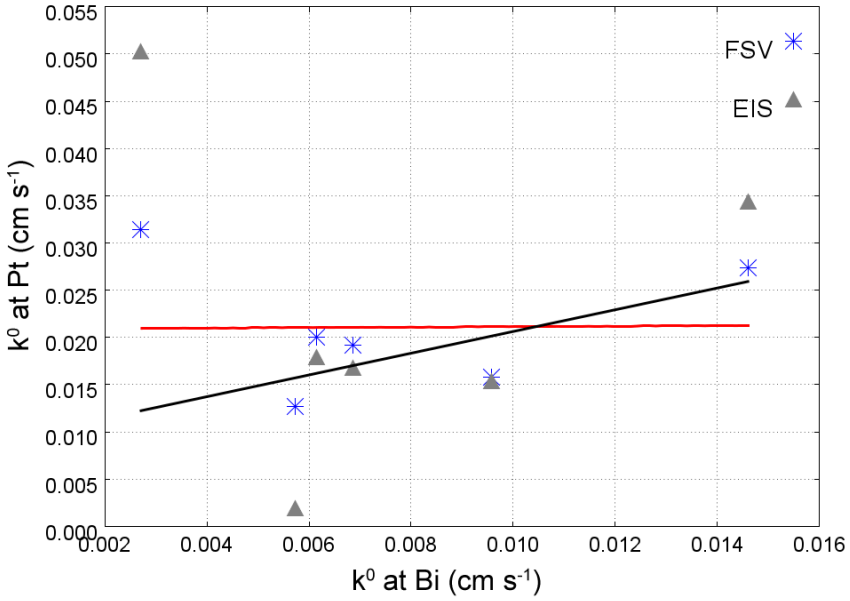

Figure 5.24: Frumkin corrected standard rate constants determined with $z = +1$ for k^0, of MV^{2+} and C1-5 measured at platinum using FSV and EIS plotted against those measured at bismuth using FSV. Two fit lines to the platinum FSV data are included in the plot. The red line is fitted using all of the data points. The black line is fitted after the data point corresponding to molecule C5 is disregarded.

Molecule	k^0_{FC} **at Pt (cm s^{-1})** measured by FSV	k^0_{FC} **at Pt (cm s^{-1})** measured by EIS	k^0_{FC} **at Bi (cm s^{-1})** measured by FSV
MV^{2+}	1.9×10^{-2}	1.7×10^{-2}	6.9×10^{-3}
C1	2.0×10^{-2}	1.8×10^{-2}	6.1×10^{-3}
C2	2.7×10^{-2}	3.4×10^{-2}	1.5×10^{-2}
C3	1.6×10^{-2}	1.5×10^{-2}	9.6×10^{-3}
C4	1.3×10^{-2}	1.9×10^{-3}	5.7×10^{-3}
C5	3.1×10^{-2}	5.0×10^{-2}	2.7×10^{-3}

Table 5.7: Frumkin corrected standard rate constants, k^0_{FC}, determined using $z = +1$.

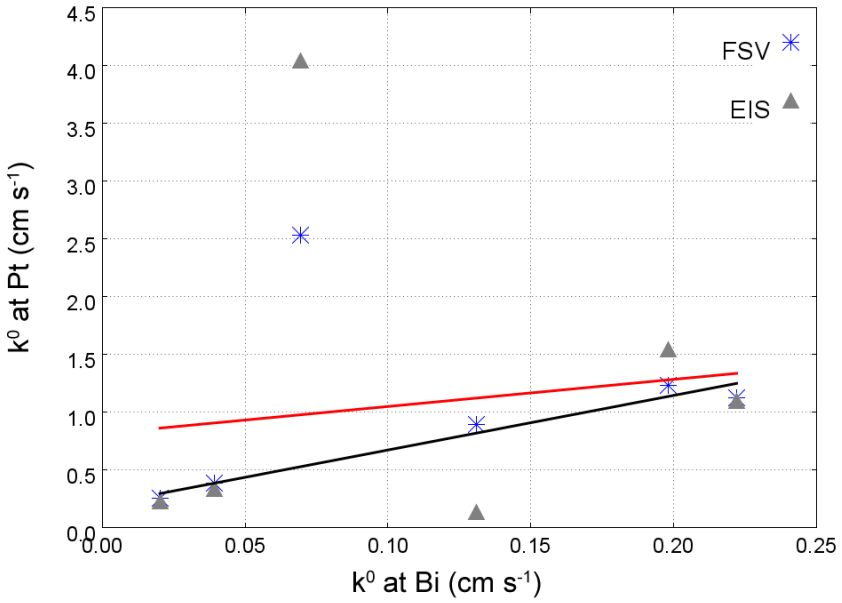

Figure 5.25: Frumkin corrected standard rate constants determined with $z = 0$ for k^0, of MV^{2+} and C1-5 measured at platinum using FSV and EIS plotted against those measured at bismuth using FSV. Two fit lines to the platinum FSV data are included in the plot. The red line is fitted using all of the data points. The black line is fitted after the data point corresponding to molecule C5 is disregarded.

Molecule	k^0_{FC} **at Pt (cm s^{-1})** measured by FSV	k^0_{FC} **at Pt (cm s^{-1})** measured by EIS	k^0_{FC} **at Bi (cm s^{-1})** measured by FSV
MV^{2+}	3.8×10^{-1}	3.3×10^{-1}	3.9×10^{-2}
C1	2.5×10^{-1}	2.3×10^{-1}	2.0×10^{-2}
C2	1.2×10^{0}	1.5×10^{0}	2.0×10^{-1}
C3	1.1×10^{0}	1.1×10^{0}	2.2×10^{-1}
C4	8.9×10^{-1}	1.3×10^{-1}	1.3×10^{-1}
C5	2.5×10^{0}	4.0×10^{0}	6.9×10^{-2}

Table 5.8: Frumkin corrected standard rate constants, k^0_{FC}, determined using $z = 0$.

5.6 Electron Transfer Rates at Platinum and Bismuth

It has been found by Lewis et. al. that the value of k^0_{FC} found at a metallic surface (k^0_m) can be related to that observed at a semi-metallic surface (k^0_{sm}) by means of Equation 5.26 which is based upon Fermi's golden rule.[2] The parameter D_m refers to the Fermi-level DOS of the metal, while $D_{sm}(-qE_{PZC})$ refers to the Fermi-level DOS at the semimetal after taking into account the filling of states that results from the application of a potential. The atomic densities of the metal and semimetal are denoted d_m and d_{sm} respectively. The reorganisation energy associated with the electron transfers at the metal and semi-metal surfaces are denoted λ_m and λ_{sm} respectively. The theory predicts that rates at two surfaces will be directly proportional and predicts a constant of proportionality based on the aforementioned parameters. Here we use the Frumkin corrected platinum and bismuth rate constants that have been determined in this chapter to test the ability of this theory to predict this constant of proportionality.

$$k^0_{sm} = k^0_m \frac{D_{sm}(-qE_{PZC})}{D_m} \left(\frac{d_m}{d_{sm}}\right)^{\frac{2}{3}} \times \left(\frac{\lambda_m}{\lambda_{sm}}\right)^{\frac{1}{2}} \exp\left(\frac{\lambda_m - \lambda_{sm}}{4k_BT}\right) \tag{5.26}$$

The Fermi-level DOS of platinum is 1.2×10^{23} cm^{-3} eV^{-1},[7–10] and it has an atomic density of 6.62×10^{22} atoms cm^{-3}. The atomic density of bismuth is 2.80×10^{22} atoms cm^{-3}. The appropriate bismuth

DOS is that of the surface, and a DOS range determined by STS studies (2.8×10^{21} to 2.8×10^{22} cm^{-3} eV^{-1},[11] see Section 4.7) will be used. Given the high DOS of the bismuth surface, the DOS is not expected to change significantly with applied potential. Given the metallic nature of the two surfaces,[1] the electrostatic contribution to the reorganization energy arising from image forces can be expected to be similar at Bi and Pt and therefore the reorganization energies at the two surfaces are expected to be equal.

Figure 5.26 shows the rates measured at platinum using FSV plotted against those determined at Bi. The grey line corresponds to the rate ratios predicted using the upper limit of the bismuth DOS determined by STS measurements. The red line is a linear fit to the data points. If the value used for the bismuth DOS is correct, Equation 5.26 successfully predicts the ratio of the rate constants to within an order of magnitude but the k^0 values determined at bismuth are roughly double what would be predicted. Given the high k^0 values measured at bismuth, it is clear that kinetic behaviour at bismuth is dominated by the properties of the surface and not the bulk of the material. According to Equation 5.26, the slope of the plot (0.75 ± 0.14) corresponds to a DOS of $9.1 \times 10^{22} \pm 1.4 \times 10^{22}$ cm^{-3} eV^{-1}.

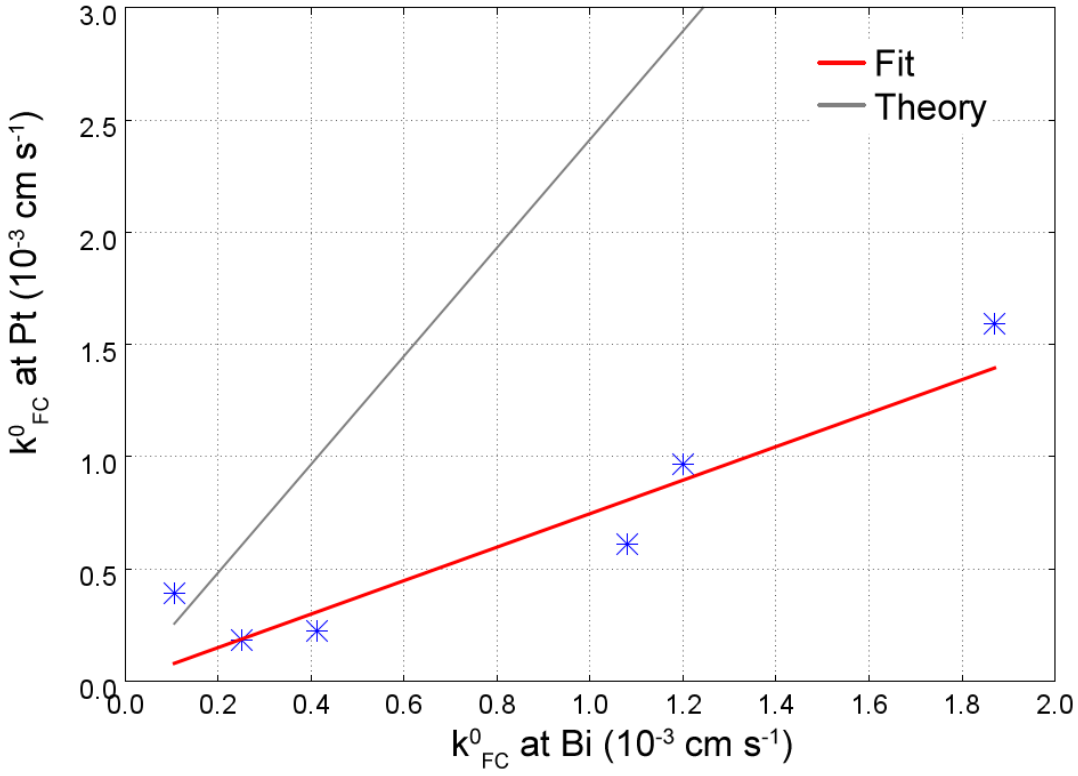

Figure 5.26: A plot of Frumkin corrected standard rate constants determined with z=+2 for MV^{2+} and C1-5 measured at platinum using FSV plotted against those measured at bismuth using FSV. The red line is a linear fit to the data and corresponds to a DOS of $9.1\times10^{22}\pm1.4\times10^{22}$ cm^{-3} eV^{-1} (determined using Equation 5.26). The grey line is the slope predicted by Equation 5.26 given a bismuth DOS value of 2.8×10^{22} cm^{-3} eV^{-1} which is the upper limit placed on the DOS according to STS measurements.

5.7 Electron Transfer Rates and Molecular Structure

Given the similarities of the molecules studied here, it was thought that trends in the standard rate constants of the molecules might be discovered by plotting these rate constants against parameters describing the molecules (see Section 3.2). It has been shown that when the Frumkin correction is applied to the data under the assumption that ion pairing effects are fully absent, the most meaningful comparison between Bi and Pt rate constants can be made. The same arguments apply to comparisons made between individual molecules and those same corrected constants will be employed here. Given the similarities in the values measured at both surfaces, and with both EIS and FSV, it is reasonable to employ all three data sets in these tests. Computation data from Section 3.2 are used to make the plots shown below.

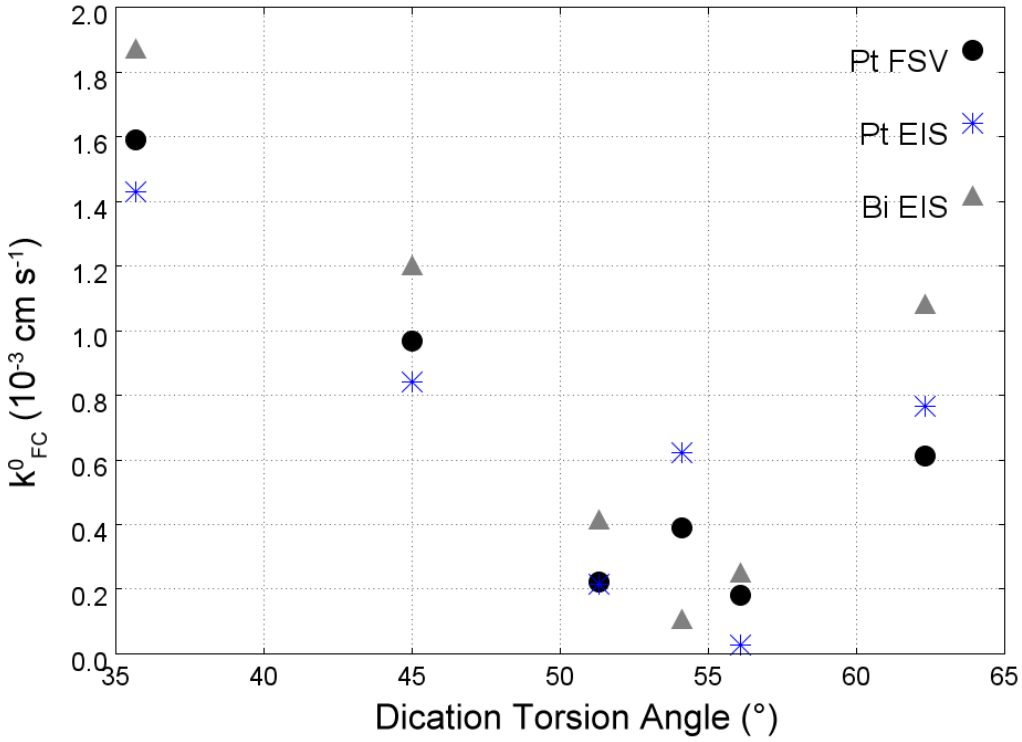

Figure 5.27: Rate constants determined at platinum and bismuth for MV^{2+} and C1-5 plotted against the torsion angle between the two aromatic rings of the dication.

5.7.1 Dication Torsion Angle

In Figure 5.27 determined k^0_{FC} values at platinum and bismuth are plotted against dication torsion angle. A rough trend in rate constants is observed, with a minimum located near 55°. A minimum at 90° would be explainable by considering the degree of conjugation between the two rings at each angle. At 90°, the level of conjugation is at its lowest and the stabilisation of the radical in the product at its lowest. There is no obvious theoretical explanation for a minimum in rate being observed at 55°. The downward trend is broken by molecule C2 which has a computed torsion angle of 62.3°. A rank correlation coefficient of -0.60 is observed between the values of k^0 at platinum measured by FSV, and the dication torsion angle.

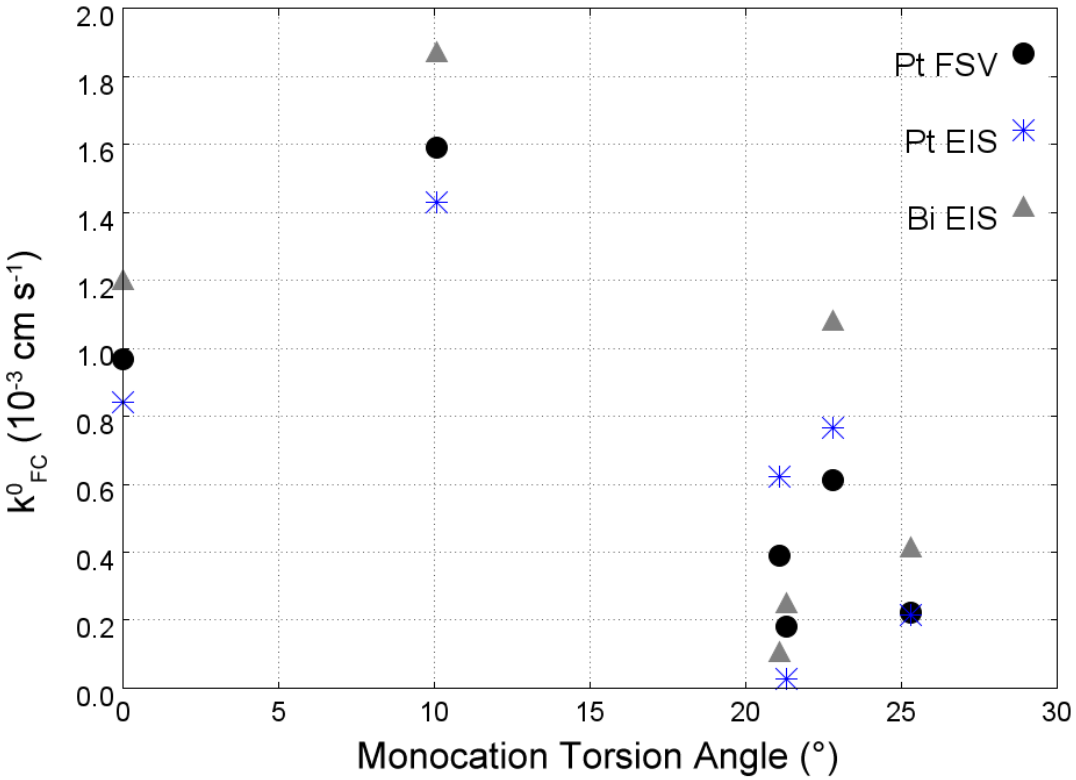

Figure 5.28: Rate constants determined at platinum and bismuth for MV^{2+} and C1-5 plotted against the torsion angle between the two aromatic rings of the monocation.

5.7.2 Monocation Torsion Angle

In Figure 5.28 the determined k^0_{FC} values at platinum and bismuth are plotted against the torsion angle of the monocations. Stabilisation of the radical in the product molecule is expected to be greatest for molecules with the lowest torsion angle. However, no obvious trends are seen in the plotted data. A rank correlation coefficient of -0.66 is observed between the values of k^0_{FC} at platinum measured by FSV, and the dication torsion angle.

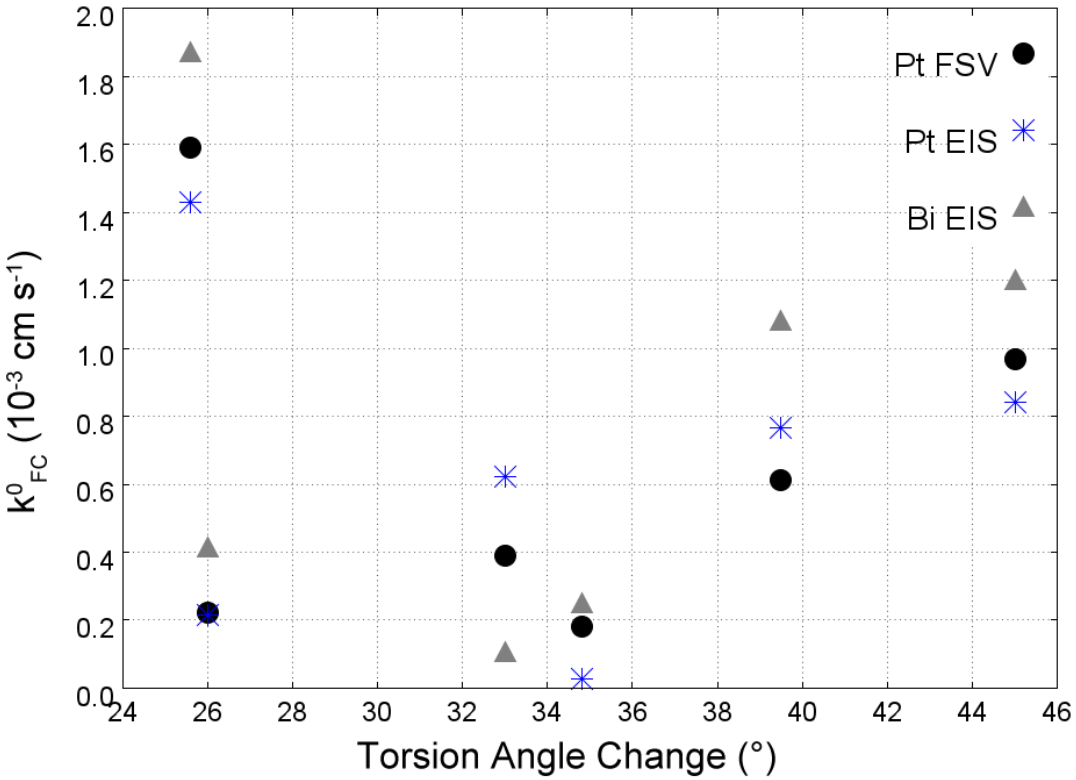

Figure 5.29: Rate constants determined at platinum and bismuth for MV^{2+} and C1-5 plotted against the difference in torsion angle between the dication and monocation forms.

5.7.3 Torsion Angle Change

In Figure 5.29 the determined k^0_{FC} values at platinum and bismuth are plotted against the change in torsion angle that occurs upon reduction. A major portion of the inner-sphere reorganisation energy associated with the reaction is expected to be in the changing of this angle, yet no obvious trends are seen in the plotted data. The total reorganisation may be much more dependent upon the outer-sphere reorganisation energy, or other factors may have a greater impact on the rate of the reaction. A rank correlation coefficient of -0.03 is observed between the values of k^0_{FC} at platinum measured by FSV, and the dication torsion angle.

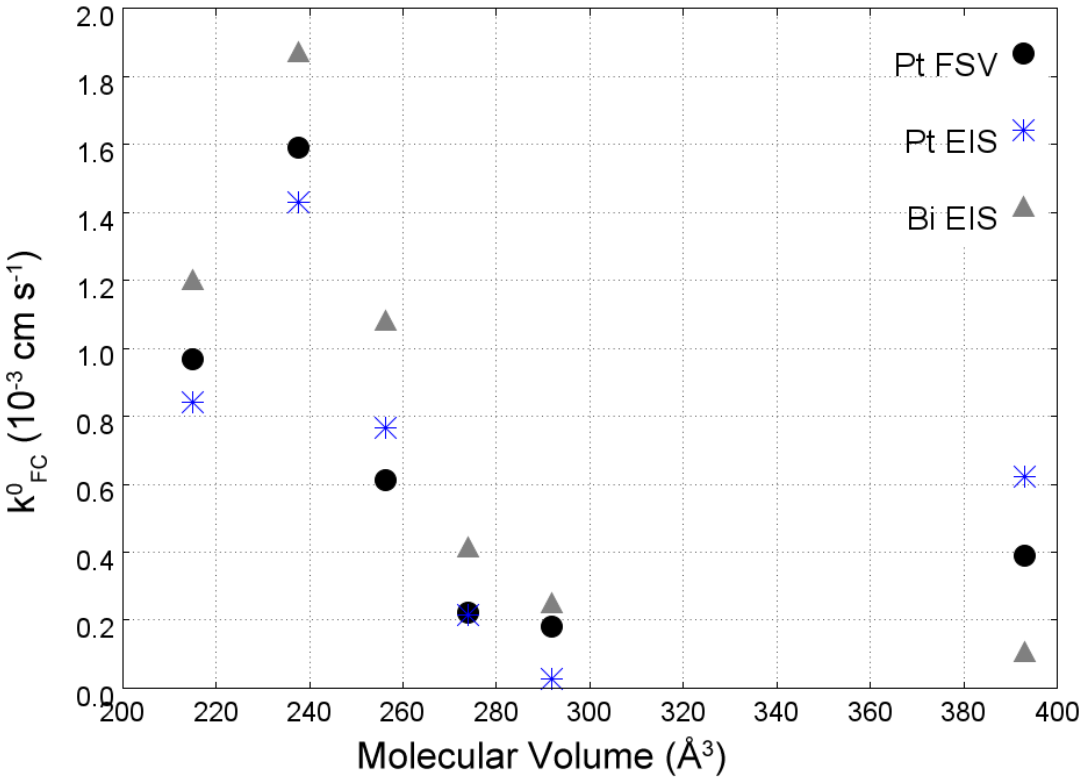

Figure 5.30: Rate constants determined at platinum and bismuth for MV^{2+} and C1-5 plotted against the molecular volume of the molecule.

5.7.4 Molecular Volume

In Figure 5.30 the determined k^0_{FC} values at platinum and bismuth are plotted against the molecular volumes. Disregarding MV^{2+}, a downward trend in rate constant with molecular volume is observed. A possible explanation for such a trend could be the restrictions on the orientation of the reactant imposed by the presence of the linking tether. The LUMO of the dications are localised upon the aromatic rings preventing electron transfer on to the tether. A possible reason for MV^{2+} not obeying this trend is that it does not have oxygen atoms bound to its aromatic ring systems. It may be that a difference in the electronic structure of the rings results and has a significant effect on

the standard rate constant. A rank correlation coefficient of -0.77 is observed between the values of k^0_{FC} at platinum measured by FSV, and the dication torsion angle. Given the relatively high correlation coefficient and the ability to explain this observation based on an orientation factor, it seems plausible that this parameter may have a significant effect on the k^0_{FC} of these derivatives. However, it is not possible to make any strong conclusions on the basis of the available data.

5.8 Conclusion

The standard rate constants for the reduction of MV^{2+} on platinum were measured using EIS, and at platinum and bismuth using FSV. For platinum, EIS are generally in good agreement with FSV data suggesting that these measurements are accurate. Upon Frumkin correction of the two sets of rate constants obtained by FSV using ϕ_2 values determined from capacitance data, a linear relationship is found between rates at platinum and bismuth. The correction works in this manner only when a charge of +2 is assumed for the molecules. It has been shown that k^0 for an electron transfer reaction at bismuth can be predicted based upon the value measured at platinum and vice versa. However a bismuth DOS of $9.1 \times 10^{22} \pm 1.4 \times 10^{22}$ cm^{-3} eV^{-1} is needed to explain the observed ratios of k^0. This DOS value higher than experimental measurements of the DOS suggest. Given the low DOS of the bismuth bulk, it is clearly the metallic surface of bismuth which controls kinetic behaviour at a bismuth electrode.

A possible relationship between the molecular volume of the molecules

studied here and their standard rate constants has been proposed, though a larger set of derivatives would be required to demonstrate this more conclusively. Some evidence of a dependence of the standard rate constant upon the torsion angle between the two aromatic rings in the dications has also been shown, though C2 does not fit this trend.

Bibliography

[1] P. Hofmann, *Progress in Surface Science*, 2006, **81**, 191–245.

[2] W. J. Royea, T. W. Hamann, B. S. Brunschwig and N. S. Lewis, *The Journal of Physical Chemistry B*, 2006, **110**, 19433–19442.

[3] K. Aoki, *Electroanalysis*, 1993, **5**, 627–639.

[4] C. P. Andrieux, P. Hapiot and J. M. Saveant, *Chemical Reviews*, 1990, **90**, 723–738.

[5] A. J. Bard and L. Faulkner, *Electrochemical Methods: Fundamentals and Applications*, John Wiley & Sons, 2nd edn., 2001.

[6] J. Savéant and D. Tessier, *Journal of Electroanalytical Chemistry and Interfacial Electrochemistry*, 1975, **65**, 57–66.

[7] F. Y. Fradin, D. D. Koelling, A. J. Freeman and T. J. Watson-Yang, *Physical Review B*, 1975, **12**, 5570–5574.

[8] J. van der Klink and H. Brom, *Progress in Nuclear Magnetic Resonance Spectroscopy*, 2000, **36**, 89–201.

[9] M. Weinert and A. J. Freeman, *Physical Review B*, 1983, **28**, 6262–6269.

[10] A. H. MacDonald, J. M. Daams, S. H. Vosko and D. D. Koelling, *Physical Review B*, 1981, **23**, 6377–6398.

[11] A. Ofitserov and V. Edelman, *Physica B: Condensed Matter*, 2003, **329-333, Part 2**, 1094–1095.

Chapter 6

Photoelectrochemical Kinetics of Silicon Monolayers

6.1 Aim

The electron transfer reaction taking place between a ferrocene group and a silicon surface to which it is bound was examined in a series of silicon monolayers. After varying the carbon chain binding the ferrocene to the silicon, and the dilution of the ferrocene using alkyl chains, the resulting effect upon the electron transfer reaction was examined. It was thought that the relative electron transfer rates could possibly be explained in terms of linker conductivity and ferrocene dilution.

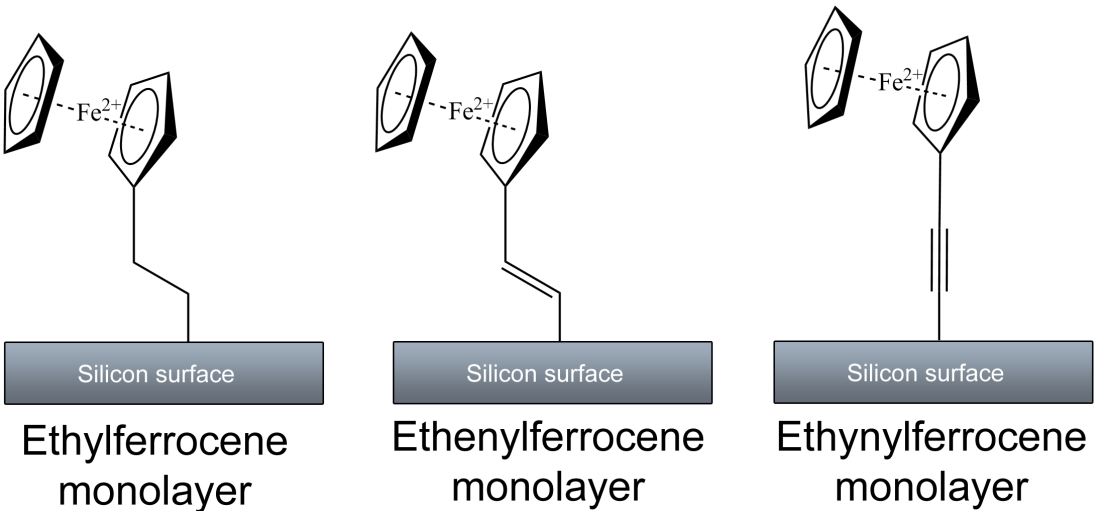

Figure 6.1: Ferrocene monolayers upon n-type silicon surfaces. The bond to the surface is a Si-C bond. Surface concentrations, as determined in aqueous solution, are given in Table 6.2.

6.2 Monolayers

A series of monolayers were produced upon silicon for electrochemical study. These monolayers were all prepared and characterised by Mufida Abdualla (Chemical Nanoscience Laboratory, Newcastle University) and their preparation is detailed in Section 2.1.

6.2.1 Pure Monolayers

Three ferrocene group containing silicon monolayers were prepared and are depicted in Figure 6.1.

A monolayer containing only undecyl chains was also prepared for use as a control.

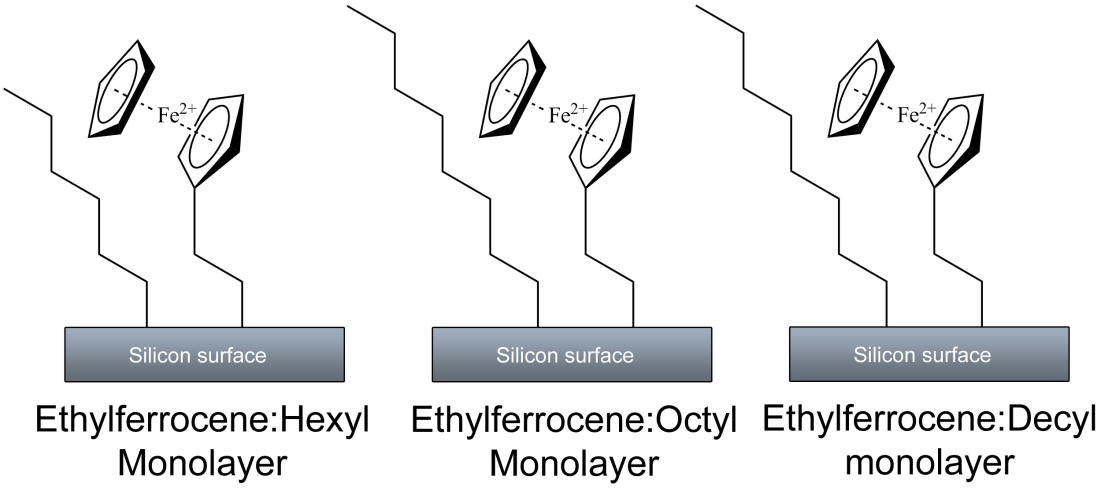

Figure 6.2: Ferrocene mixed monolayers upon n-type silicon surfaces. The bond to the surface is a Si-C bond. Ethylferrocene surface concentrations, as determined in aqueous solution, are given in Table 6.2. Surface concentrations of alkyl chains and their positions relative to ethylferrocene are unknown.

6.2.2 Mixed Monolayers

A series of monolayers containing both ethylferrocene and an inert alkyl chain were prepared and are depicted in Figure 6.2. All three monolayers were prepared with the ferrocene group and the alkyl groups in equal concentration in solution during formation of the monolayers. These monolayers will be referred to using the monolayer name followed by "50:50", e.g. "ethylferrocene:hexyl 50:50". The ethylferrocene:octyl and ethylferrocene:decyl monolayers were also prepared with ferrocene groups and alkyl groups at a ratio of 1:99, and these monolayers will be referred to using the suffix "1:99". This gives a total of 5 mixed monolayers.

Monolayer	Fe-Si separation distance (nm)
Ethylferrocene	0.5628
Ethenylferrocene	0.5773
Ethynylferrocene	0.5911

Table 6.1: Intramolecular distances between Fe and Si in optimised geometries of molecular cluster models calculated using the B3LYP functional, 6-31G* basis set and pseudopotentials as implemented in Spartan 04 (Wavefunction Inc, CA, USA).

6.3 Molecular Modelling

Optimised geometries of molecular cluster models for ethylferrocene, ethenylferrocene and ethynylferrocene on silicon were calculated using the B3LYP functional, 6-31G* basis set and pseudopotentials as implemented in Spartan 04 (Wavefunction Inc, CA, USA). The calculated distances between the central iron atom of the ferrocene moiety and the silicon atom to which the alkylferrocene is bound are tabulated in Table 6.1. This distance is of interest as it may control the rate of electron transfer, and it also may determine how easily the silicon surface near the ferrocene group is oxidised and hydrolysed. The optimised structures are shown in Figure 6.3.

6.4 Monolayer Characterisation

Monolayer characterisation was performed via atomic force microscopy, infrared spectroscopy and x-ray photoelectron spectroscopy by Mufida Abdualla (Chemical Nanoscience Laboratory, Newcastle University).

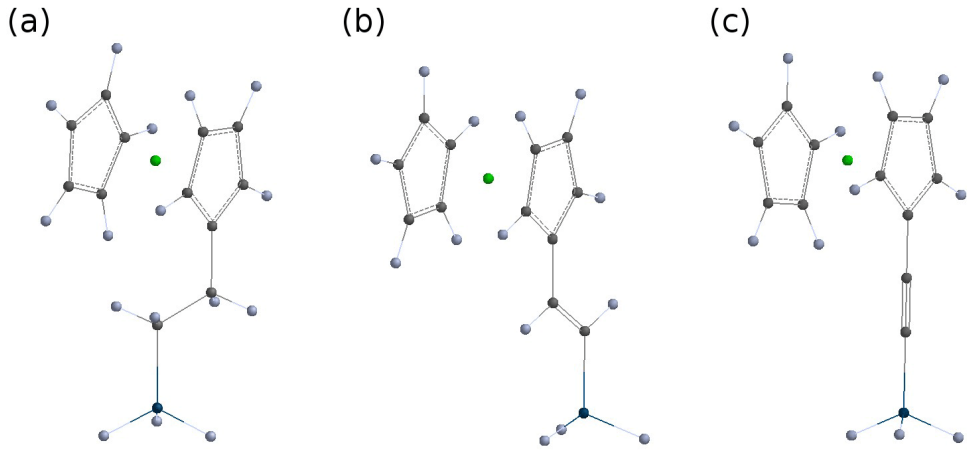

Figure 6.3: Optimised molecular cluster models for ethylferrocene/Si (a), ethenylferrocene/Si (b) and ethenylferrocene/Si (c) as calculated using the B3LYP functional, 6-31G* basis set and pseudopotentials as implemented in Spartan 04 (Wavefunction Inc, CA, USA).

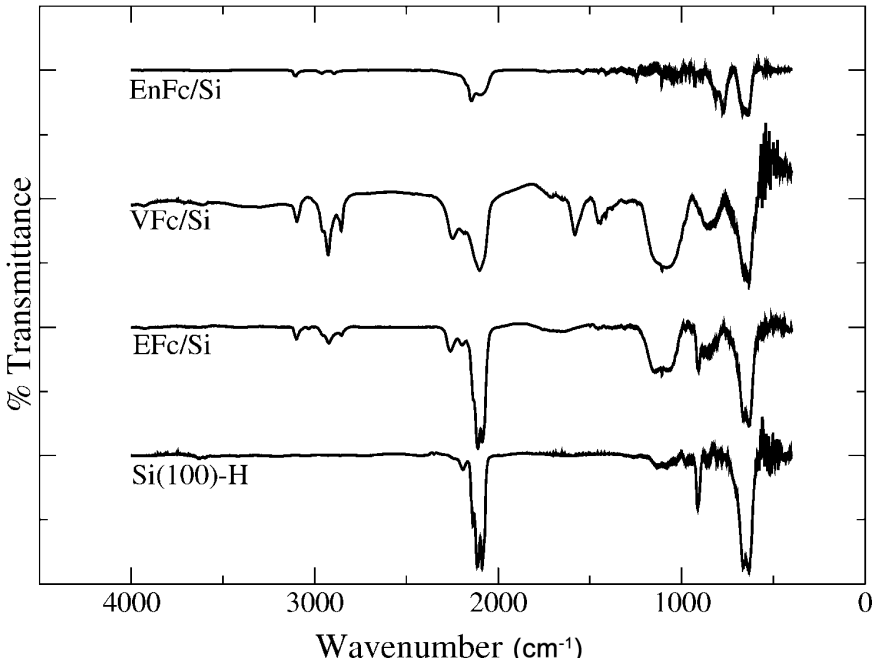

Figure 6.4: Transmission FTIR spectra of porous Si (Si(100)-H), ethylferrocenyl-porous Si (EFc/Si), ethenylferrocenyl-porous Si (VFc/Si) and ethynylferrocenyl-porous Si (EnFc/Si). Figure courtesy of Mufida Abdualla (Chemical Nanoscience Laboratory, Newcastle University).

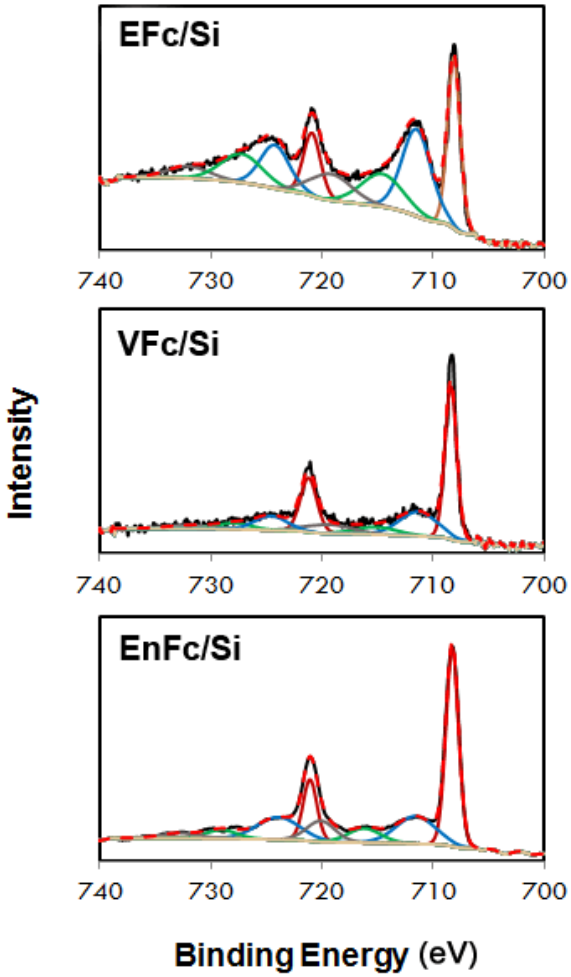

Figure 6.5: XPS spectra in the Fe 2p region for ethylferrocene (EFc/Si), ethenylferrocene (VFc/Si), and ethynylferrocene (EnFc/Si). Experimental spectra are shown as a black line, the fit is shown in red dashes and separate components of the fit are shown in colour. Figure courtesy of Mufida Abdualla (Chemical Nanoscience Laboratory, Newcastle University).

Fourier transform infrared (FTIR) spectra of the three pure monolayers on porous silicon, and the spectra of unmodified porous silicon are shown in Figure 6.4. Porous silicon was used to ensure the maximum signal to noise ratio. Strong bands at 2088, 2112 and 2140 cm^{-1} are caused by the presence of Si-H, SiH_2 and SiH_3 surface species. Also present are a strong band at 915 cm^{-1} due to the Si-H_2 scissor mode and 660 cm^{-1} due to Si-H bending. The Si-H stretches in the spectra become less intense following alkylation and less structured due to heterogeneous broadening.[1] The spectra of the modified silicon surfaces show aromatic C-H stretches, indicating that ferrocene groups are present upon the surfaces. The chemisorption of ethylferrocene can be confirmed due to the absence of the C=C stretching mode at 1632 cm^{-1}. In the spectrum of the ethenylferrocene, a peak at 1581 cm^{-1} can be attributed to the presence of a Si-C=C mode.[2,3] A peak at 2140 cm^{-1} is characteristic of Si-C≡C alkynyl-linked-monolayers.[4] Chemisorption of ethenylferrocene and ethynylferrocene is confirmed by the absence of an alkylnyl terminal $v(\equiv CH)$ peak around 3328 cm^{-1}.[2,5]

Photoemission spectra of the three pure monolayers on silicon, and the spectra of unmodified silicon are shown in Figure 6.5. The presence of ferrocene in these monolayers is confirmed by the presence of Fe(II) singlet components near 708 and 724 eV. Also present are Fe(III) singlet components near 711 and 724 eV and a peak at 714.9(5) eV which is a Fe(III) shake-up satellite peak. This Fe(III) is likely to be generated by oxidation of Fe(II) by trace oxygen.[6] The recorded spectra are generally in good agreement with previous reports of photoemission data for ferrocene monolayers[6–8]

6.5 Cyclic Voltammetry

The monolayers were studied using cyclic voltammetry with the silicon working electrode arrangement, and light source, described in Section 2.1. Aqueous electrolyte solutions of KCl (0.1M) were employed, with Pt wire serving as a counter electrode. All potentials were recorded against a solid state Ag/AgCl wire reference. Water was employed as the solvent because the O-ring used in the silicon electrode cell (see Section 2.1) was found to provide a poor seal against acetonitrile but performed well in water. The recording of CV data was performed with the assistance of Mufida Abdualla (Chemical Nanoscience Laboratory, Newcastle University).

CVs of the undecyl monolayer are shown in Figure 6.6. When the potential of this surface is scanned positive of +0.2V, the current increases rapidly. This current is likely to be caused by oxidation of surface Si-H and occurs to a greater extent under illumination. This process limits the operational potential window during photoelectrochemical experiments. A reversible wave is observed near −0.2V with a standard potential that shifts negative by roughly 100 mV upon illumination. The peak is small and likely the result of a silicon surface state being populated/depopulated.

CVs of the ethylferrocene monolayer recorded in light and dark conditions are displayed in Figure 6.7. Under illumination the standard potential of this wave is seen at −142 mV and no significant separation is observed between the forward and reverse waves. This wave can be attributed to the oxidation of surface bound ferrocene (see Section 1.7). In the dark, the oxidation reaction occurs to some extent but with a greater overpotential and peak separation.

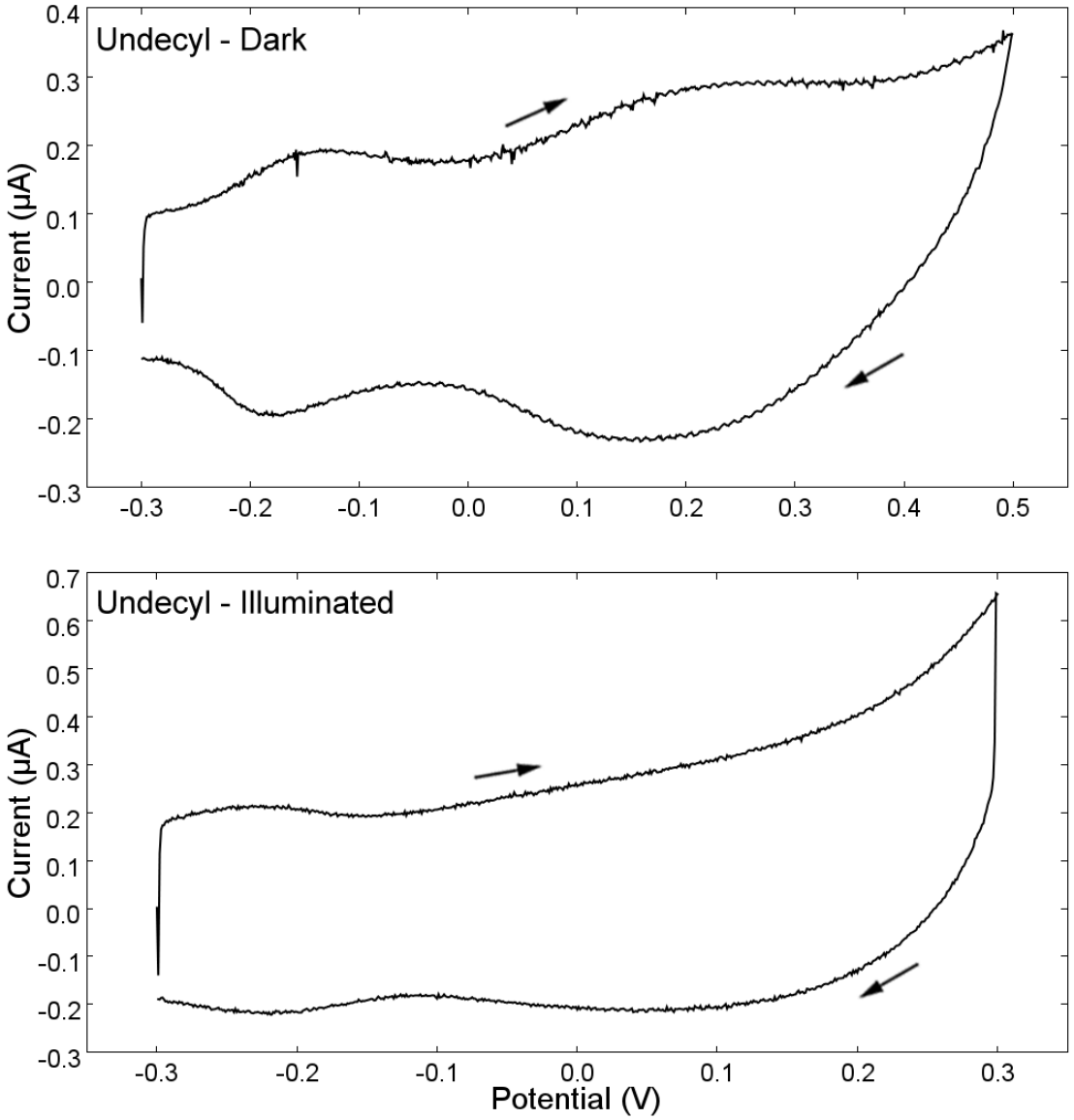

Figure 6.6: CVs recorded with a scan rate of 1 V s^{-1} using a modified silicon surfaces as the working electrode. The silicon electrode was immersed in water containing KCl (0.1M). The arrows indicate the scan direction. A small reversible wave occurs near -0.2 V. Large currents believed to be caused by silicon oxidation are observed at positive potentials under illumination.

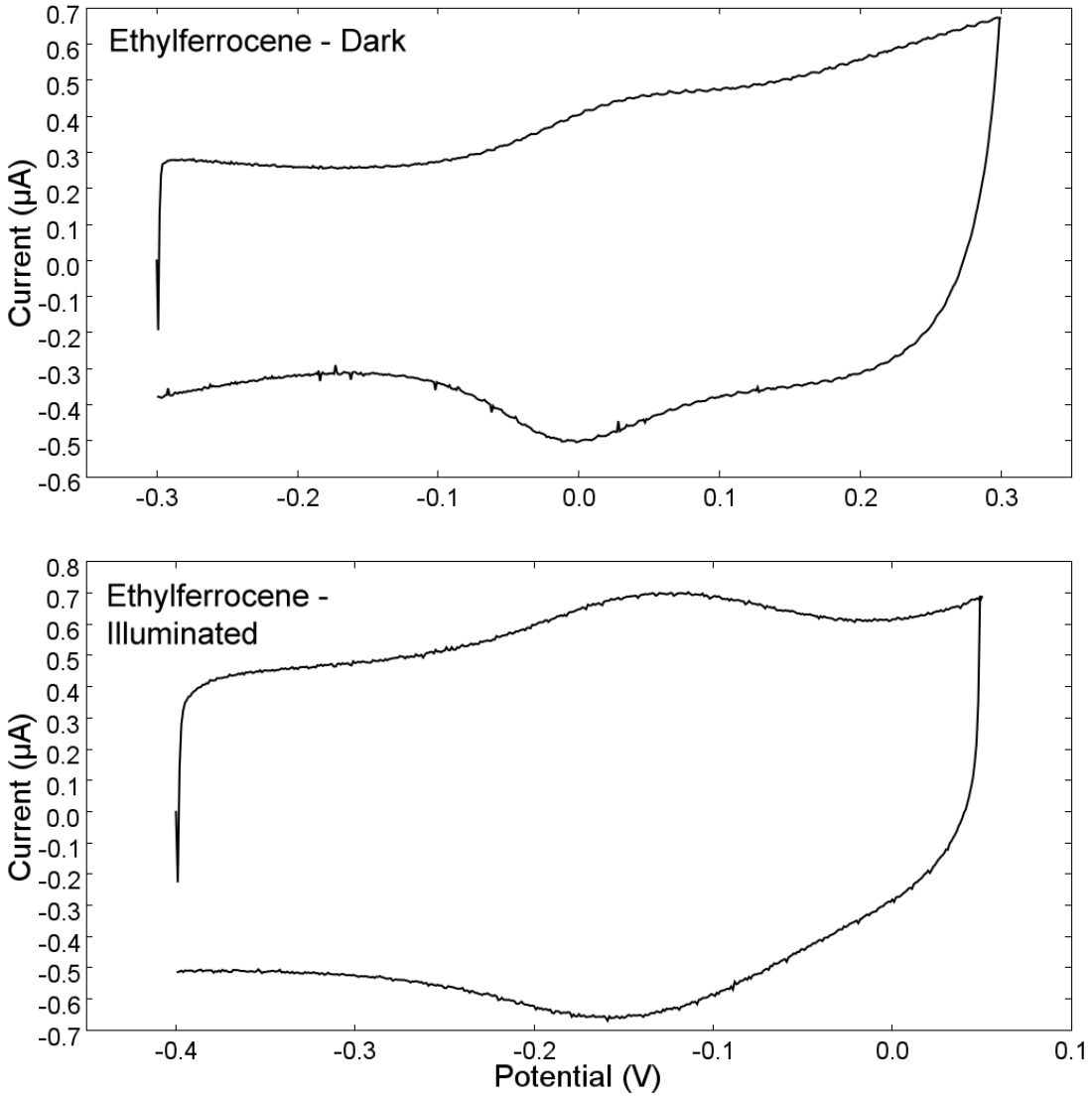

Figure 6.7: CVs recorded with a scan rate of 1 V s^{-1} using a modified silicon surfaces as the working electrode. The silicon electrode was immersed in water containing KCl (0.1M). The arrows indicate the scan direction. Reversible waves are observed in both cases, however a more positive standard potential is observed in dark conditions.

CVs of illuminated ethenylferrocene and ethynylferrocene monolayers are displayed in Figure 6.8. The ethenylferrocene monolayer shows a reversible wave similar to that of the ethylferrocene monolayer. However, the oxidation of ferrocene in the ethynylferrocene monolayer was found to be irreversible and the monolayer unstable in water when a positive potential was applied.

CVs of the mixed monolayer surfaces under illumination are displayed in Figure 6.9. These CVs all show reversible waves but in each case some degree of peak distortion is seen. The most obvious distortion observed is a flattening of the forward wave for each surface. In the case of the ethylferrocene:hexyl 50:50 monolayer a flattening of the reverse wave is also observed. Possible causes of these distortions will be suggested in the discussion section below.

CVs of monolayers containing diluted amounts of ferrocene under illumination are displayed in Figure 6.10. A significant shift in the standard potential of the ferrocene/ferrocenium couple in the mixed decyl monolayer is observed.

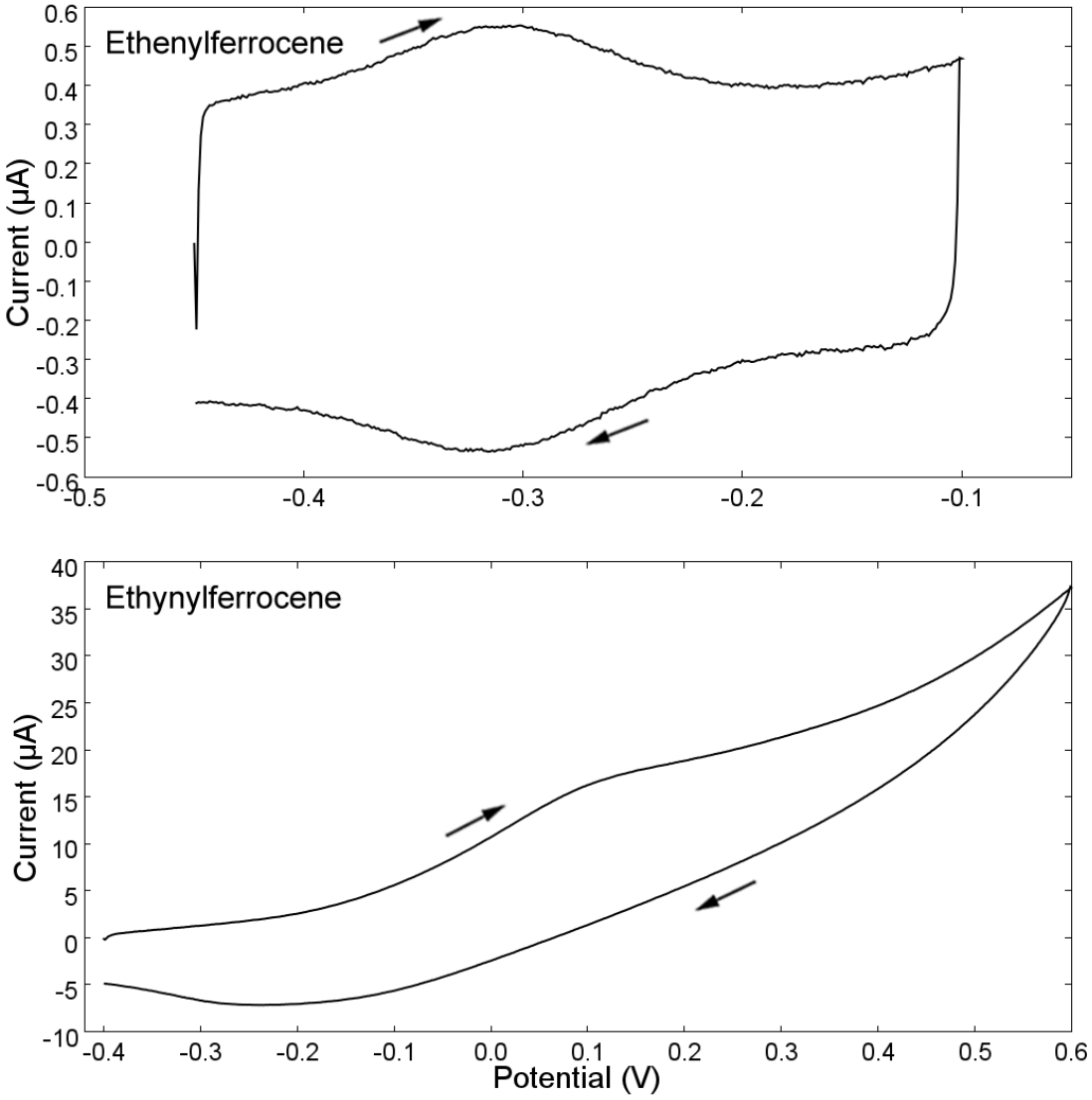

Figure 6.8: CVs recorded with a scan rate of 1 V s^{-1} using a modified silicon surfaces as the working electrode. The silicon electrode was immersed in water containing KCl (0.1M). The arrows indicate the scan direction. Electrode surfaces were illuminated during the recording of the voltammograms. A reversible wave is observed for the ferrocene/ferrocenium redox couple for the ethenylferrocene monolayer, but the ethynylferrocene shows a wave corresponding to the oxidation reaction only.

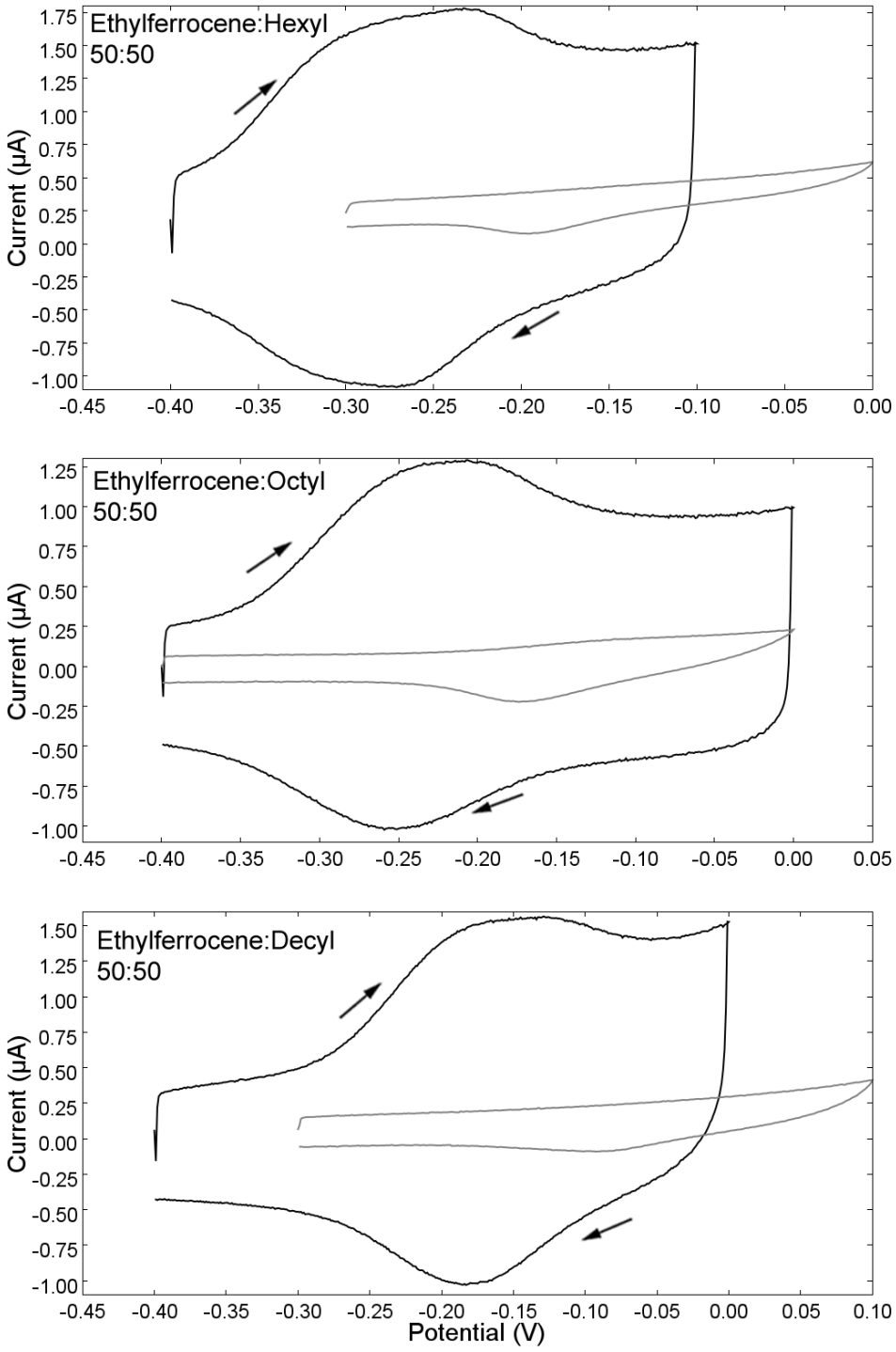

Figure 6.9: CVs recorded at a scan rate of 1 V s^{-1} under illumination using modified silicon surfaces as working electrodes (black lines). Recorded in water containing KCl (0.1M). Reversible waves are observed for the ferrocene/ferrocenium redox couple and some clear distortion of the peaks is seen in each case. Also shown are CVs recorded at 500 mV s^{-1} in the dark (grey lines).

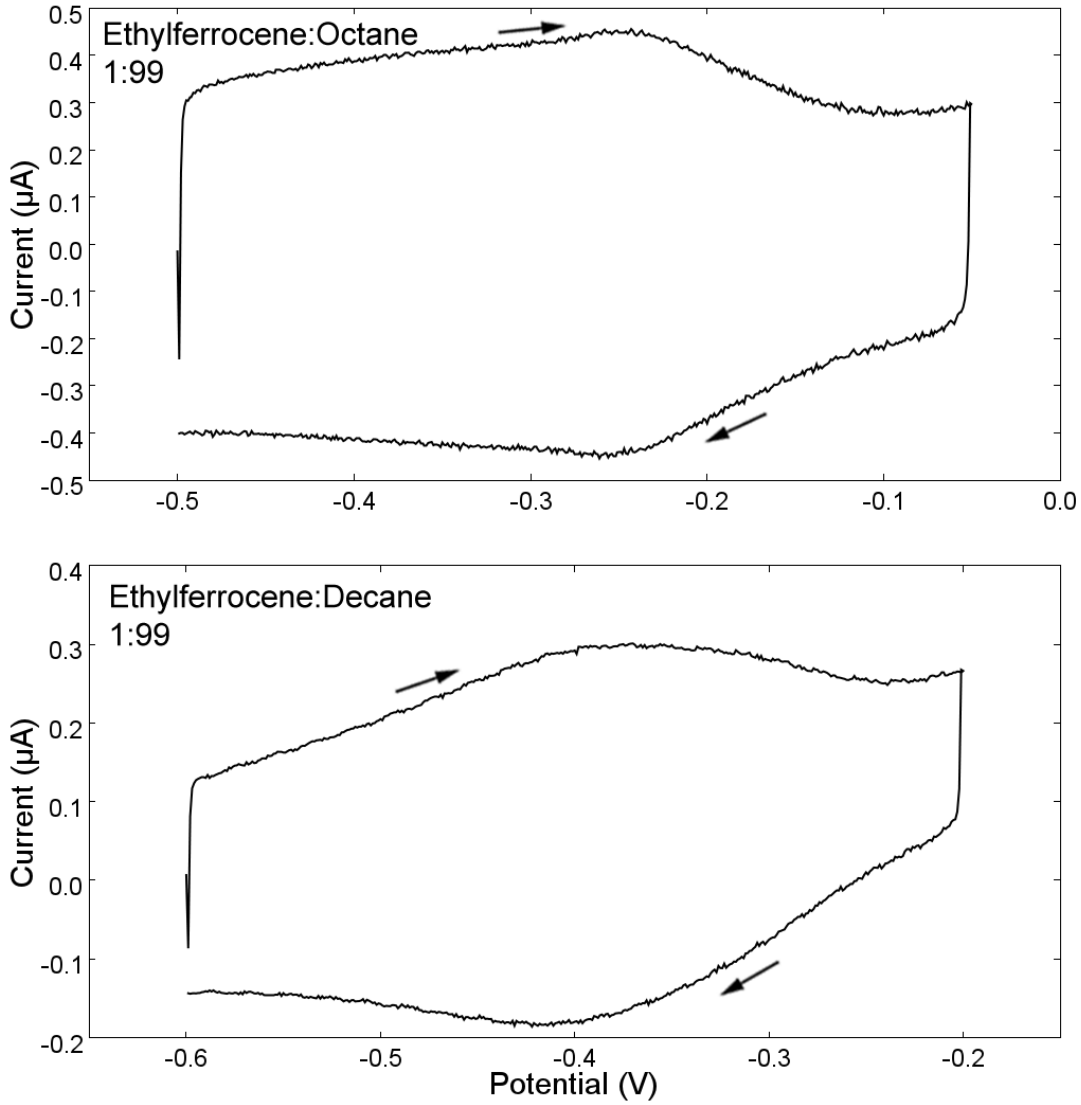

Figure 6.10: CVs recorded at a scan rate of 1 V s^{-1} using modified silicon surfaces as working electrodes. The silicon electrodes were immersed in water containing KCl (0.1M) and their surfaces illuminated during the recording of the voltammograms. Reversible waves are observed in both cases.

Monolayer	Surface ferrocene concentration (pmol cm^{-2})	$E^{0'}$ (mV)
Ethylferrocene	1.8	−142
Ethenylferrocene	1.9	−317
Ethylferrocene:Hexyl 50:50	10.4	−260[a]
Ethylferrocene:Octyl 50:50	9.5	−235
Ethylferrocene:Decyl 50:50	15.7 [c]	−184[b]
Ethylferrocene:Octyl 1:99	2.0	−252
Ethylferrocene:Decyl 1:99	2.0	−401

Table 6.2: The surface concentration of ferrocene in each monolayer and the standard potential of the ferrocene/ferrocenium redox couple determined via CV in water with 0.1M KCl. [a] This is a rough estimate due to the highly distorted waves in the CV. [b] Only the forward wave was used due to the high distortion of the reverse wave. [c] The distorted shape of the CV and the onset of silicon oxidation near $E^{0'}$ for this monolayer mean that this value is possibly inaccurate.

These voltammograms were used to determine the standard potential for each ferrocene/ferrocenium redox couple and these values are given in Table 6.2. Surface coverages were also determined by integration of the oxidation peak in each CV. To find peak areas numerical integration was used after a linear background current was assumed and subtracted. Surface coverages are also tabulated in Table 6.2. The observed surface coverages are discussed below in Section 6.8.

The shape of an ideal surface wave in a voltammogram can be described by Equation 6.1.[9]

$$i(E) = \frac{K \exp[\theta]}{(1 + \exp[\theta])^2} \tag{6.1}$$

The quantity θ is the dimensionless potential given by Equation 6.2 and K is a constant, with dependence on scan rate (v) and surface concentration (Γ), given by Equation 6.3.

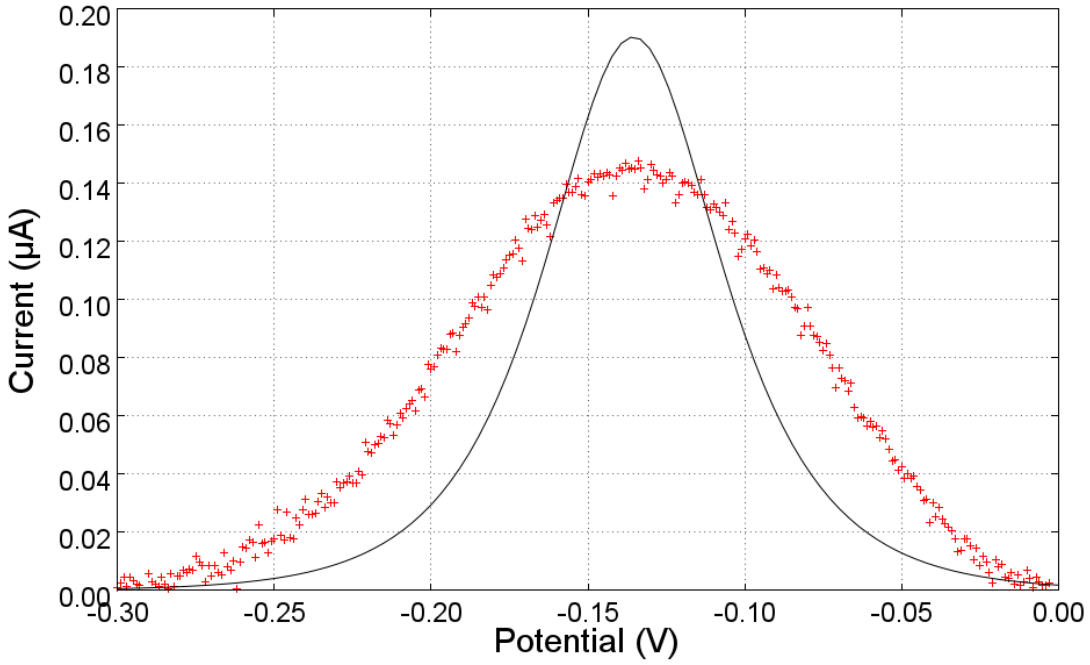

Figure 6.11: Equation 6.1 fitted to the forward wave of the ethylferrocene monolayer CV after background subtraction.

$$\theta = \frac{F(E - E^{0'})}{RT} \tag{6.2}$$

$$K = \frac{n^2 F^2}{RT} v A \Gamma \tag{6.3}$$

An attempt to fit Equation 6.1 to the ethylferrocene voltammogram after background subtraction is shown in Figure 6.11. The values of K and $E^{0'}$ were floated to produce the fit. Clearly, the observed surface wave is far from ideal and the poor quality of the fit means that the determined value of K (0.38 ± 0.01A) is physically meaningless. Such non-ideal waves are often the result of the activity coefficients of the reduced and oxidised forms of the redox active species not being equal. A possible cause is a change in the free energy of surface

bound species resulting from the close proximity of charged species produced by the reaction. In this case, the oxidation of ferrocene produces positively charged ferrocenium. Ferrocene oxidation can be expected to require more energy in the presence of ferrocenium due to the energy associated with placing two positive charges in close proximity.

Non-ideal wave shapes observed in cyclic voltammetry can be modelled using parameter based isotherms[10] or using statistical mechanical treatments.[11,12] However, the application of these models is challenging as they require some knowledge of the degree to which solvent molecules penetrate the monolayer, and the location of counter ions. Instead, a means of estimating the ratio of the activity coefficients of the reduced and oxidised forms of the redox active species is proposed.

The behaviour of these non-ideal waves can be described by a form of the Nernst equation, Equation 6.4, which takes into account differences in the activity of the ferrocene and ferrocenium.[9] The parameters Γ_O and Γ_R denote the surface concentrations of the oxidised species (ferrocenium) and the reduced species (ferrocene) respectively. Their activities are given by γ_O and γ_R.

$$E = E^{0'} + \frac{RT}{nF} \ln \left(\frac{\gamma_O \Gamma_O}{\gamma_R \Gamma_R} \right) \tag{6.4}$$

By taking the definition of θ given by Equation 6.2 and defining $\Gamma = \Gamma_R + \Gamma_O$, Equation 6.4 can be rearranged to give Equation 6.5.

$$e^{\theta} = \frac{\gamma_O \Gamma_O}{\gamma_R(\Gamma - \Gamma_O)} \tag{6.5}$$

This can be expressed in terms of γ_O/γ_R as in Equation 6.6.

$$\frac{\gamma_O}{\gamma_R} = e^{\theta}\frac{\Gamma - \Gamma_O}{\Gamma_O} \tag{6.6}$$

To determine the ratio of the activity coefficients from a CV, we note that $\Gamma_O = 0$ when the CV is started at a sufficiently negative potential, and that the charge that must pass to generate a given Γ_0 is given by Equation 6.7.

$$Q = nFA\Gamma_O \tag{6.7}$$

If a charge Q_0 must pass to oxidise all of Γ_R, then using Equation 6.7, Equation 6.6 can be expressed as Equation 6.8.

$$\frac{\gamma_O}{\gamma_R} = e^{\theta}\frac{Q_0 - Q}{Q} \tag{6.8}$$

For a given potential, Q can be found by numerical integration of the CV current with respect to time up to that point. Integration of the entire surface wave gives Q_O. Plots of $\ln(\gamma_O/\gamma_R)$ determined by this method plotted against potential for each CV are shown in figures 6.12 to 6.18. Prior to analysis the background was subtracted from each CV under the assumption that the background current was linear. Note that as $Q \to 0$, $\gamma_O/\gamma_R \to \infty$, and as $Q \to Q_0$, $\gamma_O/\gamma_R \to 0$.

This limits the potential range over which the analysis is useful, and causes the calculated ratio at the edge of the redox waves to be invalid. On the plots this appears as a sudden downturn in γ_O/γ_R to the left of the plot, and a sudden upturn on the right of the plot. Note that an incorrect determination of $E^{0'}$ would result in incorrect values of γ_O/γ_R, but would not affect the gradient of the plot when this ratio is plotted against the applied potential.

For an ideal surface wave, $\ln(\gamma_O/\gamma_R) = 0$. For the surfaces examined here, the general trend is that when $E < E^{0'}$, $\ln(\gamma_O/\gamma_R) < 0$. This corresponds to the net interactions between redox active species being attractive. However, $\ln(\gamma_O/\gamma_R)$ increases as potential is made more positive, and when $E > E^{0'}$, $\ln(\gamma_O/\gamma_R) > 0$, indicating that repulsive interactions dominate.

If repulsive interactions between neighbouring ferrocenium groups was responsible for the non-ideal shape of the voltammograms, then the slope of the activity coefficient ratio plots would be expected to show some dependence on the surface concentration of ferrocene. However, no such relationship is seen. Another possibility is that the surface ferrocene exists in a range of environments in each monolayer, which this heterogeneity giving rise to the non-ideal CV behaviour. In the case of the 50:50 mixed monolayers, a decrease in the slope of the plot can be seen when the potential is scanned +25 mV versus $E^{0'}$. This decrease in the slope is difficult to explain in terms of repulsive ferrocenium interactions and appears to be another effect of monolayer heterogeneity.

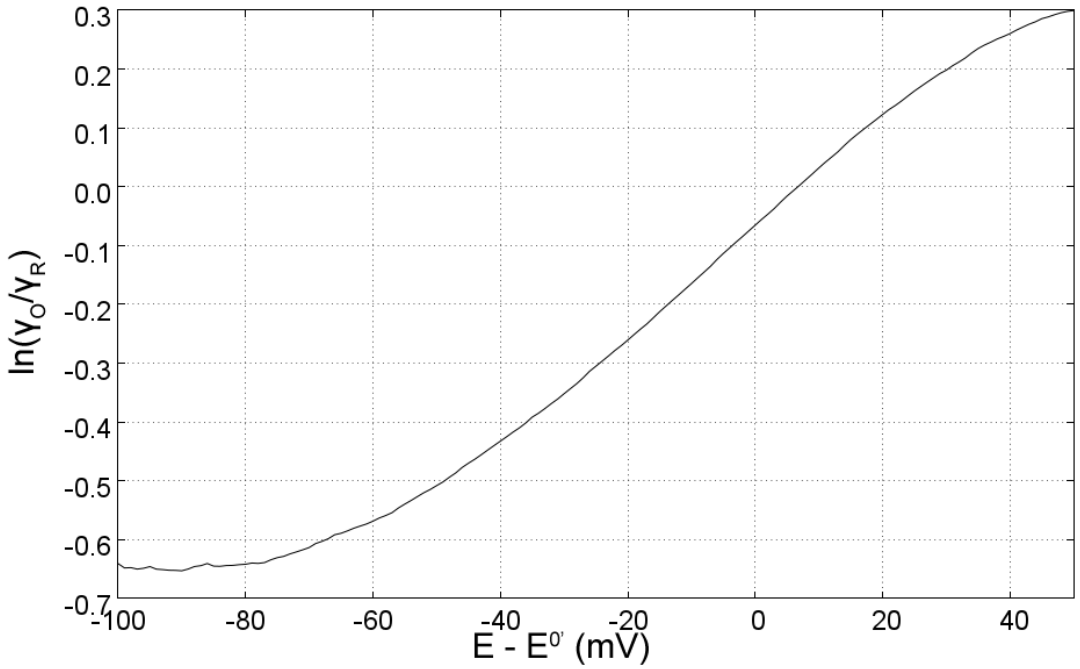

Figure 6.12: The activity coefficient ratio determined using the forward wave of a background subtracted ethylferrocene monolayer CV.

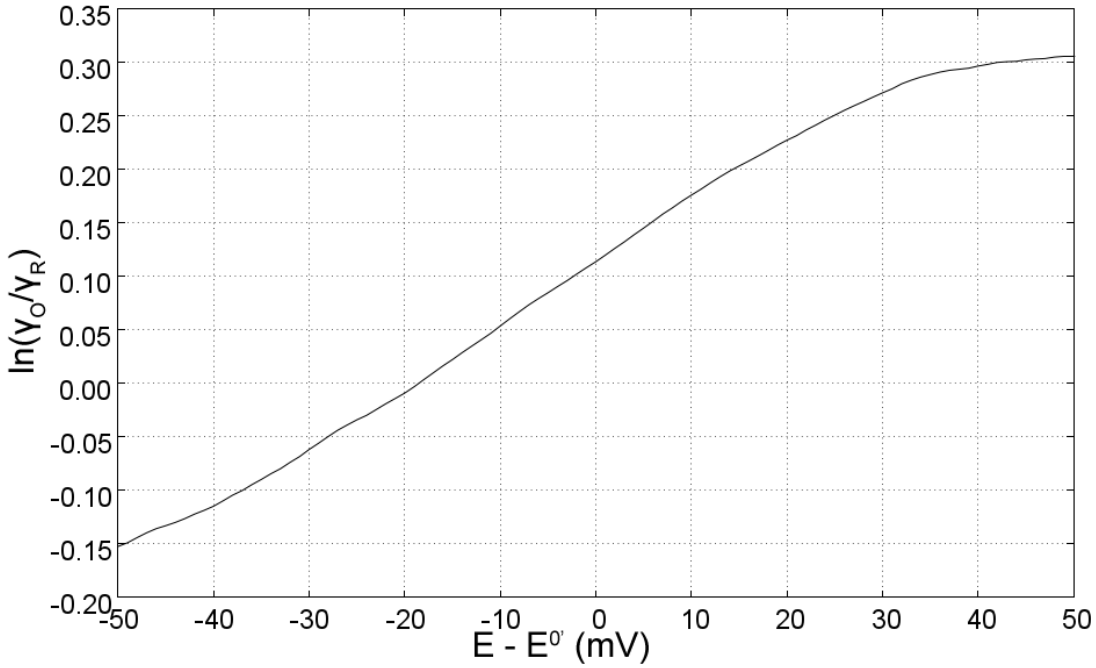

Figure 6.13: The activity coefficient ratio determined using the forward wave of a background subtracted ethenylferrocene monolayer CV.

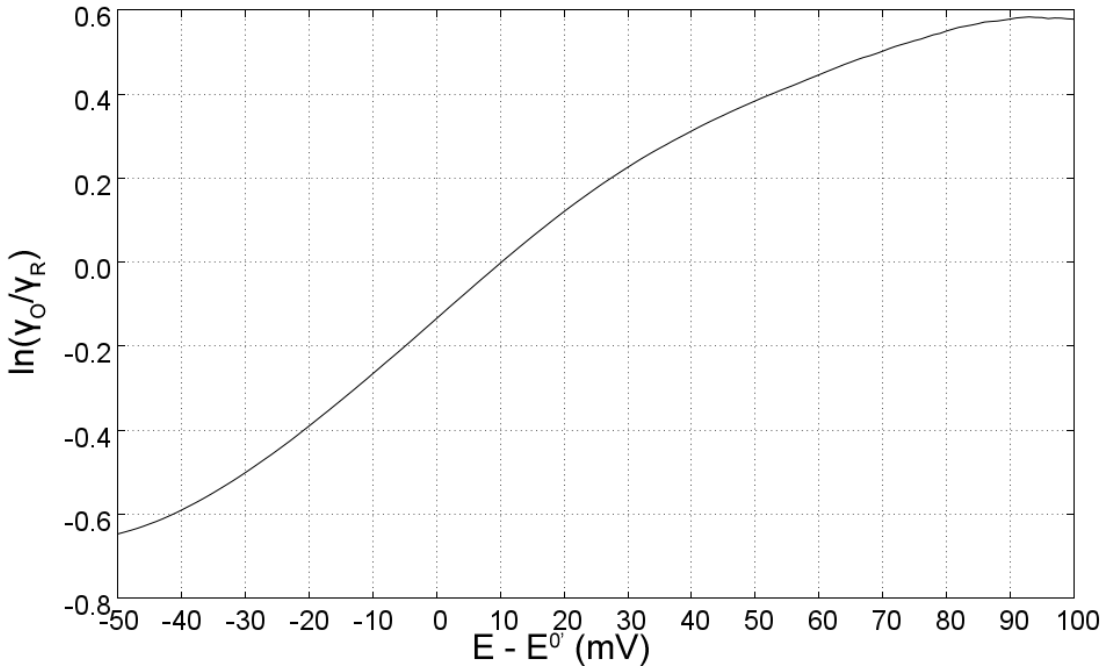

Figure 6.14: The activity coefficient ratio determined using the forward wave of a background subtracted ethylferrocene:hexyl 50:50 monolayer CV.

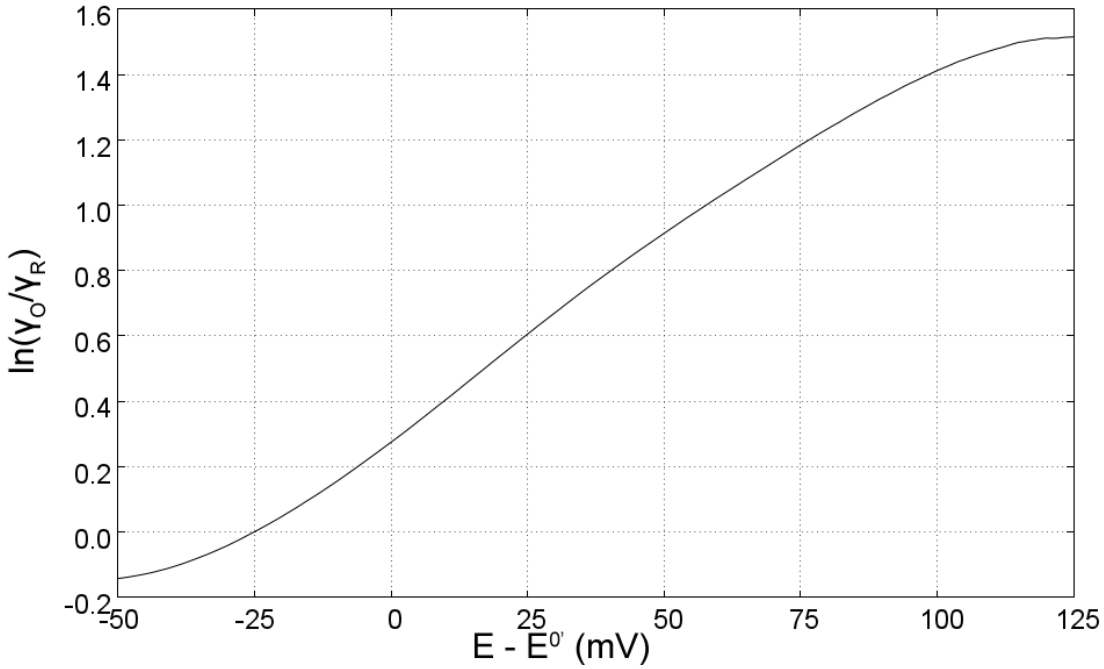

Figure 6.15: The activity coefficient ratio determined using the forward wave of a background subtracted ethylferrocene:octyl 50:50 monolayer CV.

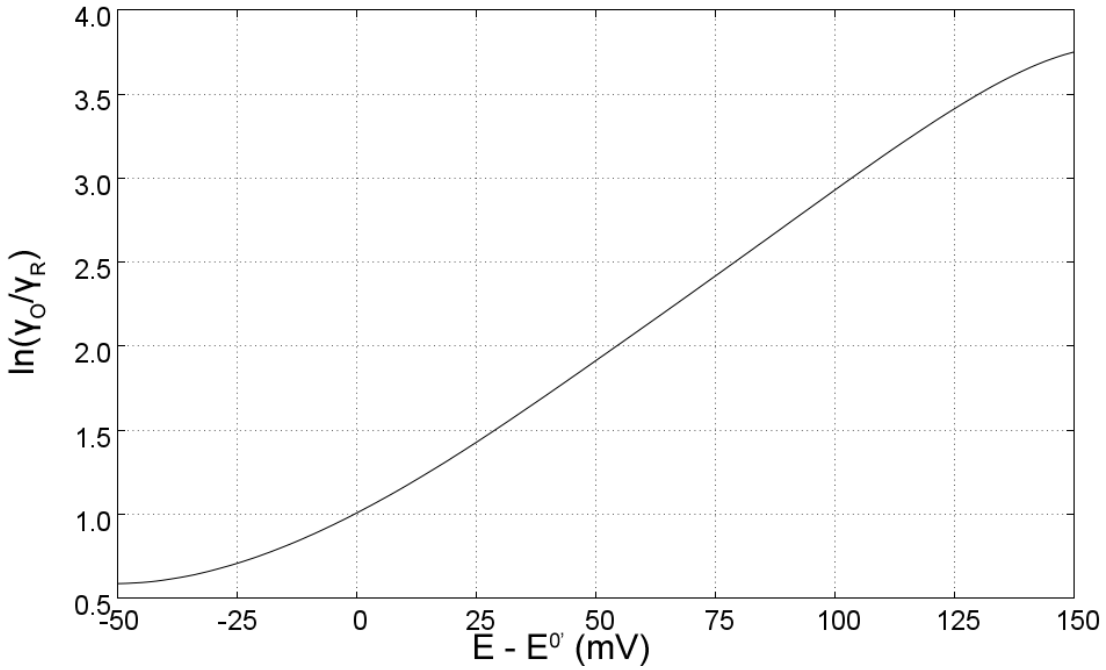

Figure 6.16: The activity coefficient ratio determined using the forward wave of a background subtracted ethylferrocene:decyl 50:50 monolayer CV.

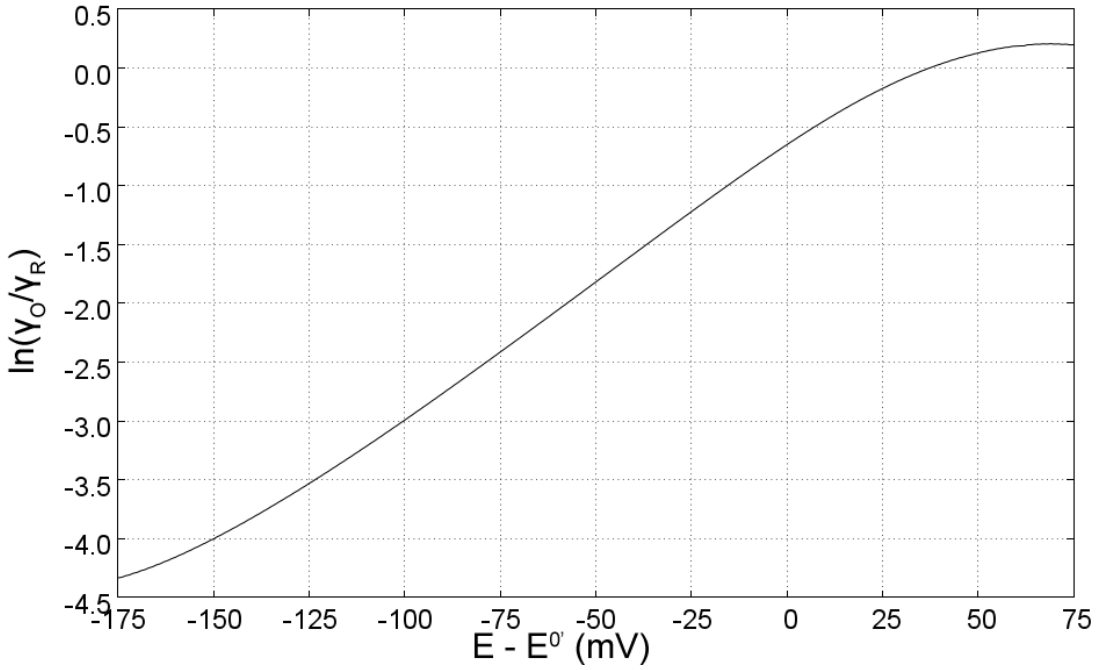

Figure 6.17: The activity coefficient ratio determined using the forward wave of a background subtracted ethylferrocene:octyl 1:99 monolayer CV.

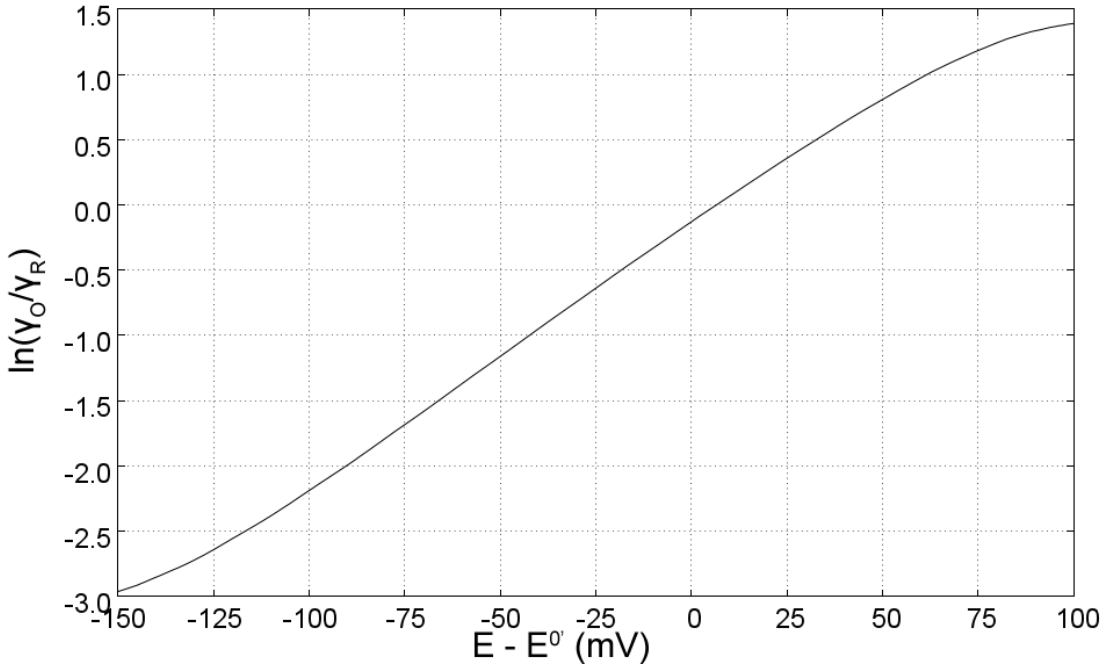

Figure 6.18: The activity coefficient ratio determined using the forward wave of a background subtracted ethylferrocene:decyl 1:99 monolayer CV.

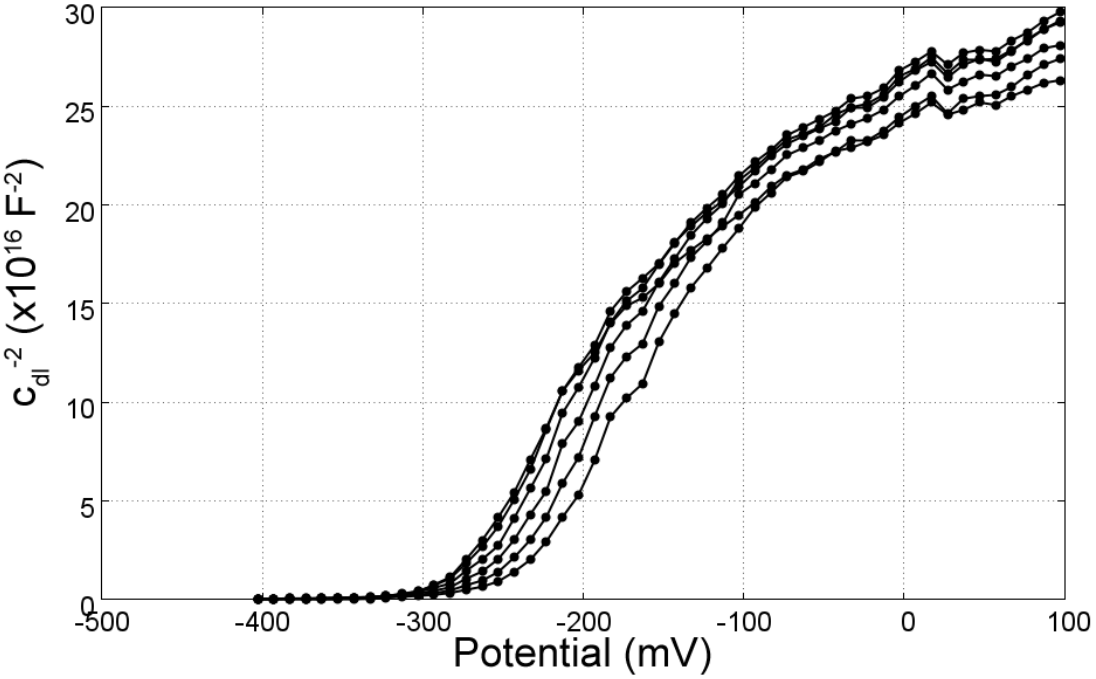

Figure 6.19: Mott-Schottky plot for the ethenylferrocene monolayer on silicon recorded using electrochemical impedance spectroscopy over a frequency range of 40 kHz to 2.5 kHz.

6.6 Determination of Flat-band Potential

EIS spectra were recorded over a range of potentials using the ethenylferrocene monolayer. The capacitance values determined were used to create a Mott-Schottky plot (see Section 2.2.8) and thereby determine flatband potential for the silicon chips modified with these monolayers.[13] Frequencies of 40 kHz to 2.5 kHz were used to create the plot shown in Figure 6.19. Precise determination of flatband potential via extrapolation is not possible due to the non-linearity of the plot. However, flatband potential can be estimated as -300 mV on the basis of the rapid rise in c_{dl}^{-2} that occurs as the potential is scanned positive of this potential.

6.7 Photoelectrochemical Chronoamperometry

PC experiments (see Section 2.2.9) were performed using silicon chips, coated with the monolayers discussed, as working electrodes. A Ag/AgCl wire reference electrode and a tungsten wire reference electrode were used in each case. A solution of KCl (0.1M) in water was used as an electrolyte solution. Light steps from 0 to full intensity were used to generate the transient responses. The recording of PC data was performed with the assistance of Mufida Abdualla (Chemical Nanoscience Laboratory, Newcastle University). Equation 6.9 was fitted to the transient responses by floating k_1, k_2, β, I_∞ and I_0. See Section 2.2.8 for further details. The parameters used to generate the theory curves are found via non-linear least squares regression using GNU Plot, and parameters are seeded such that k_1 will always correspond to the higher of the two rate constants.

$$i(t) = I_0[\beta \exp(-k_1 t) + (1-\beta)\exp(-k_2 t)] + I_\infty \qquad (6.9)$$

The above equation is arrived at when one considers the fates of charge carriers within n-type silicon upon illumination in the presence of a redox active surface species. In the absence of faradaic processes, the concentration of generated holes, h^+, within the silicon will decay as described by Equation 6.10. The parameters e_T and e^- refer to the concentrations of electrons trapped in surface states and valence band electrons respectively. The rate constants k_T and k_R describe the rates of hole recombination with trapped electrons and valence band electrons respectively.

$$\frac{\partial h^+}{\partial t} = -k_T h^+ e_T - k_R h^+ e^- \tag{6.10}$$

A non-faradaic current resulting from the filling of surface traps can be described by Equation 6.11.

$$\frac{i}{nFA} = \frac{\partial e_T}{\partial t} = -k_T h^+ e_T \tag{6.11}$$

Immediately following illumination, h^+ will increase rapidly and holes will begin to fill the surface traps causing e_T to decay. Current resulting from the filling of these states can be described by a simple exponential decay with pseudo first-order rate constant k_1. The parameter k_1 is described by Equation 6.12 where h^+_{SS} denotes the surface concentration of valence band holes.

$$k_1 = k_T h^+_{SS} \tag{6.12}$$

A second pseudo first-order process takes place in the form of holes reacting with surface ferrocene, generating a faradaic current that can be described by Equation 6.13 when the silicon surface is in depletion.

$$\frac{i}{nFA} = \frac{\partial \Gamma_{Fc}}{\partial t} = -k_f h^+ \Gamma_{Fc} \tag{6.13}$$

The pseudo first-order rate constant for this process, k_2, is given by equation 6.14.

$$k_2 = k_f h_{SS}^{+} \tag{6.14}$$

Equation 6.13 is valid only for a surface under depletion because it does not take into account the effect of photoelectrons present in the conduction band near the silicon surface. For a surface near flatband potential, the presence of photoelectrons may result in a back reaction taking place and an apparently lower k_2 being measured. This will be considered in the analysis of the k_2 measurements below.

The total current is the sum of the faradaic and non-faradaic components given by equations 6.11 and 6.13. When $I_\infty = 0$, taking the first derivative of this sum gives an equation identical in form to Equation 6.9.

A sample of the current transient data collected during PC experiments with an undecyl monolayer and fitted theory curves based on the regression model Equation 6.9 are shown in Figure 6.20 and residual plots below each current plot serve as a measure of the fit quality. An initial upward trend in residual is observed in each case, most likely as a result of the simulated response not accounting for the rise time of the system. This rise time was determined using electrochemical impedance spectroscopy and found to be approximately 10 μs. Similar trends in residual will also be shown for other monolayers. The fits are of high quality in each case, with systematic deviations from the fit being limited to time scales on the order of 10 μs. The values of free parameters used to the generate the theory curves at all potentials are plotted in Figure 6.21. For this monolayer, the determined β values are very close to 1 over a range of potentials suggesting that a single electron transfer, with rate constant k_1, is

almost completely responsible for the observed transient. It will be shown that this is in contrast to the parameters determined for ferrocene containing monolayers (excepting ethylferrocene:decyl 1:99) for which β always shows significant variation across the potential range. As expected, the initial current, i_0, increases in magnitude as the potential is made increasingly positive. Given that the current at the end of the data range approaches 0, to a good approximation i_0 is generated entirely as a consequence of the light step. It will be seen that this approximation is good for all the PC experiments performed here. The high β values mean that the fits are highly insensitive to k_2. Observations similar to those made for the undecyl surface are commonly made for unmodified silicon where the current can be attributed to photocapacitance and its decay via recombination of charge carriers at the surface. Photocapacitance is a non-faradaic process which occurs in response to a step in light intensity and does not require the presence of any redox active species (see Section 1.4). This photocapacitance response is expected to be present in data collected at all of the monolayers.[14–16]

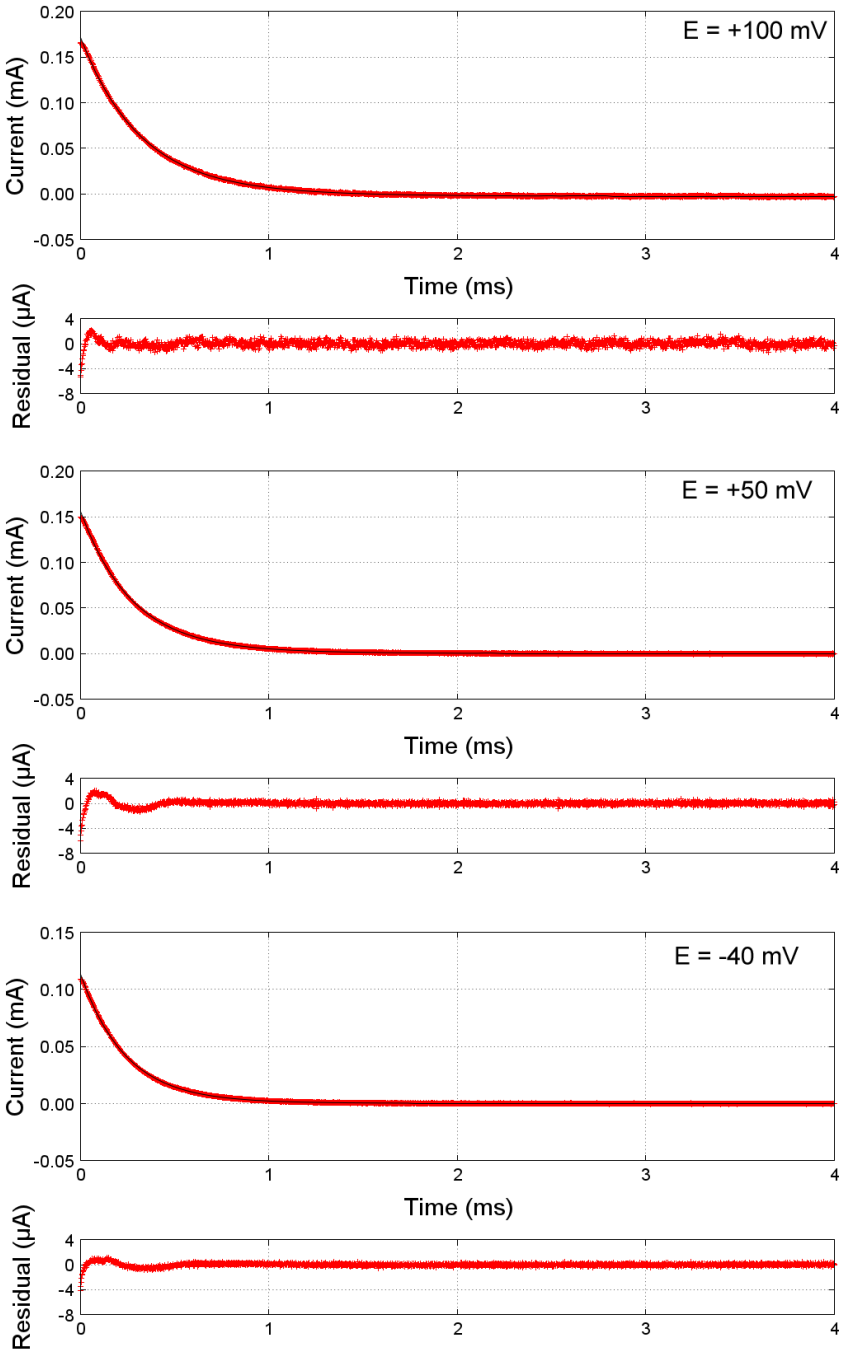

Figure 6.20: Current transients recorded during PC experiments using a silicon electrode coated with an undecyl monolayer plotted as red data points. Equation 6.9 was used as the regression model to generate the theory curves shown in black and the residual plotted below each current plot. The potential at which the experiment was carried out is given on each plot.

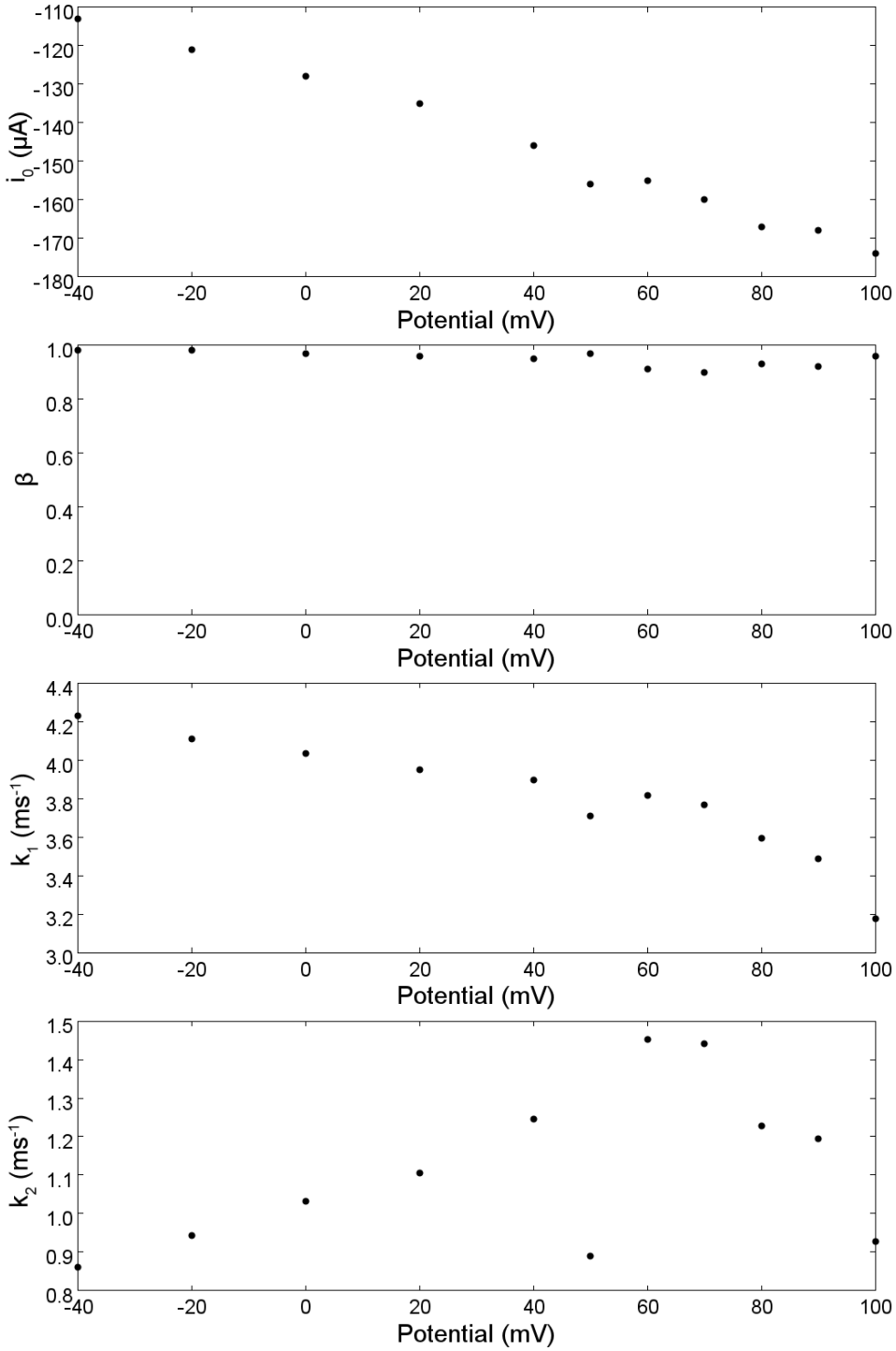

Figure 6.21: Parameters used to fit Equation 6.9 to experimental PC data recorded using a silicon electrode coated with an undecyl monolayer. The symbols i_0, β, k_1, k_2 refer to the peak current, the fraction of current corresponding to photocapacitance, the rate of recombination, and the rate of ferrocene oxidation respectively.

Transients observed for the ethylferrocene monolayer, and the fitted theory curves based on the regression model Equation 6.9, are shown in Figure 6.22. The free parameters used to generate the theory curves are plotted in Figure 6.23. In this case a second exponential decay must be introduced to simulate the current response. The first is almost certainly the photocapacitance response also observed for the undecyl monolayer, and the second caused by the oxidation of surface bound ferrocene. Given the similarity in values of k_1 observed at undecyl and ethylferrocene monolayers, these parameters are believed to correspond to the same process at both surfaces. Therefore k_2 is believed to be a measure of the rate of ferrocene oxidation, though the nature of this parameter is discussed in more detail below. At potentials of -20 mV and more positive, a β value close to 1 is observed meaning that the process corresponding to k_2 occurs to no significant extent. In this region, the process corresponding to k_1 dominates. Prior to the increase in β, k_2 has an average value of 1.4×10^3 s^{-1} and only a small dependence on potential. Potential independent rate constants are often observed at silicon surfaces due to the energy of the band edges and minority carrier concentration being constant at the surface of the silicon across a range of potentials.[17] The increase in β is the result of ferrocene being converted to ferrocenium prior to illumination as sufficient overpotential is supplied. This is consistent with the CV data shown in Figure 6.7 where oxidation is shown to occur without illumination. The light step experiment therefore provides a simple means of determining whether monolayer discharge may occur in the dark.

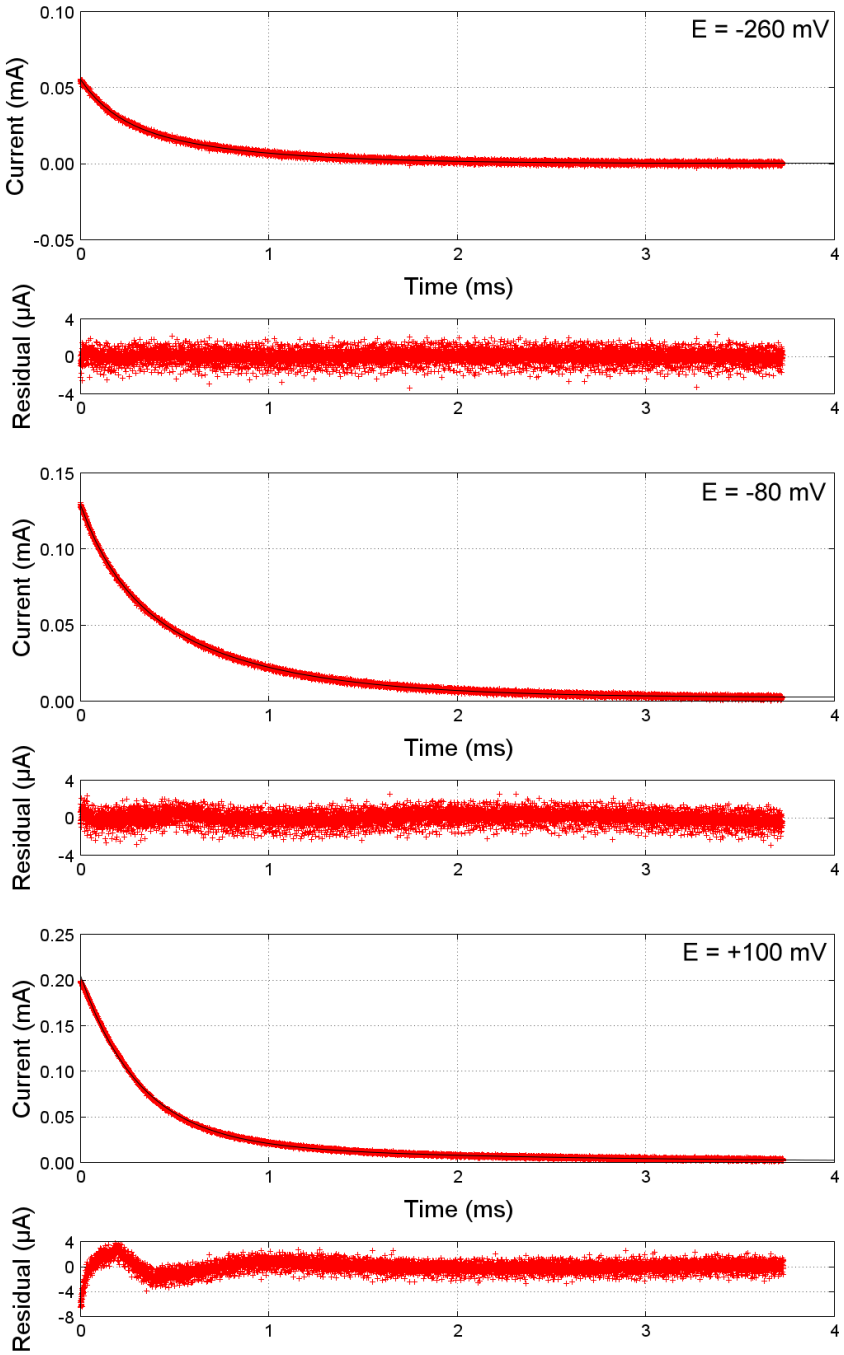

Figure 6.22: Current transients recorded during PC experiments using a silicon electrode coated with an ethylferrocene monolayer plotted as red data points. Equation 6.9 was used as the regression model to generate the theory curves shown in black and the residual plotted below each current plot. The potential at which the experiment was carried out is given on each plot.

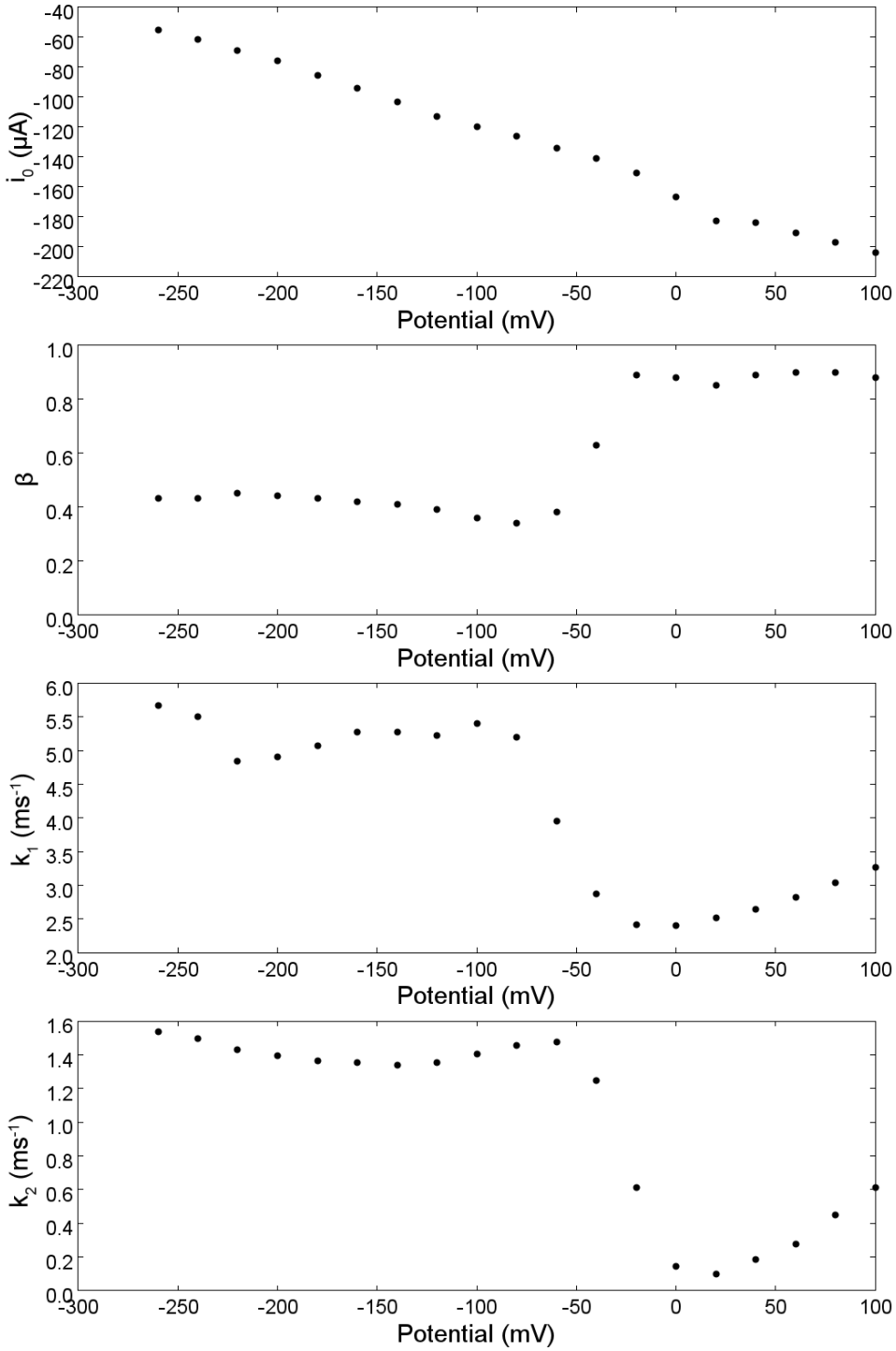

Figure 6.23: Parameters used to fit Equation 6.9 to experimental PC data recorded using a silicon electrode coated with a ethylferrocene monolayer. The symbols i_0, β, k_1, k_2 refer to the peak current, the fraction of current corresponding to photocapacitance, the rate of recombination, and the rate of ferrocene oxidation respectively.

Very similar observations are made for the ethenylferrocene monolayer. An average k_2 value of 1.5×10^3 s^{-1} is seen before the increase in β occurs. Although β decreases when the potential increases beyond -150 mV, this may be due to the onset of another process.

For the 50:50 mixed monolayers, no sharp increase in β is observed indicating that the monolayers do not discharge in the dark. This is consistent with CVs recorded in the dark which show no clear peak for the oxidation of ferrocene (Figure 6.9) Similar values of k_2 are observed for these monolayers as in the case of the pure monolayers, though k_2 is seen to be dependent upon potential for these monolayers.

For the ethylferrocene:octyl 1:99 monolayer, it can be seen that oxidation proceeds in the dark when sufficient overpotential is applied. The observed k_2 values and trends with potential are similar to those observed for the ethylferrocene:octyl 50:50 monolayer. For the dilute decyl monolayer, the data fits to a single exponential, which may indicate that monolayer oxidation requires a very low overpotential in the dark. This prevented k_2 from being determined for this monolayer.

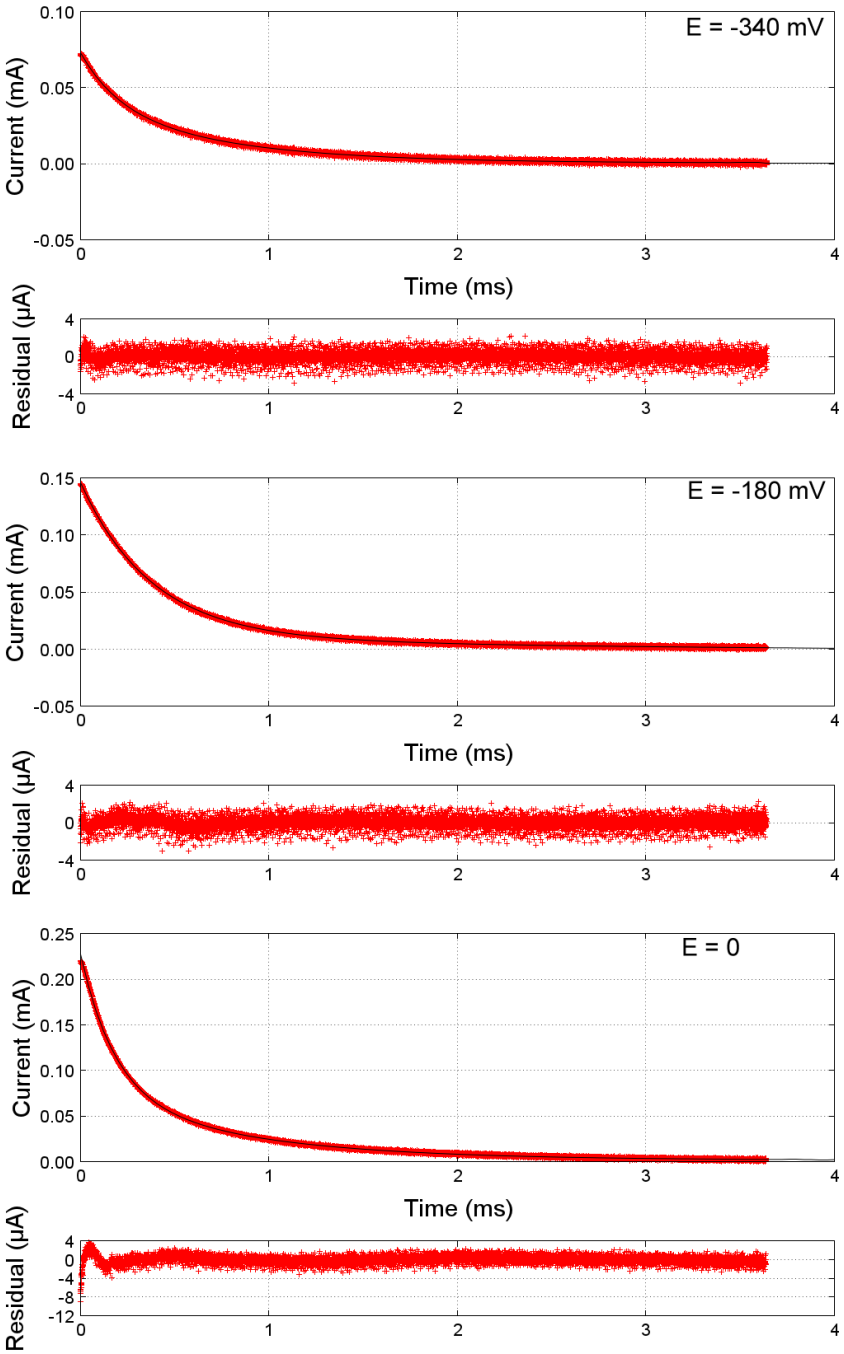

Figure 6.24: Current transients recorded during PC experiments using a silicon electrode coated with an ethenylferrocene monolayer plotted as red data points. Equation 6.9 was used as the regression model to generate the theory curves shown in black and the residual plotted below each current plot. The potential at which the experiment was carried out is given on each plot.

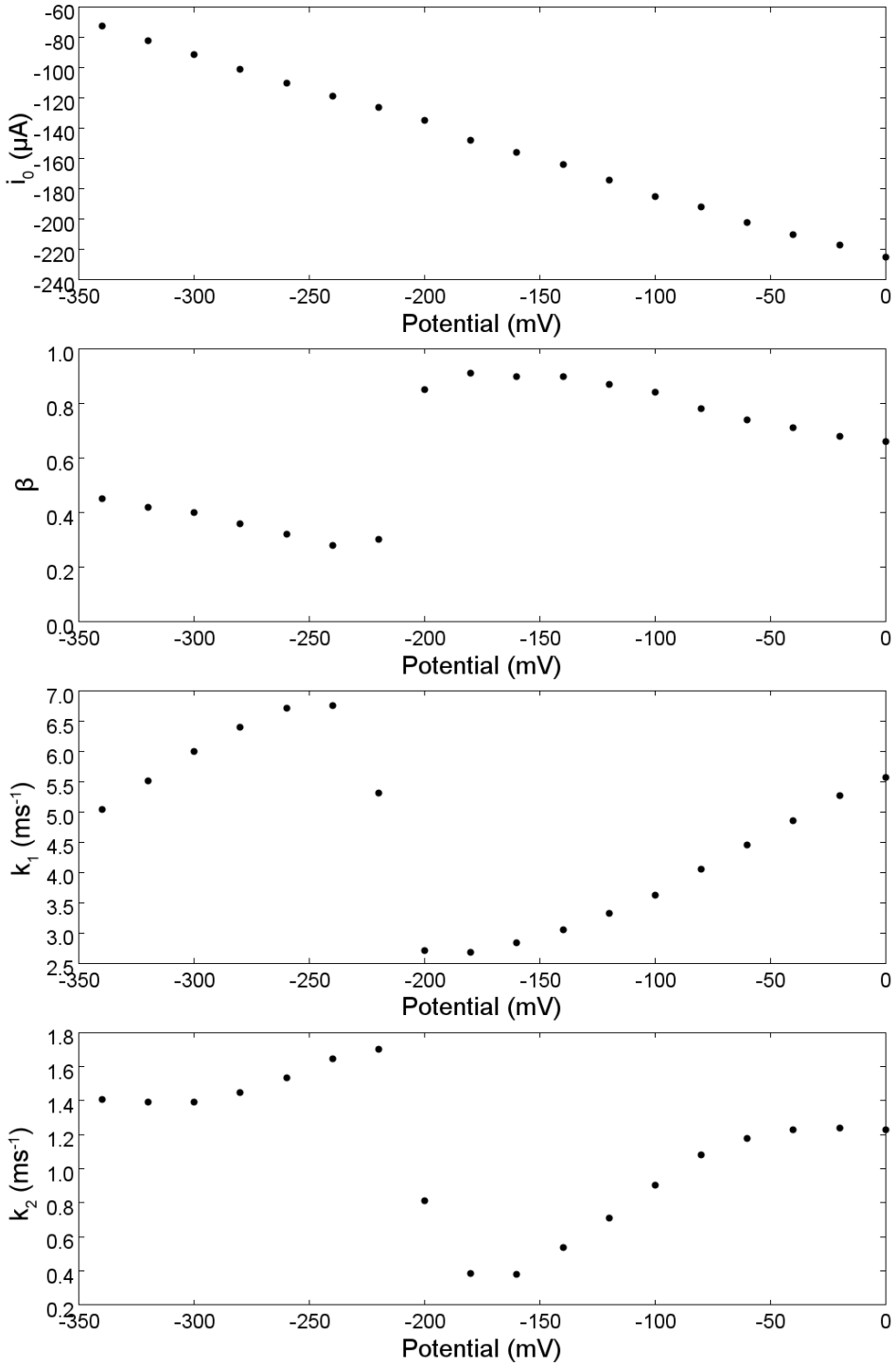

Figure 6.25: Parameters used to fit Equation 6.9 to experimental PC data recorded using a silicon electrode coated with a ethenylferrocene monolayer. The symbols i_0, β, k_1, k_2 refer to the peak current, the fraction of current corresponding to photocapacitance, the rate of recombination, and the rate of ferrocene oxidation respectively.

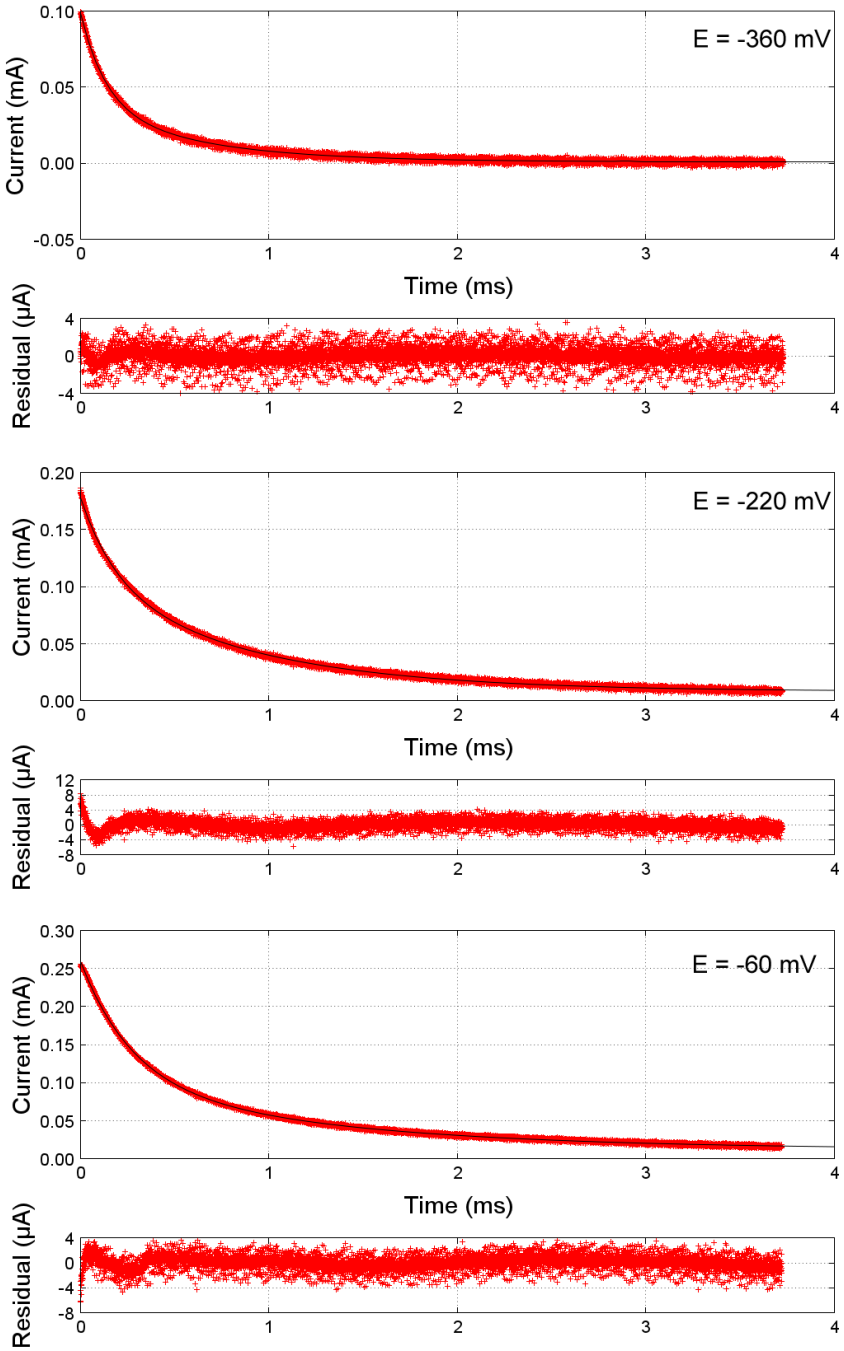

Figure 6.26: Current transients recorded during PC experiments using a silicon electrode coated with an ethylferrocene:hexyl 50:50 monolayer plotted as red data points. Equation 6.9 was used as the regression model to generate the theory curves shown in black and the residual plotted below each current plot. The potential at which the experiment was carried out is given on each plot.

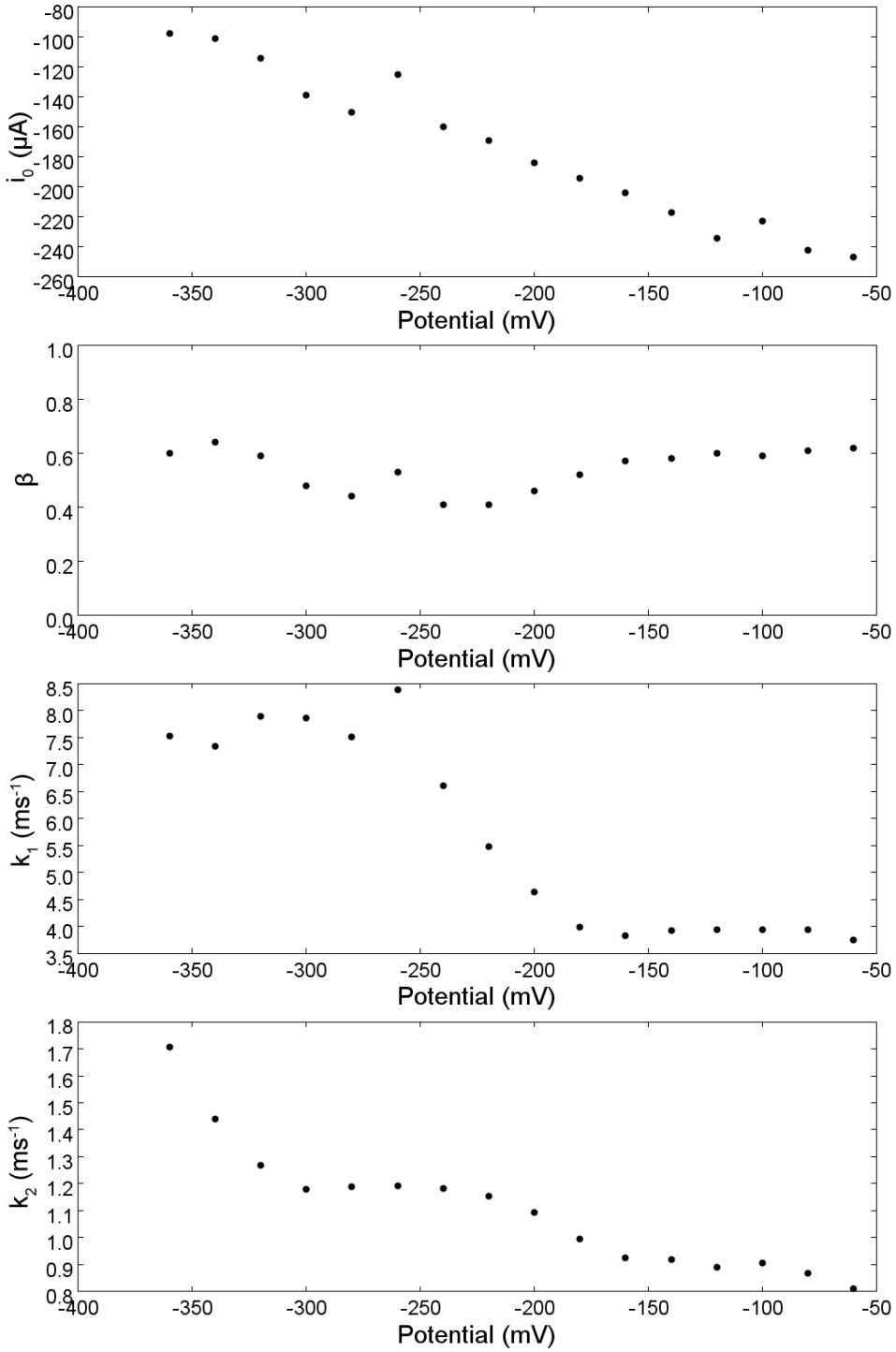

Figure 6.27: Parameters used to fit Equation 6.9 to experimental PC data recorded using a silicon electrode coated with a ethylferrocene:hexyl 50:50 monolayer. The symbols i_0, β, k_1, k_2 refer to the peak current, the fraction of current corresponding to photocapacitance, the rate of recombination, and the rate of ferrocene oxidation respectively.

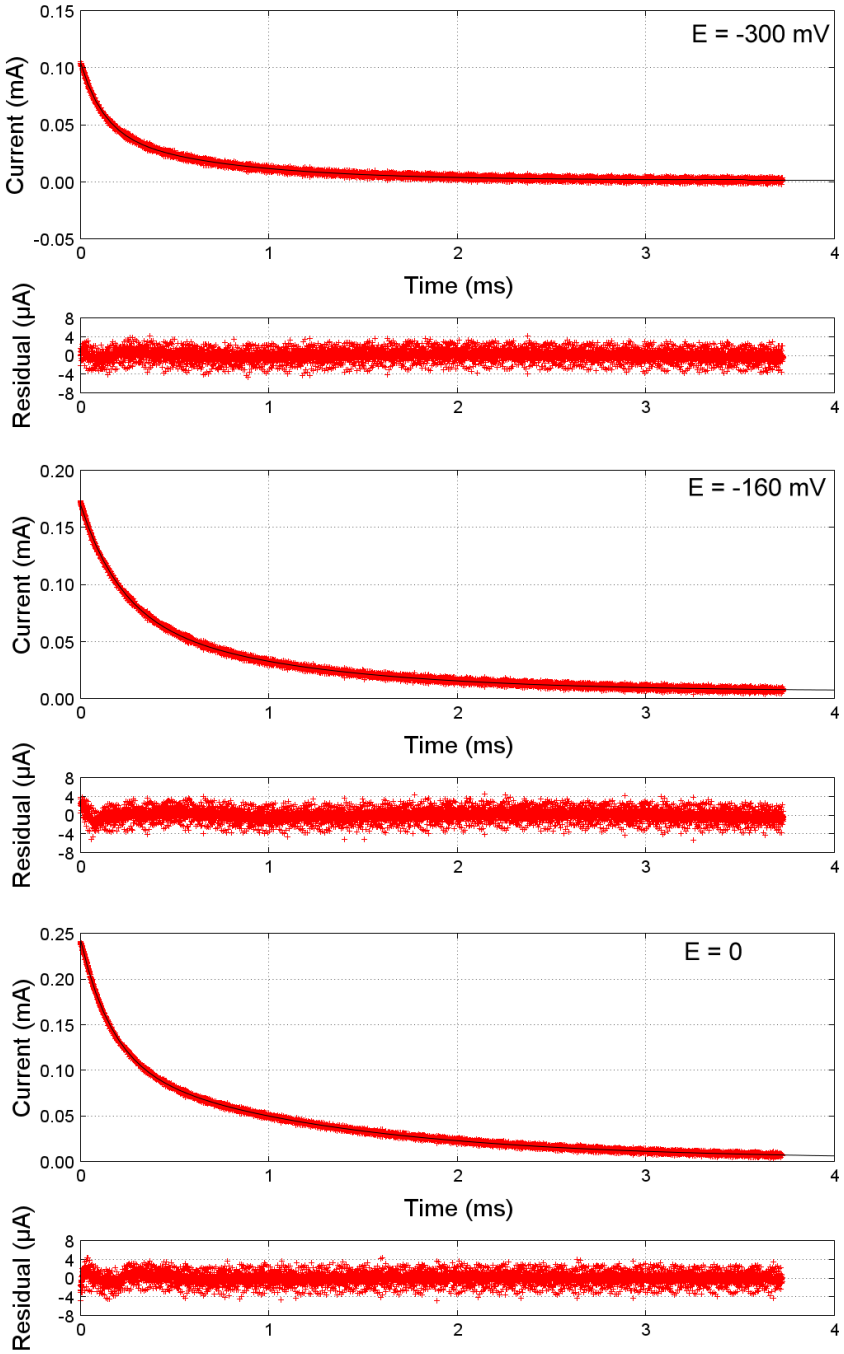

Figure 6.28: Current transients recorded during PC experiments using a silicon electrode coated with an ethylferrocene:octyl 50:50 monolayer plotted as red data points. Equation 6.9 was used as the regression model to generate the theory curves shown in black and the residual plotted below each current plot. The potential at which the experiment was carried out is given on each plot.

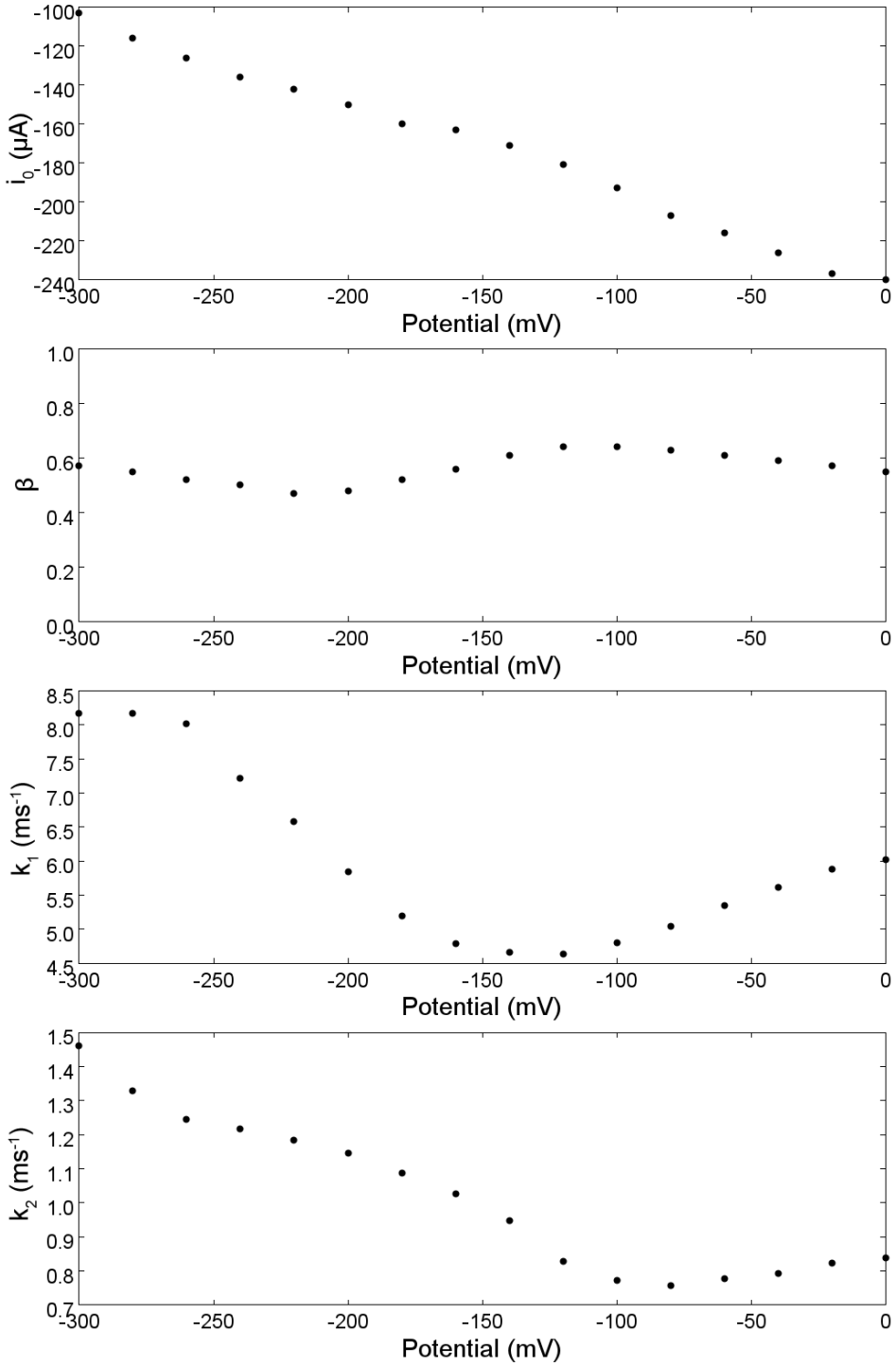

Figure 6.29: Parameters used to fit Equation 6.9 to experimental PC data recorded using a silicon electrode coated with a ethylferrocene:octyl 50:50 monolayer. The symbols i_0, β, k_1, k_2 refer to the peak current, the fraction of current corresponding to photocapacitance, the rate of recombination, and the rate of ferrocene oxidation respectively.

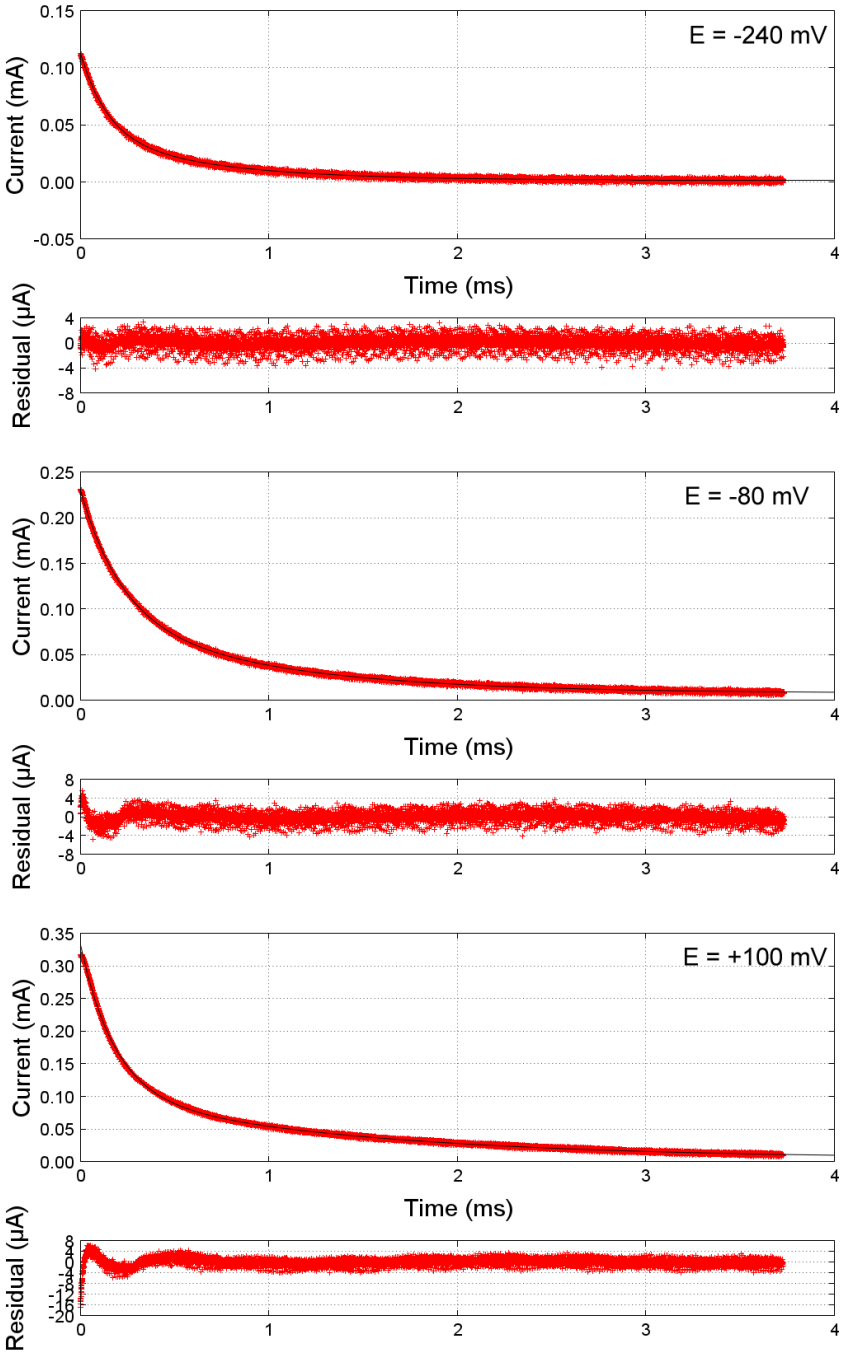

Figure 6.30: Current transients recorded during PC experiments using a silicon electrode coated with an ethylferrocene:decyl 50:50 monolayer plotted as red data points. Equation 6.9 was used as the regression model to generate the theory curves shown in black and the residual plotted below each current plot. The potential at which the experiment was carried out is given on each plot.

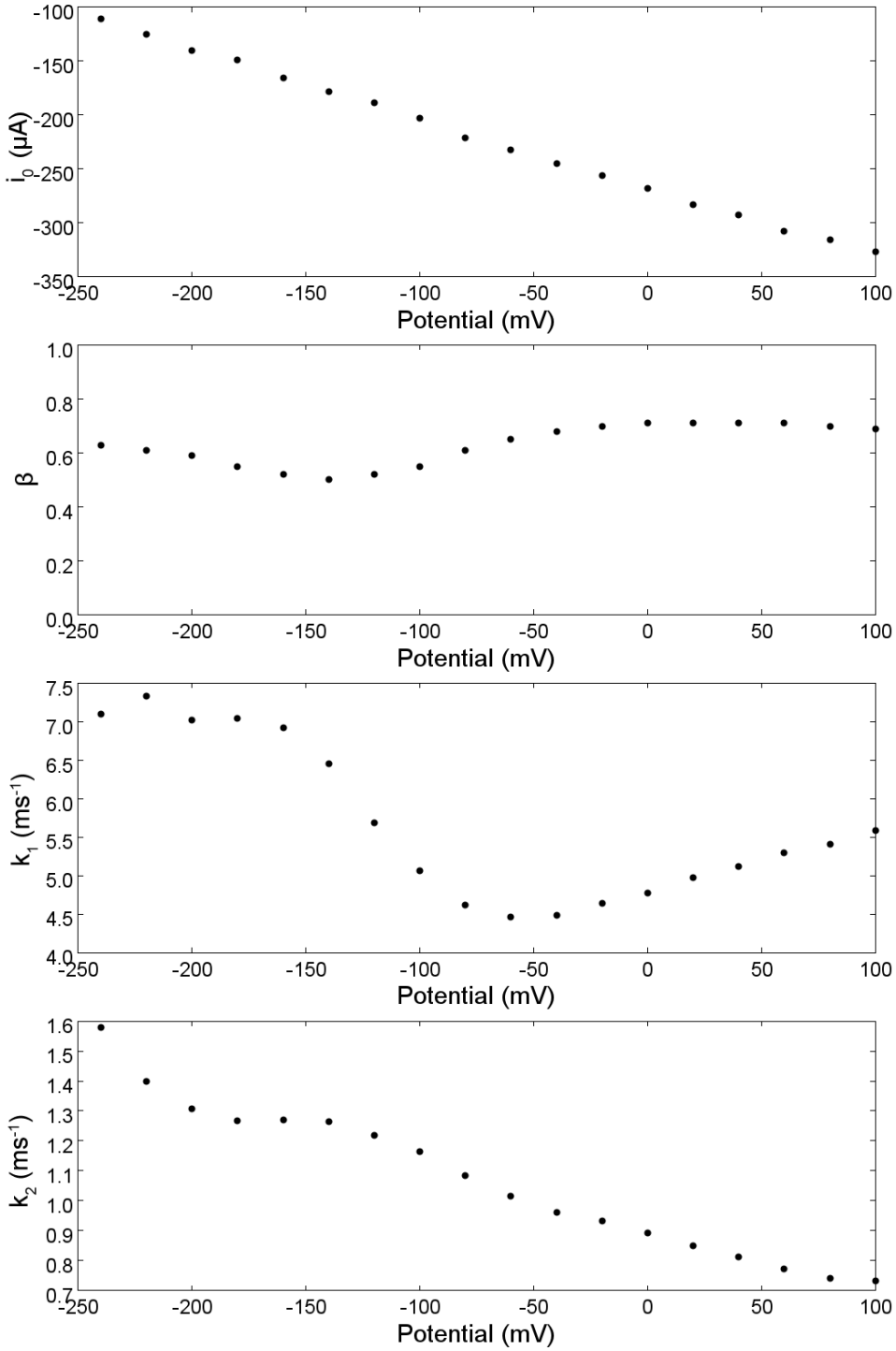

Figure 6.31: Parameters used to fit Equation 6.9 to experimental PC data recorded using a silicon electrode coated with a ethylferrocene:decyl 50:50 monolayer. The symbols i_0, β, k_1, k_2 refer to the peak current, the fraction of current corresponding to photocapacitance, the rate of recombination, and the rate of ferrocene oxidation respectively.

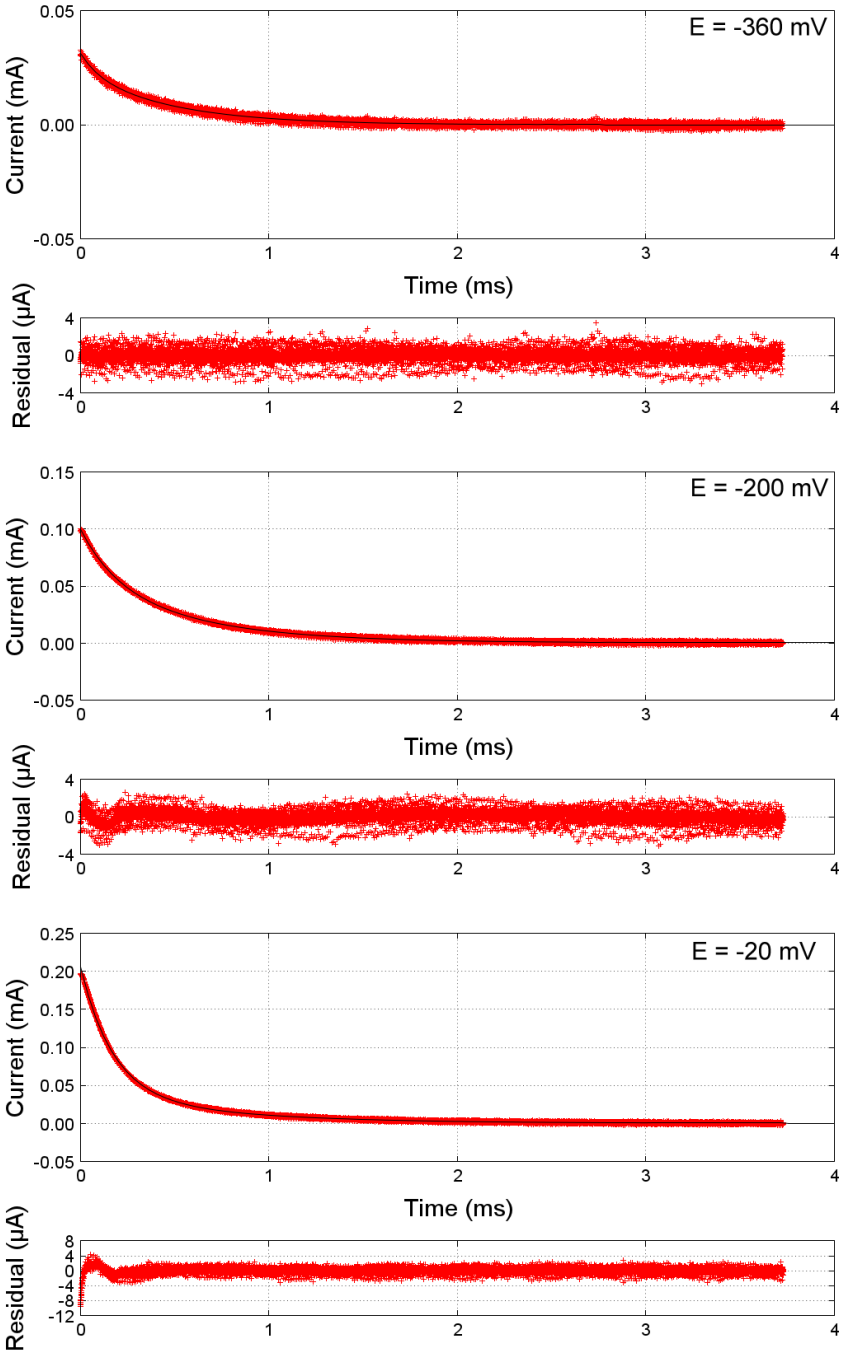

Figure 6.32: Current transients recorded during PC experiments using a silicon electrode coated with an ethylferrocene:octyl 1:99 monolayer plotted as red data points. Equation 6.9 was used as the regression model to generate the theory curves shown in black and the residual plotted below each current plot. The potential at which the experiment was carried out is given on each plot.

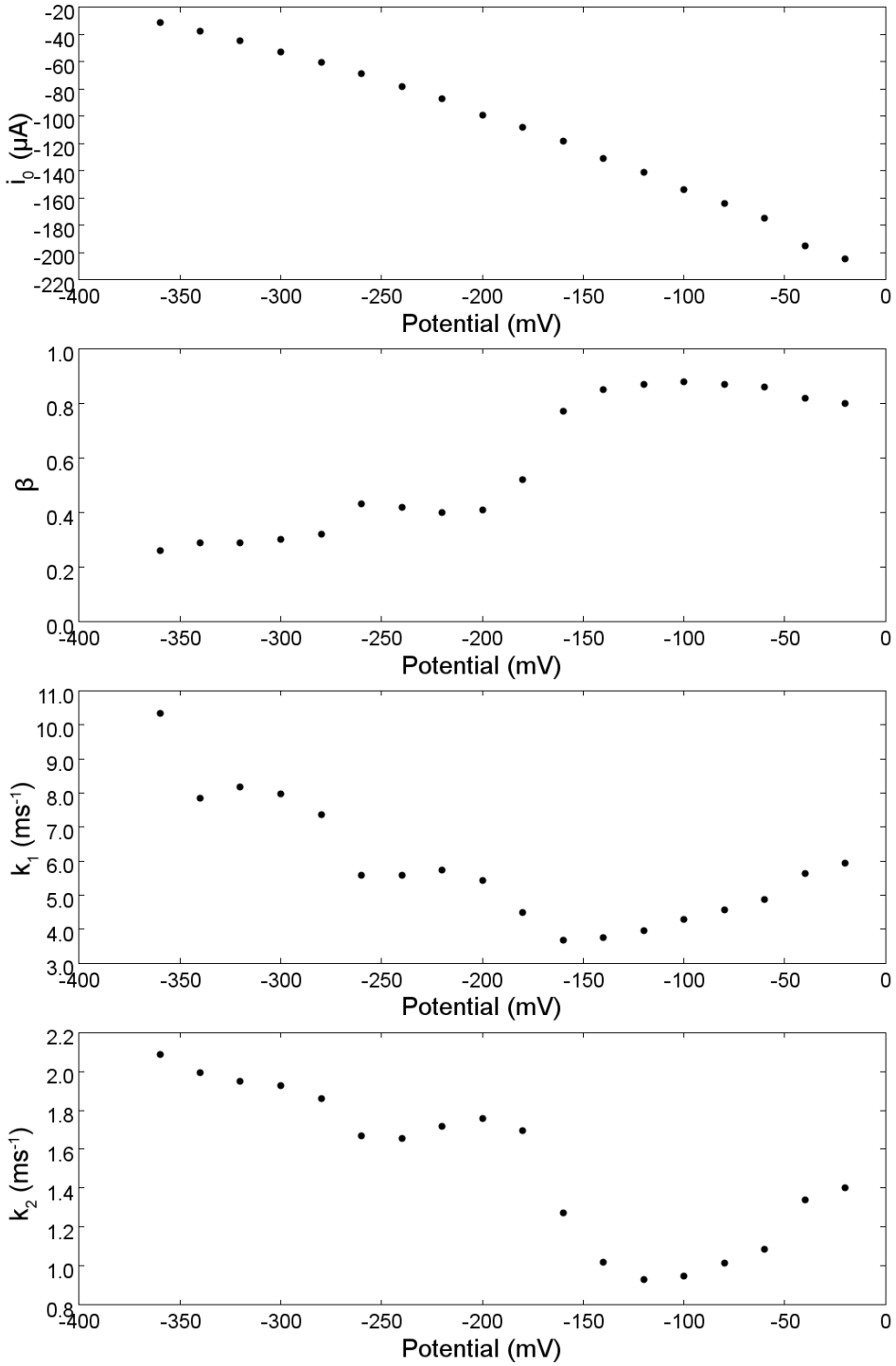

Figure 6.33: Parameters used to fit Equation 6.9 to experimental PC data recorded using a silicon electrode coated with a ethylferrocene:octyl 1:99 monolayer. The symbols i_0, β, k_1, k_2 refer to the peak current, the fraction of current corresponding to photocapacitance, the rate of recombination, and the rate of ferrocene oxidation respectively.

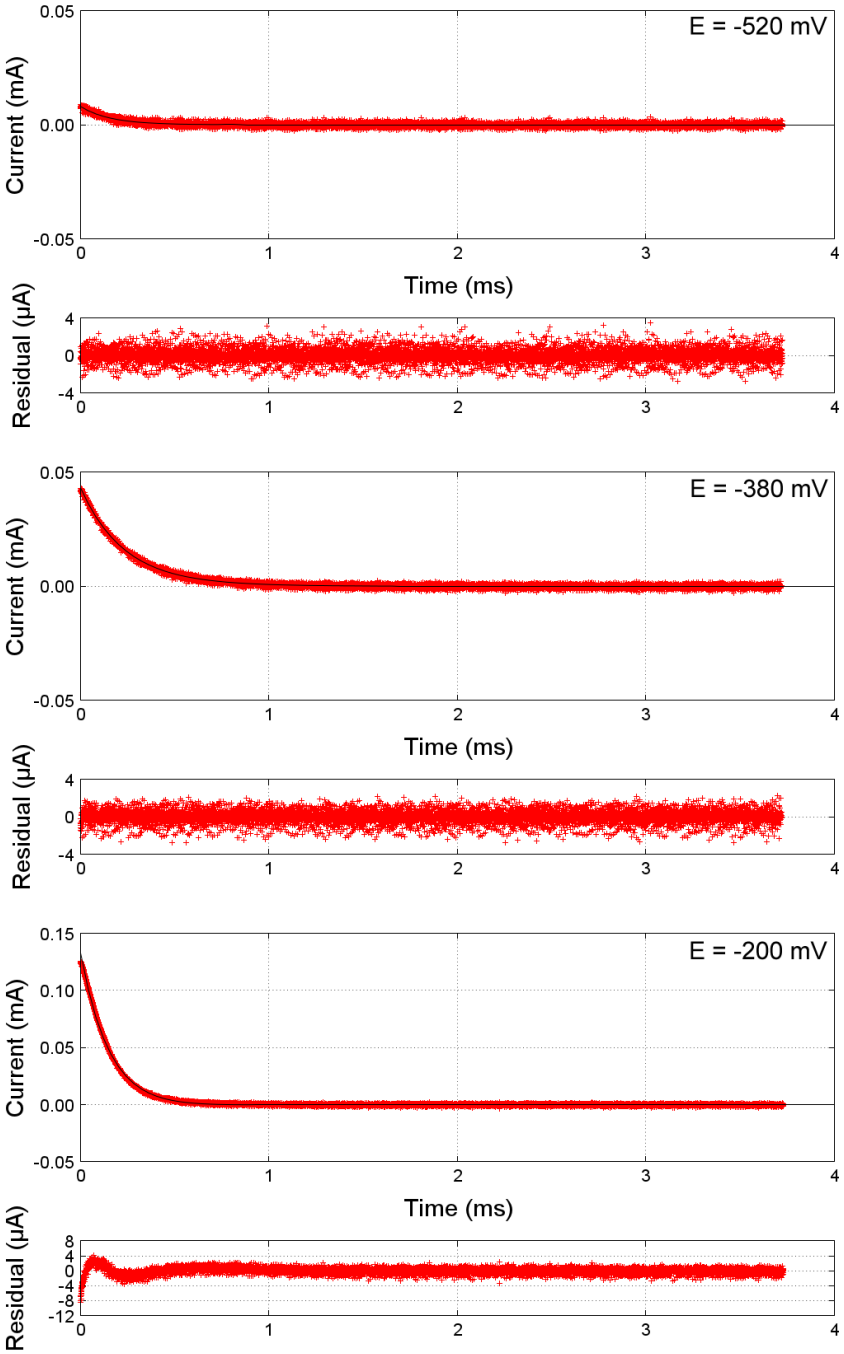

Figure 6.34: Current transients recorded during PC experiments using a silicon electrode coated with an ethylferrocene:decyl 1:99 monolayer plotted as red data points. Equation 6.9 was used as the regression model to generate the theory curves shown in black and the residual plotted below each current plot. The parameter β was fixed at 1 and the fit was completely insensitive to k_2. The potential at which the experiment was carried out is given on each plot.

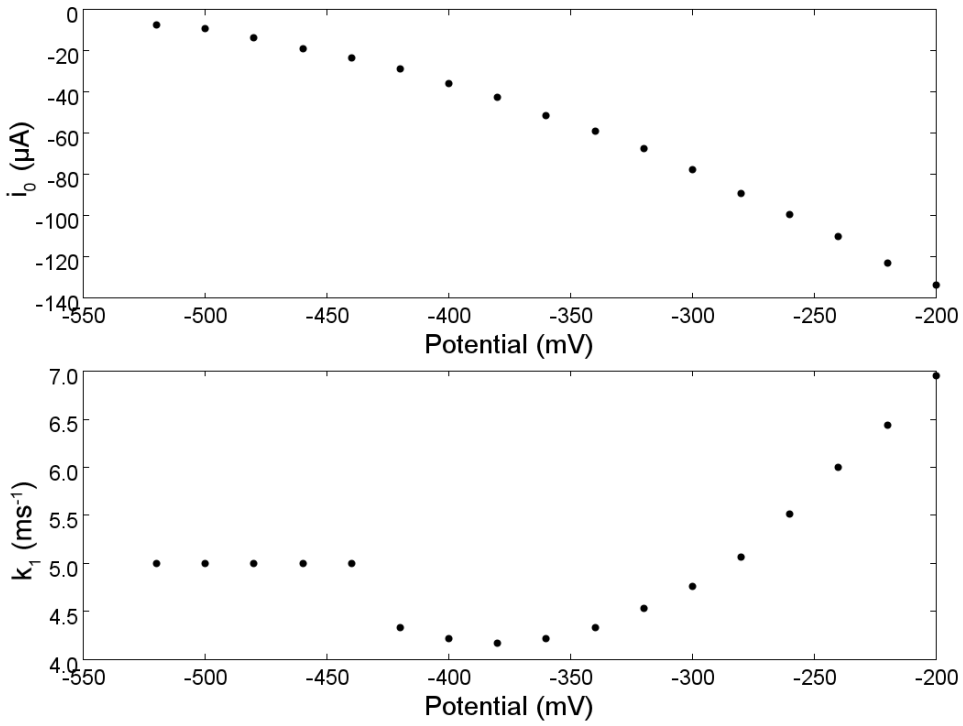

Figure 6.35: Parameters used to fit Equation 6.9 to experimental PC data recorded using a silicon electrode coated with a ethylferrocene:decyl 1:99 monolayer. The parameter β was fixed at 1 and the fits were insensitive to k_2. The symbols i_0 and k_1 refer to the peak current and the rate of recombination respectively.

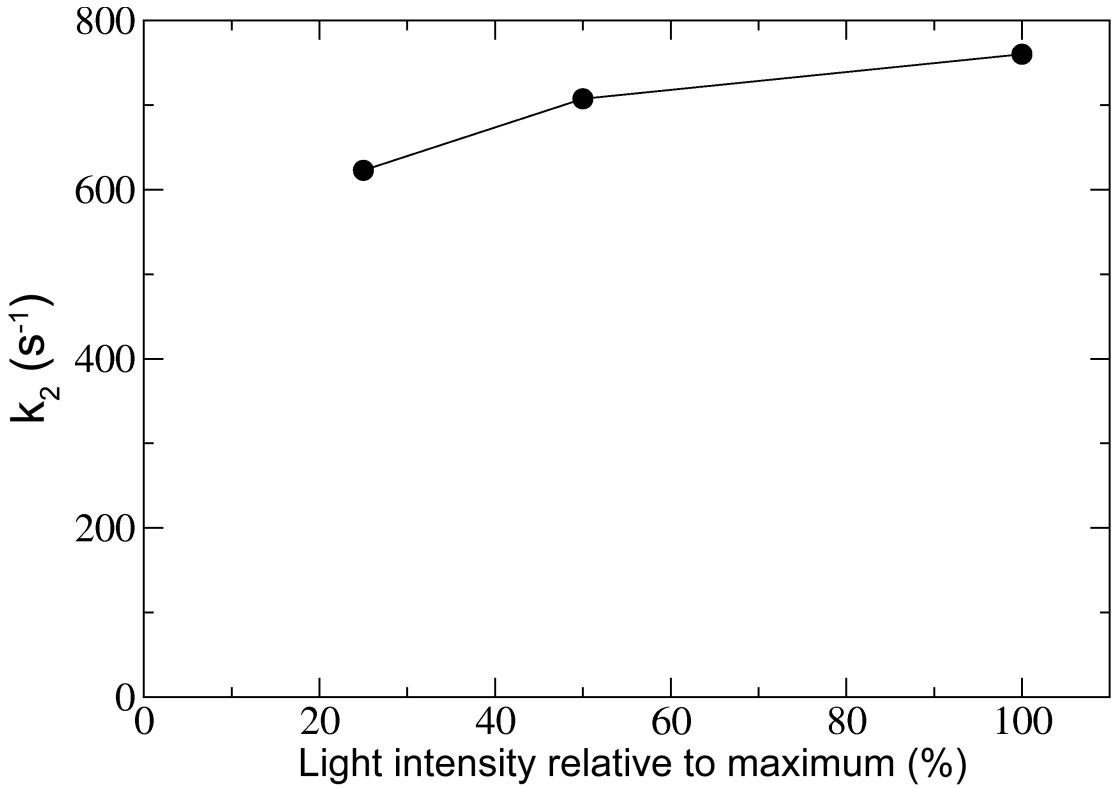

Figure 6.36: The value of k_2 for the ethylferrocene monolayer at −60 mV obtained via the PC experiment at three different light intensities.

To ensure that the measured rate constants were not limited by the minority carrier concentration within the silicon, the value of k_2 for the ethylferrocene monolayer was measured at different light intensities and the results are shown in Figure 6.36. The sublinearity of the plot demonstrates that the concentration of surface ferrocene is what limits the electron transfer rate.

6.8 Discussion

The surface coverages observed for this selection of monolayers are somewhat surprising as the 50:50 mixed monolayers show higher

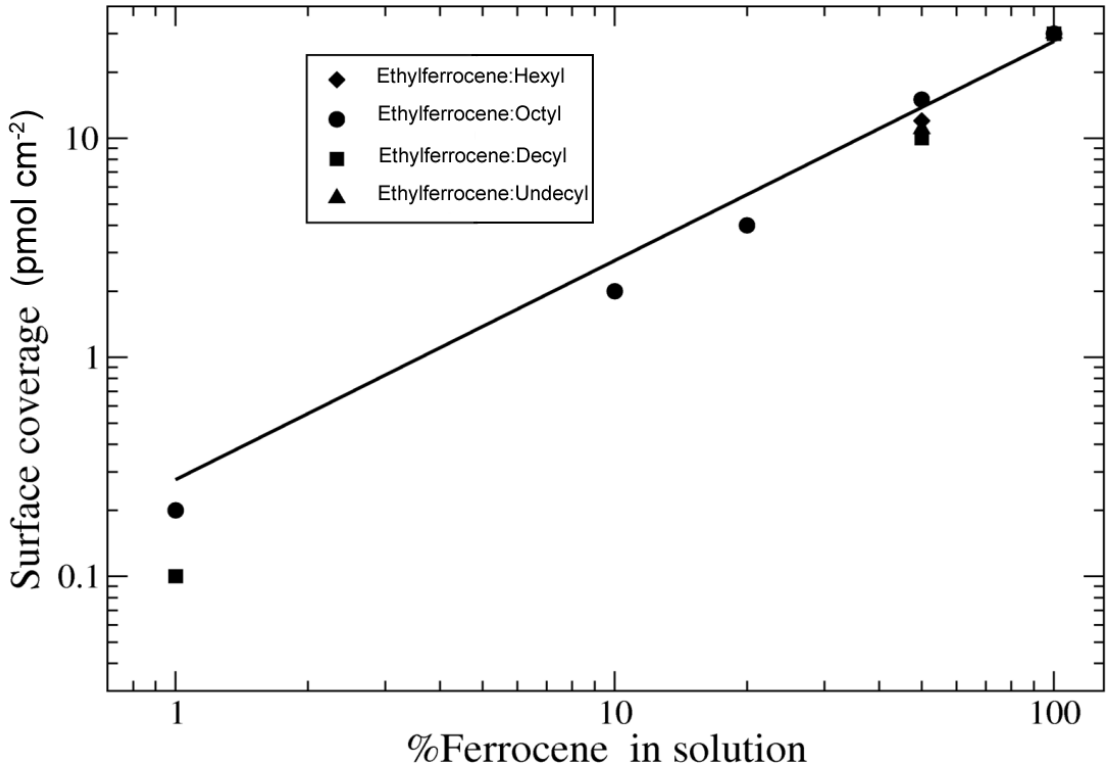

Figure 6.37: Surface ferrocene concentration as determined by integration of the anodic wave of cyclic voltammograms. Voltammograms were recorded in acetonitrile with $LiClO_4$ (0.1M) under illumination at a scan rate of 0.5 V s^{-1}. The diluting alkyl chains were present in the reaction mixture as either hex-1-ene, oct-1-ene, dec-1-ene or undec-1-ene during preparation of the mixed monolayer surfaces. The solid line is a best fit to the regression model $y = ax$. %Ferrocene indicates the mole fraction of the vinylferrocene reagent expressed as a percentage of the total number of moles of alkene in the reaction solution. Figure courtesy of Mufida Abdualla (Chemical Nanoscience Laboratory, Newcastle University).

ethylferrocene surface concentrations than those with ethylferrocene groups only. The pure monolayers normally would be expected to have higher surface coverage since they are not in competition with the alkyl chains over silicon sites. However, the observed surface concentrations can be explained via the relative stabilities of the monolayers under study. It has been shown previously that mixed monolayers are significantly more stable than their pure monolayer counterparts.[18] This difference in stability is of particular importance in an aqueous environment due to the hydrophobic nature of the alkyl chains and their ability to protect ethylferrocene groups from hydrolysis. Indeed, studies in MeCN with $LiClO_4$ (0.1M) performed by Mufida Abdualla (Chemical Nanoscience Laboratory, Newcastle University) revealed that measured surface concentrations were higher in MeCN and that the concentration of surface ferrocene groups showed the expected dependence on the mole fraction of ferrocene reagents in the reaction solution used to prepare the monolayer (Figure 6.37). The relative surface coverages observed here therefore appear to be a consequence of the solvent used.

Previous studies of silicon bound monolayer kinetics have found that the observed electron transfer rate is in many cases limited by solution side phenomena such as transport of counter ions into the monolayer.[19,20] In these circumstances the observed ET rate is not an inherent property of the monolayer itself. These effects can be mitigated by using a counter ion with a high transport coefficient and by studying monolayers with low surface coverage. The monolayers studied here have surface coverages which roughly correspond to the surface coverages at which ET rates have been measured without interference from solution side effects in previous studies. Another factor which can have a significant impact on the observed ET rate

is the presence of alkyl chains within the monolayer. The longer alkyl chains cause the ferrocene groups to become buried within the monolayer and would be expected to greatly decrease the speed of ion transport into the monolayer. However, no decrease in k_2 was observed upon incorporating alkyl chains into the monolayers, nor upon increasing the length of these chains. This suggests that the ET rates observed here are independent of ion transport rates and can be considered to be inherent properties of the monolayers under study.

The similar values of k_2 observed at all monolayers show that the rate of the oxidation of ferrocene on n-type Si is not affected by the conductivity of the linker or the presence of alkyl chains. This is consistent with an ET reaction in which an electron tunnels directly from the ferrocene group to the silicon surface with the alkyl chains and the linker playing no role in the ET process. It has been shown previously that the ET rate is affected by the length of the linker between the silicon surface and the ferrocene group and that the relationship between these variables is consistent with such tunnelling.[21] Molecular modelling studies show that the distance between the ferrocene and silicon surface is not changed to any significant extent by changing the ethyl linker to an ethenyl linker.

Some potential dependence is observed in the measured rate constants and this is most apparent in the 50:50 mixed monolayers. Surprisingly, the measured ET rate, k_2, decreases as the applied potential is made more positive. This can be explained by the presence of conduction band electrons near the surface. If electrons are present within the conduction band near the surface, the parameter k_2 will be described by Equation 6.15 where valence band hole and

conduction band electron concentrations are denoted by $[h^+_{VB}]$ and $[e^-_{CB}]$ respectively. The parameter is a measure of how quickly the ferrocene/ferrocenium surface concentration ratio reaches its equilibrium value. For a silicon surface in depletion, $[e^-_{CB}] \approx 0$ and therefore $k_2 \approx k_O[h^+_{VB}]$ (see Section 2.2.9).

$$k_2 = k_O[h^+_{VB}] + k_R[e^-_{CB}] \tag{6.15}$$

Therefore a change in the value of k_2 does not necessarily represent a change in the rate of the ferrocene oxidation reaction. For electrons to exist near the silicon surface within the conduction band, the silicon would need to be close to its flatband potential. Mott-Schottky analysis suggests that this is indeed the case (see Section 6.6).

Examination of the β values obtained across the potential ranges examined for each monolayer suggest that the 50:50 mixed monolayers studied here do not undergo oxidation in the dark even at high overpotentials, in contrast to the other monolayers studied. Given the higher surface coverages determined for the 50:50 mixed monolayers, it may be that this difference in surface coverage is responsible for this difference in behaviour.

6.9 Conclusion

A series of monolayers containing ferrocene groups in a number of environments were successfully prepared and characterised. A means of measuring the nature and extent of ferrocene-ferrocene interac-

tions was proposed. It is seen here that the interactions across these monolayer surfaces become more strongly repulsive as the potential is scanned to more positive values. However, the non-ideal behaviour seen in the voltammograms is better explained in terms of monolayer heterogeneity.

Electron transfer rates were successfully measured for a series of ferrocene monolayers using photoelectrochemical chronoamperometry (PC) (Section 2.2.9) and represent the first report of ET rates measured for a monolayer on n-type Si. These rates have been shown to be independent of the conductivity of the linker between the ferrocene and the silicon surface and unaffected by the presence of alkyl chains. In addition, the PC technique was found to provide a simple means of detecting monolayer discharge in dark conditions.

The observed rate of ferrocene oxidation was found to show some potential dependence, with slower oxidation being observed at more positive potentials. This was thought to be the result of the silicon surface entering depletion as the applied potential increased thus lowering the concentration of conduction band electrons and the rate of the back reaction in Equation 6.15.

The rates determined here are pseudo first-order rate constants which correspond to a fixed concentration of minority carriers in the silicon surface. The data suggest that through carefully designed experiments it may be possible to determine the minority carrier concentration and thus determine a true rate constant for these ET reactions.

Bibliography

[1] L. C. de Smet, H. Zuilhof, E. J. Sudhölter, G. Wittstock, M. S. Duerdin, L. H. Lie, A. Houlton and B. R. Horrocks, *Electrochimica Acta*, 2002, **47**, 2653–2663.

[2] M. P. Stewart and J. M. Buriak, *Angewandte Chemie International Edition*, 1998, **37**, 3257–3260.

[3] D. Zigah, C. Herrier, L. Scheres, M. Giesbers, B. Fabre, P. Hapiot and H. Zuilhof, *Angewandte Chemie International Edition*, 2010, **49**, 3157–3160.

[4] E. G. Robins, M. P. Stewart and J. M. Buriak, *Chemical Communications*, 1999, 2479–2480.

[5] J. Hannant, J. H. Hedley, J. Pate, A. Walli, S. A. F. Al-Said, M. A. Galindo, B. A. Connolly, B. R. Horrocks, A. Houlton and A. R. Pike, *Chemical Communications*, 2010, **46**, 5870–5872.

[6] N. Tajimi, H. Sano, K. Murase, K.-H. Lee and H. Sugimura, *Langmuir*, 2007, **23**, 3193–3198.

[7] A. G. Marrani, F. Cattaruzza, F. Decker, P. Galloni and R. Zanoni, *Electrochimica Acta*, 2010, **55**, 5733–5740.

[8] H. Sano, M. Zhao, D. Kasahara, K. Murase, T. Ichii and H. Sugimura, *Journal of Colloid and Interface Science*, 2011, **361**, 259–269.

[9] A. J. Bard and L. Faulkner, *Electrochemical Methods: Fundamentals and Applications*, John Wiley & Sons, 2nd edn., 2001.

[10] E. Laviron, *Journal of Electroanalytical Chemistry and Interfacial Electrochemistry*, 1979, **101**, 19–28.

[11] H. Matsuda, K. Aoki and K. Tokuda, *Journal of Electroanalytical Chemistry and Interfacial Electrochemistry*, 1987, **217**, 15–32.

[12] H. Matsuda, K. Aoki and K. Tokuda, *Journal of Electroanalytical Chemistry and Interfacial Electrochemistry*, 1987, **217**, 1–13.

[13] R. D. Gryse, W. P. Gomes, F. Cardon and J. Vennik, *Journal of The Electrochemical Society*, 1975, **122**, 711–712.

[14] L. Peter, J. Li and R. Peat, *Journal of Electroanalytical Chemistry and Interfacial Electrochemistry*, 1984, **165**, 29–40.

[15] J. Li and L. Peter, *Journal of Electroanalytical Chemistry and Interfacial Electrochemistry*, 1985, **193**, 27–47.

[16] L. M. Peter, *Chemical Reviews*, 1990, **90**, 753–769.

[17] L. Abrantes and L. Peter, *Journal of Electroanalytical Chemistry and Interfacial Electrochemistry*, 1983, **150**, 593–601.

[18] B. Fabre, *Accounts of Chemical Research*, 2010, **43**, 1509–1518.

[19] K. M. Roth, A. A. Yasseri, Z. Liu, R. B. Dabke, V. Malinovskii, K.-H. Schweikart, L. Yu, H. Tiznado, F. Zaera, J. S. Lindsey, W. G. Kuhr and D. F. Bocian, *Journal of the American Chemical Society*, 2003, **125**, 505–517.

[20] J. Jiao, E. Nordlund, J. S. Lindsey and D. F. Bocian, *The Journal of Physical Chemistry C*, 2008, **112**, 6173–6180.

[21] K. Huang, F. Duclairoir, T. Pro, J. Buckley, G. Marchand, E. Martinez, J.-C. Marchon, B. De Salvo, G. Delapierre and F. Vinet, *ChemPhysChem*, 2009, **10**, 963–971.

Chapter 7

Conclusions and Future Work

The electron transfer kinetic measurements and other electrochemical observations made here show the effect of adjusting a number of properties of molecules and their environments upon their electron transfer behaviour. In doing so, various aspects of models of electron transfer have been tested, and data has been gathered which may prove useful in the development of molecular devices.

7.1 Electron Transfer Behaviour of Methyl Viologen and Derivatives

The first one-electron reduction of methyl viologen (MV^{2+}) has been shown to exhibit simple, reversible redox behaviour in acetonitrile and ion pairing phenomena shown to be absent. A number of methyl viologen derivatives, C1-5, in which rotation around the bond linking the aromatic rings is restricted by a linking tether have also been shown to exhibit highly similar redox behaviour. The standard rate

constants (k^0) of these molecules were successfully measured using fast scan voltammetry (FSV) and convolution analysis at a 10 μm radius platinum disc. Their standard rate constants were also measured at the same electrode using electrochemical impedance spectroscopy (EIS) and when the analysis was restricted to the high frequency data, good agreement was found between the rate constants found using the two methods for MV^{2+} and molecules C1-3, suggesting the values obtained are accurate. For molecules C4 and C5, the determined rate constants are of the same order of magnitude. Due to the better repeatability of the technique, the FSV data should be given higher weight when considering the rate constants determined here. The data obtained via EIS experiment was found to exhibit poor repeatability and during some measurements the system did not behave in a manner consistent with the theory used for the analysis. In particular, when measuring the rate constants away from the standard potential of the redox couple, the rate constant determined did not vary with potential in the manner predicted by theory. Although some data which conformed to the theoretical model was collected at the standard potential for all molecules, allowing k^0 determination to take place, this unexpected behaviour of the system casts doubt on the validity of rate constants determined via EIS for these compounds. Measurements of k^0 for these compounds which use other techniques, such as scanning electrochemical microscopy and voltammetry at a high speed channel electrode, would greatly increase the confidence in the k^0 values reported here. Significant systematic errors are associated with all techniques used in determining k^0 values meaning that measurements are best made using as many different techniques as possible. The standard rate constants obtained via FSV show that for all molecules, the redox couple is highly facile.

Prior to Frumkin correction, the values of k^0 at platinum range from 2.8×10^{-1} to 1.1×10^{-1} cm s^{-1} for the derivatives, and a k^0 of 1.4×10^{-1} cm s^{-1} was found for methyl viologen.

The cause of the unexpected behaviour observed during EIS has not been determined here, but it is possible that useful information regarding the behaviour of methyl viologen would be obtained in doing so. Though this information would directly apply to the molecule in acetonitrile, it could have some relevance to phenomena observed in aqueous solutions such as dimerisation, adsorption and comproportionation, which have already been the subject of much research.[1–4] The use of a silicon working electrode during EIS could provide a surface upon which adsorbed species could be characterised spectroscopically or by using ellipsometry, x-ray photoemission spectroscopy and other techniques.

For the systems examined, it was proposed that the differential capacitance (c_{dl}) could be determined for a given potential and set of experimental conditions by modelling the electrode as a constant phase element (CPE) and considering the time scale of the experiment to be performed. In the case of cyclic voltammetry, this is the time taken to scan the potential from the potential of zero charge to the standard potential of the redox couple under examination. The reciprocal of the time scale then provides an appropriate frequency for determining a value of c_{dl} of a CPE. The potential change throughout the diffuse layer (ϕ_2) was then determined by fitting the Gouy-Chapman-Stern model of electrode differential capacitance to the experimental data. The model was found to fit well to the data when the ionic strength of the solution used in the model was allowed to float to account for electrolyte ion pairing. Using these

data to Frumkin-correct the k^0 values of the molecules resulted in values which ranged from 1.6×10^{-3} to 1.8×10^{-4} cm s^{-1} for the derivatives and 9.7×10^{-4} cm s^{-1} for MV^{2+}.

An examination of the relationships between k^0 and structural properties of the molecules revealed a possible downward trend in k^0 with increasing molecular volume and with increasing inter-ring torsion angle. The data supporting these trends was not conclusive and the production of a larger series of derivatives would be necessary to provide stronger evidence. The synthesis of derivatives with different inter-ring tethers would render a greater number of inter-ring torsion angles and molecular volumes accessible.

Methyl viologen is already a commonly used redox active molecule in electrochemical systems and it may find further use in molecular electronics, sensor devices, and in applications which exploit its electrochromism. If the tuning of the redox properties of such systems becomes a necessity, investigations of the sort attempted here could provide invaluable information. Furthermore, if the standard rate constant could be convincingly shown to be related to a property of the molecule such as inter-ring torsion angle, this could lead to systems in which the kinetics of an electron transfer reaction could be modified while a measurement is in progress. Systems containing methyl viologen derivatives which change their electrochemical behaviour in response to a pulse of light have already been developed.[5,6] Though changes in the thermodynamics of these systems is currently of greater interest, kinetic behaviour could become more important if molecular devices are to approach the sophistication seen in photosynthesis.

7.2 Bismuth

The k^0 values for the first one-electron reduction of MV^{2+} and the derivatives have also been measured at the surface of platinum using FSV. Prior to Frumkin correction, the values of k^0 range from 4.7×10^{-2} to 1.3×10^{-2} cm s^{-1} for the derivatives, and a k^0 of 1.8×10^{-2} cm s^{-1} was found for methyl viologen.

The magnitude of ϕ_2 was determined in the same manner as for platinum, however the possibility of a space-charge region within the bismuth electrode was not ruled out. The application of the Frumkin correction to k^0 values obtained at bismuth gave corrected values ranging from 1.9×10^{-3} to 1.1×10^{-4} cm s^{-1} for the derivatives and 1.2×10^{-3} cm s^{-1} for MV^{2+}. A plot of these rate constants against those found at platinum was found to be linear with an intercept of 0, suggesting that the Frumkin corrections applied for the two surfaces were appropriate. It was found that the standard rate constants measured at bismuth were roughly twice what would be predicted using published theory,[7] and Fermi-level density of states measurements of the bismuth surface.[8] A bismuth DOS value of $9.1 \times 10^{22} \pm 1.4 \times 10^{22}$ cm^{-3} eV^{-1} would be required to explain the relative rates in terms of this theory. The kinetic behaviour observed at bismuth was found to be inconsistent with any analysis which used the properties of bulk bismuth, showing that a metallic bismuth surface controls the kinetics at the electrode.

7.3 Ferrocene

It has been shown that by using a high speed light source and oscilloscope, the kinetics of ferrocene oxidation upon a silicon surface can be measured using photoelectrochemical transient techniques. The analysis of the data has been shown to be very simple and the system shown to behave similar to other semiconductor systems reported previously, but with some potential dependence, probably due to the applied potentials being close to the flatband potential of the silicon. The rate of reduction of silicon bound ferrocene moieties has shown a pseudo first-order dependence on the surface concentration of ferrocene, with first-order rate constants between 1×10^3 and 2×10^3 s^{-1} being measured in each case. The data collected here suggests that determination of valence band hole concentration may be possible through careful experimental design, thus allowing the determination of the second-order rate constant of the process.

No major variation was seen in kinetic behaviour between ethylferrocene and ethenylferrocene monolayers. Ethynylferrocene monolayers were found to be highly unstable when oxidised in aqueous solution. The reason for this lack of stability is unclear and investigations into the stability and factors affecting stability for various monolayers could provide valuable data for future work. If ferrocene functionalised silicon surfaces are to be used in robust electrochemical systems, then a better understanding of their stability would greatly aid the design of such systems.[9,10] For the other monolayers, the presence of alkyl chains within the monolayer was shown to enhance stability in aqueous environments, an observation consistent with previous studies.[9]

The presence of inert alkyl chains in ferrocene monolayers had no detectable impact on the kinetic behaviour of the ferrocene moieties but a major impact on their thermodynamic behaviour. Highly distorted cyclic voltammograms (CVs) are observed for these monolayers which may be the result of non-equivalence between individual ferrocene moieties on the surface. A wide range of mixed monolayers are possible and by careful choice of monolayer for study, it may be possible to gain a greater understanding of how these alkyl chains interact with the ferrocene moieties to cause the observed distortions in the CVs. Attempts to investigate this aspect of mixed monolayers are already under way. A simple means of quantifying the ferrocene-ferrocene interactions upon the surfaces of these monolayers has been proposed here but the accuracy of the results it produces is limited by the presence of background currents on silicon.

In addition to providing kinetic data, the PC experiment was shown to provide a simple means of detecting monolayer discharge. It was found that the monolayers with higher ferrocene surface concentrations would not easily undergo oxidation without illumination, however those with lower coverage were found to have discharged via oxidation when a substantial overpotential was applied. Future work may reveal quantitative relationships between surface concentration and the overpotential at which discharge occurs.

Bibliography

[1] J. A. Alden, J. A. Cooper, F. Hutchinson, F. Prieto and R. G. Compton, *Journal of Electroanalytical Chemistry*, 1997, **432**, 63–70.

[2] K. Y. Tam, R. L. Wang, C. W. Lee and R. G. Compton, *Electroanalysis*, 1997, **9**, 219–224.

[3] E. Engelman and D. H. Evans, *Journal of Electroanalytical Chemistry*, 1993, **349**, 141–158.

[4] J. D. Norton and H. S. White, *Journal of Electroanalytical Chemistry*, 1992, **325**, 341–350.

[5] T. Masuda, M. Irie and K. Uosaki, *Thin Solid Films*, 2009, **518**, 591–595.

[6] A. C. Benniston, A. Harriman, S. Yang and R. W. Harrington, *Tetrahedron Letters*, 2011, **52**, 5315–5318.

[7] W. J. Royea, T. W. Hamann, B. S. Brunschwig and N. S. Lewis, *The Journal of Physical Chemistry B*, 2006, **110**, 19433–19442.

[8] A. Ofitserov and V. Edelman, *Physica B: Condensed Matter*, 2003, **329-333, Part 2**, 1094–1095.

[9] B. Fabre, *Accounts of Chemical Research*, 2010, **43**, 1509–1518.

[10] J. S. Lindsey and D. F. Bocian, *Accounts of Chemical Research*, 2011, **44**, 638–650.

Appendix A

Abbreviations

CA Chronoamperometry

CPE Constant phase element

CV Cyclic Voltammetry

DFT Density functional theory

DOS Density of states

EIS Electrochemical impedance spectroscopy

ET Electron transfer

Fc Ferrocene

FSV Fast scan voltammetry

GCS Gouy-Chapman-Stern

HOMO Highest occupied molecular orbital

HOPG Highly ordered pyrolytic graphite

LUMO Lowest unoccupied molecular orbital

MV^{2+} Methyl viologen dication

MV^{+} Methyl viologen monocation radical

MV^{0} Methyl viologen in its neutral form

OHP Outer Helmholtz plane

PC Photoelectrochemical Chronoamperometry

PZC Potential of zero charge

SECM Scanning electrochemical microscopy

SWV Square wave voltammetry

$TBAPF_6$ Tertbutylammonium hexafluorphosphate

UME Ultramicroelectrode

Appendix B

Symbols

A Electrode area

c Differential capacitance

C Integral capacitance

C^* Bulk analyte concentration

D Diffusion coefficient

E Potential

$E^{0'}$ Formal potential

$E_{\frac{1}{2}}$ Half wave potential

e Elementary charge

f Frequency

F Faraday's consant

i Current

i^0 Exchange current

i_l Limiting current

i_p Peak current

j Imaginary unit

K Equilibrium constant

k^0 Standard rate constant

k^0_{FC} Frumkin corrected standard rate constant

k^0_m Standard rate constant at a metal surface

k^0_{sm} Standard rate constant at a semi-metal surface

k_b Backward rate constant

k_f Foward rate constant

k_{sr} Rate of carrier recombination

k_{tr} Rate of electron transfer

L Light intensity

n Number of electrons transferred

Q Constant phase element

r Electrode radius

R Gas constant

R_{ct} Charge transfer resistance

R_u Uncompensated resistance

t Time

T Temperature

v Scan rate

W Warburg impedance

z Molecular charge

Z Impedance

α Transfer coefficient

Γ Surface concentration

ϵ Dielectric constant (Static relative permittivity)

ϵ_0 Permittivity of free space

κ Boltzman constant

λ Reorganisation energy

ω Angular frequency

ϕ Phase angle

Φ_1 Potential change across the Helmholtz plane

Φ_2 Potential change across the diffuse layer

Φ_3 Potential change across the space charge region